Massive stars before and on the main sequence

Backs, F.P.A.

Publication date
2023

Document Version
Final published version

Citation for published version (APA):
Backs, F. P. A. (2023). *Massive stars before and on the main sequence*. [Thesis, fully internal, Universiteit van Amsterdam].

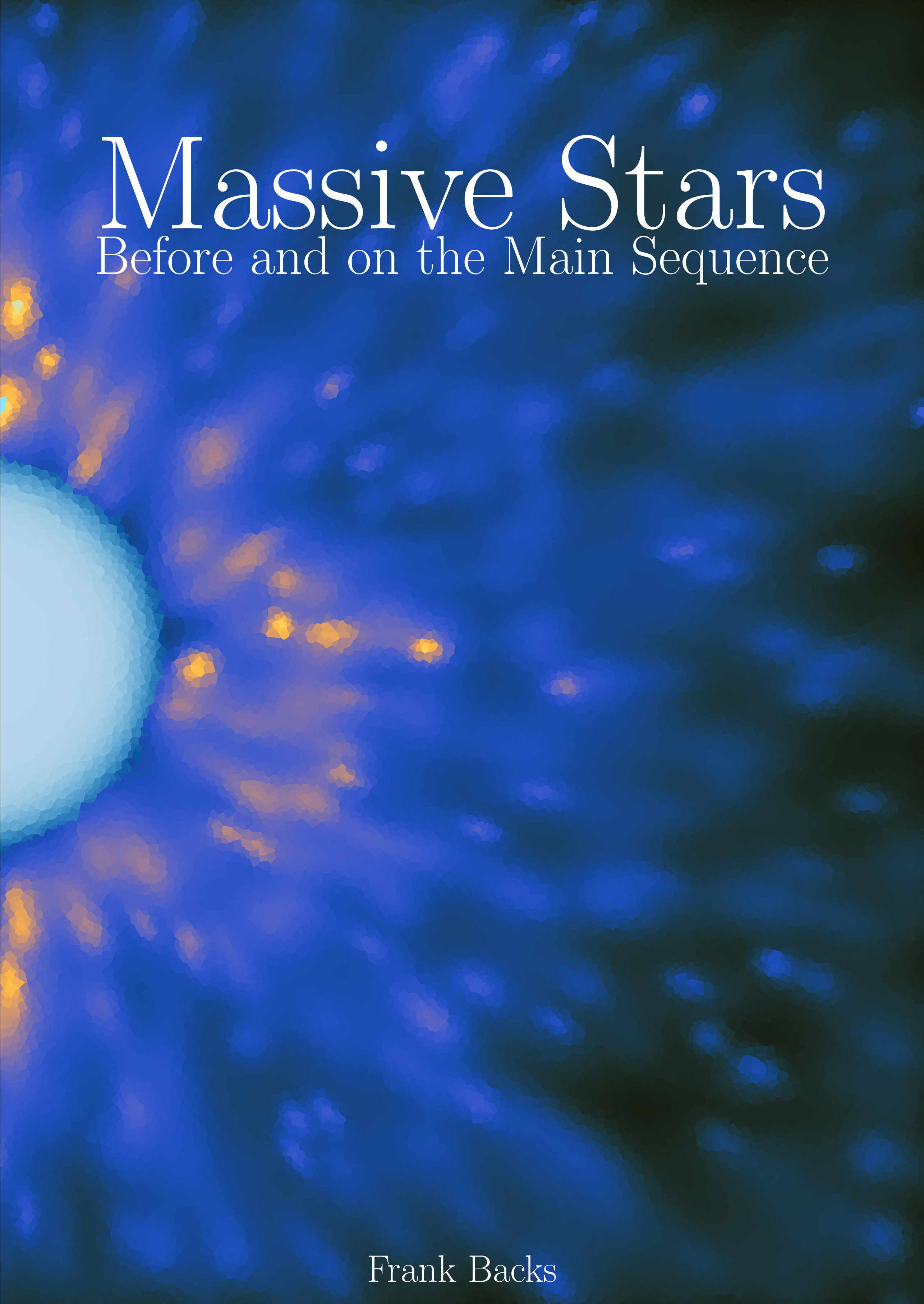

Massive Stars

Before and on the Main Sequence

Frank Backs

Massive stars before and on the main sequence

Frank Backs

contact: backsfpa@gmail.com

Massive stars before and on the main sequence
PhD Thesis, Anton Pannekoek Institute for Astronomy, Universiteit van Amsterdam

Cover: Outflowing and orbiting material. (2023)
Matplotlib on Python

Printed by: Gildeprint

UNIVERSITY OF AMSTERDAM

ANTON PANNEKOEK
INSTITUTE

The research included in this thesis was carried out at the Anton Pannekoek Institute for Astronomy (API) of the University of Amsterdam. It was part of the project ”Massive stars in low-metallicity environments: the progenitors of massive black holes” with project number OND1362707 of the research TOP-programme, which is financed by the Dutch Research Council (NWO). It was supported by the Netherlands Research School for Astronomy (NOVA). Support was occasionally provided by the Leids Kerkhoven-Bosscha Fonds (LKBF). This research makes use of data collected with the NASA/ESA Hubble Space Telescope and the Very Large Telescope (VLT) which is part of La Silla Paranal Observatory operated by the European Southern Observatory (ESO). Computations were carried out on the Dutch national e-infrastructure with the support of SURF Cooperative.

Massive stars before and on the main sequence

ACADEMISCH PROEFSCHRIFT

ter verkrijging van de graad van doctor
aan de Universiteit van Amsterdam
op gezag van de Rector Magnificus
prof. dr. ir. P.P.C.C. Verbeek
ten overstaan van een door het College voor Promoties ingestelde
commissie, in het openbaar te verdedigen in de Agnietenkapel
op 21 november 2023, te 13:00 uur

door

Franciscus Petrus Andreas Backs

geboren te Alkmaar

Promotiecommissie:

Promotor(es):	Prof. dr. Alex de Koter	Universiteit van Amsterdam
	Prof. dr. Lex Kaper	Universiteit van Amsterdam
Overige leden:	prof. dr. H.A.A. Sana	KU Leuven
	prof. dr. J.S. Vink	Armagh Observatory
	dr. A. Candian	Universiteit van Amsterdam
	prof. dr. H.J.G.L.M. Lamers	Universiteit van Amsterdam
	prof. dr. R.A.D. Wijnands	Universiteit van Amsterdam
	prof. dr. C. Dominik	Universiteit van Amsterdam

Faculteit der Natuurwetenschappen, Wiskunde en Informatica

Contents

It is dangerous to go alone! Take this.
- Old man, The Legend of Zelda

Chapter 1

Introduction

Stars with initial masses above eight solar masses are considered massive stars (Poelarends et al. 2008). This boundary of eight times the mass of the Sun is not arbitrary. It is the minimum initial mass at which stars end their life in a core collapse event that may also produce a supernova and compact object (Langer 2012). Massive stars play an important role in the formation and evolution of galaxies over cosmic time (Bromm et al. 2009; Vogelsberger et al. 2013). They are luminous and, most of their lives, hot, causing them to have intense hydrogen-ionizing radiation fields and strong outflows of gas. Their hydrogen-ionizing radiation creates hot bubbles that extend over tens of parsecs, clearing out the gas in the regions in which they formed, and sweeping up interstellar material (e.g., Spitzer 1978; Geen et al. 2015, 2016). In their stellar winds, nuclearly processed material is injected in the ambient medium (Kobayashi et al. 2020). These new elements may later serve as the building blocks of terrestrial planets and, possibly, life. Their final explosions, which can be seen up to cosmological distances, also chemically enrich and heat the medium in between the stars and may cause galactic outflows (e.g., Andersson et al. 2020). Though great strides have been made in the past decades, many aspects regarding their formation, evolution and final fate still remain uncertain. The studies presented in this thesis focus on the final stage and outcome of the formation process and the main-sequence phase that follows it.

To help improve our understanding of massive star formation we study the giant H II region M17, also known as the Omega nebula or Swan nebula. In the star cluster NGC 6618 at the center of this region, star formation started between 0–2 Myr ago (Ramírez-Tannus et al. 2017). Many of its stars have not reached the main sequence yet, i.e., they have not started core-hydrogen burning. The ones that have reached this point, only just arrived. By constraining stellar parameters of the brightest of the M17 stars, we study the outcome of star formation as close to the Zero-Age Main Sequence (ZAMS) as possible. The properties of the stars at the ZAMS set the basis or initial condition from which these stars will evolve. Some of the stars in M17 show the presence of circumstellar disks which are likely a remnant of the formation process. We scrutinize the properties of two of these disks with the goal to establish their radial and vertical extend, inner disk density and kinematic properties. These probe the process through which gas is transported from the inner disk to the stellar surface.

Massive stars suffer from mass loss throughout their lives and the process greatly impacts their evolution. We not only study it in the young M17 stars but also in stars that have long since arrived on the main sequence. A key goal in studies of massive stars is to establish how the rate of mass loss depends on stellar properties. As it is found both empirically (Mokiem et al. 2007) and theoretically (Vink et al. 2001) to also depend on the metal content – i.e., the fraction of elements heavier than helium – we study a sample of O-type stars in the Small Magellanic Cloud (SMC), a satellite galaxy of our Milky Way where the metallicity is one-fifth of that of our own galaxy. Establishing this mass loss versus metallicity dependence is essential for understanding massive star formation and evolution over cosmic time, as the metallicity content of the universe is ever increasing. We compare the outcome of this study to similar studies of stars in the Milky Way and the Large Magellanic Cloud (LMC), the latter having half the metal content of our galaxy. This allows us to quantify the effect of chemical composition on mass loss.

Stellar outflows are not simple stationary radial flows. The true intricacies of the flows are still poorly known, but already for a long time it is clear that both on small (Crowther et al. 2002; Hillier et al. 2003) and large (Henrichs et al. 1983, 1994; Eversberg et al. 1998) scales the flows show structures that are either transient in nature on short time scales, they form and dissolve while the gas is accelerating, or may persist as coherent entities over dynamical time-scales. The presence of small-scale structure complicates empirical estimates of the mass-loss rate as the optical spectral lines that serve as probes of mass loss are *also* sensitive to what is generally referred to as 'wind clumping'. We attempt to characterize the wind inhomogeneity properties of the stars studied in this thesis with advanced models in order to get the most accurate constraints on their mass-loss rates.

The lives of massive stars are further impacted by the company they keep. All massive stars born with an initial mass of at least 15 $M_\odot$ are found to have at least one companion star (Sana et al. 2014; GRAVITY Collaboration et al. 2018; Bordier et al. 2022) and once well established on the main sequence, half of these systems have periods of less than a month (Sana et al. 2012). Why all of them are binaries or higher order multiple systems and why so many are in close orbits remain open questions. To shed more light on this, we studied the properties of binaries in clusters of different ages.

All of the science topics briefly introduced above and for which studies are presented in this thesis rely on quantitative spectroscopy. Important data-sets used for these works have been obtained with the X-Shooter spectrograph mounted on UT3 of the *Very Large Telescope*, partly in the context of the X-Shooting ULLYSES project (XShootU; Vink et al. 2023), the *Hubble Space Telescope* in the context of the Ultraviolet Legacy Library of Young Stars as Essential Standards (ULLYSES; Roman-Duval et al. 2020), a program that has relied on observations with the Space Telescope Imaging Spectrograph (STIS), supplemented with archival Cosmic Origins Spectrograph (COS) data, and the *Far Ultraviolet Spectroscopic Explorer* (FUSE). The technique of quantitative spectroscopy, i.e., the analysis of spectra with models of spectral features predicted using model atmospheres, is well established (e.g., Simón-Díaz 2020). However, in this first chapter we will introduce and discuss some novel and advanced aspects of spectral modelling, techniques we employ to characterize stellar photospheres and winds as well as circumstellar disks.

In the remainder of this first chapter, we provide more context relevant for the problems at hand and of aspects of the techniques used. At the end of this introduction a brief summary is given of the main findings presented in chapters that follow.

1.1 Massive star formation

The formation of massive stars remains elusive to this day. This is caused by the combination of several hindering factors. *First*, massive stars are rare. For every $\sim$10 000 solar type stars formed, about forty 10 $M_\odot$ stars form and only a single 50 $M_\odot$ star (Salpeter 1955; Kroupa 2001). As a result, massive stars are typically far away. In dense galactic clusters or in extragalactic environments this may lead to spatial crowding problems, hindering observations of individual stars. *Second*, the formation process of massive stars is short, lasting only some 10^4 yr for a 20 $M_\odot$ star and 10^5 year for a 9 $M_\odot$ star (Hosokawa & Omukai 2009). *Third*, the formation of massive stars happens inside dense molecular clouds. Dust particles interspersed with the gas cause strong extinction of ultraviolet and optical light, hiding them from our sight. Visual extinction towards massive stars can still be as high as $\sim$10 magnitudes as they reach the zero-age main sequence (e.g. Ramírez-Tannus et al. 2017) and potentially higher. In earlier phases, the star forming clouds can have a line-of-sight extinction of several tens of magnitudes (Rygl et al. 2010). This combined with the short formation time means that a massive star is already fully assembled while still embedded and obscured. The combination of these three factors implies that it is hard to obtain observational constraints regarding formation, especially at wavelengths where the forming massive star itself is emitting more and more prominently.

1.1.1 Evolving disks and accretion mechanisms

Despite these complicating factors, constraints may be placed on the formation process through IR–radio wavelength interferometry using observatories such as *VLT Interferometer* (VLTI) at near- and mid-IR wavelengths, *Atacama Large Millimeter/submillimeter Array* (ALMA), and *Very Large Array* (VLA) at centimeter wavelengths. Into the infrared and beyond, extinction towards the sources is not as strong. Additionally, interferometry may spatially resolve the sources even if they are located at kpc distances. These observations result in an ever increasing number of disks around massive young stellar objects and pre-main-sequence stars being detected (e.g., Hanson et al. 1997; Kraus et al. 2010; de Wit et al. 2011; Cesaroni et al. 2014; Sanna et al. 2019). This strongly suggests that disk accretion plays a significant role in the formation process of massive stars, similar to their low-mass counterparts. Detections vary from large rotating toroidal structures (e.g., Zapata et al. 2008) to small remnant disks (e.g., Ramírez-Tannus et al. 2017). The former represent very early stages of formation while the latter show the later stages when the forming stars are close to the main sequence.

The large toroids have estimated masses ranging from $\sim$1 $M_\odot$ all the way up to $\sim$650 $M_\odot$ and radii varying from several hundreds of AU to $\sim$ 20 000 AU (Beltrán & de Wit 2016). The central entity may either ultimately become a single or multiple star system or even a small cluster, with the highest masses estimated to be up to $\sim$80 $\mathrm{M}_\odot$ based on observations. Given the high mass of the toroid compared to the central object, it is likely that the toroid is not stable. Moreover, the rotation is unlikely to be Keplerian. The interpretation of the velocity field in these large toroidal structures remains debated. Observations of CO, CH_3OH, and CH_3CN in hot molecular core G31.41+0.31 show motions that may be indicative of rotation as well as expansion or outflow (Araya et al. 2008; Cesaroni et al. 2011). Regardless, it is likely that these circumstellar structures feed the accretion onto the central objects despite their often high luminosity. For instance, W51 North, with an estimated luminosity of $\sim 10^5\ L_\odot$, has an accretion rate between 4 and $7 \times 10^{-2}\ M_\odot\,\mathrm{yr}^{-1}$ (Zapata et al. 2008, 2009). Toroidal systems like W51 North show the early phases of the formation of a system containing one or more massive stars.

Systems with these extended toroidal structures do not allow us to directly identify the central source, it remains deeply embedded in the cloud. Properties of such objects are therefore inferred from kinematics of the surrounding medium and the emitted luminosity. Only in much later stages of formation – actually, in the very final stage – the central object itself can be detected. Then their properties can be determined through spectroscopy and photometry (e.g., Ramírez-Tannus et al. 2017). However, this is so much later in the formation process that the circumstellar disk, if still present, possibly no longer contributes significantly to the properties of the star, specifically its mass and rotational velocity. In Chapter 2 we try to answer this question by studying the central star and remnant disk of the systems B243 and B331 in the M17 star forming region. A unique aspect of this stage of formation is that it provides the opportunity to study the interaction between disk and star, in particular the process in which the star accretes mass and angular momentum.

Two mechanisms have been proposed through which the star may accrete gas: magnetospheric accretion and boundary layer accretion. In magnetospheric accretion the central object has a strong magnetic field truncating the disk at several stellar radii. Accreting material then travels along the magnetic field lines from the inner region of the disk to the magnetic poles on the surface of the central object. Material is accelerated in this process and creates a shock where it impacts the star. During this free fall to the stellar photosphere the gas radiates resulting in characteristic emission line profiles (Hartmann et al. 1994). The shocked area, which typically only covers a small portion of the stellar surface, is heated and contributes additional continuum emission, particularly in the UV range (Calvet & Gullbring 1998). In order for magnetospheric accretion to take place the central object must have a strong magnetic field. For forming low-mass stars such a field is generated in the convective envelope (Parker 1955). However, hotter more massive stars lack the convective envelope to generate strong magnetic field (Moura et al. 2020). Spectropolarimetric observations have detected magnetic fields in only a few percent of such more massive Herbig Ae/Be stars (Bagnulo et al. 2012; Alecian et al. 2013). Mendigutía (2020) argue that the minimum magnetic field strength required to drive magnetospheric accretion is lower for massive stars compared to low-mass stars (as $B_{\mathrm{min}} \propto M^{2/3}\,R^{-3}$, where M and R are stellar mass and radius). These modest magnetic field strengths may be well below the detection threshold and therefore remain unseen.

In boundary layer accretion the material travels through the disk directly to the surface of the star. The disk and stellar surface are connected through a boundary layer. Due to viscous heating this boundary layer becomes hot causing a UV excess that can be detected. So, in terms of diagnostic signatures, similarities exist between the magnetospheric accretion model and this one. At the present time, little is known about possible differences in the efficiency of mass and momentum transfer between the two scenarios, so it is not trivial to truly distinguish between the two. Blondel & Djie (2006) study a sample of 37 pre-main-sequence Ae/Fe stars using UV spectra. They successfully fit these spectra using a boundary layer accretion model and find evidence for accretion in all but one source. Moreover, they find a correlation between accretion rate, mass, and age, with higher accretion rates for higher masses and decreasing stellar age. This work shows that, at least in principle, observed properties may be in line with the boundary layer model. For the sources B243 and B331, investigated in this thesis, we find that the inner radius almost reaches the star surface, consistent with the boundary layer accretion model.

1.1.2 Circumstellar disk diagnostics

The main diagnostic features of circumstellar disks around pre-main-sequence stars at optical to (near-)infrared wavelength are infrared excess emission, double-peaked emission lines of atomic species, and CO-bandhead emission. Fig. 1.1 shows examples of these signatures in B243 (with an estimated mass of 4.2 $M_{\odot}$) and B275 (7.2 $M_{\odot}$). In these sources, the infrared excess continuum emission is from hot circumstellar dust. In principle, this dust can be either heated through viscous heating as a result of accretion or by the radiation field of the central star. The sources shown have low accretion rates indicating that radiative heating dominates. Another potential source of excess continuum emission can be free-free radiation from an ionized surface layer of the inner disk, but only if the central star is hot enough to cause substantial hydrogen ionization.

The gas emission in the optical and NIR wavelengths originate from the hot innermost regions of the disk, regions that are exposed to direct stellar illumination. The bottom two panels of Fig. 1.1 show the emission of this hot dense circumstellar gas. The middle panel shows part of the Paschen series with the double-peaked hydrogen emission superimposed on the absorption profiles of the stellar atmosphere. The profile of this line gives us information about the kinematics of the disk material, indicative for the location of the emitting gas. In Chapter 2 we fit these emission profiles with the thermo-chemical radiative transfer disk modelling code PROTOPLANETARY DISK MODEL (PRODIMO; Woitke et al. 2009, 2016; Kamp et al. 2017; Thi et al. 2011). We find that chemistry is of great importance in the production of ionized hydrogen required to produce these lines. The bottom panel shows the CO bandhead emission from ro-vibrational transitions. It is indicative of hot dense gas. The shape, strength, and ratio between different bandheads gives great insight into the temperature and density profile of the circumstellar disk (Poorta et al. 2023). The spectra

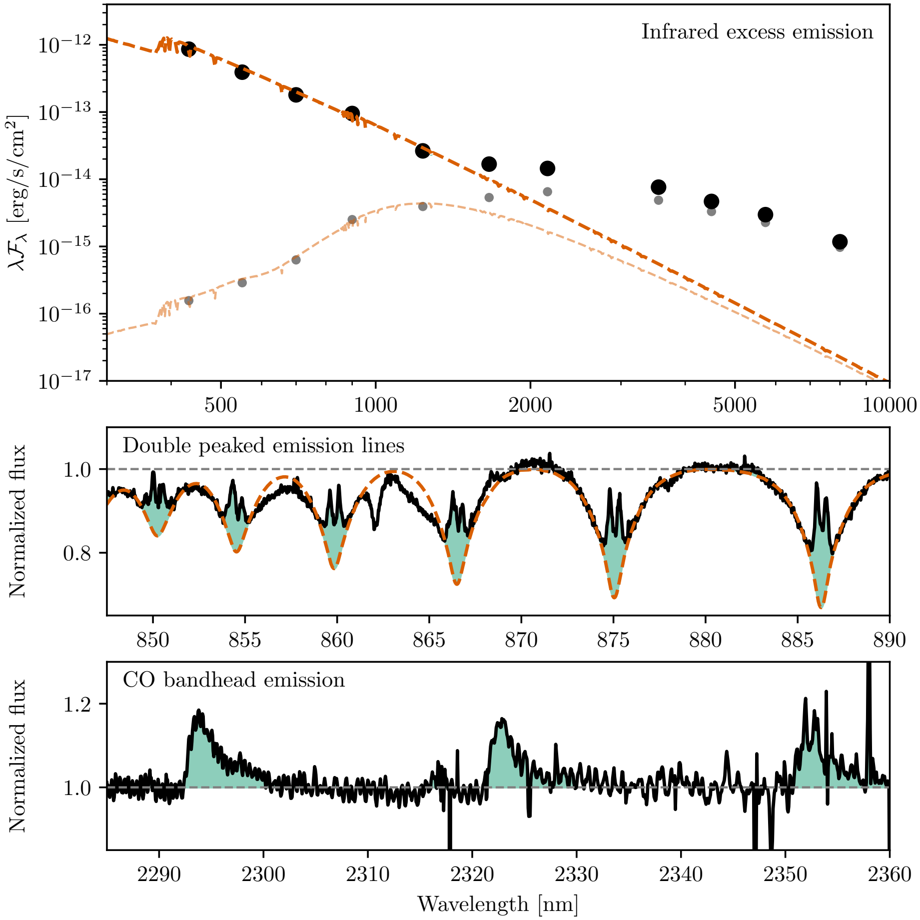

Figure 1.1: Circumstellar disk diagnostic features in late stages of star formation. *Top panel:* the infrared excess emission of B243 in M17. Black dots indicate the dereddened photometric data points with the dashed orange line a Castelli-Kurucz model spectral energy distribution (Castelli & Kurucz 2004b). The smaller and lighter dots and line indicate the reddened SED. The green marked area shows the excess emission from the circumstellar dust. *Middle panel:* the double peaked emission of the hydrogen lines superimposed on the stellar absorption lines in B243. The black line indicates the normalized observed spectrum, the orange dashed line is a BT-NextGen model fitted to the data (Hauschildt et al. 1999). The green area marks the emission from circumstellar hydrogen. *Bottom panel:* the CO bandhead emission from M17 star B275. The black line is the observed normalized spectrum, the green marked area shows the emission from CO.

of circumstellar disks may feature many other emission lines. (Derkink et al. 2023, subm.) identify a plethora of lines including hydrogen, helium, carbon, oxygen, calcium, and iron lines in the spectra of disks around pre-main-sequence stars in M17.

1.1.3 Theory of massive star formation

Observations of nearby cloud complexes indicate that 70−90 percent of all stars form in embedded clusters (Lada & Lada 2003). For massive stars ($M \gtrsim 15\,M_\odot$) this fraction appears even higher, de Wit et al. (2005) reporting only 4 ± 2 percent of O-type stars can be considered as formed outside a cluster environment. Smooth particle hydrodynamics simulations of low-mass star formation from a 500 $M_\odot$ molecular cloud show a breathtaking complexity of interactions between the many proto-stars and their disks (Bate 2018). In the first 10^5 yr these systems experience disk erosion or truncation either by ram pressure stripping or when they have a dynamical encounter with one of their siblings. Sometimes, disks are eroded and then new disks are being accreted from the molecular cloud. Star-disk encounters are common and may lead to the formation of binary systems or higher-order multiple systems. After producing bound systems from two unbound proto-stars, there is usually rapid decay of the orbital separation and eccentricity as the binary transfers angular momentum and energy to the dissipative gas, often producing a circumbinary disk. Because of the limited initial cloud mass the most massive stars formed in these simulations are about 4 $M_\odot$. However, given that almost all massive stars form in clusters and that the more massive stars tend to form in the dense central regions of the collapsing cloud (e.g. Bonnell et al. 2001; Bonnell & Bate 2006), it is extremely likely that these processes also occur in more massive molecular clouds that do form massive stars. This picture of massive star formation steers away from the idea that massive stars form in isolation, either in the field or in a molecular cloud fragment that avoids interaction with its environment (called the *monolithic collapse model;* McKee & Tan 2003; Zinnecker & Yorke 2007). Rather, massive stars form in a very dynamical environment in which they interact with other forming systems and compete for the available gas (called the *competitive accretion model*).

Does this imply that massive star formation proceeds in the same way as low-mass star formation? Possibly not, as there are distinct differences in the physics involved. We mention four such differences. *First*, feedback processes are much stronger for massive stars than for low-mass stars. Forming massive stars produce so much light that the radiation pressure they exert on the gas and dust around them is stronger than their gravitational attraction. On the one hand this could choke accretion, limiting the mass a star may accumulate; on the other hand this may heat the surrounding, changing the conditions of mass accretion (as $\dot{M}_{\rm acc} \propto T^{3/2}$). Interestingly, 3D Radiation Hydrodynamics (3D-RHD) simulations show that radiation pressure does not halt accretion, rather gas is channeled onto the star through non-axisymmetric disks and filaments that self-shield against radiation (Krumholz et al. 2009). *Second*, as mentioned above, for a massive enough proto-star the further gain in mass may proceed through a different mechanism, i.e., boundary-layer accretion rather than magnetospheric accretion. If the presence of a convective envelope would dictate the occurrence of strong surface magnetic fields, possibly a requirement for magnetospheric accretion, the boundary between the two modes of accretion would be at about 4 $M_\odot$ (Moura et al. 2020) (but see above). *Third*, stars gaining more than about 8 $M_\odot$ lack a pre-main-sequence phase (Palla & Stahler 1993), i.e. they may still accrete a significant fraction of their final mass while already on the main sequence. *Fourth*, because massive stars are expected to form in the densest parts of collapsing molecular clouds, they may be more susceptible to merging with other forming stars. Stellar merging requires a high (proto-)stellar density and is expected to be more probable between binary-single and binary-binary systems than for single-single systems (Bonnell & Bate 2005). For molecular clouds forming Globular Clusters densities may indeed be high enough to cause collisions (Fregeau et al. 2004). Whether these conditions are sufficiently representative for star-forming sites in the present-day Milky Way is unclear. In the low-mass star-forming simulations discussed above (by Bate 2018) no mergers of sink particles were found. 2D/3D-RHD simulations of isolated massive-star system formation, however, show disk fragmentation due to gravitational instabilities of the disk and the (onset of the) formation of massive companions (Krumholz et al. 2009; Kuiper et al. 2010; Oliva & Kuiper 2020). If migration of such companions is efficient for massive primaries, possibly merging could be more important for massive stars than for low-mass stars. In Chapter 3 we show and quantify, for the first time, that migration of companions is happening for young massive stars. Whether this results in merger events remains an open question.

1.1.4 Close binary formation

3D-RHD simulations of isolated massive star formation that account for heating by ionizing and non-ionizing photons tend to form companions rather far from the primary star (Peters et al. 2010; Oliva & Kuiper 2020), at a few times 10^1 to $\sim 10^3$ AU. Heating by stellar radiation can suppress gravitational instabilities from occurring in dense filaments close to the central object, but shielding of such filaments further out prevents the whole disk from becoming stable.

Still, massive stars of $\sim 2-4$ Myr tend to be found in binary systems in close orbit (e.g., Moe & Di Stefano 2017) with about half of the systems having periods of less than a month (Sana et al. 2012). Binaries with such short orbital periods, hence separations, are expected to interact and possibly merge during their lifetime, often already on the main sequence. Indeed, such merging events may explain part of the blue straggler population (Schneider et al. 2015) and potentially also the presence of strong large-scale magnetic fields in some massive stars (Schneider et al. 2016; Keszthelyi et al. 2021), as such fields are expected to be created in the merging process. Ultimately, it is also massive close binaries that are responsible for gravitational wave detections of compact object mergers (e.g. Abbott et al. 2016, 2017).

Sana et al. (2017) study the binary statistics of a small sample of young intermediate mass and massive stars in the young ($\lesssim 1$ Myr) cluster M17. They indeed find evidence for the binaries in this young region to be wider than those of the older clusters studied in Sana et al. (2012), later supported by work by Bordier et al. (2022). As Chapter 3 of this thesis builds on this discovery, we briefly outline the applied technique that leads to their result. For a

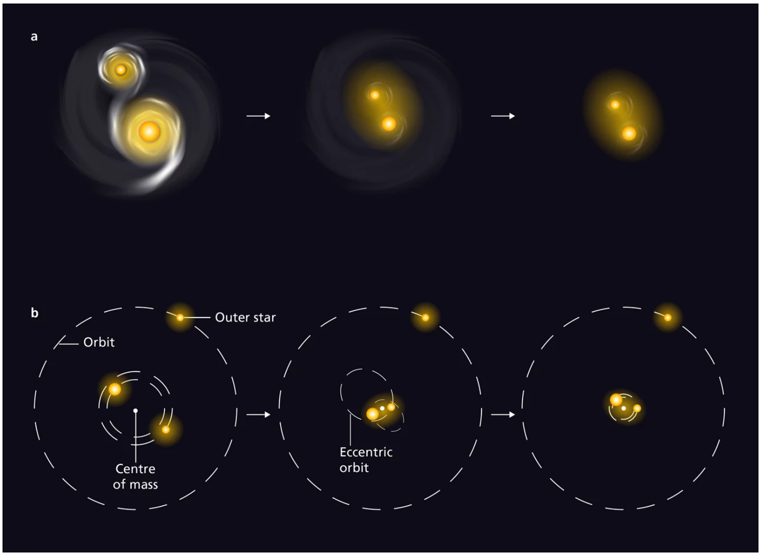

Figure 1.2: Possible binary hardening scenarios. *Top:* A forming binary system grows closed through interactions of their (remnant) circumstellar material. *Bottom:* Binary hardening though interactions in a multiple star system. A third star perturbs a inner binary resulting in a smaller orbit. Figure credit: MPIA graphics department.

single epoch of observation they measure the radial velocity of a sample of M17 stars. The dispersion of the distribution of these velocities is $\sigma = 5.6\,\mathrm{km\,s^{-1}}$, which is narrow compared to the velocity distribution of the older clusters (which have $\sigma \sim 20-30\,\mathrm{km\,s^{-1}}$). Two effects contribute to the radial velocity distribution of the cluster stars; *first*, a dispersion due to random motions of the stars, and *second*, a dispersion due to orbital motion in binaries. When these binaries have short orbits, one measures large radial velocities, hence a large dispersion. Dismissing the possibility that their findings are simply the result of an anomalously low binary fraction in M17, supported by the notion that the binary fraction of massive star-forming clusters seems ubiquitous at $\sim 60-70$ percent (e.g. Kouwenhoven et al. 2007a; Sana et al. 2008; De Becker et al. 2006), they conclude that the binaries in M17 should be in relatively wide orbits.

By implication, this suggests that over time the binaries in M17 should harden (i.e., reduce their orbital period) for the cluster to get similar radial velocity dispersions to the older massive clusters. What mechanisms could cause such binary hardening? Fig. 1.2 shows schematic scenarios for two such mechanisms. The top scenario involves two stars formed at a large separation with circumstellar material. The interaction between the stars and their disks allows the system to lose angular momentum and the stars to move to a closer orbit. Notice that the angular momentum of the system cannot decrease if only a circumbinary disk is present (Muñoz et al. 2019). The bottom scenario assumes a triple star system. The outer star, at a relatively large separation and inclined with respect to the plane of the inner binary, perturbs the inner system through the Kozai-Lidov effect, allowing it to harden over time. A third method for hardening binaries (not depicted in Fig. 1.2) could be through dynamical binary-binary or binary-single star interactions. In such interaction, one star or system may be ejected from the cluster entirely, resulting in a runaway (e.g., Oh & Kroupa 2016; Stoop et al. 2023). The kinetic energy for the runaway is taken from the orbital energy of the binary system responsible for the ejection, hardening it.

1.2 Properties and age of Messier 17

Three of the chapters in this thesis concern the analysis of young massive star systems in the star-forming region Messier 17 (M17), also known as the Swan Nebula, Horseshoe Nebula or Lobster Nebula, among other names. What makes M17 so special is it exceptionally young age, its relative proximity, and the possibility to see the photospheres of the deeply embedded and obscured massive star population using 8m/4m-class telescopes. In this section, we introduce this key region for furthering our understanding of the processes involved in and outcome of massive star formation.

M17 is one of the best studied giant H II regions. It is located in the Carina-Sagittarius spiral arm of the Galaxy at a distance of 1675^{+19}_{-18} pc (Stoop et al. 2023, submitted). The bright nebula measures 11.2' or 5.5 pc across. The ionized hydrogen indicates the presence of young hot stars. These are located at the core of the region in cluster NGC 6618. The cluster contains about 20 O-type stars; more than a 100 B-type stars are identified as well (Hoffmeister et al. 2008). The total luminosity of M17 is $2.4\times10^6\,\mathrm{L}_\odot$ (Povich et al. 2007). The ionized region is still embedded in a giant molecular cloud. Fig. 1.3 shows optical to near-infrared (NIR) images of M17. The bright H II region is located in the center. Dark molecular clouds can be seen to the north, east, and south in the top image. Some highly reddened sources can be seen in or behind the cloud. In the center, in front of the ionized material, some of the dense molecular gas remains, best seen in the bottom image. It causes a darker spot with reddened stars inside. Some filamentary structures of cold material can be seen crossing in front of and inside the bright hot material.

The presence of the cold, dense molecular gas (Nguyen-Luong et al. 2020) suggests that the stars have formed very recently or are in the process of being assembled. Studies of the stellar content of M17 reveal stars with clear signatures of circumstellar material in the form of hot dust, double-peaked hydrogen emission lines, and CO-bandhead emission (Hanson et al. 1997; Ramírez-Tannus et al. 2017). These reveal (remnants of) accretion disks signifying the youth of the stellar population in M17 with possibly a pre-main-sequence component. The age of cluster has been estimated to be between 0 to 2 Myr (Ramírez-Tannus et al. 2017) and is constrained from a comparison of stellar properties with main-sequence evolutionary tracks. The upper limit on this age is set by the lack of evolved (massive) main-sequence stars. The pre-main-sequence population more luminous than $10^3\,L_\odot$ will reach the zero-age main-sequence within $\sim 10^5$ yr and have started formation up to 0.2 Myr ago. An alternative way of determining the age of the cluster is based on the time it has taken runaway O- and B-type stars from the cluster to travel to their current location (Stoop et al. 2023). This employs *Gaia* proper motions to trace back the path of the runaway stars to the cluster core. Assuming that

Figure 1.3: Giant H II region M17 in the Sagittarius-Carina arm of the Milky Way. The images have the same field of view ($\sim$18’). *Top panel*: Composite image based on the *Two Micron All Sky Survey* (2MASS) data with the J band represented in blue, H in green, and K in red. *Bottom panel*: Composite image from *VLT Survey Telescope* (VST) OmegaCAM with the G band represented in blue, R in green, and I in red. Credit: ESO/INAF-VST/OmegaCAM.

Table 1.1: Overview of global and atmospheric properties or modelling parameters investigated in the studies presented in this thesis. The middle column indicates the units used in this work.

Parameter	Units	Description
		Stellar atmosphere
T_{eff}	K	Effective temperature
g	cm s^{-2}	Gravitational acceleration
$v \sin i$	km s^{-1}	Projected equatorial rotation
He	$n_{\mathrm{He}}/n_{\mathrm{H}}$	Abundance of helium relative to hydrogen
C, N, O, Si, P	$\log n_{\mathrm{x}}/n_{\mathrm{H}} + 12$	Abundance of C, N, O, Si, and P relative to hydrogen
L	$\mathrm{L}_{\odot}$	Luminosity of the star
		Wind
$\dot{M}$	$\mathrm{M}_{\odot}$ yr^{-1}	Mass-loss rate
v_{∞}	km s^{-1}	Terminal wind velocity
β	-	Index of the β velocity law
f_{cl}	-	Clumping factor
f_{ic}	-	Inter-clump density contrast
f_{vel}	-	Velocity porosity
v_{windturb}	v_{∞}	Wind turbulence velocity
$v_{\mathrm{cl,start}}$	v_{∞}	Velocity at which clumping starts

stars can be ejected from the cluster directly after formation through dynamical interactions, the oldest runaways will give an estimate of the age. Stoop et al. (2023, submitted) also apply this method to M17 and find an age of $\sim$ 0.75 Myr. In Chapter 4 we reassess the age for M17 using stellar properties for a larger sample than employed by Ramírez-Tannus et al. (2017) and confronting these to evolutionary tracks. We find $0.4^{+0.6}_{-0.2}$ Myr, in line with previous results. Therefore it is firmly established that indeed M17 is a very young cluster, ideally suited to study the pre-main sequence evolution and (almost) zero-age main-sequence properties of massive stars.

1.3 Stellar atmospheres and winds

Accurate stellar properties are essential for identifying and quantifying the physical processes that control the lives of massive stars, such that their present-day age and evolutionary state may be established as well as the course of their past and future evolution. Table 1.1 lists some of the most important global, surface and wind parameters as they are used in this work. In the following, we describe these parameters and discuss how they are derived. In doing so, we will focus on a discussion of wind and, especially, wind clumping parameters, as the studies presented in this book are among the first that apply a prescription for outflow inhomogeneities that accounts for both optically thin and thick clumps of gas. For an excellent expose on quantitative spectroscopy of hot stars, see Simón-Díaz (2020).

1.3.1 Properties of stellar atmospheres and how to diagnose them

Understanding massive stars begins at their atmospheres. Fig. 1.4 shows an example of three stellar atmosphere properties and corresponding diagnostic features. The first, effective temperature T_{eff}, is typically determined in O-type stars based on the ratio of the strength of He I and He II lines. Such ratios, like He II 4541 / He I 4471, are great indicators of the temperature of the star as helium is an abundant element with strong lines in the optical range from 4000 to 5000 Å. A hotter star would have more ionized helium in its atmosphere, and therefore stronger He II lines. As more helium gets ionized, the He I lines become weaker. Nearly all lines, including wind lines, in the spectrum of a star are affected by the effective temperature.

The middle panels of Fig. 1.4 show two examples of lines that are sensitive for surface gravity. Hydrogen lines are strongly affected by collisional or pressure broadening through the linear Stark effect. In high surface gravity stars (say, dwarf stars) the density in the photosphere is relatively high, favoring collisions of the hydrogen atom with free electrons. This causes strong broadening of the Balmer lines. For low surface gravity stars (say, supergiants) the photospheric density is relatively low, consequently collisional broadening is not as severe and the Balmer lines are narrower. If the surface gravity g is constrained, the mass of the star may be derived using $M_{\text{spec}} = gR^2/G$, where R is the stellar radius and G the gravitational constant. The stellar radius follows from an absolute flux calibration of the spectrum and requires the distance to the source to be known. The subscript 'spec' distinguishes this mass estimate from that from comparing stellar properties (especially, L and T_{eff}) to evolutionary tracks.

The bottom panels of Fig. 1.4 show the effect of surface rotation. Stellar rotation both blue-shifts and red-shifts the spectral lines as a result of the Doppler effect. In case of strong rotation the appearance of the star can be significantly different, with subtle features becoming blended with the continuum light and getting lost in the noise of the spectrum. We observe the projected surface rotation, $v \sin i$, and as we generally do not know the inclination of the system, we can not access the true rotation speed v.

Surface abundance affects the strength of line features of the respective species, with a higher abundance resulting in stronger spectral lines (unless they are saturated). The abundance of elements heavier than helium give insight in the metallicity of the star. Surface abundances are probes of the mixing processes ongoing inside of the star and of stellar age. Through convective and rotational mixing, material may be transported from the stellar core, where thermo-nuclear reactions are ongoing, to the surface.

Finally, we determine the stellar luminosity $L = 4\pi R^2 \sigma T_{\text{eff}}^4$, where σ is Stefan-Boltzmann's constant. As pointed out above, in order to constrain the luminosity an absolute flux estimate is required. Often photometry of part of the spectral energy distribution (SED) is used, which allows to correct for possible interstellar extinction in the line-of-sight toward the stars. To do so, the observed SED is compared to theoretical SEDs selected using constraints of the temperature and other photospheric properties. To match up the two, one simultaneously fits the stellar radius and wavelength-dependent extinction, for an adopted distance.

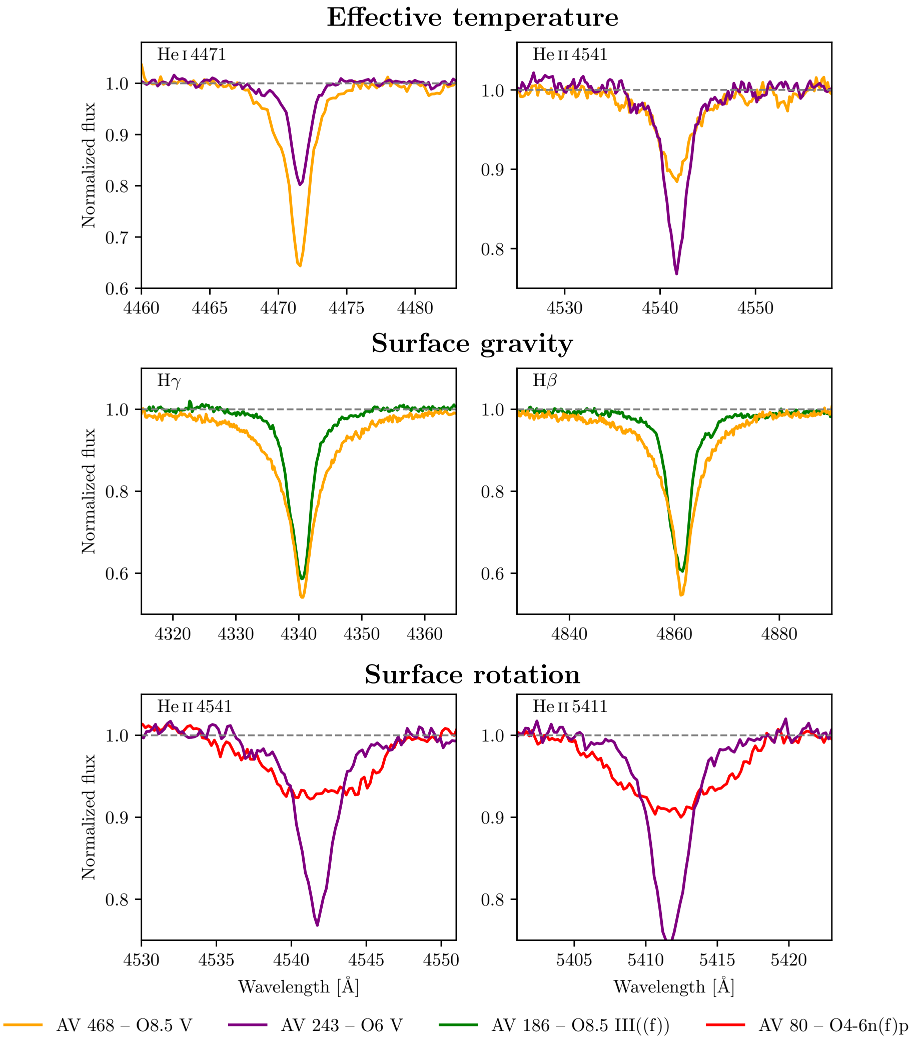

Figure 1.4: Examples of diagnostic lines of stellar parameters. *Top panels* show the He I 4471 and He II 4541 lines of two example SMC stars, AV 468 and AV 243. These lines are important for the determination of the effective temperature of a star. *Middle panels* display the Hγ and Hβ lines of AV 468 and AV 186. These lines are sensitive to the surface gravity of the star. *Bottom panels* present the effect of surface rotation on the profiles of two He II lines of AV 243 and AV 80.

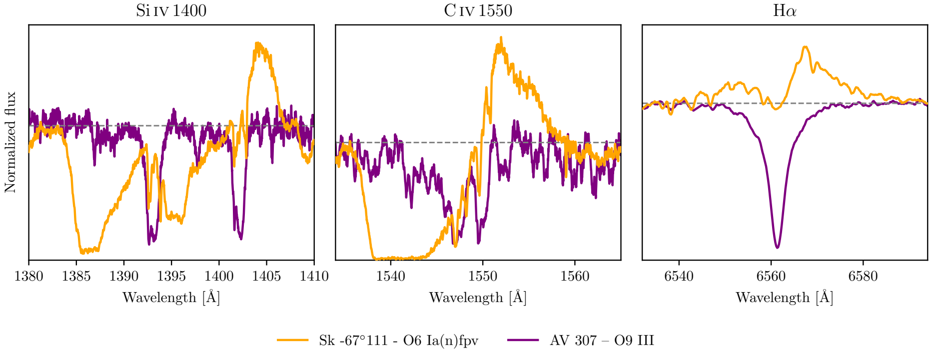

Figure 1.5: Example of diagnostic lines for stellar winds. The orange line shows the normalized line profiles of the high mass-loss rate LMC star Sk -67° 111, the purple lines show the low mass-loss rate SMC star AV 307. Clear P Cygni profiles are visible for the UV lines of the star with the strong wind, with the C iv 1550 line even being partly 'flat-bottomed' at zero flux indicating saturation. AV 307 shows photospheric profiles for all lines, with only a weak absorption on the blue side of the carbon line. The Hα line is in emission for the high mass-loss star and in absorption for the low mass-loss star. Interstellar and metal absorption lines are visible throughout the UV spectra.

1.3.2 Properties of stellar winds and how to diagnose them

Stellar winds of hot massive stars can be detected in several ways. Lau et al. (2022), e.g., detect the wind of a Wolf-Rayet star and its companion by directly imaging it with high spatial resolution. Unfortunately, the winds of the vast majority of stars cannot be spatially resolved. Most often, one relies on spectral features revealing the presence of outflows. For instance, one may measure the excess (sub-)millimeter or radio emission of the star (Wright & Barlow 1975; Abbott et al. 1980). The ionized outflow produces free-free continuum emission which can be observed at long wavelengths with spectral slope $\mathscr{F}_\nu \propto \nu^{0.6}$. This emission can be modelled with a relatively simple model as the observed flux only depends on the mass-loss rate and terminal velocity of the outflow, the distance to the star, and the clumping of the wind (see below). X-ray flux, originating in shocks in the stellar outflow (Lucy & White 1980) or at the interface of a wind blown bubble and the ambient medium (e.g., Geen & de Koter 2022) too may be a diagnostic of the presence of a stellar wind.

In this work we will focus on spectral lines as wind diagnostics. Fig. 1.5 shows an example of three of those diagnostic lines, the Si iv 1400 doublet, the C iv 1550 doublet, and Hα. Two stars are shown: the LMC O6 supergiant Sk -67° 111 and SMC O9 giant AV 307. The latter is an example of a star with a weak wind. The former shows strong wind features with pronounced P Cygni profiles in the UV lines in the left two panels. The two lines are resonance lines, meaning that they originate from an allowed transition between the ground state and the first excited state of an ion. The third line, Hα, shown in the rightmost panel, is in emission. Hα is a recombination line and the emission is the result of a cascade of the captured electron from high excitation states to low excitation states, passing through the levels with main quantum numbers $n = 3$ and $n = 2$. As two particles are involved, a proton and a free electron, the strength of recombination lines essentially scales with the square of the density. For resonance lines the strength depends linearly on the density of the relevant ion.

All other things being equal, stronger wind features indicate higher mass-loss rates. Still, it is good to realize that other stellar properties may strongly impact the strength and shape of the lines used to probe wind properties. For instance, relatively cool stars won't show the Si IV 1400 line regardless of mass-loss rate. A larger radius, for fixed mass-loss rate, will decrease the density in the onset region of the wind, decreasing the strength of recombination lines, which are formed relatively close to the stellar surface, as their strength depends on ρ^2, where ρ is the density. The terminal velocity of the wind is best measured from the blue edge of saturated P Cygni profiles. A smaller v_∞ therefore narrows the P Cygni lines. In addition, it will boost the emission in Hα as for the same mass-loss rate the wind density is increased. Next to mass-loss rate and terminal velocity, the acceleration profile of the outflow is also considered a main wind property. It is parameterized by an acceleration parameter, β, which will be introduced below. The parameter β influences the wind density profile and mostly impacts the shape of P Cygni profiles and the strength of Hα.

1.3.3 Smooth and clumped outflows

For an idealized spherically symmetric outflow the density at radius r is given by

$$\rho(r) = \frac{\dot{M}}{4\pi r^2 v(r)}, \tag{1.1}$$

where $\dot{M}$ is the mass-loss rate and v is the velocity of the wind. In models, the flow speed is usually parameterized by a β-velocity law (e.g., Castor & Lamers 1979)

$$v(r) = v_\infty (1 - b/r)^\beta, \tag{1.2}$$

with v_∞ the terminal, or maximum, velocity of the wind; $b \sim R$ is the onset radius of the wind, or wind boundary, with R the stellar radius, and β is the wind acceleration parameter. Typically, β is between 0.5–2.0.

Ample evidence has accumulated that the winds aren't perfectly behaving radial flows, but show inhomogeneities on small spatial scales, referred to as clumping. Local density concentration due to the development of shocks was already suggested by observations of X-ray emission from the wind (e.g., Feldmeier et al. 1997); differences in inferred mass-loss rates from resonance lines and recombination lines (e.g., Bouret et al. 2003; Fullerton et al. 2006) too have been ascribed to clumping. Let us illustrate the latter dichotomy by explaining the essence of the effect of clumping on spectral signatures. Assume a volume V in which the density is ρ and the medium is optically thin. We compare this volume to an equal sized volume in which the same amount of gas occupies only half of the available space. For a resonance line, the strength of which depends linearly on density, the line is not affected, i.e.,

$$\rho \cdot V = 2\rho \cdot \frac{1}{2} V = \rho \cdot V, \tag{1.3}$$

as the density in the part where the gas resides in the latter case is twice as high. For a recombination line, however, the line strength scales with density squared, hence

$$\rho^2 \cdot V \neq (2\rho)^2 \cdot \frac{1}{2} V = 2\rho^2 \cdot V. \tag{1.4}$$

Therefore, more recombinations occur and the line becomes stronger. Studies implementing this so-called 'optically thin clumping', however, did not lead to consistent UV/optical mass-loss rates. It was realized that the reason for this is that clumps very easily become optically thick especially in the strong P Cygni wind lines, and that the associated leakage of line-photons actually produces weaker resonance line profiles than predicted by models that assume a smooth wind or one in which clumps remain optically thin (Oskinova et al. 2007; Hillier 2008; Sundqvist et al. 2010, 2011; Šurlan et al. 2012, 2013; Sundqvist et al. 2014, 2018). In the analysis presented in this thesis, especially those in the final chapter, we therefore account for clumps that may be either optically thin or thick. In concluding our discussion of our approach to quantitative spectroscopy, we detail the adopted clumping parameterization and show how wind lines may be affected.

We employ the prescription of wind structure by Sundqvist et al. (2014) as implemented in the non-Local Thermodynanic Equilibrium (non-LTE) code of choice, FASTWIND (Santolaya-Rey et al. 1997; Puls et al. 2005; Sundqvist et al. 2018). The wind is assumed to consist of a two component medium. One part consists of relatively high density gas, which we will refer to as the 'clump medium', with density $\rho_{\rm cl}$, the other part, the 'inter-clump medium', has a low density ρ_{rmic}. The clumps fill a fraction of the total volume $f_{\rm vol}$ and the inter-clump medium constitutes the rest. The mean density of the wind is then given by

$$\langle\rho\rangle = f_{\rm vol}\,\rho_{\rm cl} + (1 - f_{\rm vol})\,\rho_{\rm ic}. \tag{1.5}$$

The mean density is equal to the density described in Eq. (1.1). The density of the inter-clump medium is parameterized by the contrast between the inter-clump density and the mean density, i.e.,

$$f_{\rm ic} \equiv \frac{\rho_{\rm ic}}{\langle\rho\rangle}. \tag{1.6}$$

We define the clumping factor as

$$f_{\rm cl} \equiv \frac{\langle\rho^2\rangle}{\langle\rho\rangle^2} = \frac{f_{\rm vol}\,\rho_{\rm cl}^2 + (1 - f_{\rm vol})\,\rho_{\rm ic}^2}{[f_{\rm vol}\,\rho_{\rm cl} + (1 - f_{\rm vol})\,\rho_{\rm ic}]^2}. \tag{1.7}$$

So, it is the ratio between the square of the density, relevant for the recombination lines, and the density, relevant for the resonance lines. If we assume no inter-clump medium, so $\rho_{\rm ic} = f_{\rm ic} = 0$, we get $f_{\rm cl} = 1/f_{\rm vol}$ or $f_{\rm vol} = 1/f_{\rm cl}$. If we allow for a non-void inter-clump medium we obtain

$$f_{\rm vol} = \frac{(1 - f_{\rm ic})^2}{f_{\rm cl} - 2f_{\rm ic} + f_{\rm ic}^2}. \tag{1.8}$$

Suppose the internal velocity dispersion of a clump is δv. For two clumps, spatially separated by some distance, the difference in bulk radial velocity between the clump centers may be derived from the velocity law, Eq. 1.2. Let us assume this bulk velocity difference is Δv. Then, we may introduce a normalised velocity filling factor

$$f_{\mathrm{vel}} = \frac{\delta v}{\delta v + \Delta v} \tag{1.9}$$

that describes which fraction of the Doppler shifted line frequencies allowed by the accelerating radial flow are actually capable of absorbing line photons given the clumped nature of the gas. $f_{\mathrm{vel}} \to 0$ is the case where the internal velocity dispersion of clumps is very small and the clumps are fairly separated in the main acceleration part of the outflow. In case $f_{\mathrm{vel}} \to 1$, the velocity dispersion is large and distances between clumps are relatively modest. In a sense, f_{vel} may be considered to be velocity-porosity or 'vorocity'.

The main free parameters used to describe the clumped wind are therefore f_{cl}, f_{ic}, and f_{vel}. Auxiliary parameters are the onset location of wind clumping expressed in velocity space, $v_{\mathrm{cl,start}}$; the location, $v_{\mathrm{cl,max}}$, where wind clumping reaches it maximum, given by f_{cl}, and a micro-turbulent velocity v_{windturb}. It is assumed that wind clumping increases linearly in velocity space; in our analysis we adopt $v_{\mathrm{cl,max}} = 2 \cdot v_{\mathrm{cl,start}}$. Wind turbulence is only considered when the spectral line profile is synthesized and affects the broadening of line profiles. The wind turbulent velocity scales linearly in velocity space from the micro-turbulent velocity in the photosphere to the value v_{windturb} at the terminal velocity.

In the general case an exponential distribution of clump optical depths is assumed; part of the clumps will be optically thin and part optically thick. In this thesis, we refer to this general case as 'optically thick clumping'. FASTWIND also allows for a simplified treatment in which all clumps are assumed to be optically thin and the inter-clump medium is void, following prescriptions by Owocki (2004).

Fig. 1.6 illustrates the effects of both the optically thick and optically thin clumping assumption on a set of wind sensitive lines. In this example we use a model with $T_{\mathrm{eff}} = 38\,000\,K$, $\log g = 3.6$, $\log \dot{M} = -6.2$, and f_{cl} ranging from 1 (i.e., a smooth flow) to 50 (i.e, a very clumped flow). The top four panels show UV resonance lines, safe for C III 1176 which is the transition from a meta-stable level above a semi forbidden transition to the ground state. Resonance lines most often suffer from clump optical thickness effects; once optically thick clumps are present, part of the wind material is shielded from radition, therefore does not contribute to line emission. This typically makes wind features less pronounced, but subtleties exist. The bottom two panels show recombination lines in the optical. The recombination lines are mostly optically thin, so allowing clumps to become optically thick does not affect their line profiles much. However, these lines are strongly affected by clumping, with significantly stronger lines for higher clumping factors.

First, we focus on the optically thin case (solid lines in Fig. 1.6). If a line is strong and saturated, it might not be affected by clumping at all, as is the case for C IV 1550 line. C III 1176 and Si IV 1400 both originate from an ion that is below the dominant ionization stage. This implies that the increased clumping factor, which increases the recombination rate due to the increased density, increases the strength of these lines. For N V 1240 the opposite is the case. N V lies above the main ionization stage, so increased recombination

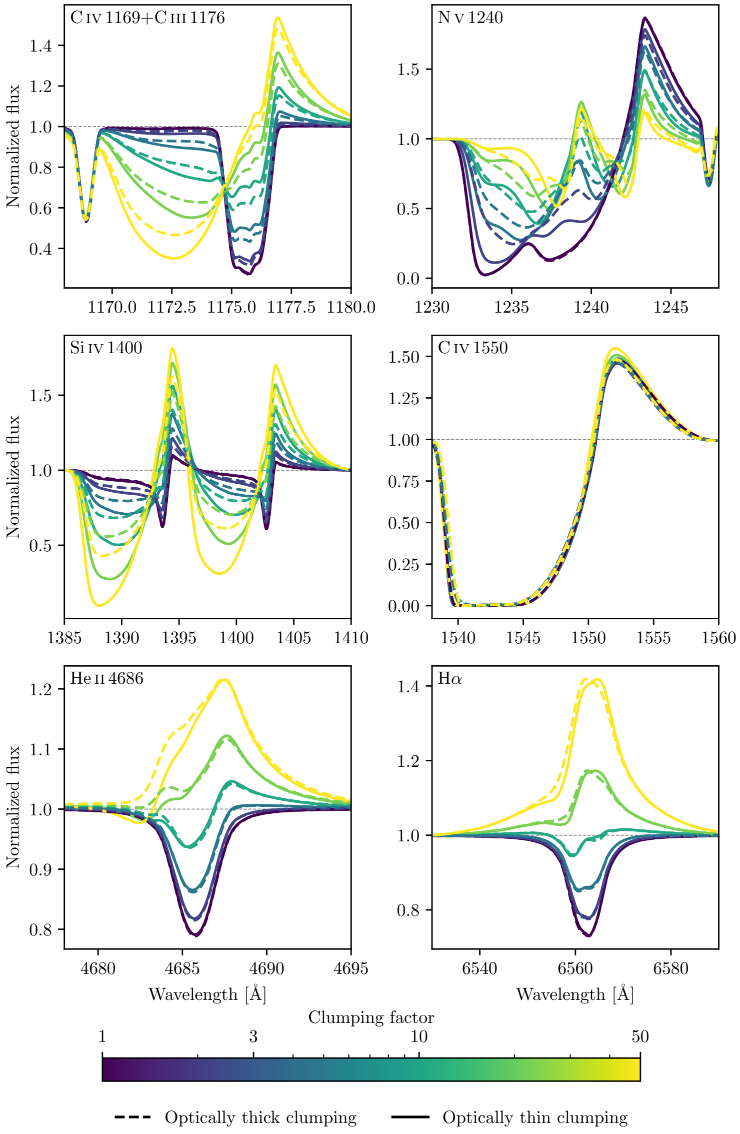

Figure 1.6: Effect of optically thin and optically thick clumping on wind sensitive lines. The model profiles are calculated using both the optically thin and optically thick clumping prescriptions in FASTWIND. The models has $T_{\text{eff}} = 38\,000$ K, $\log g = 3.6$, and $\log \dot{M} = -6.2$. In the optically thick case we use $f_{\text{ic}} = 0.1$ and $f_{\text{vel}} = 0.5$. In both cases no wind turbulence is included. The color of the line indicates the clumping factor, which is varied between 1 (a smooth wind) and 50. Dashed lines indicate optically models for the optically thick clumping prescription, and solid lines those for the optically thin clumping prescription.

results in less nitrogen in the N v stage. As a result, the wind feature of this line becomes less pronounced with an increased clumping factor. The behaviour described here may differ per star, a hotter or cooler star may show different trends.

When considering optically thick clumping the wind profiles of the resonance lines become less pronounced, as essentially less of the material in the wind is contributing. This pertains to the C iii 1176 line and Si iv 1400 doublet, and to some extent the N v 1240 doublet. The C iv 1550 doublet remains saturated and therefore unchanged. The behaviour of N v 1240 is slightly more complex as the optically thick clumping case considers the inter-clump medium. This low-density material is more easily ionized, which may help the formation of the N v line.

1.3.4 Theory of stellar winds

In the final chapter of this thesis, we shift gear from massive stars that are still approaching or have just arrived on the ZAMS to stars that have already progressed in their main-sequence evolution. Moreover, the stars scrutinized in Chapter 5 are located in the low-metallicity SMC satellite galaxy. Like the study of the M17 stars in the preceeding chapter, we are concerned with an analysis of photospheric and wind properties. In particular, we want to explore the way in which mass loss depends on metal content when also considering the possibility that the outflows of stars contain both optically thin and thick clumps.

The driving mechanism of hot massive stars has been identified as radiation pressure exerted on spectral lines of mostly CNO and iron-group species (Castor et al. 1975; Abbott & Lucy 1985). These feature copious numbers of lines in the ultraviolet, where the stars output the bulk of their light. This implies that stars relatively abundant in metals drive stronger winds than those with relatively few metals, all other properties remaining the same (e.g. Vink et al. 2001). As mass loss is such an important factor in the lives of stars, this has far reaching consequences for, e.g., the end products of evolution. Indeed, it is found that several types of exotic supernovae, including long-duration gamma-ray bursts (e.g., Savaglio et al. 2009; Modjaz et al. 2008), super-luminous supernovae (e.g., Chen et al. 2017), and pair-instability supernovae (e.g., Young et al. 2010), favor lower metallicity environments. It also implies that metal free primordial stars, composed of the species formed in baryogenesis only (e.g., Hirano et al. 2015), must have lost relatively little mass (e.g., Kudritzki 2002), with important consequences for their end of life products such as relatively massive black holes (e.g., Marigo et al. 2003).

It is therefore important to establish the empirical relation between mass-loss and stellar properties, including metallicity, and to confront these to theoretical models. Predictions to allow for such a comparison have become available over the past decades (de Koter et al. 1997; Vink et al. 2001; Krtička & Kubát 2018; Björklund et al. 2021). Empirical studies focusing on the brightest stars ($\log L/L_\odot \gtrsim 5$) find $\dot{M} \propto Z^{0.5-0.8}$ (Mokiem et al. 2007), essentially in agreement with theory. Interestingly, recently Marcolino et al. (2022) reported a shallower dependence $\dot{M} \propto Z^{0.1}$ at lower luminosities ($\log L/L_\odot \sim 4.5$).

As the winds of hot massive stars are driven by radiation one may anticipate that the mechanical momentum of the stellar wind flow is mostly a function of photon momentum (Kudritzki & Puls 2000). Indeed, the theory of line-driven winds (Castor et al. 1975; Puls et al. 2000) predicts that

$$D = \dot{M} v_{\infty} (R/\mathrm{R}_{\odot})^{1/2} \propto L^{1/\alpha'} \left[M(1-\Gamma)\right]^{3/2-1/\alpha'} , \tag{1.10}$$

where D is the *modified wind momentum* and $M(1-\Gamma)$ the effective mass, i.e., the mass corrected for the Eddington factor Γ. The index $\alpha' = \alpha - \delta$ is composed of the exponent α of the line-strength distribution function and a correction factor δ for a gradient in the ionization fraction of wind driving lines if one proceeds through the wind. A small value of α implies many weak, optically thin lines contribute to the wind driving; a maximum value of $\alpha = 1$ would imply only optically thick lines contribute. For O-type stars and early-B supergiants typical values are $\alpha \sim 2/3$ and $\delta \sim 0.05 - 0.1$ (Puls et al. 2000; Kudritzki & Puls 2000). These values imply that the absolute value of the exponent of the effective mass is very modest, reducing its influence on D. It is for this reason that an analysis of modified wind momentum is more straightforward than one that directly addresses the mass-loss rate. In Chapter 5 we therefore study the dependence of mass-loss on metallicity and luminosity in terms of this quantity.

1.4 This thesis

In Chapter 2 we present the analysis of two disks around pre-main-sequence stars in the giant H II region M17. The stars B243 and B331, with estimated masses of 6 and 12 $\mathrm{M}_{\odot}$, show IR-excess emission, double-peaked hydrogen emission lines, and CO-bandhead emission along with other double-peaked emission lines. We study in detail the IR-excess and hydrogen emission lines using the thermo-chemical radiative transfer code ProDiMo. We find that the chemistry in the disk is essential to producing the ionized hydrogen required to reproduce the strength of the observed emission. Additionally, the line profiles of the hydrogen lines indicate that the disk reaches down to the stellar surface consistent with boundary layer accretion. The analysis of the IR emission indicates that the more massive of the two stars, B331, has a large dust-free inner cavity. The disk of this star is lacking hot dust; dust is only present at temperatures below about 400 K. The dust disk of B243 does reach down to the dust sublimation radius at ~3 AU, where the solid-state particles reach temperatures of 1500 K. The relatively low flux at the longest available wavelength point (at 8 μm) provides tentative indications that the disk of B243 may be truncated. The thermal infrared spectral energy distribution suggests that only a thin ring of hot dust is present around B243. The presence of an dust free inner cavity for B331 and possible truncation of the dust disk of B243 indicates the possible disruption of the disks.

Chapter 3 is concerned with the radial velocity dispersion of massive stars in several young clusters. We establish a trend in this radial velocity dispersion with the age of the cluster, with older clusters having broader radial velocity distributions. This dispersion is an indirect indication of the multiplicity statistics of the cluster stars. If a cluster contains many close binaries the dispersion of radial velocities will be relatively wide, as the contribution of orbital velocities to the radial velocity of the stars will be significantly larger than that due to cluster dynamics. Using this concept, we determine that the youngest clusters either have a lower binary fraction, or that binaries form at large separations and harden in 1 to 2 Myr to become close binaries.

The stellar parameters of 18 young stars in M17 are studied in Chapter 4 to investigate the outcome of massive star formation. The sample covers stars with spectral types ranging from B9 to O4.5, of which the later types are still pre-main-sequence stars. New superior quality VLT/Xshooter spectra revealing the atmospheres of these highly extincted stars are fitted using the non-LTE radiative transfer code FASTWIND, allowing, for the first time, to place constraints on the mass-loss rates of massive PMS stars. From the temperature and luminosity of the stars we infer masses and ages from MIST pre-main-sequence evolutionary tracks. We find an average age of the cluster of only $0.4^{+0.6}_{-0.2}$ Myr. Based on this young age, we empirically identify the location of the ZAMS for massive stars, which is consistent with the predicted location by MIST tracks. We signal a strong trend in stellar age and mass, with the lower-mass stars appearing older. This is not in line with a co-eval crossing of the birthline. Furthermore, we determine the projected rotational velocity of the stars at the ZAMS and find a tentative bimodal distribution. The mass-loss rates of the stars are well constrained for the bright ($L > 10^4\,\mathrm{L}_\odot$) stars, but for the fainter (pre-main-sequence) stars we find values that may need to be considered upper limits up to $10^{-8.5}\,\mathrm{M}_\odot\,\mathrm{yr}^{-1}$.

Chapter 5 focuses on the mass-loss and clumping properties of winds of O-type stars in the SMC. We study a sample of 13 stars with spectral types ranging from O4 to O9.5 and luminosity classes III to I. Through quantitative spectroscopic analysis of UV and optical spectra from HST, FUSE, and VLT/Xshooter, using FASTWIND stellar atmosphere models, we infer stellar atmosphere and wind properties. We allow for optically thick clumps in our analysis. We determine an empirical mass loss vs. luminosity relation and find good agreement with theoretical predictions. We find strongly varying wind clumping properties with values for the clumping factor ranging from 2 to 30 for well reproduced stars. Additionally, the location of the onset of clumping varies from the stellar surface to 0.23 times the terminal velocity. Despite the excellent data quality it remains challenging to constrain many of the wind structure parameters. We compare the results of the SMC sample to similar studies of LMC and MW stars to determine an empirical mass-loss vs. metallicity relation taking into account optically thick clumping. With $\dot{M} \propto Z^m$ we find $m = 1.02 \pm 0.30$ at $L = 10^{5.75}\,\mathrm{L}_\odot$, which is consistent with earlier works. At lower luminosity this dependence gets steeper with $m > 2$, i.e., the mass-loss versus metallicity relation is also a function of luminosity. Such a dependence has already been found in mass-loss rate predictions, but significantly weaker than the empirical result found here.

If every porkchop were perfect, we wouldn’t have hot dogs.
– Greg Universe

Chapter 2

Massive pre-main-sequence stars in M17: Modelling hydrogen and dust in MYSO disks

---

F. Backs, J. Poorta, Ch. Rab, A. R. Derkink, A. de Koter, L. Kaper, M. C. Ramírez-Tannus, I. Kamp

Astronomy & Astrophysics, 2023, 671, A13

Abstract

Context. The young massive-star-forming region M17 contains optically visible massive pre-main-sequence stars that are surrounded by circumstellar disks. Such disks are expected to disappear when these stars enter the main sequence. The physical and dynamical structure of these remnant disks are poorly constrained, especially the inner regions where accretion, photo-evaporation, and companion formation and migration may be ongoing.

Aims. We aim to constrain the physical properties of the inner parts of the circumstellar disks of massive young stellar objects B243 ($6\,M_\odot$) and B331 ($12\,M_\odot$), two systems for which the central star has been detected and characterized previously despite strong dust extinction.

Methods. Two-dimensional radiation thermo-chemical modelling with ProDiMo of double-peaked hydrogen lines of the Paschen and Brackett series observed with X-shooter was used to probe the properties of the inner disk of the target sources. The model was modified to treat these lines. Additionally, the dust structure was studied by fitting the optical and near-infrared spectral energy distribution.

Results. B243 features a hot gaseous inner disk with dust at the sublimation radius at ∼3 AU. The disk appears truncated at roughly 6.5 AU; a cool outer disk of gas and dust may be present, but it cannot be detected with our data. B331 also has a hot gaseous inner disk. A gap separates the inner disk from a colder dusty outer disk starting at up to ∼100 AU. In both sources the inner disk extends to almost the stellar surface. Chemistry is essential for the ionization of hydrogen in these disks.

Conclusions. The lack of a gap between the central objects and these disks suggests that they accrete through boundary-layer accretion. This would exclude the stars having a strong magnetic field. Their structures suggest that both disks are transitional in nature, that is to say they are in the process of being cleared, either through boundary-layer accretion, photo-evaporation, or through companion activity.

2.1 Introduction

The evolution of high-mass protostars and their descendants, the massive young stellar objects (MYSOs), is expected to be very fast, $\sim 10^5$ yr (e.g. Hosokawa & Omukai 2009), and, until very late in the build-up process, hidden from view as it unfolds deep within dusty natal clouds. Though much is still unclear about the mechanism that leads to the assembly of a massive star, most theories agree on the need for a dense and massive accretion disk (e.g. Tan et al. 2014; Beltrán & de Wit 2016), possibly in combination with bipolar polar outflows at relatively early phases of formation. Likely, the massive disks that develop are complex in structure with multiple processes acting to cause instabilities, for example magneto-rotational instabilities leading to turbulence and associated angular momentum redistribution (e.g. Balbus & Hawley 1998) and gravitational instabilities giving rise to the formation of companions (e.g. Kratter et al. 2010; Oliva & Kuiper 2020).

The inner parts of the disk are particularly interesting for at least two reasons. First, from these regions the accretion of mass and redistribution of angular momentum takes place. Important open problems are the gas content of the inner disk reservoir and the accretion efficiency of this material close to the arrival of the star on the main sequence. The assembly of angular momentum is particularly interesting in view of the buildup and outcome of the surface rotation velocity, the latter property being key to reaching a new level of understanding of main sequence single and binary star evolution (Wang et al. 2022). Second, the mechanism(s) disrupting the circumstellar disk likely act first fairly close to the central star. The main candidates for this process are disk winds, outflows resulting for example from photo-evaporation (e.g. Gorti & Hollenbach 2009; Owen et al. 2010; Gangi et al. 2020), stellar winds, and stellar or planetary companion formation (e.g. Müller & Kley 2013). Our understanding of disks that are in the process of clearing themselves out (so-called transitional disks) stems mostly from low- and intermediate-mass stars, where the process takes 10-20% of the total YSO lifetime (Furlan et al. 2011). Given the short duration of the MYSO phase ($10^4 - 10^5$ yr; Hosokawa & Omukai 2009), it remains to be seen whether such a modest fraction of the MYSO lifetime will suffice, or whether perhaps the majority or even all MYSO disks are transitional in nature.

Atomic recombination and CO bandhead emission lines are the main (gas-phase) diagnostics of the properties, structure, and kinematics of the inner dust-free regions of the disks of MYSOs. The hydrogen line-formation mechanism near the end of the MYSO phase is complex, as the stars are likely not accreting enough to cause significant hydrogen ionization as a result of viscous heating and shocks, and the central stars' photospheres are not hot enough to produce sufficient ionizing radiation and associated hydrogen photo-ionization.

Evidence is mounting that the hydrogen emission originates from very close to the stellar surface. Koumpia et al. (2021) present an interferometric K-band study of a sample of MYSOs spatially resolving the dust and Brγ emission in objects ranging from 9 to 16 $M_\odot$. They find Brγ emission to originate from $\sim$0.9 to 6 AU from the central star and the 2.2 μm emission to originate from $\sim$1.4 to 6.8 AU from the central star depending on the object. They conclude that the hydrogen emission originates from a more compact region than the 2.2 μm dust emission, with the continuum dust emission being consistent with originating from the dust sublimation radius. This is in line with the findings of Caratti o Garatti et al. (2016) who find a Brγ emitting region of 6–13 AU and a further out continuum emitting region of 17 AU for a 20 M$_\odot$ MYSO. Additionally, they detected an outflow in Brγ. Kraus et al. (2010) also find a dust free cavity analogous to those found in lower mass YSOs compatible with the dust sublimation radius. Gravity Collaboration et al. (2020) detect CO emission in the inner gaseous disk of the massive (15 $M_\odot$) YSO NGC 2021 IRS 2, which is well within the dust sublimation radius. The dynamical nature of this hot gas close to the central star is still a matter of debate. MYSOs could have weak or absent magnetic fields similar to their main-sequence counterparts in which few stars are observed to have strong magnetic fields (e.g. Fossati et al. 2015; Wade et al. 2016). Thus accretion might proceed through boundary layer (BL) accretion rather than magnetospheric accretion. Therefore, disks might potentially extend all the way to the stellar surface, becoming dust free inside of the dust sublimation radius. Alternatively, the nearby gas could result from bipolar outflows (Frost et al. 2021).

On the basis of infrared spectroscopy, photometry, and high-spatial resolution imaging of optical scattered light from small dust grains, disks around YSOs have been classified into two groups (e.g. Garufi et al. 2017), reflecting large-scale morphological properties. Group I sources show large extended disks with a pronounced gap in the centre. This results in low or lacking near-infrared excess due to the absence of hot dust. Such inner dust-free cavities extending beyond the dust sublimation radius are observed in MYSOs (Frost et al. 2021). Group II sources show strong NIR-excess, but limited excess at longer wavelengths. This suggests the presence of hot dust near the star, but the absence of cooler dust further out, which can be caused by a small truncated disk, or a self-shadowed disk. Though this classification does clearly imply a different structure of the inner disk (where the hot dust is located), it does not link to a potential gas reservoir in these inner regions. Scrutinizing this hot gas, if present, may help to understand the processes shaping the inner disk regions.

In this paper we present the modelling of hydrogen emission lines and dust continuum emission from two MYSOs using the radiation thermo-chemical code ProDiMo (Woitke et al. 2009; Kamp et al. 2010; Thi et al. 2011; Woitke et al. 2016; Kamp et al. 2017). We fitted X-shooter data of the hydrogen lines (Ramírez-Tannus et al. 2017) and archival photometry of the dust emission for two sources in M17. The H II region containing the stars and the data are described in Section 2.2. In Section 2.3 we introduce the model and the modifications applied to the model to enable our analysis. Section 2.4 shows the results; these are discussed in Section 2.5. Conclusions are outlined in Section 2.6.

2.2 Description of the data

M17 is one of the most luminous H II regions in the Galaxy (3.6×10^6 L$_\odot$; Povich et al. 2009). It is located in the Carina-Sagittarius spiral arm at a distance of 1.98 ± 0.14 kpc (Xu et al. 2011). The young cluster NGC 6618 ($\sim$1 Myr; Hanson et al. 1997; Broos et al. 2007; Povich et al. 2009), containing 16 O-type stars and over 100 B-type stars, is located at the centre of the H II region (Chini et al. 1980; Hoffmeister et al. 2008), while the surrounding molecular cloud hosts pre-main-sequence (PMS) stars (Hanson et al. 1997; Ramírez-Tannus et al. 2017). On the basis of a near-infrared (NIR) excess in the spectral energy distribution (SED) and the presence of hydrogen and CO bandhead emission lines, Hanson et al. (1997) identified a sample of massive (6-20 $M_\odot$) young stellar object (YSO) candidates embedded in the molecular cloud. Using X-shooter (Vernet et al. 2011) mounted on the ESO Very Large Telescope, Ramírez-Tannus et al. (2017, hereafter RT17) carried out a spectroscopic follow-up of 12 of these objects, providing the spectroscopic confirmation that these objects are massive pre-main-sequence stars. The stellar parameters were determined from photospheric line fitting or SED fitting. In the nine cases where the objects have visible photospheres, they modelled the stellar spectrum using the non-LTE radiative transfer code FASTWIND (Puls et al. 2005; Rivero González et al. 2012) together with the genetic algorithm PIKAIA (Mokiem et al. 2005; Charbonneau 1995). Otherwise SED fitting was used to determine stellar properties. The obtained temperatures, luminosities, and projected rotational velocities allowed them to place these MYSOs in the Hertzprung-Russell Diagram (HRD) and compare their position with pre-main-sequence (PMS) evolutionary tracks from Hosokawa & Omukai (2009). Two of the observed objects (B111 and B164) have spectra characteristic of O-type stars and are located at the zero-age main-sequence (ZAMS). Two other objects (B215 and B289) show an IR excess longwards of 2.3 μm but do not show emission lines nor NIR excess in the X-shooter spectral range. This is a sign that they are surrounded by dusty disks. Six of the observed objects (B163, B243, B268, B275, B331, and B337) have H I, O I, and Ca II double-peaked emission lines as well as CO bandhead emission and a NIR excess in their SED; this indicates that they are surrounded by a gaseous disk with a dust component. RT17 conclude that they are MYSOs with disks that are probably a remnant of the assembly process on their way to become main-sequence stars with masses between 6 and 15 $M_\odot$ consistent with having undergone high mass-accretion rates ($M_{\rm acc} \sim 10^{-4} - 10^{-3}\ M_\odot\ {\rm yr}^{-1}$), hence with formation timescales of $\sim 10^5$ yr.

2.2.1 Target objects, observations, data reduction, and contaminants

In this paper, we focus on modelling the circumstellar disks of two MYSOs in M17: B243 and B331, whose stellar properties are summarized in Table 2.1 (RT17). These two targets show pronounced disk features, namely strong and clearly detected double-peaked hydrogen emission lines up to high order in the Paschen series and an infrared excess. B331 also shows Brackett series lines. Their X-shooter spectra cover the optical to NIR (300 - 2500 nm) with a spectral resolution of 5100 in the UVB arm, 8800 in the VIS arm, and 11 300 in the NIR arm. The observed spectra are flux calibrated using spectrophotometric standards from the ESO database.

The H I circumstellar emission in the spectra of the two sources can be contaminated with various other features, including nebular emission, stellar absorption, circumstellar emission by metallic species, and interstellar absorption. Some of these can and need to be corrected for in order to isolate the hydrogen emission from the disk itself.

The spectrum of B331 shows strong nebular emission, which contaminates the hydrogen circumstellar emission by adding a strong central component. Most of this emission was

Table 2.1: Stellar properties and extinction parameters of B243 and B331 updated from RT17.

Name	Sp. Type	M	T_{eff}	$\log g$	$v \sin i$	R_V	A_V	$\log L/L_\odot$	$R_\star$
		$\mathrm{M}_\odot$	K	$\mathrm{cm\,s^{-2}}$	$\mathrm{km\,s^{-1}}$	(SED)	mag		$R_\odot$
B243	B8 V	6	13500^{+1350}_{-1250}	$4.34^{\uparrow}_{-0.3}$	$110^{+106}_{\downarrow}$	$4.7^{\uparrow}_{-0.8}$	$8.5^{\uparrow}_{-1.0}$	$3.21^{+0.07}_{-0.06}$	$7.5^{+1.0}_{-0.8}$
B331	Late-B	12	$\sim$13000	$-^{a}$	$-^{b}$	$4.6^{+0.5}_{-0.5}$	$13.3^{+0.9}_{-0.9}$	$4.10^{+0.37c}_{\downarrow}$	$21.8^{+9.6}_{-7.2}$

[a] We assume $\log g = 4.0$
[b] We assume $v \sin i = 110$
[c] Value from SED fitting

corrected for using multiple Gaussians fitted to off-source nebular emission as described by van Gelder et al. (2020). The nebular emission in B243 was not as substantial, and did not require further correction. Additionally, the studied hydrogen lines are blended with other emission lines originating from the disk, such as weak Ca II λ8498, λ8542, λ8662 Å emission in B243, blending the blue wings and peaks of Pa-16, -15, and -13. It is beyond the scope of this study to investigate the emission mechanism of these blending lines. Consequently, we cannot accurately predict their strengths and we refrain from correcting for their presence.

The H I cirsumstellar emission lines are superimposed on the stellar hydrogen absorption lines. The measured flux needs to be corrected for this absorption to isolate the disk contribution. The applied procedure to do so is described in section 2.2.3.

Finally the spectrum also shows relatively wide absorption features originating from the interstellar medium. These so-called diffuse interstellar bands (DIBs) are likely due to large carbonaceous molecules such as C_{60}^{+} (e.g. Sarre 2006; Cox et al. 2017; but see Campbell et al. 2015). An example of such a feature is seen in Fig. 2.1 at λ8630 Å. We exclude regions with known DIBs when estimating the continuum level.

Slight variations in the continuum of the normalized spectrum are still visible after applying the correction for stellar and nebular emission. These variations, due to unknown features, irregularities in the response curve, flux calibration, and uncertainties in the correction and normalization method, are the main uncertainty on the data. We conservatively estimate these uncertainties to be approximately 5% of the continuum on average and assume this to be normally distributed.

2.2.2 Photometric data

The photometric data used in this work is taken from the literature and catalogues. For both stars we included data from DENIS (Fouqué et al. 2000), 2MASS (Skrutskie et al. 2006), and Spitzer GLIMPSE (Reach et al. 2005). WISE photometric data were included for B243 (Wright et al. 2010), as well as points from Kassis et al. (2002) for B331. SOFIA photometry of B331 at 20 μm and 37 μm (Lim et al. 2020) shows very high flux and, due to SOFIA's low spatial resolution, likely contains emission from outer material not belonging to the circumstellar disk. Therefore, it was not included in the analysis. Additionally, the spatial

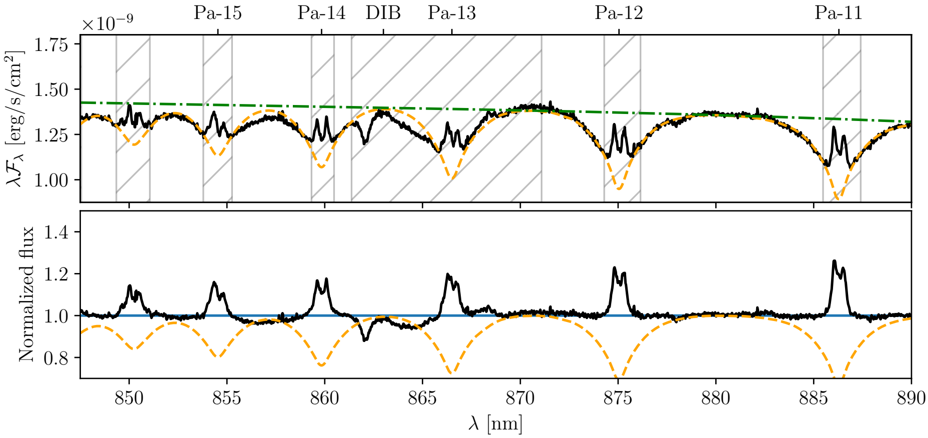

Figure 2.1: Illustration of the normalization method. *Top panel*: The flux calibrated observed spectrum of B243 in black. The photospheric model spectrum is indicated by the orange dashed line and the continuum of this model by the green dash-dotted line. The model spectrum is matched to the observed spectrum using a least squares method in the unhatched wavelength ranges. At the top the location of the Paschen lines and a DIB are indicated. *Bottom panel*: The photosphere corrected and normalized observed spectrum (in solid black) and photospheric model (in dashed blue). The horizontal blue line indicates unity.

distribution of the SOFIA data does not agree with the 2MASS and Spitzer data, with the SOFIA data being significantly offset with respect to the others.

2.2.3 Normalization and correction of stellar features

To correctly model the disk emission lines contaminant stellar absorption features had to be removed, that is the flux absorbed in the stellar atmosphere had to be added back to the observed flux. To do so, a good estimate of the continuum is essential. However, in and around the hydrogen line series it is not possible to accurately make this estimate based on the observed spectra alone, as the Paschen line wings blend to form a 'secondary' continuum flux almost everywhere in the studied part of the spectrum; see the top panel of Fig. 2.1. As the stellar properties of B243 and B331 were already determined by RT17, see Table 2.1, we chose to simultaneously normalize and correct for the stellar features by matching model spectra to the flux calibrated observed spectra, for which we used a BT-NextGen atmospheric model computed with the PHOENIX code (Hauschildt et al. 1999; Allard et al. 2012).

The model spectrum, with $T_{\mathrm{eff}} = 13000\,\mathrm{K}$ and $\log g = 4.0$, is rotationally broadened and convolved with the spectral resolution of the observation. Then the flux is scaled to match the observed spectrum using a least squares algorithm only taking wavelength ranges into account free from circumstellar or interstellar features (non-hatched regions in Fig 2.1). As the calibrated spectrum has slight flux variations this scaling is done piece wise to find the best agreement between model and observation. The thus obtained scaled model is continuum subtracted to obtain the stellar features, which are then added to the observed spectrum. The resulting spectrum now only contains stellar continuum, disk features, and interstellar features. This spectrum is then divided by the stellar continuum from the model to get a normalized spectrum. Fig. 2.1 shows an example of this process in part of the Paschen series regime of B331. A more extended part of the spectrum of both B243 and B331 is shown in Fig. I.1 The uncertainty on the stellar parameters will affect this normalization. Overestimating the surface gravity of the star results in wider hydrogen lines, which would result in stronger wings in the circumstellar emission profile. Underestimating the gravity would result in absorption features in the wings. The uncertainty in the temperature slightly affects the strength of the hydrogen lines.

2.3 Model

The double peaked hydrogen emission lines observed in B243 and B331 suggests that the emission originates in a circumstellar disk. Neither of the two objects show strong indication of outflows present in the X-shooter slit or other images. Therefore, we assume that the bulk of the emission originates from the central star and a circumstellar disk. A disk wind may be present, possibly contributing to the observed hydrogen emission, however, this is not modelled.

The disks are modelled using the radiation thermo-chemical code ProDiMo[1] (Woitke et al. 2009; Kamp et al. 2010; Thi et al. 2011; Woitke et al. 2016; Kamp et al. 2017). ProDiMo self-consistently solves the chemistry, gas and dust heating and cooling, as well as line and continuum radiative transfer. The disk is assumed to be azimuthally symmetric and in steady state, and to follow a Keplerian rotation profile.

The applied chemical network accounts for 13 elements, namely H, He, C, N, O, Ne, Na, Mg, Si, S, Ar, Fe, and Polycyclic Aromatic Hydrocarbons (PAHs). In the present work, the latter only contribute to the free electron density. A total of 100 chemical species can form and interact. For the elemental abundances we adopt the Proto-Sun based values of Lodders (2003). These abundances are not depleted to compensate for the metals that are trapped in dust grains, as the chemistry we focus on takes place in the dust free inner region of the disk. The chemical reactions and rate coefficients are taken from the UMIST 2006 database (Woodall et al. 2007).

The dust temperature and continuum emission are solved for the given stellar and interstellar radiation field and dust opacities. The adopted dust composition is a mix of olivine (Mg_2SiO_4), amorphous carbon, and vacuum. Dust settling is taken into account following Dubrulle et al. (1995) adopting a turbulent viscosity parameters $\alpha = 10^{-3}$. A complete description of the treatment of solids can be found in Woitke et al. (2016).

Next, the gas heating and cooling are solved simultaneously with the chemistry as these are coupled. The gas temperature is based on 100 heating and 93 cooling processes implemented in ProDiMo revision number 3053.

---

[1] Version 1.0 revision 3053

Because the (free) parameters describing the density structure in the disk are found to be most influential on the studied lines (see section 2.3.2), we briefly describe their relations. The relevant parameters are the total dust and gas mass $M_{\rm disk}$; inner and outer radius of the disk, $R_{\rm in}$, and $R_{\rm out}$, respectively; radial column density exponent ϵ; reference vertical scale height H_0 specified at a reference radius R_0, and scale height flaring power index β. The inner and outer radii specify the extent of the disk. The radial profile of the vertically integrated column density, Σ, of the disk is given by

$$\Sigma(r) = \Sigma_0 \left(r/R_{\rm in}\right)^{\epsilon}, \tag{2.1}$$

where Σ_0 is determined such that the integration of this profile over the radial extent of the disk results in $M_{\rm disk}$. The vertical density structure at a given radius r is defined by

$$\rho(z,r) \quad = \quad \rho_0(r)\, \exp\left[-\left(z/H\right)^2/2\right], \tag{2.2}$$

$$\tag{2.3}$$

and using equation 2.1

$$\Sigma(r) \quad = \quad 2\int_0^\infty \rho(z,r)\, dz, \tag{2.4}$$

is solved to find the midplane density $\rho_0(r)$. The vertical scale height H is a function of the distance to the central star, that is

$$H(r) = H_0 \left(\frac{r}{R_0}\right)^{\beta}, \tag{2.5}$$

where, H_0 is the scale height at the reference radius, R_0, and β is the flaring power.

The disk is in Keplerian rotation. It is irradiated by a central star of mass $M_\star$, effective temperature $T_{\rm eff}$, and luminosity $L_\star$. Additionally, an X-ray luminosity is included referred to as $L_{\rm X}$ which is plays an important role in the chemistry and thermal balance of the gas. A mass accretion rate $\dot{M}$ can be specified as well. This causes viscous heating in the disk. For B243 we include a minor mass accretion, however, the heating resulting from this is minor, $<$1%, compared to that of the radiation field. The accretion rate was chosen such that the disk would have a reasonable lifetime given its mass. In B331 no effect was seen as result of similar accretion rates, therefore no accretion heating was implemented.

We divide the disk in two regions, referred to as inner disk and outer disk. The inner disk is located closest to the star and is purely gaseous. This zone has a negligible dust mass as temperatures are too high for solid particles to exist for any appreciable amount of time. The hydrogen line emission originates in this part of the disk. The outer disk also contains dust, hence determines the infrared continuum emission. The inner radius of the outer disk results from a fit to the SED. For the outer disk the model parameters are given the label ‘2’; for instance, the total mass of the outer disk is $M_{2,\rm disk}$.

2.3.1 Model modifications

ProDiMo is originally designed to model T Tauri and Herbig disks, that is planet forming disks around cooler less-luminous stars, where a photospheric EUV radiation field is not expected to significantly affect disk processes. Therefore, hydrogen-ionizing photons with energies between 13.6 and 100 eV were previously ignored. For hotter stars the EUV contribution becomes stronger, and needs to be considered. ProDiMo does include X-ray radiation (Aresu et al. 2011; Rab et al. 2018), defined as photons with energies > 100 eV, as the ionizing properties of such photons are essential for the chemistry in the disk (Glassgold et al. 1997). In order to properly treat hydrogen ionization, we extended the code to also include the EUV radiation field.

The standard atomic model for hydrogen in ProDiMo considers 25 $(n, \ell)^1$ energy levels up to $n = 5$. This does not allow for a prediction of the observed Paschen and Brackett series, reaching up to $n = 16$. Therefore, the model atom was replaced by a new model using the NIST atomic database (Kramida 2019) to include the energy levels up to $n = 20$ and the transitions between these states. The collisional excitation cross sections are calculated using Jefferies (1968) as

$$q_{ul} = 2.16 \left(\frac{E_0}{kT}\right)^{-1.68} T^{-3/2} f_{lu} \frac{g_l}{g_u} \quad [\mathrm{cm^3 s^{-1}}], \tag{2.6}$$

with E_0 the energy of the transition between energy levels u and l, k the Boltzmann constant, T the temperature of the gas, f_{lu} the oscillator strength of the transition, and g_l and g_u the statistical weights of the lower and upper levels.

For the treatment of photo-ionization, see for example Mihalas (1978), we use

$$\alpha_\nu^{\mathrm{bf}} = 7.91 \times 10^{-18} \frac{n}{Z^2} g_{\mathrm{II}}(\nu, n) \left(\frac{\nu_0(n)}{\nu}\right)^3 \quad [\mathrm{cm^2}], \tag{2.7}$$

with ν the frequency of a given photon, the charge of the ion $Z = 1$ for hydrogen, g_{II} the bound-free Gaunt factor, which we assume to be 1, and $\nu_0(n)$ the ionization frequency for energy level n.

2.3.2 Model fitting and model grid

We fitted the emission lines and SED separately, by varying certain parameters of the inner and outer disk, respectively. In the inner disk the hydrogen line profiles were fitted using an interpolated 4-dimensional grid of models. The free parameters of this grid are inner radius (R_{in}), reference scale height (H_0), inner disk mass (M_{inner}), and inclination (i). These parameters have a strong effect on the resulting line profiles. This is illustrated in Fig. 2.2, where large variations in line strength and shape are visible. Increasing the inner radius of the disk results in weaker and narrower lines, as the disk moves further from the star where it is less illuminated and orbital velocities are lower. The smallest sampled scale heights result in weaker and wider lines. As the material is confined closer to the mid-plane of the

---

[1] With n the principal quantum number, indicating the excitation level, and ℓ the azimuthal quantum number.

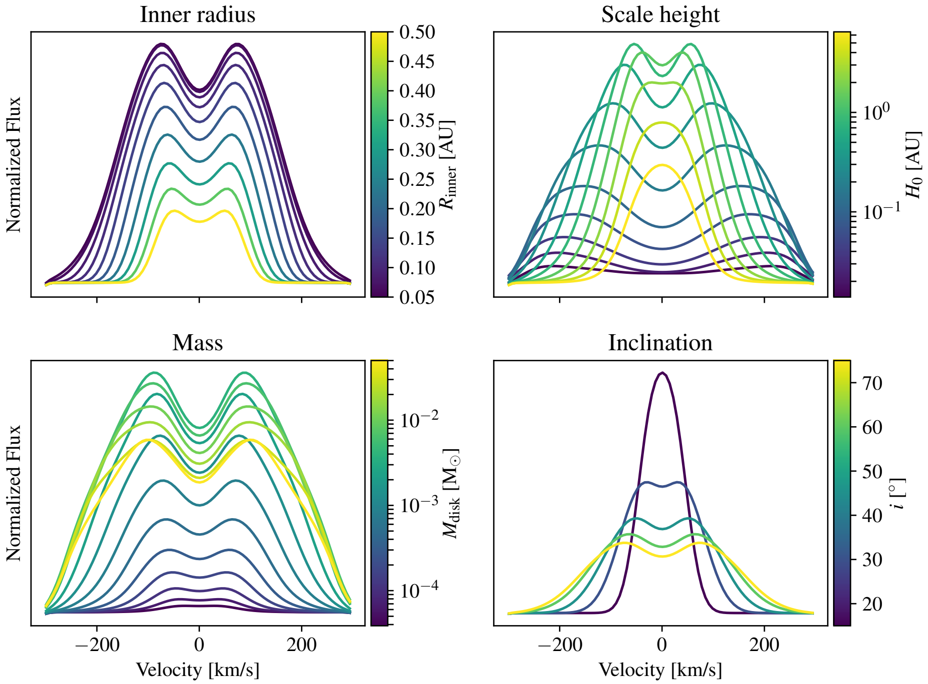

Figure 2.2: Line profile of Pa-14 from the model of B243 for various parameter values. In each of the panels one parameter is varied, while the others remain fixed at an inner radius of 0.06 AU, a reference scale height of 0.5 AU, a total disk mass of 10^{-3} $M_\odot$, and an inclination of 75°.

disk, less of the stellar radiation reaches the disk; moreover, it is harder for this radiation to reach more (radially) distant parts of the disk due to the high density. Consequently, line emission emanates from regions with relatively high Keplerian velocities. As the volume density of the disk decreases with increasing scale height and light reaches larger radial distances, the peak separation decreases. The line strength initially increases, because more radiation is intercepted by the disk. However, at the highest scale heights, the decrease in volume density starts to outweigh the increased illumination and the line strength decreases again. Increasing the mass of the disk results in a higher density and thus a stronger emission line, until it saturates from which point on the line strength will decrease. Changing the inclination angle changes the projected velocity distribution of the emission.

Other parameters such as the flaring power, β, and column density exponent, ϵ, are degenerate with the varied parameters in how they influence the line profiles. This degeneracy results from the small area of the disk (see section 2.4.4) from which the H I emission lines originate. Therefore, the surface density exponent and disk mass affect the density of the emission region in a similar way. The flaring power affects the scale height of this region in a similar way as the reference scale height. A fiducial flaring power (of e.g. 1.2) results in an

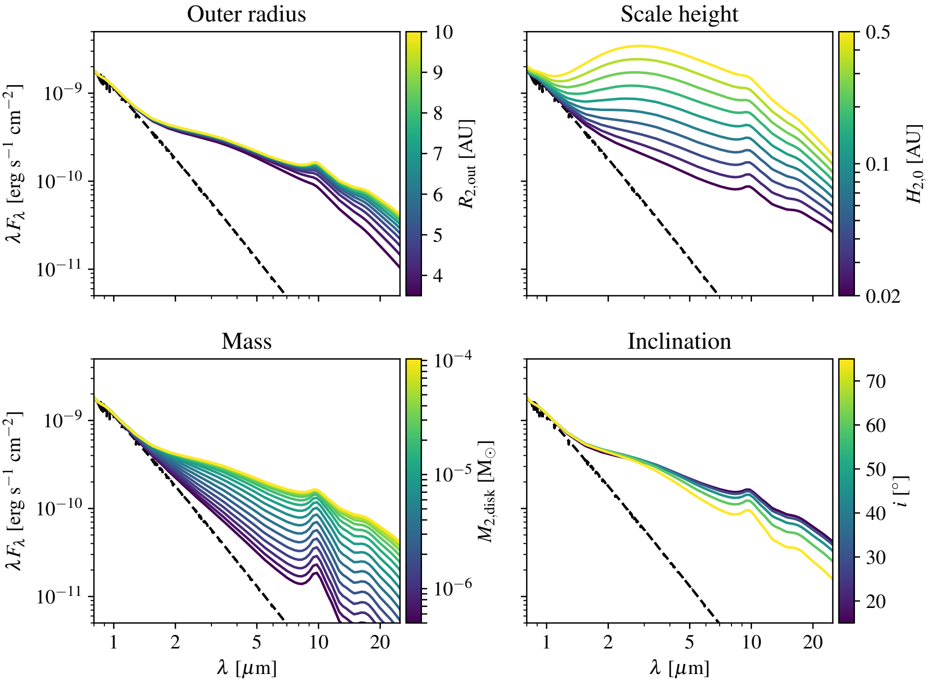

Figure 2.3: Models of the SED for B243 for various parameter values. In each of the panels one parameter is varied, while the others are held fixed at an outer radius of 10 AU, a reference scale height of 0.04 AU, a disk mass of 10^{-4} M$_\odot$, and an inclination of 15°.

extremely large vertical extent in the outer parts of the inner disk as a relatively large scale height is required close to the star. To prevent this, we adopt a value of $\beta = 0.5$ for the inner disk.

The outer disk is modelled using a similar grid, varying the outer radius, scale height, and mass. An example of the effects of the parameters on the SED is shown in Fig. 2.3. The inclination has a modest effect on the SED. For consistency with the inner gaseous disk we set this parameter to the best fit value of the line profiles. The scale height has a strong effect on the continuum disk emission. For the relatively massive disk shown here, a larger outer radius allows for cooler dust causing stronger mid-infrared emission. However, for a relatively low disk mass (not shown here) the redistribution of mass that results from assuming a larger outer radius causes the inner regions of the disk to become optically thin, reducing the near-infrared flux. The mass of the disk affects the full spectral range. For a higher mass the emission increases until the disk becomes optically thick. This happens first at shorter wavelengths.

The parameter values of the calculated grid points are listed in Tab. 2.2. The range of adopted values allow for both much weaker and much stronger lines than observed. As the range

Table 2.2: Overview of the model grid used to analyse B243 and B331.

Inner disk

		R_{in} [AU]	H_0 [AU]	M [$\mathrm{M}_\odot$]	i [°]
B243	min	0.05	0.0139	3.87×10^{-5}	15
	max	0.5	6.46	0.05	75
	steps	10	13	15	5
B331	min	0.11	0.1	1.94×10^{-4}	15
	max	0.30	10.0	0.25	75
	steps	10	10	15	5
Interpolation		50	50	50	25
Spacing		Log	Log	Log	Lin

Outer disk

		$R_{2,\mathrm{out}}$ [AU]	$H_{2,0}$ [AU]	M_2 [$\mathrm{M}_\odot$]
B243	min	3.5	0.02	5.0×10^{-7}
	max	10	0.5	1.03×10^{-4}
	steps	10	10	17
B331	min	110	0.05	10^{-3}
	max	500	10.0	0.5
	steps	10	10	10
Interpolation		50	50	50
Spacing		Log	Log	Log

The numbers indicate the minimum and maximum values of a parameter, and the number of steps between those values. Interpolation and spacing indicate the number of grid points and spacing between steps in the interpolated grid. The inner disk grid for B243 consists of 9750 models and for B331 of 7500 models.

can cover several orders of magnitude we opt for a relatively coarse grid and interpolate between the models using an N-dimensional linear interpolation algorithm (Virtanen et al. 2020). With this interpolation a significantly higher resolution grid consisting of 3 125 000 points is calculated. This finer grid is used to fit the data. The interpolated data is verified to be accurate by calculating full models at interpolated grid points. Typically, the interpolated line profiles diverge by $<1\%$ from full model calculations, however in some cases the stronger lines can differ by up to 10%.

A summary of input parameters for ProDiMo is shown in Tab. 2.3. Parameters not listed are identical to the ProDiMo standard parameter values obtained in the DIANA project (Woitke et al. 2016). Full input files can be found online[1]. Parameter values listed in the table that are held fixed are the result of exploratory fitting. The fixed parameters are either degenerate with other parameters (see section 2.3.2) or do not impact the fitting strongly, therefore should not be considered well constrained. Notably, the outer radius of the inner disk is poorly determined as the H I lines form within the first one to two AU of the inner disk, see Fig. 2.8 and Fig. 2.9.

---

[1] A reproduction package can be found at https://doi.org/10.5281/zenodo.7024846

Table 2.3: Overview of the input parameters for both the central star and the disk.

Component	Name	Symbol	B243 Value	B331 Value
Central star	Mass	$M_\star$	6.0 $M_\odot$	12 $M_\odot$
	Effective temperature	T_{eff}	13 500 K	13 000 K
	Luminosity	$L_\star$	1 622 $L_\odot$	12 500 $L_\odot$
	X-ray luminosity	L_X	10^{32} erg s^{-1}	5×10^{32} erg s^{-1}
	Accretion rate	$\dot{M}$	10^{-7} $M_\odot$ yr^{-1}	-
Density structure inner disk	Mass	M_{disk}	Varied	Varied
	Inner radius	R_{in}	Varied	Varied
	Outer radius	R_{out}	$>$ 2 AU (set at 3.5 AU)	$>$ 2 AU (set at 20 AU)
	Column density exponent	ϵ	0.0	-1.0
	Reference scale height	H_0	Varied	Varied
	Reference radius	R_0	3.5 AU	10 AU
	Flaring power-index	β	0.5	0.5
Density structure outer disk	Mass	$M_{2,\text{disk}}$	Varied	Varied
	Inner radius	$R_{2,\text{in}}$	3.0 AU	100 AU
	Outer radius	$R_{2,\text{out}}$	Varied	Varied
	Column density exponent	ϵ_2	-1.0	-1.5
	Reference scale height	$H_{2,0}$	Varied	Varied
	Reference radius	$R_{2,0}$	3.5 AU	100 AU
	Flaring power-index	β_2	1.2	1.2
Dust in outer disk	Minimum grain size	a_{min}	0.5 μm	
	Maximum grain size	a_{max}	1000 μm	
	Grain size exponent	a_{pow}	3.5	
	Turbulent mixing parameter	α_{settle}	10^{-3}	
	Dust-to-gas ratio	$M_{\text{dust}}/M_{\text{gas}}$	0.01	
Other	Distance	d	2.0 kpc	
	Inclination	i	Varied	

The hydrogen emission lines studied in this work are for B243: Pa-β through P-16, save for Pa-8 and Pa-10 which are in regions of strong telluric absorption. The same lines are studied for B331 as well as Br-γ, Br-10, Br-11 Br-12, Br-14, and Br-16. The disk parameters are determined by fitting a subset of the lines simultaneously. The subset aims to include the lines most representative of the inner region of the disk. This subset consists of Pa-16 to Pa-9 for B243 and for B331 Br-16 to Br-11 is added to that set. Additionally, each line if fitted separately allowing the inner radius, scale height, and mass to vary. The inclination is fixed to the best fit value of the combination of lines.

2.4 Results

We present the results of our fitting efforts of the photometric data and X-shooter spectra using ProDiMo. First, we discuss the source of the hydrogen ionization in section 2.4.1. Subsequently, we describe the fitting results for B243 and B331 in sections 2.4.2 and 2.4.3. Correlations between parameters are briefly presented in appendix I.3.1. Finally, we present the derived physical properties of the modelled disks in section 2.4.4. All results are also available online[1].

Only the disk contribution to the emission is fitted. For the stellar contribution we use the best fit properties as listed in Tab. 2.1. We report the scale heights at the inner radius of

Table 2.4: Table with the best fit model parameters and their 1σ uncertainties.

Parameter	B243	B331
Inner disk		
$R_{\rm in}$ [R$_\star$]	$1.4^{+0.4}_{\downarrow}$	$1.1^{\rm ND}_{\downarrow}$
H_0 [AU]	$0.527^{\rm ND}_{-0.06}$	$2.4^{\rm ND}_{\rm ND}$
$M_{\rm disk}$ [M$_\odot$]	$5^{\rm ND}_{\rm ND} \times 10^{-4}$	$1.8^{\rm ND}_{\rm ND} \times 10^{-4}$
i [°]	$75^{\uparrow}_{-10}$	$75^{\uparrow}_{\rm ND}$
$H_{\rm inner}$ [R$_\star$]	$1.8^{+0.3}_{-0.2}$	$2.5^{\rm ND}_{\rm ND}$
$\Sigma_{\rm inner}$ [g cm^{-2}]	$124^{\rm ND}_{\rm ND}$	$1.1^{\rm ND}_{\rm ND} \times 10^3$
Outer disk		
$R_{2,\rm out}$ [AU]	$6.5^{+2.1}_{-2.4}$	$246^{\uparrow}_{\downarrow}$
$H_{2,0}$ [AU]	$0.039^{+0.003}_{-0.005}$	$0.18^{+0.02}_{-0.02}$
$M_{2,\rm disk}$ [M$_\odot$]	$1.0^{\uparrow}_{-0.3} \times 10^{-4}$	$0.44^{\uparrow}_{-0.42}$
$H_{2,\rm inner}$ [$R_\star$]	$0.9^{+0.1}_{-0.1}$	$1.8^{+0.2}_{-0.2}$
$\Sigma_{2,\rm inner}$ [g cm^{-2}]	14^{+27}_{-5}	$55^{\uparrow}_{-36}$

The inner disk properties are determined by fitting a subset of hydrogen lines simultaneously. An arrow indicates that the confidence interval extends beyond the model grid. ND indicates that the uncertainty could not be determined as it is smaller than the step size of the grid.

the disk rather than at the reference radius, which is used to set up the grid of models. The mass is translated to the column density at the inner radius of the disk, as the latter is better constrained. These quantities are calculated using the equations in Section 2.3. An overview of the best fit parameters is shown in Tab. 2.4.

2.4.1 Source of hydrogen line emission

The spectra of both B243 and B331 show significant hydrogen line emission. The mechanism through which these lines form is recombination, as the temperatures in these disks are not high enough to allow collisional excitation of the relevant levels. Photo-ionization by the central stars cannot account for the hydrogen ionization rates (see section 2.4.4 and Figs. 2.8 and 2.9) required to produce the observed line strengths – the stars are simply too cool ($T_{\rm eff}$ being 13 500 K and 13 000 K). Therefore, an alternative source of ionization in the inner part of the disk is required. In the simulations we find charge exchange reactions between ionized sulfur (S^+) and hydrogen, that is

$$S^+ + H \rightarrow S + H^+, \tag{2.8}$$

to be the dominant source of hydrogen ionization. Sulfur is ionized by UV photons with energies of at least 10.3 eV and then collides with neutral hydrogen, ionizing it. Other

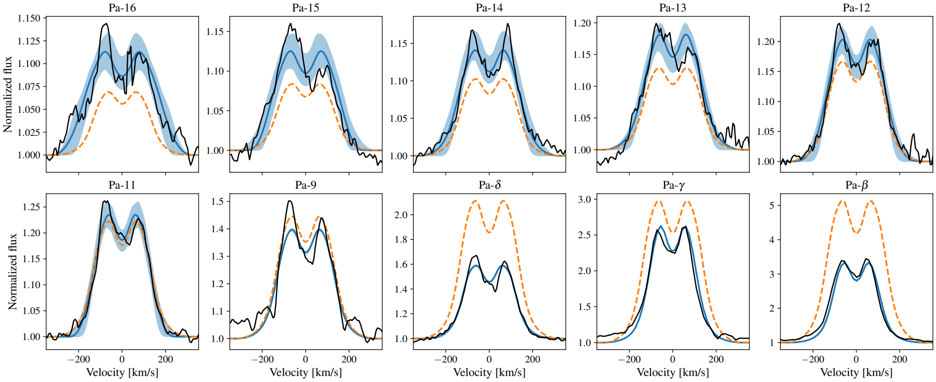

Figure 2.4: Best fitting models in blue to the observed lines in black for B243. The blue shaded regions indicate models that fall within the 1 σ confidence interval. Each line is fitted individually with the inclination set to 75°, the respective parameters are shown in Fig. 2.5. The orange profiles indicate the best fit when fitting Pa-16 to Pa-9 simultaneously. Notice the factor ~30 range in line strengths covered by the Paschen series.

charge exchange reactions with hydrogen also take place, however these do not contribute to the total hydrogen ionization significantly.

2.4.2 B243

2.4.2.1 Hydrogen emission lines

All of the Paschen lines in B243 show clear double peaked emission consistent with being formed in a rotating disk; see Fig. 2.4. Higher Pa-series lines become weaker and display more pronounced wings and a larger velocity separation of the peaks, see Fig. 2.12 and RT17. The range in line strength is large, Pa-β peaking about three times over continuum while for Pa-16 this is only about 10%.

The blue lines in Fig. 2.4 show fits to each line individually. These match the observed profiles very well, save for the blue wing and blue peak of Paschen 16, 15, and 13, which are contaminated with superimposed Ca II triplet emission (see Section 2.2.1). The corresponding model parameters are shown in blue in Fig. 2.5 as function of oscillator strength (bottom axis) and line identifier (top axis). The parameters derived from the Paschen lines show fair agreement with one another though we note that for this star the uncertainties are sizable, in part due to some level of degeneracy in several of the model parameters. For instance, the inner radius R_{in} and scale height H both impact the line broadening – increasing R_{in} leads to narrower lines requiring a lower scale height and higher mass (see Fig. 2.2). We find that the Paschen lines indicate a small inner radius, that is the disk extends to the stellar surface to within the order of a stellar radius ($R_\star = 0.035\,\mathrm{AU}$). The surface density at the inner radius is at least $\sim 100\,\mathrm{g\,cm^{-2}}$. The vertical scale height of the disk at its inner radius is $\gtrsim 2\,R_\star$, which is significantly larger than implied by vertical hydrostatic equilibrium. Such a

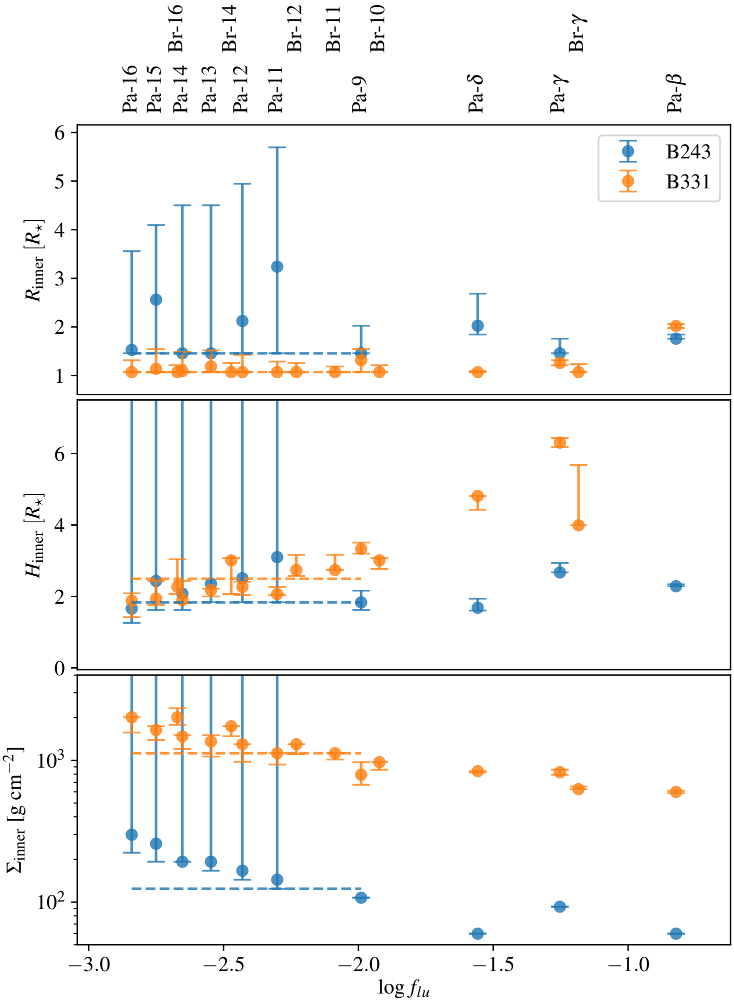

Figure 2.5: Parameter values of the inner disk with their uncertainties for each modelled line of B243 and B331 as function of their oscillator strength. The horizontal dashed lines indicate the best fit parameters for B243 when fitting Pa-9 and Pa-11 to Pa-16 simultaneously and for B331 when fitting Pa-9, Pa-11 to Pa-16 and Br-11 to Br-16. The corresponding line profiles are shown in Fig. 2.4 and Fig. 2.7 for B243 and B331, respectively. For each fit an inclination of 75° is used.

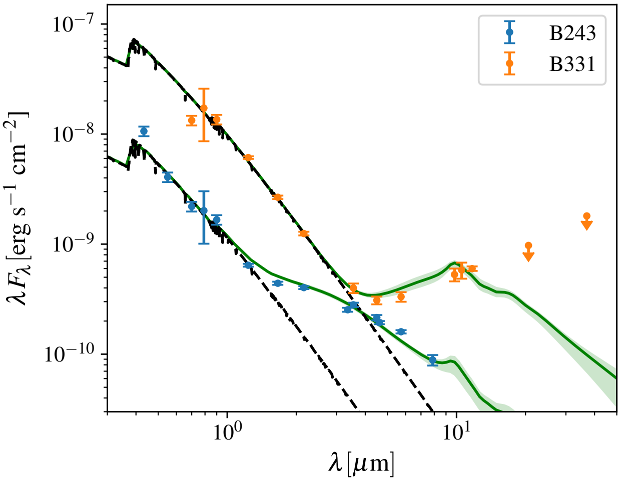

Figure 2.6: Observed and best fit SED of B243 and B331. For each star, the scatter points indicate the dereddened observed photometry and the black dashed lines the Kurucz model used as input for the stellar spectrum in ProDiMo. The best fitting models are drawn in green, with the shaded region indicating the 1σ uncertainty. For B331 the photometry from Lim et al. (2020) is indicated as upper limits; these are not considered in the fitting procedure.

puffed-up inner zone is quite common in HAeBe stars (e.g. Dullemond et al. 2001) and may originate from its direct exposure to stellar light (see also Section 2.5.2). The radial extent of the inner disk cannot be constrained from the hydrogen lines, hence, such constraints – if any – should come from the dust modelling.

The horizontal dashed line in Fig. 2.5 shows the best fit parameters when analysing Pa-9 and Pa-11 to Pa-16 simultaneously. The corresponding line profiles are shown in orange in Fig. 2.4. We find a best fit inclination of 75°, which is used for the individual line fits. The best value for the column density at the inner radius of the disk lies lower than the confidence intervals of some of the individual fits. This is due to a local minimum in the χ^2. The combined fit recovers all line strengths – that overall vary by a factor of $\sim$30 – to within a factor of two. It does reveal a systematic trend in that the model under-predicts the higher (i.e. weaker) Paschen lines and over-predicts the lower Paschen (i.e. stronger) lines. We discuss this discrepancy in Section 2.5.

2.4.2.2 SED

The NIR excess of B243 is well fitted with dust particles emitting at an almost constant temperature of $\sim$1500 K; see Fig. 2.6. This temperature is about the condensation temperature of silicate-based and carbonaceous grains placing the inner radius of the dust disk at 3 AU distance from the star. We use the best fit inclination of the inner gaseous disk of 75°. We find that the outer radius of the disk is poorly constrained; the best fit lies at $\sim$6.5 AU from the central star. The disk may appear truncated due to some self-shadowing. Longer wavelength photometry is needed to better investigate the extend of the disk. This implies a very small truncated dust disk, containing only a small amount of hot dust. The scale height at the inner rim of the dusty outer disk is $0.9^{+0.1}_{-0.1}\,R_\star$, therefore the dust is more confined to the disk mid-plane than is the gaseous material at the inner edge of the inner disk, consistent with the inner most parts of the disk being puffed up.

We find a lower limit of the surface density at this inner rim of the dusty disk of $\sim$9 g cm^{-2}, the material becoming optically thick and insensitive to further increases of the surface density.

In summary, the gas and dust analysis points to B243 having a disk with a best fit outer radius of 6.5 AU of which the inner part, up to 3 AU, is dust free. The mass contained in this small disk is at least $\sim 2 \times 10^{-5}\,\mathrm{M}_\odot$ when adopting a surface density exponent $\epsilon = -1$ for both the inner and outer disk, or $\sim 3 \times 10^{-4}\,\mathrm{M}_\odot$ when assuming $\epsilon = 0$ for the inner disk. As we lack photometric and spectroscopic information at wavelengths longwards of 10 μm we cannot exclude the presence of a (tenuous) cold disk further out, but a gap or self-shadowed region should be present based on the best fit model.

2.4.3 B331

2.4.3.1 Hydrogen emission lines

Most of the hydrogen emission line profiles are clearly double peaked and show relatively broad line wings. The latter correspond to high rotational velocities of up to $\sim$ 200 km s^{-1}. This suggests a Keplerian rotating disk extending down to the stellar surface. We find a best fitting inner radius of <0.12 AU (<1.2 $R_\star$) for nearly all lines. The scale height at the inner rim is quite similar as for B243 and points to the inner disk being puffed up. The surface density at the inner radius is well constrained at 1.1×10^3 g cm^{-2}. A similar column density has been found for NGC 2021 IRS based on CO emission (Gravity Collaboration et al. 2020).

For B331 too the observed Paschen and Bracket series span a large range in line strengths, of about a factor of 20 (Fig. 2.7). The dashed blue lines in Fig. 2.5 show the best fit parameters taking into account the same set of Paschen lines as for B243 and, in addition, Br-11 to Br-16. With this set, the line strengths are again reproduced to within a factor of two save for Paβ and Brγ for which the difference is somewhat larger; see the orange line in Fig. 2.7. None of the models within the confidence interval reach the upper limits. The best fit yields an inclination of about 75°.

Similar to B243 we find a systematic trend in that the observed line strengths vary less with Paschen and Bracket line number than do the model predictions. We return to this in Section 2.5.

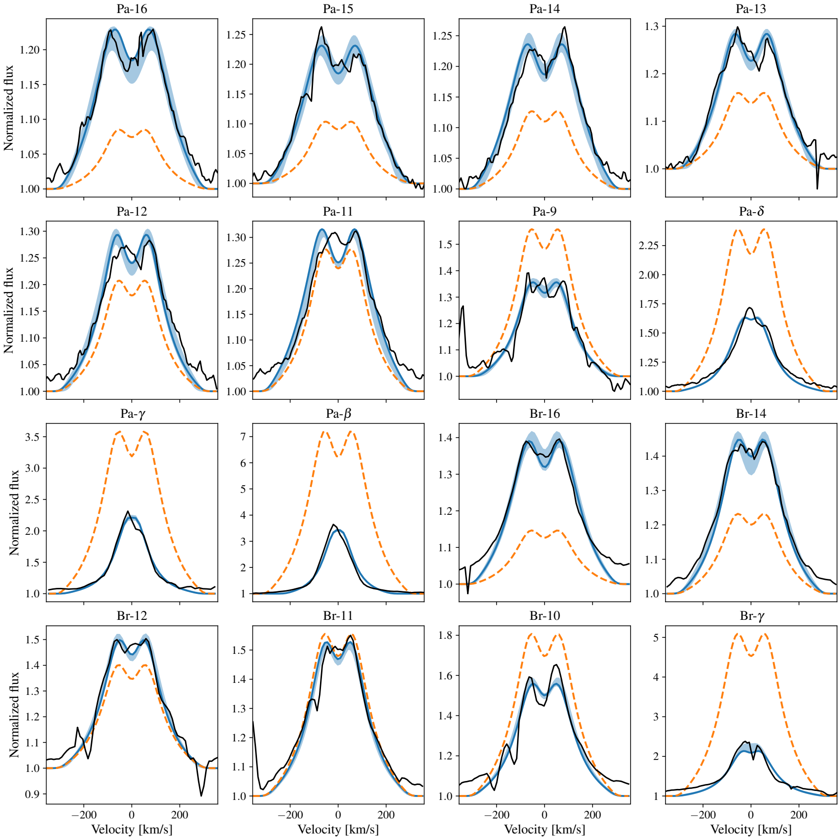

Figure 2.7: Best fitting models in blue to the observed lines in black for B331. The blue shaded regions indicate models that fall within the 1 σ confidence interval. Each line is fitted individually with the inclination fixed at 75°, the respective parameters are shown in Fig. 2.5. The orange profiles indicate the best fit when fitting Pa-16 to Pa-9 and Br-16 to Br-11 simultaneously. Notice the factor ~20 range in line strengths covered by the Paschen series.

2.4.3.2 SED

The SED of B331 shows an IR excess at $\lambda > 3\,\mu$m; see Fig. 2.6. We use the best fit inclination of the inner disk of 75°. The ProDiMo dust model results in a maximum temperature of ~400 K positioning this warm dust at ~100 AU from the star. The outer radius of the dusty disk remains unconstrained, simply because we lack photometric or spectroscopic constraints at wavelengths well beyond 10 μm. The amount of 3-10 μm flux is a function of the scale height of the inner rim of the outer dusty disk. We find for this scale height $0.18^{+0.02}_{-0.02}$ AU. The surface density at this location should be at least 19 g cm^{-2}, with improving fits for higher values up to at least ~700 g cm^{-2}.

In summary, the overall disk properties of B331 are quite different from those of B243. B331 lacks hot dust; warm dust seems only present starting at about 100 AU. This suggests that for this source a disk gap is created. The inner boundary of this gap, if present, is poorly constrained (the hydrogen spectral lines indicate it should start at a distance > 2 AU). The properties of the inner gaseous disk up to 3.5 AU appear quite similar to B243, both having a puffed-up inner rim.

2.4.4 2D Disk structure of B243 and B331

Figures 2.8 and 2.9 show the hydrogen ionization fraction, density, and temperature structure of the best fitting inner disk models for B243 and B331, respectively. The distance axis is linear in the case of B243 and logarithmic in case of B331. The hydrogen ionization fraction throughout the disks is low, even at the inner rim of the gaseous disk (where it reaches 10^{-3}). This is essentially due to the fairly low effective temperatures of the two stars. The ionizing photons do not penetrate far into the disk as the mostly neutral (hydrogen) medium becomes quickly optically thick for Lyman continuum radiation. B331 is almost an order of magnitude more luminous than B243, which is why for this star the thin somewhat ionized shell reaches deeper disk layers. For the same reason, the disk of B331 is heated to higher temperatures further out.

The black contours in the figures indicate the origin of half of the Pa-16 line flux. The formation region stretches out to about a radial distance somewhat less than one AU, that is hydrogen lines probe the very inner part of the disk only – dominated by the puffed up inner zone. Similar to the work by Koumpia et al. (2021), Caratti o Garatti et al. (2016), and Kraus et al. (2010), we find the hydrogen emission to originate from a region closer to the central star than the continuum emission, based on the location of the inner radius of the dust disk. We find the extent of the hydrogen emission region to reach up to $\sim$1 AU, which is in line with the most compact emitting regions found in interferometric studies of Koumpia et al. (2021) and Caratti o Garatti et al. (2016), but is more compact than what they typically derive.

2.5 Discussion

Before summarizing and discussing the disk properties of the M17 members B243 and B331, we show their positions in the Hertzsprung-Russell diagram (HRD) in Fig. 2.10. RT17 estimate an age for the M17 star-forming region of less than 1 Myr. This, combined with both sources showing both stellar absorption and disk emission features, strongly suggests that the stars are pre-main-sequence objects on Thomson or Henyey (a.k.a. radiative) tracks; in the final phase of their formation contracting towards the zero-age main sequence. The luminosity (and associated mass of $\sim 12\,M_{\odot}$) classifies B331 as an MYSO source. The estimated mass (of $\sim 6\,\mathrm{M}_{\odot}$) of the lower luminosity source B243 is more representative of the high-mass end of Herbig Be sources. The total MYSO lifetime, defined as the time from passing the birthline until arrival on the main sequence, is less than 10^5 yr for B331 and a few times 10^5 yr for B243 (Hosokawa & Omukai 2009); both stars have progressed considerably

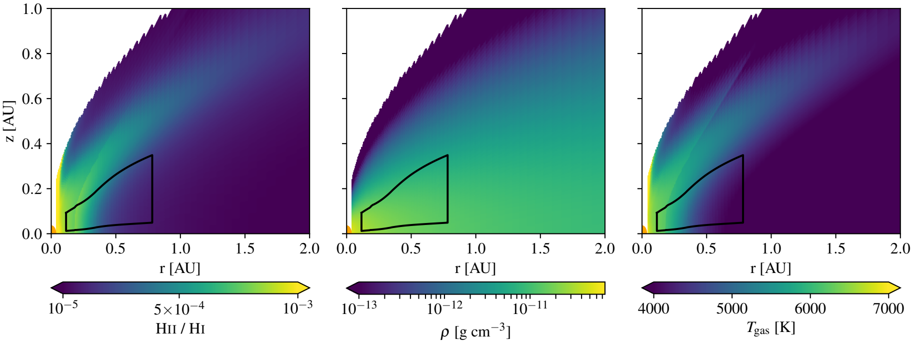

Figure 2.8: Hydrogen ionization, density, and temperature structure of the inner region of B243. The parameters used match the values indicated by the full red line in Fig. 2.5. The black contour indicates the approximate origin of 50% of the Pa-16 line emission based on vertical escape probabilities. The orange circle on the left indicates the central object.

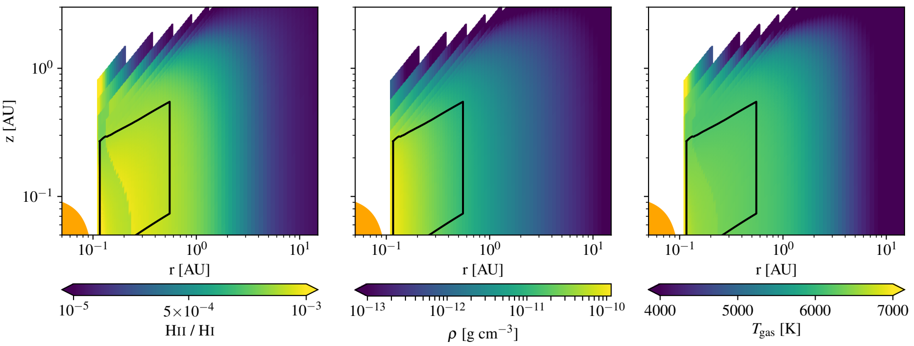

Figure 2.9: Same as Fig. 2.8, but now for B331 on a logarithmic spatial scale. The parameters used match the values indicated by the dashed red line in Fig. 2.5.

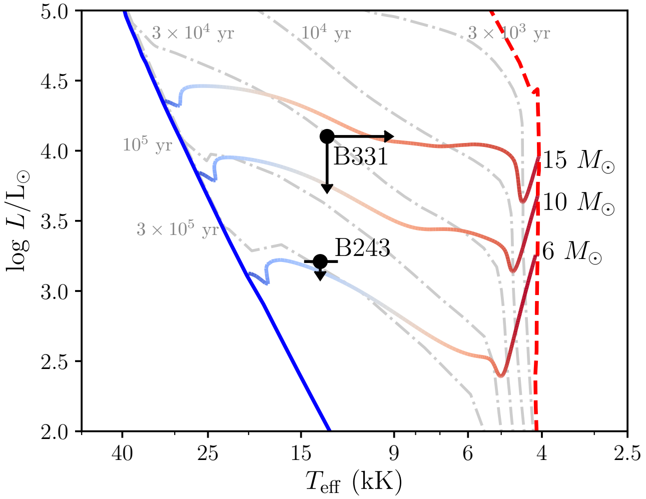

Figure 2.10: Adapted from Fig. 9 of (RT17). Positions of B243 and B331 in the Hertzsprung-Russel Diagram. The solid blue line on the left indicates the zero age main sequence. The dashed red line on the right indicates the birth line. The solid line connecting the birth line and the zero age main sequence indicate the MIST pre-main sequence evolutionary tracks of stars with masses indicated on the right (Dotter 2016). The colour of this line indicates the relative time between birth and reaching the main sequence. The dash dotted grey lines indicate the isochrones corresponding to 3×10^3, 10^4, 3×10^4, 10^5 and 3×10^5 years from top to bottom respectively.

in this evolution. Given these short evolutionary time scales and the observation that higher mass main-sequence stars in M17 lack disk signatures (RT17), one may anticipate that the disks of B331 and B243 are in the process of being cleared.

A schematic diagram illustrating the main properties derived for the two disks is shown in Fig. 2.11. Both stars feature a gaseous disk that almost (within a stellar radius or ~0.1 AU) reaches the stellar surface. The hydrogen emission lines originate from within the first AU of these disks, signifying that the full extend and properties of the gaseous disk are not probed by these diagnostics. The disk of B243 contains hot dust of ~1500 K, whereas the hottest grains surrounding B331 have a much lower temperature of 400 K implying a significant dust free inner zone spanning ~100 AU. The extend of the dust free inner zone depends on the continuum optical depth of the gaseous disk. A very opaque gas disk would move the dust disk closer to the star. The best fit model for the dust disk of B243 suggests an outer radius of ~6.5 AU, however, this is poorly constrained. The SED modelling suggests B243 is consistent with having a Group II disk and B331 a Group I disk. However, as our diagnostics are not sensitive to cool dust (our longest wavelength point is at 8 μm), we cannot rule out the presence of a (large) gap and cool dusty outer disk or a self-shadowed region in B243. Without the 8 μm point the outer radius of the hot dust disk would not be constrained. We conclude that both disks appear disrupted and identify them as transitional disks. Though not subject to analysis, both disks show pronounced CO-bandhead emission (RT17, Poorta et al. in prep.).

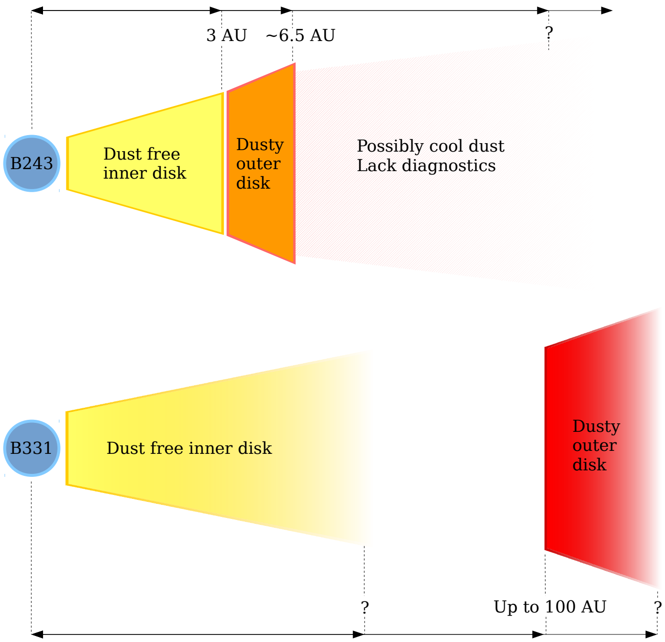

Figure 2.11: Schematic overview of the geometric properties of the disks of B243 and B331.

The gaseous inner disks of both stars have significantly larger scale heights close to the star than would be expected from standard hydrostatic calculations, consistent with puffed-up inner rims (Dullemond & Dominik 2004). This is further discussed in Section 2.5.2. We adopt a Keplerian rotation profile and did not find any indication that parts of the disk regions probed by the Paschen lines experience significant sub- or super-Keplerian motion. Still, we cannot fully exclude deviations from Keplerian motion as the rotation velocity is somewhat degenerate with the inner radius and inclination of the disk.

The small gaseous disk inner radii (of less than $2\,R_\star$) differs from the situation in lower mass YSOs. In these lower mass counterparts the disk material does not directly reach the stellar surface, but gas loops towards the surface via magnetospheric accretion (e.g. Ingleby et al. 2013). This leaves a gap between the disk and star. Fairlamb et al. (2015) study a large sample of Herbig AeBe stars and find the UV excesses of early type Be stars to be inconsistent with magnetospheric accretion (see also Wade et al. 2007). This suggests that higher mass stars lack strong magnetic fields. Another indication for the absence of a strong magnetic field is consistent with Keplerian rotation. Strong magnetic fields can cause the disk to co-rotate with the stellar surface. This results in lower than Keplerian velocities close to the star and would likely result in too low velocities to reproduce the observed line profiles. In conclusion, the disks reaching almost the stellar surface and being compatible with Keplerian rotation close to the inner rim is in line with a lack of magnetospheric accretion, consistent with the general consensus that most higher mass stars lack a strongly magnetized envelope (Mottram et al. 2007; Oudmaijer et al. 2017).

2.5.1 Uncertainties in stellar properties

Table 2.1 shows the stellar parameters of B243 and B331. For B243 they result from quantitative spectroscopy; for B331 from SED fitting. The main uncertainties on the properties of these stars are the temperature, extinction (A_V and R_V), and luminosity. The extinction parameters do not affect this work significantly as we fitted the normalized line profiles, and the extinction at the NIR is modest. The luminosity affects the dust sublimation radius of B243 and location of warm dust for B331. A higher luminosity also results in higher hydrogen line flux (but not necessarily a higher *normalized* line flux, as the continuum flux is also increased).

The surface gravity of B331 is unconstrained; we assume a value $\log g = 4.0$. The gravity of the star mostly affects the wings of the circumstellar H I emission profiles through the normalization process (see section 2.2.3), a too high gravity giving a broader emission profile. This would have to be compensated by a lower scale height or smaller inner radius.

2.5.2 Puffed up inner rim

At the inner rim, both B243 and B331 have a scale height significantly larger than expected based on the hydrostatic equilibrium approximation $H \sim c_{\rm s}/\Omega_{\rm K}$, with $c_{\rm s}$ the sound speed and $\Omega_{\rm K}$ the Keplerian rotation frequency. For $T = 6000\,{\rm K}$, $r = 0.2\,{\rm AU}$ and $M = 6\,{\rm M}_\odot$ the adopted scale height for B243 is 15 times the hydrostatic value. This 'puffed' up region is unlikely to extend far in to the disk. Despite such puffed up regions have been found before in efforts to model the inner region of disks (e.g. Woitke et al. 2009; Dullemond et al. 2001). A possible explanation for the large scale height could be that a disk wind contributes to the observed emission. However, a disk wind would possibly have a velocity profile distinct from a puffed up Keplerian disk. However, the velocity may still be dominated by orbital motion if the emission originates from close to the disk, with only a slight broadening of the profile.

We also investigated the effect of mass accretion on the inner rim structure. To this end, we performed test calculations of the best fit models to both B243 and B331 in which we use an accretion rate of $10^{-4}\,{\rm M}_\odot\,{\rm yr}^{-1}$. In these cases the line emission gets significantly stronger with 5 and 1.5 times more line flux for B243 and B331, respectively. The increase in line strength could be compensated by lowering the scale height. This would require a significant gas reservoir to be present to feed these accretion flows.

2.5.3 Origins of the hydrogen line emission and the role of chemistry

The hottest parts of the disks of B243 and B331 reach temperatures of ~7000 K and hydrogen ionization fractions of $\sim 10^{-3}$. We find charge exchange reactions to be the main source of hydrogen ionization. These reactions are facilitated by various heavier elements, in particular sulfur. Therefore, the abundance of these metallic species are of importance to the line formation. A lower metallicity will result in weaker lines. We note that the reaction rate coefficient of the charge exchange reaction with sulfur is highly uncertain. In ProDiMo an estimate for the reaction rate coefficient of $5 \times 10^{-12}\,\mathrm{cm}^3\,\mathrm{s}^{-1}$ is supplied. However, Butler & Dalgarno (1980) find an upper limit of $3 \times 10^{-15}\,\mathrm{cm}^3\,\mathrm{s}^{-1}$ at a temperature of 10^4 K for the reaction rate coefficient. The hydrogen emission line strength scales nearly linearly with the reaction rate coefficient, with a reaction rate reduced by a factor of 50 resulting in 40 times weaker lines. This would significantly affect the derived properties of the disk, requiring substantially higher disk masses.

Presently, the central stars' temperatures are too low to produce sufficient ionizing photons. Therefore, we conclude that the stars appear to be in a phase of formation in which chemistry dominates the production of ionized hydrogen. We note that as the stars move closer to the zero-age main sequence (ZAMS) photo-ionization may take over as the main mechanism of hydrogen ionization, particularly so for B331 (which may reach a ZAMS temperature of about 30 000 K), if a close-in gaseous disk should prevail to such a late stage.

The key role of chemistry also highlights the importance of the chemical network and the corresponding reaction rates. In this work we use the UMIST 2006 reaction network. We note that employing the UMIST 2012 reaction network results in ~20% weaker hydrogen emission lines. The charge exchange reaction rate coefficients of hydrogen and sulfur are not included in these networks, but instead are supplied by a separate ProDiMo input. We also do not find a significant difference in hydrogen line emission between the fiducial large and small chemical networks available in ProDiMo (Kamp et al. 2017).

2.5.4 Origin of the hydrogen line emission and accretion

Hydrogen emission lines are generally considered to be tracers of accretion when observed in (massive) young stellar objects (e.g. Ilee et al. 2014; Fairlamb et al. 2017; Mendigutía et al. 2011). This raises questions as to the possibility and nature of accretion in the disks. Fairlamb et al. (2017) speak of a correlation of line luminosities with accretion rate, while also noting that accretion need not be the physical origin of the lines. Their empirical relation between hydrogen line strength and accretion rate implies an accretion rate of $\sim 10^{-5}$ and $\sim 10^{-3}\,\mathrm{M}_\odot\,\mathrm{yr}^{-1}$ for B243 and B331, respectively. If a gap of at least tens of AU indeed separates the inner disks from more distant disk material (if present at all), these rates would deplete the inner disks, up to a few AU, of the order of years. The very small chance of detecting the systems at the exact moment of inner disk accretion suggests that either the inner disk is being fed from a more extensive outer reservoir, or, that the hydrogen emission is not an accurate tracer of accretion in these systems.

To expand on the latter possibility, the empirical relation mentioned above is derived using calibrations based on magnetospheric accretion modelling. Following from our previous discussion of disk geometry and magnetic fields, as well as drawing from recent literature on accretion luminosities in Herbig AeBe stars (e.g. Wichittanakom et al. 2020; Grant et al. 2022; Mendigutía 2020) it is likely that higher mass YSOs ($\gtrsim 4\,\mathrm{M}_\odot$) accrete by a different mechanism. An obvious alternative is boundary-layer accretion, where disk material slows down in a transition layer between the disk and the star, releasing its kinetic energy in that boundary layer. Lynden-Bell & Pringle (1974) relate the mass accretion rate to a black body emission from an annulus with temperature T_{BL}. They assume all orbital kinetic energy is dissipated through radiation from the boundary layer. However, this assumes the layer to be optically thick and the radiation from the central star heating up the material is ignored. Despite those assumptions, using the accretion rates above we find T_{BL} to be larger than the temperature in the inner rim of the disk for both B243 and B331. A more detailed modelling of boundary-layer accretion including the stellar radiation field and more accurate heating and cooling processes would be required to accurately link the temperature of the inner disk and the accretion rate of the star. Currently, there is no model that relates (hydrogen) line emission to accretion rate in the BL regime.

2.5.5 Disk effect on the central star

The disks, given their small inner radii and the possibility of ongoing accretion, might still affect the properties of their central star on its way to the main-sequence.

Following the arguments made in the previous section and based on the derived disk masses, it is likely that the central stars have accumulated the mass at which they will start central hydrogen fusion. However, the inner disk mass may contain a sizable amount of angular momentum. Here we estimate the effect of the disk on the surface rotational velocity of the star once it reaches the ZAMS.

Assuming conservation of angular momentum for the stars and no further accretion we can calculate the surface rotational velocity upon arrival on the ZAMS. On the basis of their assumed stellar masses, we adopt radii of 2.5 $\mathrm{R}_{\odot}$ and 4.2 $\mathrm{R}_{\odot}$ at the ZAMS for B243 and B331, respectively (Brott et al. 2011). The radial density structure of the stars is approximated using the solution of the Lane-Emden equation for a polytropic index of 1.5 in both the current state and at the ZAMS. We further assume solid body rotation. Taking an inclination of 75° converts the $v \sin i$ of 110 $\mathrm{km\,s^{-1}}$ into $v_{\mathrm{rot}} = 114$ $\mathrm{km\,s^{-1}}$ for the present-day state of B243. After contracting to the main sequence this results in a rotational velocity of 342 $\mathrm{km\,s^{-1}}$, which is $\sim$0.50 v_{crit}, where v_{crit} is the critical rotation rate. If we adopt a column density at the inner radius of the disk of 1000 $\mathrm{g\,cm^{-2}}$ and a relatively flat column density exponent of $\epsilon = -0.5$, the angular momentum of a 5 AU inner disk would be $\sim$17% of that of the star. The current v_{rot} has not been constrained for B331. Doing the same calculation for this star under the same assumptions and taking the current $v \sin i = 110$ $\mathrm{km\,s^{-1}}$, the same value as for B243, yields a ZAMS spin velocity of $\sim$ 592 $\mathrm{km\,s^{-1}}$, which is $\sim$0.80 v_{crit}. The angular momentum of the disk is then $\sim$ 7% of that of the star.

These estimates suggest that the inner disk is unlikely to still contribute strongly to the ZAMS rotational velocity of the central star; its value is essentially controlled by stellar contraction. Spin velocities of 0.5-0.9 v_{crit} upon arrival on the main sequence are in line with previous findings for stars in the same mass range (Huang et al. 2010). For stars with a weak or lacking magnetic connection to the disk (see above) gravitational torques are expected to limit the ZAMS spin velocity to about half critical (Lin et al. 2011). This may be an indication that the current projected spin rate of B331 is less than the adopted 110 km s^{-1}.

2.5.6 Disk disruption scenarios

The leading mechanisms responsible for the dispersal of disks around young stars are photo-evaporation (e.g. Gorti & Hollenbach 2009; Owen et al. 2010), stellar or planetary companion formation (e.g. Müller & Kley 2013), and possibly stellar winds for the most massive YSOs (Bik et al. 2006). Given the relatively high temperatures of the MYSO sources studied here relative to pre-main sequence stars of lower mass, photo-evaporation may be a contender for disk dispersal. Owen et al. (2010) provide a simple scaling relation for the characteristic radius where thermal evaporation by EUV light starts, after which more inner parts of the disks are cleared on a timescale of a few times 10^4 yr assuming the disk dispersal time is only a weak function of stellar mass as suggested by Owen et al.. For our sources this radius is at about 100 AU; it corresponds well to the size of the dust free gap or zone we observe in both sources. In this mechanism, the innermost parts of the disks (i.e. those probed by H lines) survive the longest (Alexander et al. 2006). So, photo-evaporation as a disk dispersal mechanisms seems congruent with the derived disk properties for both B243 and B331. We remark however that photo-evaporation models do not take into account a puffed-up inner disk, as found for both stars, that may extinct a sizeable amount of the ionizing radiation, limiting the EUV-illumination of further out regions and hence efficient disk dispersal. Gorti & Hollenbach (2009) study the effect of X-ray, EUV, and FUV radiation on the photo-evaporation of disks. They find the photospheric FUV radiation to be the dominant energy source driving mass-loss from the outer regions of the disk, and EUV radiation to only affect the inner regions of the disk. We expect the inner gaseous disk to be optically thin to FUV radiation and the central stars to be bright in the FUV, therefore it would be a potential energy source for photo-evaporation.

Ongoing photo-evaporation would result in observable spectral features such as forbidden oxygen emission and H_2 emission (e.g. Gangi et al. 2020). Though we have not detected any H_2 emission, B243 shows forbidden [O I] λ630 nm emission. Its behaviour is different on-source than off-source pointing at a possible circumstellar origin (Derkink et al. in prep.). The [O I] emission of B331 does not allow us to make this distinction.

Gaps in proto-planetary disks are commonly observed in the low mass counterparts of MYSOs and were first identified in Strom et al. (1989). Kim et al. (2013) collate 105 of these disks. They propose the gaps are likely due to companions orbiting the central object, and that an origin linked to grain growth, turbulence or photo-evaporation processes is less likely.

Companions formation through gravitational instabilities in efficiently cooling disks appears feasible on the timescales of MYSO formation, at least theoretically (e.g. Rice et al. 2003; Oliva & Kuiper 2020). In this scenario the companion will create a gap in the disk, preventing material to flow through its orbit efficiently. A small amount of gas may travel past the gap to sustain the observed gaseous inner disk while blocking dust, creating a dust free inner disk (e.g. Lubow & D'Angelo 2006). This scenario too seems in line with the derived disk

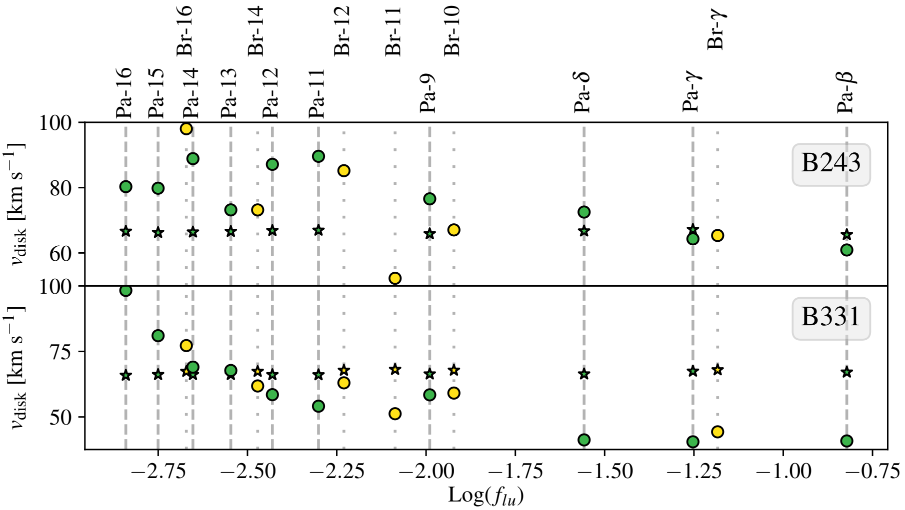

Figure 2.12: Orbital velocity of the hydrogen gas based on the peak separation of the observed (circles) and simulated (stars) emission lines as function of their oscillator strength. Green markers indicate Paschen lines and yellow markers Brackett lines. The velocity is determined by fitting double gaussians to the profile. The simulated profiles are from Figures 2.4 and 2.7.

properties for both stars. We note that such companion forming disks are expected to develop a spiral structure, which, if indeed the correct scenario, may perhaps play a role in explaining the (modest) discrepancies between predicted and observed H line profiles discussed below.

We conclude that both disk dispersal mechanisms appear reasonable candidates to explain the observed disk structures in B243 and B331.

2.5.7 Deviating trends in hydrogen series properties

Figures 2.4 and 2.7 show that a single model cannot fully recover the line strengths of all modelled Paschen and Brackett series lines: lower (higher) series lines are predicted stronger (weaker) than observed. Differences remain within a factor of two though, while the range of line strengths spans a factor ∼20−30. In addition to this, we observe a modest discrepancy in the trend of peak separation versus line strength.

Figure 2.12 shows that the disk velocity decreases for increasing oscillator strength for both B243 and B331. As in our Keplerian disk model all line emission originates from the optically thin inner disk region (i.e. from the first AU) no such trend is predicted. For classical Be stars a similar trends in found as in our systems (e.g. Kraus et al. 2012). These authors could spatially resolve the emitting region of different groups of hydrogen lines for one such Be disk and find spatially different formation regions. This indicates that in this Be disk the hydrogen lines are optically thick (unlike in our MYSO modelling).

Though we cannot pinpoint the cause of the mismatch in peak separation trend, part of it may possibly be explained by deviations from azimuthal symmetry in the inner disk. It also remains to be investigated how the inclusion of (boundary-layer) accretion and disk winds would affect the modelled lines. Massive YSO sources in M17, including the objects studied here, show variability in their spectra originating in their circumstellar disks (Derkink et al. in prep.). This variability includes excess line emission moving from the red to the blue part of the line on timescales consistent with the rotation period of the inner disk, underlining that likely there are processes active in the inner disks that break axial symmetry. Possible features include spirals, warps, large scale clumps or other, more chaotic, forms of asymmetries.

2.6 Summary

We have investigated the inner disk regions of two MYSO sources, B243 (with an estimated mass of 6 $M_\odot$) and B331 (12 $M_\odot$) in the star-forming region M17, using the thermo-chemical code ProDiMo. Likely, these inner disks are remnant structures from the star assembly process.

Our main diagnostics are (double-peaked) hydrogen lines of the Paschen and Brackett series and near-IR photometry. The first allow us to probe the kinematics and structure of the gaseous inner disk and the second the thermal emission of hot dust. The effective temperatures of the central stars are such that photo-ionization of hydrogen is much less important than ionization through charge exchange reactions, so it is chemistry that dominates the H line-formation.

Our main findings are:

1. A small puffed-up gaseous disk extends to very close to the stellar surface in both Group II source B243 and Group I source B331. In B243 a dust free cavity of 3 AU is present with hot dust of 1500 K at the inner rim of the dusty disk. We find a best fit outer radius of ~6.5 AU, but this is poorly constrained. The inner disk of B331 is dust free and probably of similar dimension, cool dust indicating an outer disk starting at about 100 AU with a dust free (and possibly gas free) gap in between.
2. The inner disk extending to almost the stellar surface suggests that some accretion might still be ongoing, likely through boundary-layer (BL) accretion. Magnetospheric accretion is less likely as the geometry of this accretion mechanisms suggests an inner gaseous disk gap. A lack of magnetospheric accretion is in line with the general consensus that a different accretion mechanism is at work in higher mass stars. A first order approach indicates that it would be interesting to investigate the BL mechanism for higher mass Herbig Be stars and MYSOs with detailed line modelling. The presence of disk winds remains an open question.
3. The inner disk contains too little mass and too modest angular momentum to significantly change the final (i.e. ZAMS) mass and final spin velocity of the stars. Concerning the latter, contraction towards the main sequence is the main effect impacting the spin velocity in the remainder of pre-main sequence evolution (see also Ramírez-Tannus

et al. 2017). The angular momentum of the inner disk is of the order of 10% of that of the central star.

4. The disk structures of both sources strongly suggest that the disks are in the process of being cleared, that is they are transitional disks. Possible disk dispersal mechanisms are photo-evaporation and stellar or planetary companions formation. The derived properties of the disks are compatible with both scenarios, specifically the presence of a small inner disk and a disk gap towards a more distant ($\sim$100 AU) outer disk (in B331 and possibly in B243).

The study presented here does not fully characterize the disks orbiting B243 and B331; but it does present the first detailed 2D thermo-chemical radiative transfer modelling of hydrogen lines in such sources. High resolution, longer wavelength imaging with for example ALMA would greatly add to our insight in the properties of the outer regions of the disk. Whether such regions (if they exist at all in B243) would still play a role in the formation process of the central object remains to be seen, given the proximity of the stars to the ZAMS. The fate of such outer disks may simply be that they are dispersed by the concerted action of the star's H II region and stellar wind upon arrival on the ZAMS (e.g. Geen et al. 2021). Studies of line variability may contribute to our understanding of dynamical process in the inner disks, possibly due to the presence of companions. The combination of these different approaches may greatly help in unravelling the architecture of companion systems around massive stars, their possible migration (Ramírez-Tannus et al. 2021), and pre-main sequence or early main sequence merging with the primary star (Wang et al. 2022); topics that constitute new and exciting problems in massive star formation.

Chapter 3

A relation between the radial velocity dispersion of young clusters and their age: Evidence for hardening as the formation scenario of massive close binaries

---

M.C. Ramírez-Tannus, F. Backs, A. de Koter, H. Sana, H. Beuther, A. Bik, W. Brandner, L. Kaper, H. Linz, Th. Henning, J. Poorta

Astronomy and Astrophysics, 2021, 645, L10

Abstract

The majority of massive stars ($> 8\,\mathrm{M}_\odot$) in OB associations are found in close binary systems. Nonetheless, the formation mechanism of these close massive binaries is not understood yet. Using literature data, we measured the radial-velocity dispersion (σ_{RV}) as a proxy for the close binary fraction in ten OB associations in the Galaxy and the Large Magellanic Cloud, spanning an age range from 1 to 6 Myrs. We find a positive trend of this dispersion with the cluster's age, which is consistent with binary hardening. Assuming a universal binary fraction of $f_{\mathrm{bin}} = 0.7$, we converted the σ_{RV} behavior to an evolution of the minimum orbital period P_{cutoff} from ∼9.5 years at 1 Myr to ∼1.4 days for the oldest clusters in our sample at ∼6 Myr. Our results suggest that binaries are formed at larger separations, and they harden in around 1 to 2 Myrs to produce the period distribution observed in few million year-old OB binaries. Such an inward migration may either be driven by an interaction with a remnant accretion disk or with other young stellar objects present in the system. Our findings constitute the first empirical evidence in favor of migration as a scenario for the formation of massive close binaries.

3.1 Introduction

It is well established that the vast majority of massive stars ($M > 8$ M$_\odot$) come in pairs or as higher-order multiples (e.g., Mason et al. 2009; Chini et al. 2012; Peter et al. 2012; Kiminki & Kobulnicky 2012; Kobulnicky et al. 2014; Sana et al. 2014; Dunstall et al. 2015). A large fraction of these binaries have orbital periods on the order of 2 months or shorter (Sana & Evans 2011; Sana et al. 2012; Kiminki & Kobulnicky 2012; Almeida et al. 2017; Barbá et al. 2017). These binaries are efficiently detected with spectroscopic techniques measuring periodic Doppler shifts of the photospheric lines. Massive binaries produce a variety of exotic products later in their evolution such as X-ray binaries, rare types of supernovae (Ibc, IIn, super-luminous SNe, Whelan & Iben 1973; Yoon et al. 2010; Langer 2012), gamma-ray bursts (Woosley et al. 1993; Cantiello et al. 2007), and, eventually, gravitational wave sources (e.g., Ivanova et al. 2013; Mandel & de Mink 2016; de Mink & Mandel 2016; Eldridge & Stanway 2016). However, the origin of massive close binaries remains unknown.

The first effort to characterize the binarity properties of a sample of O stars in compact H II regions was performed by Apai et al. (2007). They did a multi-epoch (two to three epochs) radial velocity (RV) study of a sample of 16 embedded O stars in seven massive star-forming regions. They identified two close binary stars based on their RV variations (~ 90 km s^{-1}) and measured an RV dispersion ($\sigma_{\rm RV}$) of 35 km s^{-1} for the whole sample and 25 km s^{-1} when excluding the two close binaries.

After pioneering studies to spectroscopically characterize single massive young stellar objects (mYSOs) such as those carried out by Bik et al. (2006, 2012), Ochsendorf et al. (2011), and Ellerbroek et al. (2013), Ramírez-Tannus et al. (2017) performed a single-epoch VLT/X-shooter spectroscopic study of a sample of eleven candidate mYSOs in the very young giant H II region M17 ($\lesssim 1$ Myr). The stars range in mass from $6 - 25$ M$_\odot$ which is the mass range that dominates the samples from which multiplicity characteristics of 2-4 Myr old main-sequence OB stars are derived (Sana et al. 2012; Kobulnicky et al. 2014). The measured radial-velocity dispersion of these mYSOs is $\sigma_{\rm 1D} = 5.6 \pm 0.2$ km s^{-1}. In low density clusters, such as M17, $\sigma_{\rm RV}$ of a single epoch is strongly dominated by the orbital properties of the binary population. For example, if a given cluster has several close binaries of similar masses, one would expect the individual radial velocities of the stars to differ significantly from each other and, therefore, for $\sigma_{\rm RV}$ to be large. For 2-4 Myr clusters, with binary fractions > 0.5 and minimum periods of ~ 1.4 days, a dispersion of 30 to 50 km s^{-1} is typical (e.g., Kouwenhoven et al. 2007b; Sana et al. 2008, 2012; Sota et al. 2014; Kobulnicky et al. 2014). The latter is in stark contrast with our observation of M17, suggesting a lack of close massive binaries in this region.

In Sana et al. (2017), two scenarios are explored that may explain the low $\sigma_{\rm RV}$ observed in M17: a small binary fraction $f_{\rm bin}$ and/or a lack of short-period binaries. They conclude that the observed dispersion can be explained either if $f_{\rm bin} = 0.12^{+0.16}_{-0.09}$ or if the minimum orbital period $P_{\rm cutoff} > 9$ months. Parent populations with $f_{\rm bin} > 0.42$ or $P_{\rm cutoff} < 47$ days can be rejected at the 95% significance level. Since it is unlikely that the binary fraction for M17 would be so far below that of other clusters, this very interesting result suggests that massive binaries form in wide orbits that migrate inward over the course of a few million years. In this letter, we refer to the generic mechanism of shrinking binary periods as the migration scenario. One strong test for this scenario is to compare the velocity dispersion observed in clusters spanning a range of ages. If the binary orbits harden with time, one would expect $\sigma_{\rm RV}$ to increase as the cluster age increases.

In Ramírez-Tannus et al. (2020), VLT/KMOS spectra of around 200 stars in three very young clusters (M8, NGC 6357, and G333.6-0.2) were obtained. Introducing an automatic method to classify the spectra, the effective temperatures, and luminosities of the observed stars were characterized in order to place them in the Hertzsprung-Russell diagram (HRD). The age and mass range of the observed populations was constrained by comparison to MESA evolutionary tracks obtained from the MIST project (Paxton et al. 2011, 2013, 2015; Dotter 2016; Choi et al. 2016). The main sequence stars in M8 have masses between $\sim$ 5 and $\sim$ 70 $M_\odot$ and the age of this cluster is between 1 and 3 Myr. In G333.6-0.2, the main sequence population ranges in mass between $\sim$ 5 and $\sim$ 35 $M_\odot$ and the estimated age of this region is $<$ 3 Myr. The main sequence stars in NGC 6357 have masses between $\sim$ 10 and $\sim$ 100 $M_\odot$ and their ages range from $0.5 - 3$ Myr.

The goal of this paper is to provide a first test of the migration scenario for the formation of massive close binaries. We aim to study a possible age evolution of $\sigma_{\rm RV}$, and $P_{\rm cutoff}$, to constrain a timescale for binary hardening assuming a universal binary fraction ($f_{\rm bin}$= 0.7; Sana et al. 2012). We base our analysis on clusters younger than 6 Myr to ensure that neither secular evolution nor the effect of binary interactions (Wellstein & Langer 1999; de Mink et al. 2007) affect our results significantly. In Section 3.2 we measure the radial velocities of the high-mass stars in M8 and NGC 6357 and calculate their $\sigma_{\rm RV}$. Next, we compare our findings with those presented by Sana et al. (2012) for Galactic clusters of 2-4 Myr, with those from Zeidler et al. (2018) for Westerlund 2 (Wd2), with those from Hénault-Brunet et al. (2012) for R136 in the Large Magellanic Cloud, and with those from Ramírez-Tannus et al. (2017) for the very young massive-star forming region M17. This reveals a temporal behavior of $\sigma_{\rm RV}$ (Section 3.3) that is converted into an evolution of the minimum binary period (Section 3.4), as binary motion is dominating the velocity dispersion of young massive clusters. In Section 3.5 we discuss and conclude this work.

3.2 Observations

The sample studied in this paper consists of the OB stars in M8 and NGC 6357. The data acquisition and reduction are described in detail in Ramírez-Tannus et al. (2020). In short, we obtained around 200 H and K-band intermediate resolution spectra (with spectral resolution power, $\lambda/\Delta\lambda$, between 6700 and 8500, i.e., $30 < \Delta v < 40$ km s^{-1}) of stars in the abovementioned giant H II regions with VLT/KMOS (Sharples et al. 2013). The final samples of massive stars consist of 16 stars in M8, 22 in NGC 6357, and four in G333.6-0.2. We discarded G333.6-0.2 from our analysis because there are not enough stars with RV measurements to calculate $\sigma_{\rm RV}$. A description of the age and mass range determination can be found in Ramírez-Tannus et al. (2020), and Appendix II.1 presents a detailed discussion about the accuracy of the age determination.

The radial velocity (RV) of the intermediate to high-mass stars was obtained by measuring the Doppler shifts of a suitable set of photospheric lines. Tables II.1 and II.2 list the RV obtained for each star together with its error and the spectral lines used in our analysis.

The RV-fitting approach is similar to the one adopted by Sana et al. (2017). First, for the profile fitting, we adopted Gaussian profiles. Second, we clipped the core of diagnostic lines that were still contaminated by residuals of the nebular emission. Third, we simultaneously fit all spectral lines available, thereby assuming that the Doppler shift is the same for all lines (see Section 2 and Appendix B of Sana et al. 2013).

Figure II.1 shows the radial-velocity distribution for the two regions. We calculated the errors of the histogram bins by randomly drawing RV values from a Gaussian centered at each measured RV and with a sigma corresponding to the measurement error; we repeated that process 10^5 times. The value shown for each bin is the mean of all the RVs in that bin's measurements and the error bar corresponds to the standard deviation. We obtained $\sigma_{\rm RV}$ by calculating the weighted standard deviation of the measured RVs. The weighted mean and standard deviation are listed in the top-left corner of each histogram in Fig. II.1. The measured $\sigma_{\rm RV}$ for M8 and NGC 6357 are 32.7 ± 2.6 and $26.9 \pm 1.3\,\mathrm{km\,s^{-1}}$, respectively.

3.3 Velocity dispersion versus cluster age

Based on single-epoch radial-velocity measurements of young massive stars in M17, Sana et al. (2017) conclude that this young ($\sim$1 Myr) star-forming region hosts only a few close binary systems. This is in contrast to the observation that most massive stars in somewhat older clusters are in close binaries. Under the hypothesis that massive stars form in wide binary systems that harden their orbits within the first million years of evolution, one would expect that during those initial couple of million years the radial-velocity dispersion, $\sigma_{\rm RV}$, increases with time.

We plotted $\sigma_{\rm RV}$ of the clusters studied in this paper and compare it with the results by Sana et al. (2012, NGC 6231, IC 2944, IC 1805, IC 1848, NGC 6611), Zeidler et al. (2018, Wd2), Hénault-Brunet et al. (2012, R136), and Sana et al. (2017, M17). R136 and Wd2 are very relevant for our study given their relatively young age (1-2 Myr) which is in between the age measured for M17 (Ramírez-Tannus et al. 2017) and that of the somewhat older clusters (Sana et al. 2012). In order to compare the multi-epoch RV data provided by Sana et al. (2012) with the single epoch data of M17, M8, NGC 6357, and Wd2, we drew the RV measured for each star in a given cluster in a random epoch and we computed the RV dispersion. We repeated this procedure 10^5 times and then calculated the most probable $\sigma_{\rm RV}$ and its standard deviation. The $\sigma_{\rm RV}$ obtained for each cluster is listed in the third column of Table 3.1. The second and seventh columns show the age of the clusters and the respective references.

Table 3.1: Age, radial-velocity dispersion, number of stars, and mass range for our sample of young clusters hosting massive stars.

Cluster	Age	σ_{1D}	N	Mass	$P_{\rm min}$	Age
	Myr	km s^{-1}	stars	M$_\odot$	days	ref.
IC1805	1.6 – 3.5	65.5 ± 3.1	8	15 – 60	$1.4^{+0.8}$	1
IC1848	3.0 – 5.0	50.3 ± 12.8	5	15 – 60	$1.4^{+3.2}$	2
IC2944	2.0 – 3.0	31.4 ± 0.3	14	15 – 60	$6.3^{+17.8}_{-4.5}$	3
NGC6231	3.5 – 5.4	67.6 ± 0.4	13	15 – 60	$1.4^{+0.7}$	4
NGC6611	2.0 – 6.0	25.3 ± 1.6	9	15 – 60	$10.1^{+43.0}_{-8.5}$	5
Wd2	1.0 – 2.0	15.0 ± 0.1	44	6 – 60	$62.2^{+74.9}_{-36.1}$	6
M17	0.0 – 2.0	5.5 ± 0.5	12	6 – 20	3500_{-2834}	7
M8	1.0 – 3.0	32.7 ± 2.6	16	6 – 20	$2.4^{+3.8}_{-1.0}$	8
NGC6357	0.5 – 3.0	26.9 ± 1.3	22	6 – 30	$5.4^{+8.5}_{-3.4}$	8
R136	1.0 – 2.0	25.0 ± 5.9	332	15 – 60	$24.1^{+9.0}_{-5.1}$	9

(1) Sung et al. (2017); (2) Lim et al. (2014); (3) Baume et al. (2014); (4) van der Meij et al. (2021); (5) Gvaramadze & Bomans (2008); (6) Zeidler et al. (2018); (7) Ramírez-Tannus et al. (2017); (8) Ramírez-Tannus et al. (2020); (9) Hénault-Brunet et al. (2012)

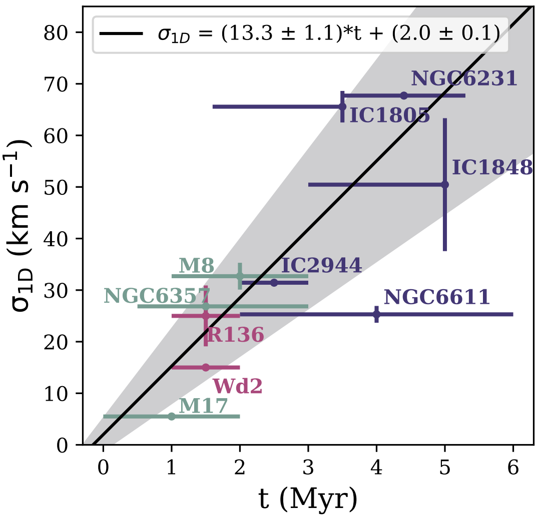

Figure 3.1: Radial-velocity dispersion ($\sigma_{\rm RV}$) versus age of the clusters. The purple data points show the data from Sana et al. (2012), the magenta points show Wd2 and R136 (Zeidler et al. 2018; Hénault-Brunet et al. 2012), and the green data points show the clusters studied in Ramírez-Tannus et al. (2020) and Sana et al. (2017). The solid black line represents the linear fit to the data and the gray area shows the 1-σ errors on the fit.

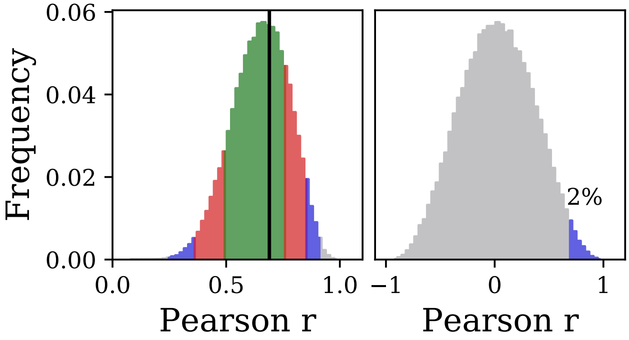

Figure 3.2: Distribution of Pearson coefficients after randomly drawing 10^5 samples from the data shown in Figure 3.1. *Left:* 2D Gaussians centered at our data points and with σ equal to our error bars. The green, red, and blue areas show the 68, 95, and 99% confidence intervals, respectively. The black line shows the observed coefficient. *Right:* 2D Gaussians centered at random locations of the parameter space (age between 0 and 7 Myr and σ_{RV} between 0 and 80 km s^{-1}) and with σ equal to our error bars. The blue shaded area represents the probability (2%) that the observed coefficient is caused by a random distribution.

In Figure 3.1 we show σ_{RV} versus age of the clusters. We performed an orthogonal distance regression (ODR; Churchwell 1990) to the data and find a positive correlation between the age of the clusters and σ_{RV}. The solid black line represents the best fit to the data and the gray area represents the 1-σ error on the fit. The Pearson coefficient for the observed relation is 0.7, which indicates a strong positive correlation. Nevertheless, this coefficient does not take into account the errors in the parameters. To test the validity of our results we performed two Monte Carlo tests whose results are shown in Figure 3.2. The left panel shows the distribution of Pearson coefficients obtained from drawing random points centered on our data (age, σ_{RV}) with a standard deviation equal to our error bars. The right panel shows the probability (2%) that a random distribution causes the observed coefficient.

Even though the scatter is substantial, we conclude that for the present data there is a positive correlation between σ_{RV} and the age of the clusters. Although the number of clusters considered here remains limited and there are sizable uncertainties as to the individual age determinations, our results indicate an increase in the fraction of close binary systems as the clusters get older. M17 seems to be a unique cluster given its very young age and extremely low σ_{RV}. Trumpler 14 in this sense seems comparable, being $\sim$1 Myr old and having no evidence for close binaries amongst its O stars (Sana & Evans 2011). We do not include this cluster in the analysis because there are not enough stars with RV measurements to calculate σ_{RV}.

3.4 Physical parameters

Our aim is to characterize the multiplicity properties of observed clusters based on the observed $\sigma_{\rm RV}$. This section presents the results of Monte Carlo population syntheses computed with different underlying multiplicity properties.

3.4.1 Binary fraction and minimum period

We focus on the effect that the binary fraction, $f_{\rm bin}$, and minimum orbital period, $P_{\rm cutoff}$, have on the observed $\sigma_{\rm RV}$. The methodology is similar to that used in Sana et al. (2017). A parent population of stars is generated with a certain $f_{\rm bin}$ and $P_{\rm cutoff}$. The binary star systems in this population are described by their orbital properties. These are the primary mass, M_1, mass ratio, q, period, P, and eccentricity, e. For the multiplicity properties that we do not vary, we adopt the values from Sana et al. (2012) for Galactic young clusters as the basic properties for our population. For the primary star, we adopt a Kroupa mass distribution (Kroupa 2001). The mass ratio distribution is uniform with $0.1 < q < 1$. The probability density function of the period is described as $\mathrm{pdf}(P) \propto (\log P)^{-0.5}$, with the period in days and $\log P_{\rm cutoff} < \log P < 3.5$. The eccentricity distribution depends on the period of the binary system. For $P < 4$ days, we assume circular orbits; for periods between 4 and 6 days, the eccentricities are sampled from $\mathrm{pdf}(e) \propto e^{-0.5}$, with $0 \leq e < 0.5$; for periods longer than 6 days the same distribution is used, but with $0 \leq e < 0.9$.

In order to calculate the radial velocity of the binary star systems, they are given a randomly generated inclination, i, longitude of periastron, ω, and eccentric anomaly, E. The latter is determined by generating a random mean anomaly and numerically solving Kepler's equation to find the corresponding eccentric anomaly using Brent's method (Brent 1973)[1]. This gives all of the information required to calculate the binary component of the radial velocity of the primary star through

$$v_{\rm r,b} = K_1 \left(e\cos(\omega) + \cos\left[2\arctan\left(\sqrt{\frac{1+e}{1-e}} \tan\left(\frac{1}{2}E\right) \right) + \omega \right] \right), \tag{3.1}$$

with K_1 being the amplitude of the orbital velocity of the primary star. The binary component of the radial velocity is added to the velocity due to cluster dynamics, $\sigma_{\rm dyn}$. This results in a population of stars with radial velocities based on either cluster dynamics only (in the case of $f_{\rm bin}$=0) or both cluster dynamics and binary orbits. The secondary stars are assumed to be undetected. We adopt a cluster velocity dispersion for all clusters of 2 km s^{-1}, which corresponds to the typical value found by Kuhn et al. (2019) who measured $\sigma_{\rm dyn}$ for several massive clusters in the Milky Way. Adopting $\sigma_{\rm dyn} = 1$ or $\sigma_{\rm dyn} = 5$ km s^{-1} has no significant effect on our results. Sana et al. (2012) also conclude that the dynamical dispersion of young clusters is negligible with respect to the dispersion due to binary motions. Each Monte Carlo run consists of a generated parent population of 10^5 stars, which is sampled 10^5 times to simulate the observation of a cluster. The mass distribution of the stars in the parent distribution are matched to the mass distribution in the observed cluster. The samples

---

[1] https://docs.scipy.org/doc/scipy/reference/generated/scipy.optimize.brentq.html

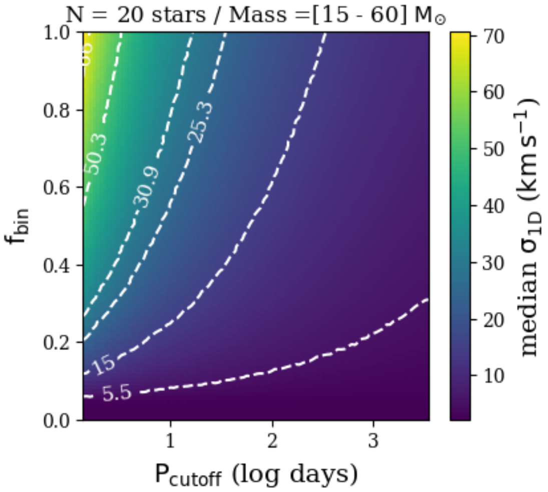

Figure 3.3: Median $\sigma_{\rm RV}$ obtained for distributions with different combinations of $f_{\rm bin}$ and $P_{\rm cutoff}$. For this set of simulations, we used a sample of 20 stars ranging in masses from 15 to 60 $\mathrm{M}_\odot$. The contours show the trends followed by $\sigma_{\rm RV}$ values of 5.5, 15, 25.3, 30.9, 50.3, and 66 $\mathrm{km\,s^{-1}}$.

contain the same number of stars and measurement accuracy as the observed sample. We then constructed density distributions of $\sigma_{\rm RV}$ for each parent population. Each grid point in Figure 3.3 shows the median $\sigma_{\rm RV}$ obtained for a simulated cluster of 20 stars sampled from a parent population with masses between 15 and 60 $\mathrm{M}_\odot$, where we varied $f_{\rm bin}$, and $P_{\rm cutoff}$. The color bar corresponds to $\sigma_{\rm RV}$ in $\mathrm{km\,s^{-1}}$. The dashed lines show the $\sigma_{\rm RV}$ contours for 5.5, 15, 25.3, 30.9, 50.3, and 66 $\mathrm{km\,s^{-1}}$, which correspond to the $\sigma_{\rm RV}$ measured for our clusters. As the number of stars and the mass ranges are different for each cluster, the contours do not represent the exact way in which we measured $P_{\rm cutoff}$ but are meant to show examples of the trends that a certain $\sigma_{\rm RV}$ follows in this diagram. A comparison of our results with Sana et al. (2017) is shown in Appendix II.4.

3.4.2 Timescale of binary hardening

Assuming that the binary fraction of massive stars is consistent with that observed in OB stars in young open clusters ($f_{\rm bin} = 0.7$; Sana et al. 2012), but that binary stars are born in wider orbits, we can estimate $P_{\rm cutoff}$ which best represents the observed $\sigma_{\rm RV}$ for each cluster. For each cluster, we kept the distribution of orbital properties fixed and we adjusted the sample size and mass ranges in accordance to those of the observed samples (see Table 3.1). This allowed us to make a similar plot as in Figure 3.1 but in terms of $P_{\rm cutoff}$. Figure 3.4 shows the estimated $P_{\rm cutoff}$ for each cluster as a function of cluster age. We determined that, assuming $f_{\rm bin} = 0.7$, the most likely $P_{\rm cutoff}$ to explain the observed $\sigma_{\rm RV}$ of M17 is around 3500 days and that a $P_{\rm cutoff}$ of 665 days and 126 days can be rejected at the 68% and 95% confidence levels, respectively. For the clusters with the largest $\sigma_{\rm RV}$ in our sample, IC 1805, IC 1848, and

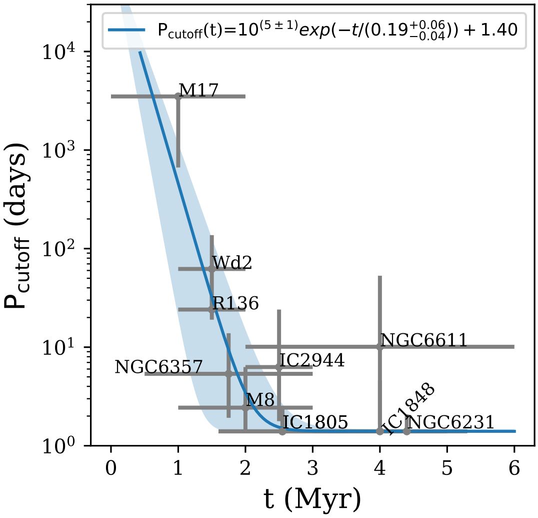

Figure 3.4: P_{cutoff} versus age of the clusters. The error bars represent the P_{cutoff} corresponding to the distributions that represent each σ_{RV} within their 68% confidence range. The blue line and shaded region show the fit to the data and its 1-σ error bars.

NGC 6231, the cutoff period that best explains the observed σ_{RV} is 1.4 days, which is the P_{cutoff} adopted by Sana et al. (2012).

In order to get a first estimate of the binary hardening timescale, we fit a function of the form $P(t) = P_0 e^{-t/t_0} + c$ to the data in Figure 3.4, where P_0 is the minimum period at the moment of binary formation and t_0 corresponds to the e-folding time. As P_0 is very uncertain, we assumed a typical value of 10^5 days, corresponding to an initial separation of ~100 AU for a pair of 10 $M_\odot$ stars. In order to find the range of t_0, we varied P_0 from 10^4 to 10^6 days. The resulting fit and corresponding parameter ranges are shown with the blue line and shaded area in Figure 3.4. We obtain a typical e-folding time of $t_0 = 0.19^{+0.06}_{-0.04}$ Myr. To harden an orbit from 3500 to 1.4 days, ~8 e-foldings are needed, this implies that a typical binary hardening timescale is ~1.6 Myr. Assuming a binary system with two 10 $M_\odot$ stars, this would imply a mean hardening rate of $\sim$ 7.5 AU yr^{-1}. For M17, we discarded periods lower than 665 d with a 68% confidence level. Following the same argument as before, the typical timescale to harden an orbit from 665 to 1.4 days would be ~1 Myr equivalent to a mean hardening rate of $\sim$ 4 AU yr^{-1}.

3.5 Discussion and conclusions

In this paper we present observational evidence that the 1D velocity dispersion of massive stars in young clusters (σ_{RV}) increases as they get older (Figure 3.1). Additionally, we performed Monte Carlo simulations which allowed us to convert the measured values of σ_{RV} to physical parameters. Assuming that stars are born with the binary fraction representative of OB stars in $2-4$ Myr clusters ($f_{\rm bin}$=0.7), we calculated the cutoff period that would correspond to each of the observed populations. From Figure 3.4 we can conclude that the orbits would harden in 1-1.5 Myrs. It is worth pointing out that the fit relies heavily on the M17 point. If the binary fraction of this cluster were lower than 0.7, the timescales derived would be larger. Nevertheless, the qualitative results of this paper remain the same.

Sana et al. (2017) propose that the inward migration process could be driven either by the interaction with the remnants of an accretion disk or with other young stellar objects. The hardening of the orbits would then stop either when the disk is destroyed, or when the third body is pushed far out or ejected from the orbit. For a typical system of two 10 $M_\odot$ stars, a total angular momentum of $\sim 6.5 \times 10^{47}$ kg m^2 s^{-1} ($\sim 3.5 \times 10^{47}$ kg m^2 s^{-1}) needs to be transferred for the binary to harden from 3500 (665) to 1.4 days. Rose et al. (2019) explored the possibility of the orbit hardening via the Eccentric Kozai-Lidov (EKL) mechanism, where a third companion perturbs the orbit of a binary system. They find that, beginning with a cutoff period of 9 months the EKL mechanism is insufficient to reproduce the population of short period binaries observed by Sana et al. (2012). They suggest that type II migration (Lin & Papaloizou 1986) might explain the tightening of binaries in such a time period. Moe & Kratter (2018) find that the main mechanism to harden binaries should be the dynamical disruption of coplanar triples that initially fragmented in the disk in combination with energy dissipation within this disk. Other mechanisms include the combination of EKL oscillations with tidal friction both during the pre-main sequence and the main sequence (Bate et al. 2002; Bate 2009). Given the densities of the clusters studied, stellar encounters are uncommon and, therefore, mechanisms such as binary-binary or single-binary interactions should not play a significant role in the formation of close binaries (Fujii & Portegies Zwart 2011).

Our findings affect predictions of binary population synthesis models that follow the evolution of an ensemble of binary systems subject to, among others, a distribution function for the zero-age orbital periods. Such models (e.g., Sana et al. 2012; Schneider et al. 2015) predict that a small fraction of systems interact within a timescale of 3 Myr, almost invariably resulting in a merging of the two components thus creating a blue straggler. Specifically, Schneider et al. (2015) report that of the population within two magnitudes in brightness of the main-sequence turnoff, only 1%, 2%, and 10% is a blue straggler after 1, 2, or 3 Myr. Therefore, unless one is specifically interested in early blue straggler formation, the temporal evolution of orbital properties in the first few million years reported here should not affect predictions made by binary population synthesis models that rely on initial conditions defined at the zero-age main sequence only. Except for the caveat mentioned, adopting initial conditions for the massive star population as reported on by Sana et al. (2012), for example, remains a justified approach.

Chapter 4

Stellar properties of the young cluster M17

F. Backs, S. Brands, A.R. Derkink, M. C. Ramírez-Tannus, A. de Koter, L. Kaper, J. Puls

Astronomy & Astrophysics, in prep.

Abstract

Context. The outcome of massive star formation is an important anchor point in the formation and evolution process of these stars. It provides insight in the physics of the assembly process, while also constituting initial conditions for stellar evolution. For massive stars this outcome is rarely observed as it unfolds in highly extincted molecular clouds.

Aims. We aim to characterise a population of deeply embedded stars in the exceptionally young massive star-forming region M17. The group of 18 O4.5 to B9 stars constitutes one of the best samples of almost zero-age main-sequence massive and intermediate-mass stars known. Their properties allow to identify the empirical location of the zero-age main sequence of massive stars, and rotation and mass-loss-rate properties of stars close to, or on arrival at, the ZAMS.

Methods. Using the model atmosphere code FASTWIND and the genetic algorithm fitting method KIWI-GA, we analyse the optical and ultraviolet spectra of 13 O-type giant to supergiant stars in the Small Magellanic Cloud galaxy, which has a metallicity 1/5th that of the Milky Way. Stellar, global outflow properties, such as mass-loss rate and terminal wind velocity, and wind clumping properties are constrained. To probe the role of metallicity, our findings are compared to studies of Galactic and Large Magellanic cloud samples that are analysed with very comparable prescriptions of wind structure.

Results. We perform quantitative spectroscopic modelling of a uniform set of over 100 spectral features in optical VLT/X-shooter spectra using the non-LTE stellar atmosphere code FASTWIND and fitting approach KIWI-GA. Spectral energy distributions of photometric observations are used to determine line-of-sight extinction. From a comparison of their positions in the Hertzsprung-Russell diagram with MIST evolutionary tracks, we infer stellar masses and ages.

Conclusions. We constrain the empirical location of the ZAMS for massive ($10 < M/M_\odot < 50$) stars and find it to agree with its location in MIST evolutionary tracks. The ZAMS rotation rates reach twice as high values for intermediate-mass stars than for massive stars, suggesting angular momentum gain processes differ between the two groups. Though we find tight constraints on the age, we also identify a correlation between pre-main-sequence age and mass, lower mass stars being older. Taking the derived mass-loss rates at face value, stellar winds already initiate in the PMS phase. The PMS-star winds are found to be substantially more powerful than predictions for line-driven outflows indicate.

4.1 Introduction

The past decades has shown tremendous progress in our understanding of low-mass star formation, from identifying morphological stages in the formation process and spectral accretion signatures, to spatially resolved imaging of proto-planetary disks, to detailed modelling of both single and cluster star formation (see, e.g., Protostars and Planets VII 2023 for references). This wealth of observations and models is not yet available for massive counterparts. The reasons are well known; because of the short formation timescales involved, the assembly of massive stars unfolds in highly obscured molecular clouds. Moreover, massive star formation is rare, therefore distant, and the physics complex due to radiative and mechanical feedback in the late-stages of assembly (Krumholz et al. 2009; Kuiper et al. 2010), and, apparently, inescapable (close) binary or higher order multiple formation (Sana et al. 2012; Bordier et al. 2022).

Fortunately, also in the research field of massive-star formation progress has been impressive. Developments in the last decade seem to point to massive stars being formed through disk accretion similar to their lower mass counterparts (e.g Shu et al. 1987; Cesaroni et al. 2006; Krumholz et al. 2009). An increasing number of (interferometric) observations confirm the presence of accretion disks at several wavelength regimes (e.g. Beltrán & de Wit 2016). Disk and companion formation is supported by state-of-the-art numerical simulations (e.g Bate 2018; Oliva & Kuiper 2020, 2023).

One route toward furthering our knowledge of massive star formation is to identify the central sources of individual systems prior to, or just at, arrival on the main sequence. As eluded to above, this is extremely difficult given the sources are deeply embedded and emit the bulk of their radiation in the ultraviolet and optical wavelength domains, where extinction has the strongest impact. Still, characterizing the outcome of massive-star formation in terms of, e.g., the location of the zero-age main-sequence (ZAMS), rotational velocities, mass-loss rates (if winds have developed), multiplicity statistics, magnetic field strengths, and remnant disk properties (if any), is of great value for understanding the formation mechanism. Moreover, these properties are important because they constitute the initial conditions of subsequent evolution.

The youngest massive star-forming clusters are most suited for this approach. One such young cluster is NGC 6618 located in Messier 17 (M17). M17 is a well studied giant H II region with a luminosity of $\sim 2.4 \times 10^6\,\mathrm{L}_\odot$ (Povich et al. 2007). It is located at a distance of 1675^{+19}_{-18} pc based on *Gaia*-DR3 data (Stoop et al. 2023, submitted). The H II region is surrounded by a giant molecular cloud with a gas content of approximately $6 \times 10^4\,\mathrm{M}_\odot$ (Povich et al. 2009). The cluster has a rich stellar population with ~20 O-type stars and over 100 B-type stars (Hoffmeister et al. 2008; Stoop et al. 2023, submitted). A unique feature of M17 is that despite the severe extinction towards the sources photospheric features have been detected along with hallmarks of circumstellar disks (Ramírez-Tannus et al. 2017, hereafter RT17). This has allowed the spectroscopic characterization of several of the sources and the confirmation of their pre-main-sequence (PMS) nature. Among detected circumstellar disk features are CO-bandhead emission in several sources (Hanson et al. 1997, also RT17). For some stars this CO-bandhead emission has been modelled in detail, confirming the presence of hot dense gas close to the star (Poorta et al. 2023). This is in agreement with circumstellar hydrogen and dust emission modelling, undertaken for two sources (Backs et al. 2023).

The presence of pre-main-sequence stars suggests that the cluster is young, with age estimates ranging from ∼1 Myr (Hanson et al. 1997; Povich et al. 2009) to ∼0.5 Myr (Hoffmeister et al. 2008) based on the fraction of stars with IR-excess emission and isochrone fits. Stoop et al. (2023, submitted), using *Gaia* DR3, find 0.65 ± 0.25 Myr tracing runaway stars back to their origin in NGC 6618.

In this paper, we study the stellar properties of a diverse population of 18 young massive and intermediate mass stars in M17. The goals are to re-assess the cluster age, to establish the empirical location of the ZAMS for massive stars, constrain initial spin velocities, and estimate mass-loss properties, especially to establish whether or not PMS stars have already developed a stellar wind. Limiting the importance of these properties to star formation, the initial rotational velocity of stars holds clues as to, for instance, angular momentum gain regulation by gravitational torques (Lin et al. 2011) or magnetic coupling between star and inner disk (Duez & Mathis 2010). The stellar wind, along with the photospheric radiation field, may cause ablation of circumstellar disks (Kee & Kuiper 2019) and, on larger spatial scales, in the self-regulation of massive star formation and the star-formation efficiency of their host cloud (Lancaster et al. 2021; Rosen 2022).

To reach our goals, we analysed VLT/X-Shooter spectra of our target stars using stellar atmosphere models. Line-of-sight extinction is estimated by fitting spectral energy distributions. This paper is set up as follows. First we introduce the observations and data in Section 4.2. We describe the quantitative spectral analysis method in Section 4.3. The results of the fitting are given in Section 4.4, which are then discussed in Section 4.5. Our main conclusions are summarized in Section 4.6.

4.2 Targets and data

We briefly describe the sample and data. For a complete overview of the spectroscopic data, see Ramírez-Tannus et al. (in prep.).

4.2.1 Sample

Table 4.1 lists the sources analyzed in this paper. The sample is selected such that it contains both some of the most massive stars in M17 as well as a population of pre-main-sequence stars (Hanson et al. 1997; Broos et al. 2013; Ramírez-Tannus et al. 2017). The spectral types range from O4.5 to B9. Due to this selection of high-mass stars and young embedded stars they span a range of 7 magnitudes in the V-band. Table 4.1 also indicates detected excess emission for the stars. Some stars have circumstellar disks showing both thermal infrared (IR) emission by dust and gas emission, others only show IR excess emission. For most stars no excess emission was detected.

Table 4.1: List of analyzed M17 sources. The final column lists the presence of circumstellar excess emission as identified in RT17.

Source	SpT	RA	DEC	V [mag]	Emission
B111	O4.5 V	18:20:34.65	-16:10:11.3	11.3	–
B164	O6 Vz	18:20:31.03	-16:10:08.9	16.9	–
B311	O8.5 Vz	18:20:22.90	-16:08:34.3	13.7	–
B181	O9.7 III	18:20:30.39	-16:10:36.2	17.4	–
B289	O9.7 V	18:20:24.43	-16:08:45.8	17.0	IR
B215	B1 V	18:20:28.55	-16:12:13.5	–	IR
B93	B2 V	18:20:35.80	-16:10:54.7	–	–
B205	B2 V	18:20:29.11	-16:11:13.3	16.1	–
CEN55	B2 III	18:20:29.08	-16:10:57.2	18.0	–
B234	B3 IV	18:20:27.42	-16:10:11.6	18.0	–
B213	B3 IV	18:20:28.61	-16:09:24.2	17.7	–
B253	B4 III	18:20:26.26	-16:11:04.4	15.7	–
B150	B5 V	18:20:31.78	-16:11:40.5	15.6	IR†
B272	B7 III	18:20:25.30	-16:09:42.7	18.2	–
B275	B7 III	18:20:25.19	-16:10:25.4	15.6	Gas and IR
B243	B9 III	18:20:26.41	-16:10:04.8	17.8	Gas and IR
B268	B9 III	18:20:25.25	-16:10:21.6	17.1	Gas and IR
B86	B9 III	18:20:36.16	-16:10:57.4	14.6	–

† Result from this work.

4.2.2 Spectra

The data consists of multi-epoch X-shooter spectra obtained in May to September 2019 with additional archival data from 2012 and 2013. Here we only use the UVB and VIS spectral arms of X-shooter, which were set to slit widths of 1” and 0.9”, respectively. This yields spectral resolutions of 5100 from ~3500 to 5500 Å and 8800 from 5500 to 10 000 Å.

The data was reduced using the ESO-pipeline esorex 3.3.5 (Modigliani et al. 2010). Relative flux calibrated data was obtained using spectrophotometric standards from the ESO database and telluric corrections were done with Molecfit 1.5.9 (Kausch et al. 2015). In the case of B243, B268 and B275, a special reduction was done to correct for severe nebular contamination (see van Gelder et al. 2020; Derkink et al. 2023, subm.).

The signal-to-noise ratio of the data varies strongly between stars due to the difference in their brightness, but also as function of wavelength due to strong extinction toward the stars. Therefore, the signal-to-noise ratio can be 10–20 at the shortest wavelengths while reaching >100 in the VIS arm.

4.2.3 Photometry

Accurate photometric data is required in order to both constrain the luminosity and line-of-sight extinction toward the sources; see Section 4.3.2. We adopt the photometry presented in RT17. For the stars not covered in RT17, we use the photometric data from SIMBAD[1], with UVB data from Reed (2003), JHK data from 2MASS (Skrutskie et al. 2006), and mid-infrared data from *Spitzer* IRAC (Benjamin et al. 2003). For all stars also a *Gaia* G-band point has been added (Riello et al. 2021).

4.3 Methods

We aim to determine accurate stellar atmosphere properties of the sample of (pre-)main-sequences sources in M17. To this end, we fitted FASTWIND (Santolaya-Rey et al. 1997; Puls et al. 2005) stellar atmosphere models to the normalized stacked spectra. KIWI-GA[2] (Brands et al. 2022) was used as the optimization method to find the best fitting parameters and their uncertainties. KIWI-GA also functions as python wrapper for FASTWIND. Section 4.3.1 describes the stacking process of the multi-epoch spectra. The extinction determination is described in Section 4.3.2 and the normalization process is explained in Section 4.3.3. Finally, FASTWIND and Kiwi-GA are described in Sections 4.3.4 and 4.3.5, respectively.

4.3.1 Data stacking

The multi-epoch spectra presented in Ramírez-Tannus et al. (in prep.) were stacked to improve the signal-to-noise ratio. We stack the relative flux calibrated spectra to preserve the uncertainties on the data and to minimize potential biases from manipulating data. First, we use the radial velocities determined by Ramírez-Tannus et al. (in prep.) to shift the observed spectra to the same rest frame. Then the spectra are put in the same wavelength binning using linear interpolation. Since the observing conditions can vary between the different observation epochs the continuum levels of the relative flux calibrated spectra do not always match. This can be problematic when determining a weighted mean for the stacked spectrum. Therefore, the continuum levels are matched first. This is done by dividing the observed spectra by each other. This results in a featureless residual that represents the difference between the continuum levels. The residual was then fitted using a linear function. In some cases an issue occurred in the flux calibration and a seventh order polynomial was fitted instead. The flux calibrated spectrum was multiplied with the fit to the residual to match it with the other observed spectra. This procedure was repeated for each observed spectrum such that the continuum levels of each epoch matched. The flux matched spectra were then stacked using weights defined as

$$w_{\lambda,i} = \frac{\sigma_{\lambda,i}^{-1}}{\sum_i^n \sigma_{\lambda,i}^{-1}}, \tag{4.1}$$

---

[1] http://simbad.cds.unistra.fr/simbad/

[2] https://github.com/sarahbrands/Kiwi-GA

with $\sigma_{\lambda,i}$ the uncertainty on the flux at wavelength (bin) λ and epoch i, and n the number of observing epochs. The weighted mean flux was determined as

$$\bar{\mathscr{F}}_{\lambda} = \sum_{i}^{n} w_{\lambda,i}\, \mathscr{F}_{\lambda,i}, \tag{4.2}$$

and the corresponding uncertainties as

$$\sigma_{\lambda,i} = \sum_{i}^{n} w_{\lambda,i}^{2}\, \sigma_{\lambda,i}^{2}. \tag{4.3}$$

This resulted in a higher signal-to-noise ratio in the relative flux calibrated spectrum compared to the individual single-epoch spectra. The stacked spectrum was then dereddened to better represent the expected shape of a stellar SED. The latter aided in the normalization process (see Section 4.3.3).

4.3.2 Extinction and luminosity determination

Accurate knowledge of the line-of-sight extinction is required to determine the luminosity of the star. Additionally, it aids in the normalization process as the shape of the spectrum is more predictable. The extinction was determined by fitting a stellar model SED multiplied by an extinction curve to the photometric SED. The stellar model SEDs we used are from Castelli & Kurucz (2004a) for the approximate temperature of the star based on their spectral type[1]. The model SEDs were convolved with the filter profile of the respective photometric filters. For stars with near-IR excess only photometric data points with wavelengths shorter than the onset of the excess emission were considered.

We use the extinction curve of Fitzpatrick (1999), with total-to-selective extinction, R_V, and total visual extinction, A_V, as free parameters. R_V was fitted because the stars are located in a dense star forming region, in which its value may be higher than the canonical value of $R_V = 3.1$ (see e.g. Schultz & Wiemer 1975). In the SED fitting we also used a third free parameter, c, that represents the approximate radius of the star if scaled with the distance to M17. The fitting was done in a two step approach. First, the best fit parameters were determined with an optimization routine in the SCIPY package for PYTHON, then a 2D brute force grid search in R_V and A_V was applied around the best fit parameters to verify their values, uncertainties and correlation.

The best fitting extinction curve was then used to determine the absolute J-band magnitude. The absolute J-band magnitude is used as luminosity anchor: the SED calculated by FASTWIND is compared to this luminosity anchor to determine the radius of the star. Longer wavelengths are less affected by extinction. We chose to use the J-band as it is the longest wavelength filter that is not affected by the IR excess emission from circumstellar material.

---

[1] The applied spectral type to temperature conversion is from http://www.isthe.com/chongo/tech/astro/HR-temp-mass-table-byhrclass.html

4.3.3 Normalization and data clipping process

The observed relative-flux-calibrated stacked data was normalized before the fitting process. Normalization was done after stacking to minimize the biases and irregularities caused by the normalization process and applied locally around the modelled features, which are listed in Section 4.3.5. A linear function was fitted to continuum points selected by eye, and the spectrum divided by this linear fit.

Due to the high extinction and the fact that the stars reside in an H II region, the spectra contain many interstellar features. These were removed to prevent them from affecting the fitting process. The clipped features include diffuse interstellar bands (DIBs), nebular hydrogen and helium lines, disk emission lines, stellar lines that are not included in the model, and instrumental artifacts. The clipping was done manually by inspecting the spectra. DIBs were mostly identified by their similar behavior in all spectra, but also by comparing to DIBs listed in Hobbs et al. (2009).

4.3.4 Fastwind

We determine stellar photosphere as wind properties simultaneously, maintaining a uniform fitting approach for the full sample. Our stellar model of choice is FASTWIND (Santolaya-Rey et al. 1997; Puls et al. 2005), version 10.6. FASTWIND treats both the stellar atmosphere and the trans-sonic outflow. The atomic model is split into ‘explicit’ and ‘background’ elements, the combination of which is used to treat the impact of a multitude of lines on radiation transport and back-heating (so-called line blocking and line blanketing). Only the radiative transfer for the explicit elements is treated in the co-moving frame; these explicit elements are H, He, C, N, O, and Si. Only for these elements can synthetic line profiles be produced. Not all ionization stages are included for the explicit ions (to reduce computation cost). For this reason some of the cooler stars have prominent lines that cannot be modelled.

4.3.5 Fitting approach and Genetic Algorithm

The stellar properties we study here are the effective temperature of the star, $T_{\rm eff}$; surface gravity, g; mass-loss rate, $\dot{M}$; projected surface rotation, $v \sin i$; helium surface abundance, $y_{\rm He}$, and surface abundance of C, N, O, and Si. This results in a total of nine free parameters. The micro-turbulent velocity is held fixed at $10\,{\rm km\,s^{-1}}$. We do not include a macro-turbulent velocity field, which accounts for motions in the photosphere other than micro-turbulent velocities or rotation. The flow velocity profile is given by a standard β-type velocity law, with $\beta = 1$. The terminal velocity v_∞ of the outflow can not be constrained from our optical spectra. We use measurements of Hawcroft et al. (2023) and the spectral type to estimate v_∞ values, but note that the results are not sensitive to the details of this procedure. We assume optically thin clumps may be present in the outflow, characterized by a clumping factor $f_{\rm cl} = 10$.

The nine free parameters are to be fitted simultaneously due to several correlations between the parameters. The exploration of such a parameter space can be computationally expensive.

Table 4.2: Diagnostic features used during fitting.

Ion	Wavelength [Å]	Part of complex
Si II	3853.7, 3856.0, 3862.6	Hζ
H I	3889.1	
O III	3961.6	Hϵ
He I	3964.7	
H I	3970.1	
He II	4025.7	He I 4026
He I	4026.3	
C III	4068.9, 4070.3	C III 4070
O II	4069.6, 4069.9, 4072.2	
	4075.9	
O III	4072.6, 4074.0	
H I	4101.8	
Si IV	4088.9	Hδ
N III	4097.4	
He II	4100.1	
H I	4101.8	
N III	4103.4	
Si IV	4116.1	
Si II	4128.1, 4130.9	
He I	4143.8	He I 4143
C III	4186.9	He II 4200
N III	4195.8, 4200.1, 4215.8	
He II	4199.9	
Si IV	4212.4, 4212.4	
C II	4267.0, 4267.3, 4267.3	C II 4267
O II	4317.1, 4319.6, 4366.9	Hγ
N III	4332.9, 4337.0, 4345.7	
He II	4338.8	
H I	4340.5	
N III	4379.0, 4379.2	He I 4387
He I	4388.0	
He I	4471.5	He I 4471
N III	4510.9, 4511.0, 4514.9	N III 4515
	4518.1, 4523.6	
N III	4534.6	He II 4541
He II	4541.7	
Si III	4552.6	
Si III	4567.8, 4574.8	Si III 4570
N III	4634.1, 4640.6, 4641.9	O II N III 46
O II	4638.9, 4641.8	O II N III 46
C III	4647.4, 4650.2, 4651.5	C III Si IV 46
Si IV	4654.3	C III Si IV 46
O II	4661.6, 4676.2	O II C III 46
C III	4663.6, 4665.9	O II C III 46
He II	4685.9	He II 4686
He I	4713.2	He I 4713
N III	4858.7, 4859.0, 4861.3	Hβ
	4867.1, 4867.2, 4873.6	
	4884.1	
He II	4859.4	
H I	4861.4	
He I	4922.0	He I 4922
He I	5015.7	He I 5015
Si II	5041.0, 5056.0, 5056.3	He I 5047
He I	5047.8	
He II	5411.6	He II 5411
O III	5592.4	O III 5592
He I	5875.7	He I 5875
Si II	6347.1, 6371.4	Si II 6347
He II	6560.2	Hα
H I	6562.8	
C II	6578.1, 6582.9	
He I	6678.2	He II 6683
He II	6683.3	
Si IV	7047.9, 7047.9, 7068.4	He I 7065
He I	7065.3	

Therefore, the optimization of parameter values was done using Kiwi-GA (Brands et al. 2022). This is a genetic algorithm (GA) and wrapper tailored to FASTWIND. The GA starts with randomly and uniformly sampling a specified parameter space. This random sampling is the first 'generation' of models, after which the next generations are determined based on the fitness of the models in the generations before them. This works by combining the parameters of two of the best fitting models up to that moment, with the better fitting models having a higher probability to 'reproduce'. The parameter values are mixed, with some values from the one 'parent model' and some from the other. Parameters can also mutate, in which case their value will not match either of the parents' values. Two types of mutation are included, which we call 'broad' and 'narrow'. The broad mutation has a low probability and samples the new parameter value from a broad Gaussian distribution spanning a significant part of the parameter space. The narrow mutation has a higher probability and is sampled from a narrow Gaussian distribution. Both distributions are centered around the value inherited from the parent. These mutations ensure proper exploration of the parameter space. Details on all the meta-parameters regarding the fitting algorithm can be found in Brands et al. (2022).

KIWI-GA is designed to fit a set of normalized spectral diagnostic features. We have opted to fit the same set of features for all stars, regardless of their temperature or spectral type. This was done to ensure that differences between stars are not the result of the line selection. The features are selected based on their strength, lack of contamination from unknown lines and features, and established reliability as a diagnostic in the temperature range probe by our stars. The full list of diagnostic features is listed in Table 4.2. Because the line selection is uniform for all stars, some fitted lines will not be present in the observed spectrum. As the selected lines are free of blends with lines that are not modelled, this should not be a problem. For example, the selected He II complexes show only noise or modelled features in the cooler (late-B) stars. Therefore, it should not negatively impact the fitting process.

The uncertainties on model parameters are based on their fitness, which is assessed using either a χ^2 statistic or a root-mean-square-error-of-approximation statistic (RMSEA; Steiger 1998). If the reduced χ^2 of the best-fit model is below 1.5 the former was used, otherwise the RMSEA was used as it is designed to produce reasonable uncertainties if the models do not perfectly reproduce the observations. More details on the RMSEA uncertainty determination can be found in Brands et al. (in prep.). Regardless of the method, the uncertainties should be considered estimates of the 1σ confidence intervals.

4.4 Results

Here we present the main results of our fitting efforts. Section 4.4.1 shows our findings regarding line-of-sight extinction properties. The atmosphere and wind analysis results are in Section 4.4.2; some parameters are highlighted. Poorer fits are mentioned in Section 4.4.3.

Table 4.3: Visual extinction, total-to-selective extinction, absolute J magnitude, and the approximate onset of IR excess for the target stars.

Source	IR cutoff	A_V	R_V	J_{abs}
B111	...	5.19 ± 0.02	3.52 ± 0.02	-4.34 ± 0.07
B164	...	8.37 ± 0.02	4.05 ± 0.03	-3.29 ± 0.07
B311	...	6.23 ± 0.03	3.65 ± 0.04	-2.98 ± 0.07
B181	...	10.55 ± 0.06	4.65 ± 0.17	-3.29 ± 0.07
B289	3.0 μm	8.13 ± 0.03	4.14 ± 0.04	-2.80 ± 0.07
B215	3.0 μm	9.14 ± 0.30	2.71 ± 0.22	-2.30 ± 0.11
B93	...	3.70 ± 0.03	4.00 ± 0.20	-0.92 ± 0.07
B205	...	7.51 ± 0.04	3.68 ± 0.06	-1.71 ± 0.07
CEN55	...	9.24 ± 0.05	3.80 ± 0.06	-1.60 ± 0.08
B234	...	8.40 ± 0.04	3.72 ± 0.06	-0.83 ± 0.07
B213	...	8.51 ± 0.05	2.73 ± 0.04	-1.46 ± 0.07
B253	...	6.73 ± 0.04	3.90 ± 0.08	-1.46 ± 0.07
B150	3.0 μm	5.40 ± 0.04	4.29 ± 0.14	-0.41 ± 0.07
B272	...	9.04 ± 0.04	3.06 ± 0.03	-1.24 ± 0.07
B275	1.5 μm	7.41 ± 0.07	4.69 ± 0.11	-2.59 ± 0.07
B243	1.5 μm	7.92 ± 0.06	5.68 ± 0.21	-0.94 ± 0.07
B268	1.5 μm	7.51 ± 0.07	4.95 ± 0.19	-1.29 ± 0.08
B86	...	3.61 ± 0.02	3.58 ± 0.14	0.16 ± 0.06

4.4.1 Extinction

The results of the extinction fitting are listed in Table 4.3 along with the approximate onset wavelength of the IR excess. Six stars show an IR excess that mandates excluding data points at wavelengths beyond the IR cutoff specified in Table 4.3 from the extinction fits. The visual line-of-sight extinction to the sources varies from 3.6 to 10.6 magnitudes and the total-to-selective extinctions vary from 2.7 to 5.7. B213 and B215 are the only objects for which an R_V value below 3 was found. This could be due to the limited photometric data available. Additionally, the V-band photometry for B213 appears to be significantly brighter than the rest of the photometric data. Both stars, and particularly B215, show a strong correlation between A_V and R_V (see Appendix III.1). Full SEDs along with the dereddened SEDs and correlations between A_V and R_V are provided in Appendix III.1.

4.4.2 Atmosphere fits

Figure 4.1 shows the best model fits to the hydrogen and helium lines and Figure 4.2 the best fits to the rest of the diagnostic features. The corresponding stellar parameters are listed in Table 4.4. The sample consists of stars with a large variety of temperatures and signal-to-noise ratios. The best fit temperatures range from $\sim$11 kK to $\sim$46 kK and luminosities from $10^2\,L_\odot$ to $3 \times 10^5\,L_\odot$. Below we discuss main findings of the fitting efforts per parameter.

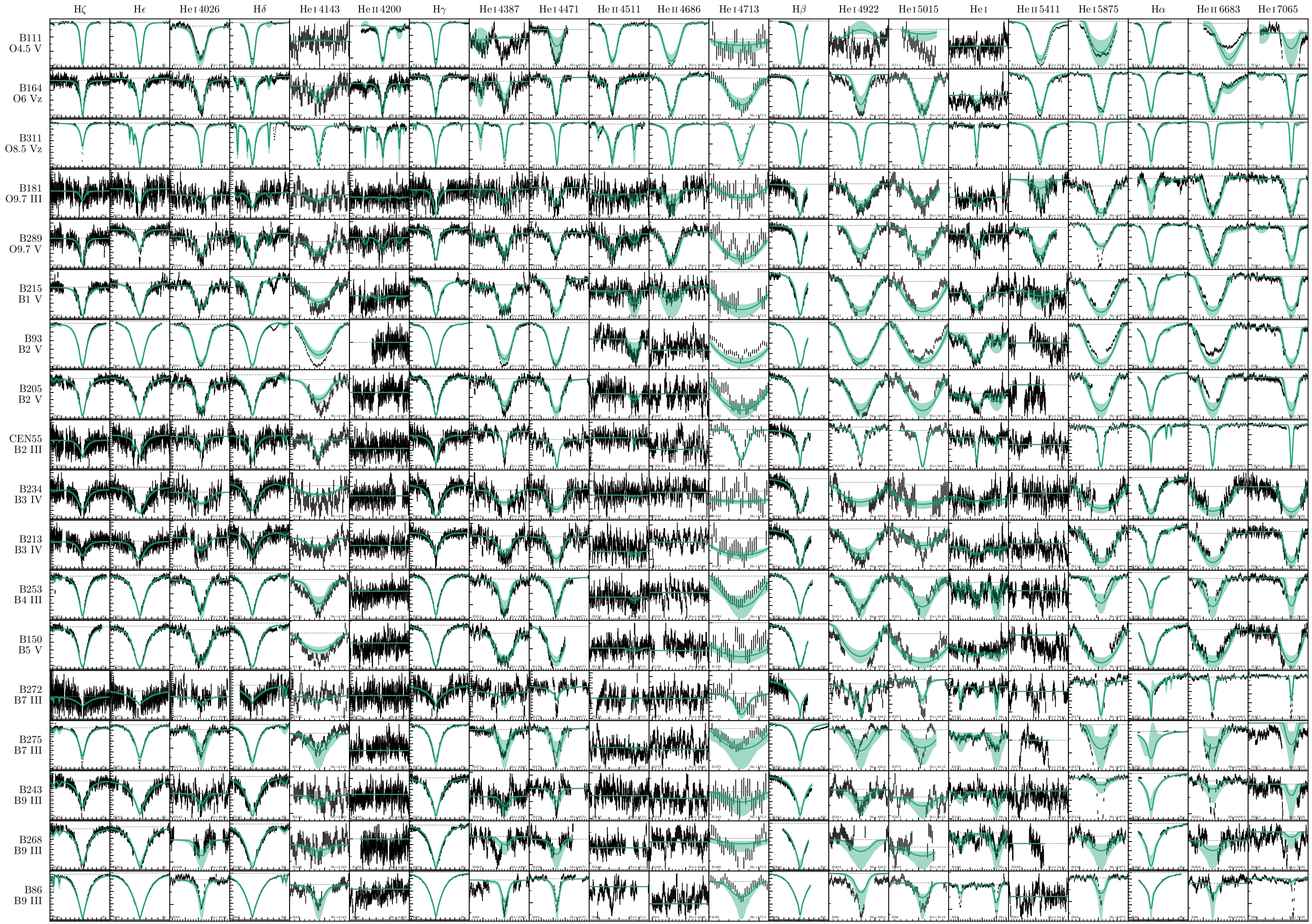

Figure 4.1: Overview of FASTWIND/KIWI-GA fits to the hydrogen and helium lines of each star in the sample. The black vertical bars indicate the observed data, with the length indicating the 1σ uncertainty on the data. The green line shows the best fit model and the shaded region the range of models in the 1σ confidence interval. A more detailed overview of the fit results is shown in Figure 4.3 for B311 and Appendix III.3 for the other targets.

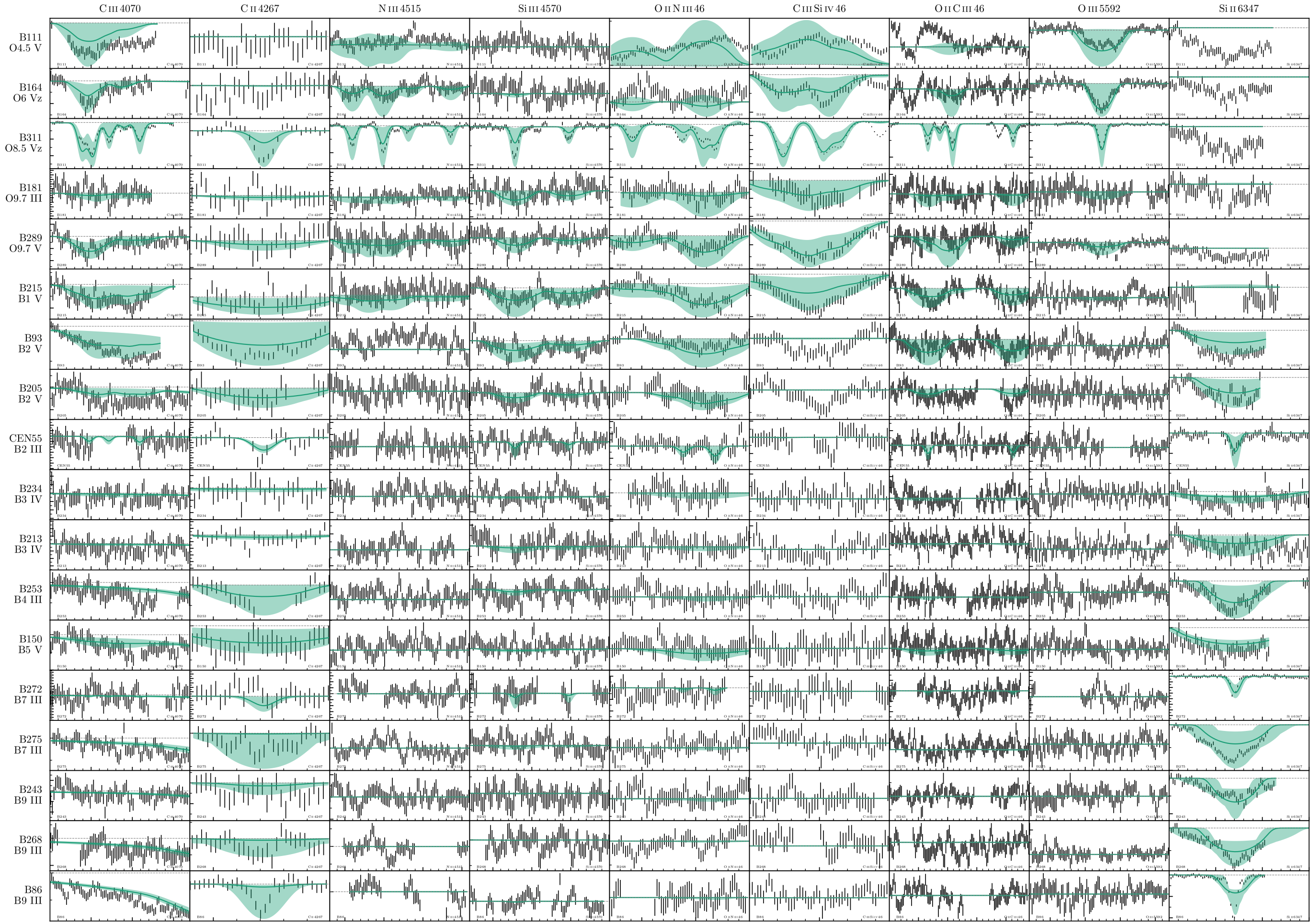

Figure 4.2: Overview of FASTWIND/KIWI-GA fits to the complexes with carbon, nitrogen, oxygen, and silicon lines as their main diagnostic of each star in the sample. The black vertical bars indicate the observed data, with the length indicating the 1σ uncertainty on the data. The green line shows the best fit model and the shaded region the range of models in the 1σ confidence interval. A more detailed overview of the fit results is shown in Figure 4.3 for B311 and Appendix III.3 for the other targets.

4.4.2.1 Temperature and gravity

The surface temperature and gravity are mostly determined by the hydrogen and helium lines and line-strength ratios between them, with additional constraints from the C, N, O, Si lines. Throughout the sample the temperature is well constrained, with relatively larger uncertainties at lower temperatures. This is likely due to a lower number of diagnostic lines available and lower signal-to-noise ratios for the fainter stars. Gravity determinations are robust with well constrained values in the range $\log g = 3.60 - 4.24$, which result in reasonable spectroscopic masses (see also Section III.2). The gravity determination of B272 is an outlier in the sample, with $\log g = 4.86$, significantly higher than for the other stars.

4.4.2.2 Mass-loss rates

The mass-loss rate determination is mostly based on the wind emission in Hα and to a lesser extend Hβ. Additionally, He II 4686 adds a mass-loss constraint for the O-type stars. For the hotter more luminous stars the mass-loss rate determinations are robust and reliable. However, at lower luminosity ($L \lesssim 10^4\,\mathrm{L}_\odot$) the mass-loss rates are lower and therefore harder to constrain. We present the mass-loss rates and their uncertainties as produced by our fitting routine and corresponding statistics. However, we would like to stress that the inferred mass-loss rates may be strongly affected by systematic uncertainties. The values should be treated with care as the sensitivity to this parameter is limited at these low values. Best fit values can change significantly through small inconsistencies in the data. We note that in our modelling we did not consider mass-loss rates $\dot{M} < 10^{-10}\,\mathrm{M}_\odot\,\mathrm{yr}^{-1}$.

4.4.2.3 Rotation rates

The projected rotation rate, $v \sin i$, of the stars is typically well constrained. Cooler stars and stars with a low signal-to-noise ratio have a less accurate $v \sin i$. This is particularly true for stars with a gaseous circumstellar disk or significant nebular contamination, as the central part of the strongest lines had to be clipped from the data. Two stars, CEN55 and B272, show a best fit $v \sin i$ of 5 $\mathrm{km\dot{s}}^{-1}$, which is the lowest value considered. Possibly these lines are affected by nebular lines blended with the stellar line profiles (see Section 4.4.3.1 and Section 4.4.3.2).

4.4.2.4 Abundances

Typically the helium abundances of the stars are well constrained, with increasing uncertainties towards lower temperatures due to less pronounced helium features. However, constraining the surface abundance of C, N, O, and Si has been challenging due to the small number of diagnostic features available in our uniform modelling approach, low signal-to-noise ratio of some of the spectra, and the high rotation rate of many of the stars. This, combined with the correlation and degeneracy of the abundances with some of the other atmosphere parameters, resulted in large uncertainties for most stars. The exception to this is B311, which has a high signal-to-noise ratio and a low projected rotation rate. This star has well constrained abundances, of which the best fit values agree very closely with the values presented in Asplund et al. (2009). This will be further discussed in Section 4.5.5.

4.4.3 Anomalous fits

Some best fit solutions appear anomalous and should be interpreted with caution. We list these cases here.

4.4.3.1 CEN55

For this star we find a very low projected rotation rate. This value for $v \sin i$ results in a good fit. However, due to the narrow stellar line profiles the nebular contributions to the He I lines are hard to distinguish. Therefore, the fit might be contaminated, resulting in an odd helium surface abundance. Indeed, we find the highest helium abundance considered in our parameter space to be the best fit, while it is not expected to be enhanced as the stars in M17 have just formed.

4.4.3.2 B272

Similar to CEN55 this star has a best fit value of $v \sin i = 5\,\mathrm{km\,s^{-1}}$, and a significantly enhanced helium abundance. We also find a high surface gravity of $\log g = 4.68$, which is significantly higher than expected for a star of this luminosity and temperature. The spectroscopic mass corresponding to this is $34.4\,\mathrm{M}_\odot$, also higher than expected (see Section III.2).

4.4.3.3 B181

B181 shows He II lines stronger than found in the best fit model. This may suggest that the temperature of the star is underestimated. However, temperatures that match the He II line strengths fall within the confidence interval. A higher temperature would place this star closer to the ZAMS.

4.5 Discussion

The unique young age of M17 allows us to investigate near-ZAMS properties of a sample of stars covering masses from about 2–30 $M_\odot$. For the most massive stars, we may identify the empirical location of the ZAMS and for the full sample we may place constraints on (pre-)ZAMS rotational velocities and mass-loss rates. We first assess the evolutionary status of the sample (Section 4.5.1) to establish stellar ages and masses, and highlight a correlation between these two properties (Section 4.5.2). Next, we discuss their present-day and (future) ZAMS surface rotation (Section 4.5.3). We compare our results to those of RT17 in Section 4.5.4. Then, we briefly discuss surface abundances (Section 4.5.5) and line-of-sight

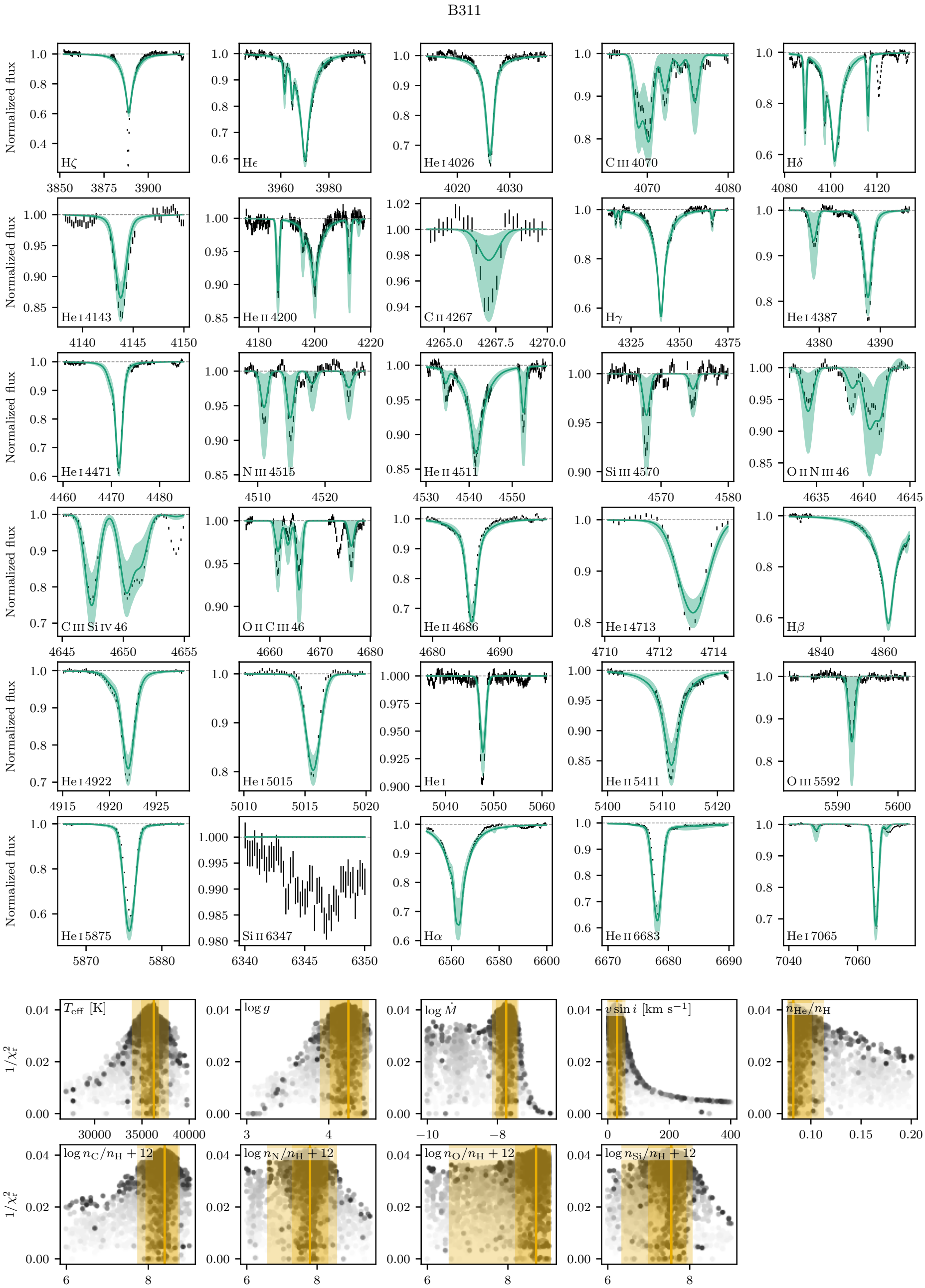

Figure 4.3: Overview of the fit to B311. The *top* part shows the fits to each diagnostic with the vertical black bars indicating the normalized observed spectra and the green line the best fit model. The length of the black bars indicate the 1σ uncertainty on the data and the shaded region shows the 1σ confidence interval of the model spectrum. The name of the diagnostic feature is given at the bottom of each panel. The *bottom* part shows the parameter distributions sampled by Kiwi-GA. The fit parameters are displayed in the top left. The shade of the points is a measure of the generation, with darker points being sampled in later generations. The vertical yellow line shows the best fit value; the darker yellow shaded region the 1σ confidence interval, and the lighter yellow shaded region the 2σ confidence interval.

Table 4.4: Best fit stellar parameters from FASTWIND/GA fitting.

Source	$T_{\rm eff}$ [K]	$\log g$	$\log \dot{M}$	$v \sin i$ [a]	$y_{\rm He}$ [b]	$\epsilon_{\rm C}$ [c]	$\epsilon_{\rm N}$ [c]	$\epsilon_{\rm O}$ [c]	$\epsilon_{\rm Si}$ [c]	$\log L/{\rm L}_\odot$	$R\,[{\rm R}_\odot]$	$M_{\rm spec}$ $[{\rm M}_\odot]$ [d]	$\log Q_0$ [e]
B111	45750^{+1250}_{-2250}	$3.92^{+0.08}_{-0.12}$	$-6.58^{+0.08}_{-0.05}$	205^{+30}_{-20}	$0.09^{+0.03}_{-0.01}$	$8.7^{+0.3}_{-0.6}$	$8.2^{+0.2}_{-0.6}$	$8.8^{+0.2}_{-2.8}$	$6.2^{+2.1}_{-0.2}$	$5.52^{+0.04}_{-0.06}$	$9.25^{+0.37}_{-0.30}$	$26.0^{+3.7}_{-5.2}$	$49.32^{+0.05}_{-0.08}$
B164	39000^{+1250}_{-500}	$4.02^{+0.18}_{-0.12}$	$-7.26^{+0.10}_{-0.28}$	120^{+15}_{-15}	$0.09^{+0.03}_{-0.01}$	$8.1^{+0.6}_{-0.3}$	$7.8^{+0.8}_{-1.1}$	$8.8^{+0.2}_{-1.0}$	$7.7^{+0.5}_{-0.8}$	$4.90^{+0.04}_{-0.03}$	$6.24^{+0.19}_{-0.21}$	$14.9^{+6.1}_{-3.2}$	$48.50^{+0.08}_{-0.04}$
B311	36250^{+500}_{-1250}	$4.24^{+0.16}_{-0.22}$	$-7.75^{+0.28}_{-0.28}$	30^{+15}_{-25}	$0.08^{+0.02}_{-0.01}$	$8.4^{+0.3}_{-0.5}$	$7.8^{+0.5}_{-0.5}$	$8.7^{+0.3}_{-0.5}$	$7.5^{+0.3}_{-0.6}$	$4.69^{+0.03}_{-0.04}$	$5.68^{+0.21}_{-0.18}$	$20.4^{+7.9}_{-7.3}$	$48.09^{+0.06}_{-0.12}$
B181	29500^{+4250}_{-2000}	$3.60^{+0.28}_{-0.26}$	$-7.37^{+0.25}_{-0.15}$	180^{+30}_{-25}	$0.09^{+0.06}_{-0.01}$	$7.8^{+0.6}_{-1.3}$	$6.9^{+2.2}_{-0.9}$	$7.7^{+0.8}_{-1.6}$	$7.6^{+0.5}_{-1.6}$	$4.58^{+0.15}_{-0.08}$	$7.55^{+0.39}_{-0.62}$	$8.3^{+6.5}_{-3.6}$	$47.33^{+0.69}_{-0.45}$
B289	34250^{+1500}_{-750}	$3.92^{+0.20}_{-0.16}$	$-7.85^{+0.18}_{-0.35}$	180^{+20}_{-20}	$0.09^{+0.03}_{-0.01}$	$8.3^{+0.3}_{-0.6}$	$7.6^{+0.8}_{-1.6}$	$8.3^{+0.7}_{-2.4}$	$7.7^{+0.3}_{-0.8}$	$4.55^{+0.05}_{-0.03}$	$5.40^{+0.18}_{-0.21}$	$8.8^{+4.4}_{-2.5}$	$47.86^{+0.14}_{-0.07}$
B215	29000^{+1600}_{-1400}	$4.18^{+0.16}_{-0.18}$	$-8.10^{+0.25}_{-0.20}$	245^{+25}_{-30}	$0.09^{+0.03}_{-0.01}$	$8.0^{+0.4}_{-0.5}$	$8.6^{+0.6}_{-2.4}$	$8.1^{+0.6}_{-0.8}$	$6.9^{+0.7}_{-0.9}$	$4.19^{+0.07}_{-0.07}$	$4.95^{+0.27}_{-0.28}$	$13.5^{+5.2}_{-4.4}$	$46.58^{+0.30}_{-0.26}$
B93	17800^{+1200}_{-200}	$3.92^{+0.18}_{-0.06}$	$-8.85^{+0.25}_{-0.30}$	260^{+20}_{-25}	$0.11^{+0.02}_{-0.03}$	$7.7^{+0.5}_{-0.6}$	$7.0^{+2.5}_{-0.9}$	$9.1^{+0.3}_{-2.9}$	$6.9^{+0.2}_{-0.6}$	$3.07^{+0.07}_{-0.03}$	$3.62^{+0.12}_{-0.17}$	$4.0^{+1.4}_{-0.4}$	$43.36^{+0.21}_{-0.04}$
B205	17200^{+400}_{-1000}	$3.82^{+0.12}_{-0.20}$	$-8.66^{+0.30}_{-0.25}$	200^{+30}_{-30}	$0.09^{+0.02}_{-0.01}$	$7.4^{+0.5}_{-1.4}$	$7.4^{+1.4}_{-1.4}$	$9.3^{+0.2}_{-1.1}$	$7.1^{+0.4}_{-0.6}$	$3.34^{+0.03}_{-0.06}$	$5.32^{+0.26}_{-0.18}$	$6.8^{+1.8}_{-2.1}$	$43.50^{+0.05}_{-0.26}$
CEN55	18000^{+1200}_{-600}	$3.74^{+0.06}_{-0.16}$	$-8.46^{+0.30}_{-1.52}$	5^{+20}_{-5}	$0.19^{+0.01}_{-0.03}$	$8.1^{+0.1}_{-0.3}$	$9.4^{+0.1}_{-3.5}$	$9.3^{+0.2}_{-0.8}$	$7.0^{+0.3}_{-0.2}$	$3.34^{+0.07}_{-0.04}$	$4.84^{+0.19}_{-0.25}$	$4.7^{+0.6}_{-1.3}$	$43.80^{+0.22}_{-0.17}$
B234	16600^{+800}_{-200}	$3.82^{+0.14}_{-0.12}$	$-9.03^{+0.18}_{-0.15}$	350^{+40}_{-25}	$0.10^{+0.03}_{-0.02}$	$7.2^{+0.6}_{-0.2}$	$7.5^{+1.9}_{-0.9}$	$8.0^{+2.1}_{-1.0}$	$7.0^{+0.6}_{-0.1}$	$2.95^{+0.05}_{-0.03}$	$3.64^{+0.12}_{-0.15}$	$3.2^{+0.9}_{-0.7}$	$42.92^{+0.20}_{-0.03}$
B213	17250^{+250}_{-1000}	$3.68^{+0.10}_{-0.18}$	$-8.88^{+0.10}_{-0.15}$	245^{+20}_{-20}	$0.10^{+0.04}_{-0.02}$	$7.7^{+0.3}_{-0.6}$	$8.4^{+0.9}_{-2.5}$	$6.1^{+2.7}_{-0.1}$	$7.0^{+0.6}_{-0.2}$	$3.24^{+0.03}_{-0.06}$	$4.72^{+0.21}_{-0.14}$	$3.9^{+0.8}_{-1.0}$	$43.43^{+0.09}_{-0.23}$
B253	15400^{+600}_{-800}	$3.86^{+0.12}_{-0.14}$	$-8.71^{+0.25}_{-1.08}$	170^{+60}_{-40}	$0.09^{+0.02}_{-0.01}$	$7.7^{+0.4}_{-1.8}$	$7.0^{+2.5}_{-1.1}$	$6.8^{+2.2}_{-0.8}$	$6.8^{+0.3}_{-0.5}$	$3.11^{+0.04}_{-0.05}$	$5.09^{+0.22}_{-0.19}$	$6.8^{+1.5}_{-1.5}$	$42.81^{+0.16}_{-0.21}$
B150	15600^{+800}_{-800}	$3.80^{+0.18}_{-0.14}$	$-8.83^{+0.15}_{-0.23}$	315^{+25}_{-30}	$0.14^{+0.04}_{-0.03}$	$8.1^{+0.3}_{-0.9}$	$6.8^{+3.3}_{-0.3}$	$9.3^{+0.6}_{-2.4}$	$7.0^{+0.2}_{-0.1}$	$2.71^{+0.05}_{-0.05}$	$3.11^{+0.14}_{-0.14}$	$2.2^{+0.8}_{-0.5}$	$42.55^{+0.13}_{-0.21}$
B272	16000^{+1200}_{-800}	$4.68^{+0.18}_{-0.20}$	$-9.67^{+1.60}_{-0.35}$	5^{+25}_{-5}	$0.30^{+0.01}_{-0.09}$	$8.8^{+0.5}_{-1.6}$	$8.3^{+1.6}_{-1.9}$	$9.5^{+0.6}_{-2.5}$	$8.0^{+0.7}_{-0.7}$	$3.06^{+0.07}_{-0.05}$	$4.44^{+0.20}_{-0.25}$	$34.4^{+14.6}_{-11.9}$	$42.98^{+0.36}_{-0.18}$
B275	12750^{+750}_{-1250}	$3.44^{+0.12}_{-0.34}$	$-9.87^{+2.00}_{-0.08}$	185^{+65}_{-75}	$0.10^{+0.10}_{-0.03}$	$6.3^{+2.0}_{-0.4}$	$9.3^{+0.2}_{-3.4}$	$6.6^{+2.5}_{-0.7}$	$6.7^{+0.6}_{-0.6}$	$3.32^{+0.05}_{-0.09}$	$9.46^{+0.72}_{-0.42}$	$9.0^{+1.9}_{-4.3}$	$42.38^{+0.26}_{-3.05}$
B243	11900^{+1400}_{-300}	$3.78^{+0.22}_{-0.14}$	$-9.80^{+1.20}_{-0.20}$	140^{+95}_{-45}	$0.09^{+0.06}_{-0.01}$	$8.0^{+0.8}_{-1.1}$	$9.8^{+0.2}_{-3.2}$	$7.3^{+2.8}_{-0.3}$	$7.0^{+0.3}_{-0.1}$	$2.58^{+0.11}_{-0.03}$	$4.61^{+0.15}_{-0.40}$	$4.7^{+1.9}_{-1.1}$	$41.00^{+0.88}_{-1.68}$
B268	11300^{+900}_{-300}	$3.78^{+0.22}_{-0.12}$	$-9.86^{+1.05}_{-0.15}$	180^{+115}_{-35}	$0.10^{+0.08}_{-0.02}$	$7.8^{+0.7}_{-0.6}$	$7.0^{+3.0}_{-0.3}$	$7.0^{+2.4}_{-0.1}$	$7.1^{+0.5}_{-0.1}$	$2.66^{+0.07}_{-0.04}$	$5.63^{+0.22}_{-0.36}$	$7.0^{+3.2}_{-1.3}$	$40.95^{+0.33}_{-2.26}$
B86	11600^{+400}_{-200}	$4.02^{+0.10}_{-0.08}$	$-9.52^{+0.38}_{-0.40}$	95^{+15}_{-35}	$0.10^{+0.03}_{-0.03}$	$7.4^{+0.4}_{-0.5}$	$6.8^{+1.8}_{-0.2}$	$7.6^{+1.8}_{-0.2}$	$7.0^{+0.2}_{-0.1}$	$2.11^{+0.04}_{-0.03}$	$2.85^{+0.09}_{-0.10}$	$3.1^{+0.6}_{-0.4}$	$40.52^{+0.45}_{-0.41}$

[a] In km s^{-1}.
[b] In number density relative to hydrogen.
[c] In number density relative to hydrogen as $\log n_{\rm x}/n_{\rm H} + 12$.
[d] The spectroscopic mass of the star based on the inferred radius and surface gravity.
[e] The number of emitted hydrogen ionizing photons.

extinction (Section 4.5.6). Finally, we discuss the mass-loss l properties (Section 4.5.7). We summarize our results in Section 4.6.

4.5.1 Evolutionary status of the sample

Figure 4.4 shows the locations of the stars in the Hertzsprung-Russell diagram (HRD). Overplotted in grey are MIST pre-main-sequence evolutionary tracks (Dotter 2016; Choi et al. 2016), based on MESA models (Paxton et al. 2011), for masses ranging between 3 and 50 $M_\odot$. The somewhat diagonal black line on the left denotes the ZAMS; the black line on the right the birthline (see below). Dashed colored lines show isochrones of which the age is given in the vertical color bar on the right of the figure. We first zoom in on the population of stars more massive than 13 $M_\odot$. As we will see below, these all suffer from severe extinction, with A_V ranging from 3.6 to 10.6 magn, which would essentially render them invisible at optical wavelengths if not for the use of an 8m class telescope. Five out of six concur very well with the predicted location of the ZAMS, with one (B181) being positioned slightly to right. As pre-main sequence evolution proceeds fast for these sources (it takes them at most $\sim 10^5$ yr to reach the ZAMS) and the moment of core hydrogen ignition signifies the transition from blueward to redward evolution, *this empirically confirms the location of the ZAMS in this mass range*. In the tracks at hand, the ZAMS is reached when the hydrogen burning luminosity exceeds 99.99 percent of the total luminosity (Dotter 2016).

Our sample does not contain stars with masses in between about 7 and 13 $M_\odot$. The stars with masses between about 3 and 7 $M_\odot$ have not yet reached the main sequence. This is in line with previous studies that indicate that the stars are in the final phase of their formation (e.g. Ramírez-Tannus et al. 2017). The stars with gaseous disks are located the furthest from the main sequence, supporting the hypothesis that these are the least evolved objects in the sample and have not yet lost their accretion disk. The three stars that show IR excess emission are located close to, or on, the main sequence indicating that in some cases circumstellar dust can persist until the end of the formation process. However, this is not ubiquitous, as most stars including potentially less evolved stars do not show any excess emission.

4.5.2 Age determination

The isochrones in Fig. 4.4 already give an indication of the age of the cluster. However, a more accurate estimate may be obtained from determining the ages of the individual stars. To that end, we interpolate the evolutionary tracks and determine the range of ages that fall within the uncertainties on L and T_{eff} of the stars. Through the same method the masses of the stars are determined. Table 4.5 lists the results. When considering only the stars that are not consistent with being on the main sequence, we find the distribution of ages as shown in Figure 4.5. Based on this distribution, we constrain the age to be $0.4^{+0.6}_{-0.2}$ Myr. This result matches very well with the dynamical age of 0.65 ± 0.25 Myr derived from tracing runaway stars back to NGC 6618 (Stoop et al. 2023, submitted) as well as with approximate estimates by Hanson et al. (1997); Hoffmeister et al. (2008); Povich et al. (2009).

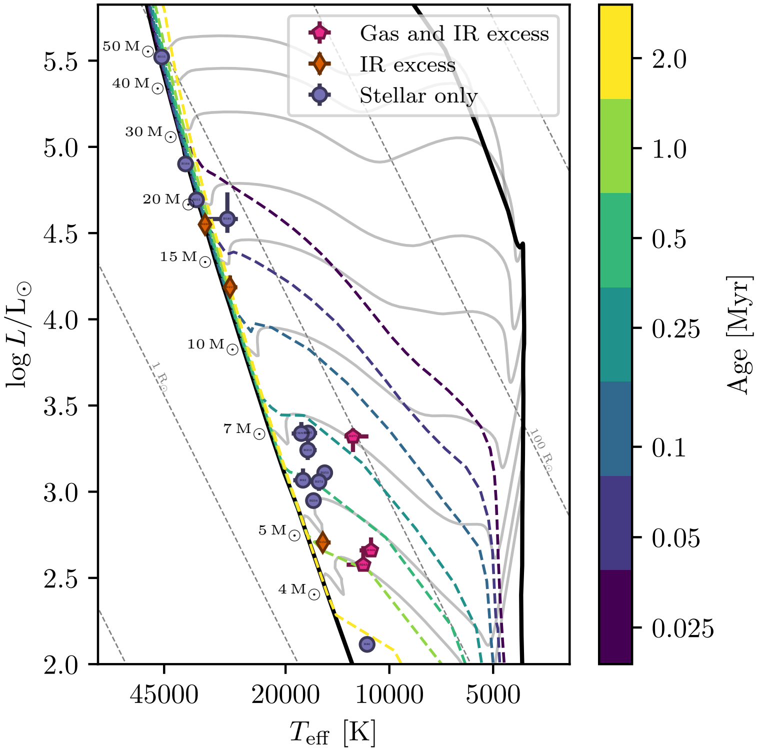

Figure 4.4: Hertzsprung-Russell Diagram of the sample of M17 stars. The stars are separated into three categories, depending on their circumstellar emission features, with in pink stars that show both emission from a gaseous disk and IR excess emission from hot dust, orange indicating stars that only show IR excess, and purple indicating that no circumstellar material was detected here or by RT17. Overplotted in grey are MIST pre-main-sequence evolutionary tracks with masses labeled on the left. In black the ZAMS (on the left) and the birthline (on the right) (Dotter 2016; Choi et al. 2016). Isochrones are shown with the dashed colored lines. The thin dashed grey lines show the equivalent radius lines to guide the eye. The names of the stars are displayed on the points, visible when zooming in.

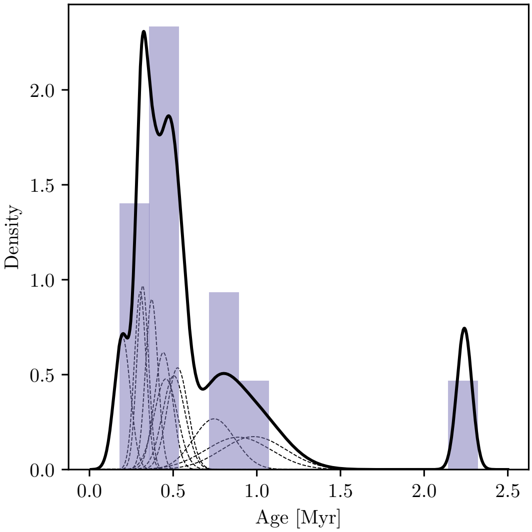

Figure 4.5: Distribution of pre-main-sequence ages of the stars in M17. The black line indicates an approximate kernel density estimate based on the best fit ages and their confidence intervals. The thin dashed lines indicate the contribution of the individual sources. Higher mass stars ($M > 10\,\mathrm{M}_\odot$) that have reached the main sequence are excluded.

Our ages are measured from the birthline, which in the MIST tracks is defined to be the locus at which the star's central temperature reaches 10^5 K; at this point the stars have already accreted their final mass. We remark that though ages are usually measured from the birthline on, the definition of the birthline is not universal. Often, it is associated with the star becoming visible at optical light, linking it the end of the main accretion phase, i.e., when the dusty natal cloud from which the star obtains its mass is depleted or dispersed. Computations applying this alternative definition find that massive stars reach the main sequence while still accreting material (Hosokawa & Omukai 2009; Hosokawa et al. 2010). Palla & Stahler (1990) involve the size of the proto-star in the definition of birthline. It is therefore important to realize that estimated 'age' may vary significantly as a result of different initial conditions and definitions of the birthline (Hosokawa et al. 2011; Kunitomo et al. 2017).

The MIST tracks allow us to determine the remaining time it will take the stars to reach the main sequence. This is beneficial as it is independent of the definition of the birthline and mainly depends on further Kelvin-Helmholtz contraction of the stars. Fig. 4.6 shows the remaining time to the ZAMS as function of stellar mass. Visible in the figure is that the most-massive stars are closest in time to reaching the main sequence and that lower-mass stars have longer to go. This is in line with the expectation that the formation timescale of more massive stars is shorter.

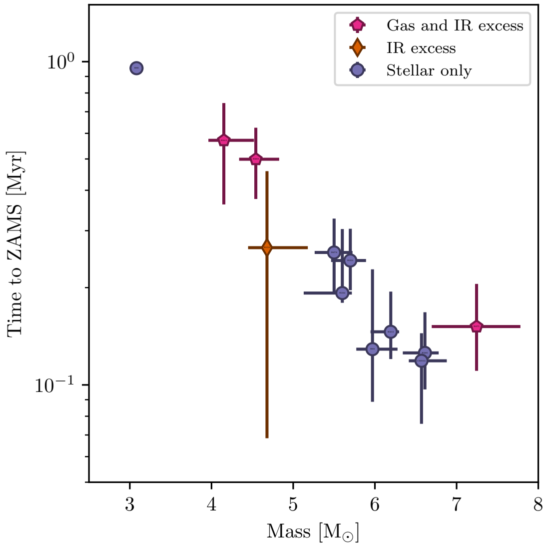

Figure 4.6: Time it takes to reach the ZAMS as function of mass for the pre-main-sequence stars in M17. The markers are identical to Fig. 4.4.

However, we not only find a correlation between remaining time to reach the ZAMS and stellar mass, but also between age and stellar mass. This is shown in Fig. 4.7, where for the pre-main-sequence sources a trend is visible of decreasing age for increasing mass. Rather remarkable, all stars appear to have completed ∼70 percent of the time needed to reach the ZAMS. A similar trend is found when using PARSEC (Bressan et al. 2012) pre-main-sequence evolutionary tracks instead of MIST tracks. This would imply that the lowest mass stars formed first. However, care should be taken with this statement as the preceding discussion has tried to convey that age definition is to some extend arbitrary. Due to the correlation with age and mass, an age determination of a cluster may depend on sample selection criteria. Moreover, pre-main-sequence models make unavoidable strong assumptions (for instance, a constant mass accretion rate and 1D geometry).

4.5.3 Surface rotation

The young age of M17 allows us to determine the spin properties of its (massive) stars as close to the ZAMS as possible. Table 4.5 lists the present-day projected surface rotation velocity in terms of the critical rotation velocity, $v_{\rm crit}$. The latter is determined based on their current radius and mass. As many of these stars have yet to reach the ZAMS, they have not yet settled to their main-sequence radii. Therefore, we also calculate the projected rotation rate at the ZAMS. To this end, we contract the stars from their current radii to their ZAMS radii in accord with their corresponding MIST evolutionary tracks. We assume that the radial density structure of the stars is represented by the solution of the Lane-Emden equation

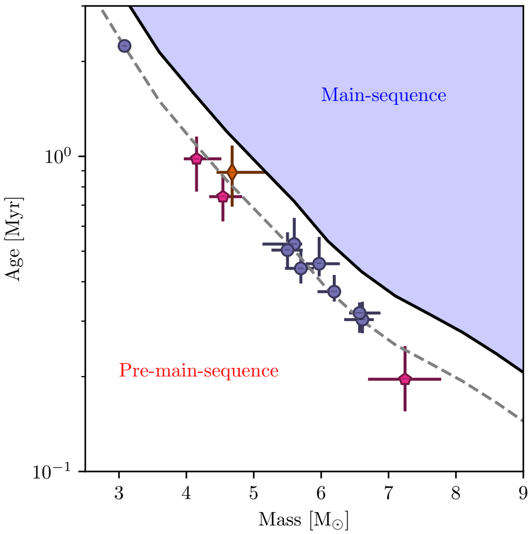

Figure 4.7: Pre-main-sequence age as function of mass. The black line indicates the ZAMS and the grey dashed line 70 percent of that age. The markers are the same as Figure 4.4.

with a polytropic index $n = 1.5$. Furthermore, we assume solid body rotation and complete angular momentum conservation. The resulting ZAMS radius and projected surface rotation velocity are also listed in Table 4.5. The values for the stars that have already arrived on the main sequence remain unchanged.

Figure 4.8 shows the distribution of projected rotation velocity in terms of the critical rotation velocity for both current radii (in orange) and expected ZAMS radii (in purple). The sample is split in two parts. In the top panel, the six stars more massive than 10 $M_\odot$ are shown. All of these have arrived on the ZAMS, with only B181 expected to do so within as little as several tens of thousands of years. In the bottom panel, the 12 stars less massive than 10 $M_\odot$ are presented. These have not yet reached the main sequence and for them further spin up because of Kelvin-Helmholtz contraction is relevant. The v_{ZAMS} distributions of both sets are strikingly different, with the massive stars showing a velocity distribution up to $\sim 0.3\, v_{\text{crit}}$ and the intermediate-mass stars one with velocities up to $\sim 0.6\, v_{\text{crit}}$. Similar differences exist between the spin distributions of well-established main-sequence O-type (Ramírez-Agudelo et al. 2013) and B-type (Dufton et al. 2013) stars. *This may suggest differences in the mechanism through which these two groups of stars gain angular momentum during formation*. Though the sample is small, the fairly low spin rates of the O-type stars at birth is consistent with the hypothesis that the high-velocity tail of spin rates seen in large studies of presumed-single main-sequence O-star populations (Ramírez-Agudelo et al. 2013) is actually due binary interaction, resulting in spun-up systems for which the companion can not be detected (de Mink et al. 2013; Ramírez-Agudelo et al. 2015).

Table 4.5: Derived properties of stars in M17 based on evolutionary tracks. For the stars consistent with being on the main sequence only a lower limit on the age is given and $v_{\rm ZAMS} \sin i / v_{\rm crit} = v \sin i / v_{\rm crit}$. The critical rotation velocity, $v_{\rm crit}$, is based on the evolutionary mass of the star.

Source	Age [Myr]	$M_{\rm ZAMS}[{\rm M}_\odot]$	$R_{\rm ZAMS}[{\rm R}_\odot]$	$v \sin i / v_{\rm crit}$	$v_{\rm ZAMS} \sin i / v_{\rm crit}$
B111	$0.01^{\uparrow}_{\dots}$	$47.4^{+1.9}_{-3.0}$	$8.82^{+0.20}_{-0.30}$	$0.15^{+0.02}_{-0.01}$	$0.15^{+0.02}_{-0.01}$
B164	$0.03^{\uparrow}_{\dots}$	$25.7^{+1.1}_{-1.1}$	$6.49^{+0.11}_{-0.16}$	$0.10^{+0.01}_{-0.01}$	$0.10^{+0.01}_{-0.01}$
B311	$0.04^{\uparrow}_{\dots}$	$20.3^{+0.6}_{-0.6}$	$5.67^{+0.11}_{-0.08}$	$0.03^{+0.01}_{-0.02}$	$0.03^{+0.01}_{-0.02}$
B181	$0.04^{\uparrow}_{\dots}$	$16.9^{+3.3}_{-1.1}$	$5.17^{+0.48}_{-0.18}$	$0.19^{+0.03}_{-0.03}$	$0.28^{+0.06}_{-0.06}$
B289	$0.04^{\uparrow}_{\dots}$	$17.9^{+0.8}_{-0.5}$	$5.33^{+0.13}_{-0.08}$	$0.16^{+0.02}_{-0.02}$	$0.16^{+0.02}_{-0.02}$
B215	$0.06^{\uparrow}_{\dots}$	$13.3^{+1.0}_{-0.9}$	$4.53^{+0.18}_{-0.15}$	$0.24^{+0.02}_{-0.03}$	$0.24^{+0.02}_{-0.03}$
B93	$0.46^{+0.10}_{-0.04}$	$6.0^{+0.3}_{-0.2}$	$2.89^{+0.09}_{-0.06}$	$0.33^{+0.03}_{-0.03}$	$0.41^{+0.05}_{-0.06}$
B205	$0.30^{+0.04}_{-0.03}$	$6.6^{+0.2}_{-0.3}$	$3.08^{+0.04}_{-0.08}$	$0.29^{+0.04}_{-0.04}$	$0.50^{+0.10}_{-0.09}$
CEN55	$0.32^{+0.03}_{-0.04}$	$6.6^{+0.3}_{-0.2}$	$3.07^{+0.07}_{-0.05}$	$0.01^{+0.03}_{-0.01}$	$0.01^{+0.05}_{-0.01}$
B234	$0.53^{+0.11}_{-0.01}$	$5.6^{+0.1}_{-0.5}$	$2.78^{+0.03}_{-0.14}$	$0.46^{+0.05}_{-0.03}$	$0.60^{+0.09}_{-0.07}$
B213	$0.37^{+0.05}_{-0.03}$	$6.2^{+0.1}_{-0.2}$	$2.96^{+0.03}_{-0.08}$	$0.35^{+0.03}_{-0.03}$	$0.55^{+0.07}_{-0.06}$
B253	$0.44^{+0.06}_{-0.05}$	$5.7^{+0.2}_{-0.2}$	$2.81^{+0.06}_{-0.07}$	$0.26^{+0.09}_{-0.06}$	$0.47^{+0.19}_{-0.12}$
B150	$0.89^{+0.19}_{-0.20}$	$4.7^{+0.5}_{-0.2}$	$2.51^{+0.15}_{-0.07}$	$0.41^{+0.03}_{-0.04}$	$0.51^{+0.07}_{-0.07}$
B272	$0.50^{+0.07}_{-0.06}$	$5.5^{+0.2}_{-0.2}$	$2.75^{+0.06}_{-0.07}$	$0.01^{+0.04}_{-0.01}$	$0.01^{+0.06}_{-0.01}$
B275	$0.20^{+0.05}_{-0.04}$	$7.2^{+0.5}_{-0.5}$	$3.23^{+0.13}_{-0.13}$	$0.34^{+0.12}_{-0.14}$	$1.00^{+0.45}_{-0.43}$
B243	$0.98^{+0.17}_{-0.21}$	$4.2^{+0.4}_{-0.2}$	$2.35^{+0.11}_{-0.06}$	$0.24^{+0.16}_{-0.08}$	$0.47^{+0.34}_{-0.18}$
B268	$0.74^{+0.13}_{-0.12}$	$4.5^{+0.3}_{-0.2}$	$2.47^{+0.08}_{-0.07}$	$0.32^{+0.21}_{-0.06}$	$0.74^{+0.52}_{-0.18}$
B86	$2.24^{+0.05}_{-0.04}$	$3.1^{+0.0}_{-0.0}$	$2.00^{+0.01}_{-0.00}$	$0.15^{+0.02}_{-0.05}$	$0.21^{+0.04}_{-0.08}$

In the intermediate-mass sample it is especially the sources with a gaseous disk (B243, B268, B275) that will spin up considerably. B275 stands out in that it shows a projected equatorial rotation velocity equal to critical after contraction to the ZAMS. This is possible, albeit rare as the star would have to be seen exactly edge on for it not to exceed critical spin. However, B275 has a gaseous circumstellar disk and is still relatively far from the ZAMS. Therefore, we should be cautious to assume that the star's angular momentum will remain conserved, as interaction with its disk may still alter the star's angular momentum. These same caveats also apply to B243 and B268, which too are relatively distant from the ZAMS and show hot circumstellar gaseous disks.

4.5.4 Comparison with Ramírez-Tannus (2017)

RT17 performed a similar study of the young stellar content of M17, including a FASTWIND/GA fit for nine stars. Our sample of 18 stars includes all of those nine objects. A point to note is that in our study we adopt the *Gaia* distance of 1675^{+19}_{-18} pc from Stoop et al.

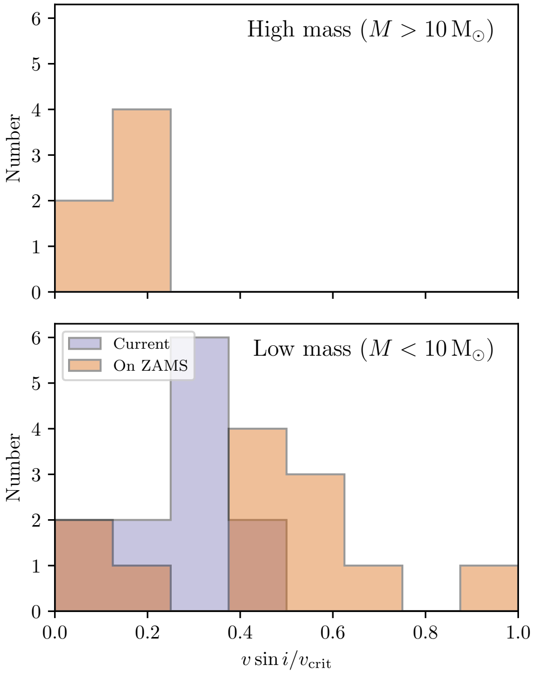

Figure 4.8: Distribution of projected equatorial rotational velocities as function of the critical rotation. *Top panel:* The higher mass stars that have reached the ZAMS are shown. *Bottom panel*: Only the lower mass stars that have not yet reached the ZAMS are shown. The value of $v \sin i / v_{\mathrm{crit}}$ is shown for both current rotation rate and the expected rotation rate once they reach the main-sequence.

(2023, submitted), while RT17 use 1980^{+140}_{-120} pc from Xu et al. (2011). In itself, this decreases the luminosity of the sources by about 30 percent. Though the spectral analysis takes the same approach, important differences exist. *First*, the quality of our spectra is superior as we stack typically three spectra of the quality used by RT17. This allows us to, *second*, include abundances of CNO and Si, lines that also contribute to a more accurate determination of photospheric properties. *Third*, RT17 use a bolometric correction on the extinction corrected absolute V magnitude, where we infer the radius of the star from anchoring our synthetic SED with the absolute J magnitude (given in Table 4.3).

We limit the comparison to pointing out systematic trends, rather than detailing differences for each of the sources separately. For all stars, our T_{eff} values are consistent within uncertanties with those from RT17. Our luminosities are on average a factor two lower, with the smallest change being ~ 10 percent and the largest a factor of about four. This results in lower evolutionary masses. Only for B215 do we find a higher luminosity, mostly because of the significantly higher extinction ($A_V = 9.14$ versus $A_V = 7.6$). The extinction to this source is however highly uncertain due to limited photometry, see Section 4.5.6 and Appendix III.1.

Possibly this is further enhanced by the higher temperature found in our analysis (29 000 K in our study versus 23 500 K by RT17). The improved data quality has been particularly beneficial for the determination of the surface gravity, resulting in considerably smaller uncertainties. This leads to an improved correspondence between spectroscopic mass, i.e., the mass resulting from the gravity and stellar radius, and evolutionary mass, i.e., from a comparison with the MIST evolutionary tracks; a comparison is presented in Appendix III.2. We find systematically higher projected equatorial rotation velocities by about 30 km s^{-1}. The higher rotation rates could be the result of stacking spectra for which the radial velocity has not been properly corrected. However, typical radial velocity shifts are up to 20 km s^{-1}, which is less than the systematic difference we find.

The difference in $v \sin i$ is significantly larger than 30 km s^{-1} for B268 and B275. This is likely due to circumstellar and interstellar contamination. The contamination has been clipped from the data, resulting in a gap in the center of many line profiles, hampering the determination of the rotation. The impact of this clipping is more severe for the data available to RT17. The visual extinction A_V agrees well for all sources except for the earlier mentioned B215. Also R_V values are consistent between this work and RT17, however, the uncertainties are relatively large and the scatter the two works is sizeable.

4.5.5 Abundances

This study has not been optimized for determining surface abundances. However, we treated the abundances as free parameters to aid the fitting process and determine them where possible. As pointed out in Section 4.4.2.4, for most stars abundance constraints are poor with the exception of B311. This O8.5 Vz star combines a high signal-to-noise spectrum with a slow projected surface rotation of $v \sin i = 30^{+15}_{-25}$ km s^{-1}, revealing many distinct narrow lines, beneficial for abundance determinations (see Fig. 4.3). The resulting abundances for this star, as listed in Table 4.4 all agree within 0.1 dex with the present-day solar photosphere abundances (Asplund et al. 2009). This supports the star and its sibling to be young objects. We remark though that it would be expected that the present-day composition of the M17 star forming gas may be somewhat more metal rich relative to solar due to cosmic enrichment over the past 4.6 Gyr, see, e.g., Kobayashi et al. (2020).

4.5.6 Extinction

Figure 4.9 shows total visual extinction A_V plotted against total-to-selective extinction R_V. The visual extinction towards the sources in M17 varies strongly, with A_V values ranging from 3.6 to 10.6 magnitudes. Next to that, we find a large scatter in R_V with values ranging from 2.7 to as high as 5.7. No correlation with spatial location in M17 of either parameter was found, suggesting that the bulk of the extinction is local to the sources. Moreover, no clear trend of A_V with mass or evolutionary stage was found. This leaves stochastic line-of-sight differences, i.e. some sources being further back and/or more deeply embedded in the natal cloud, to explain the scatter in visual extinction.

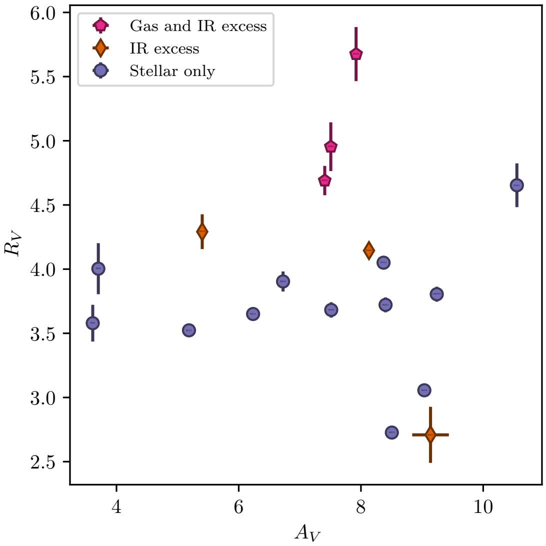

Figure 4.9: Extinction parameters A_V and R_V of the sources in M17. The markers are identical to Figure 4.4.

The total-to-selective extinction is thought to probe the size distribution and composition of the solid-state material (e.g., Draine 2003; Hirashita & Voshchinnikov 2014; Xiang et al. 2017). There is a trend for R_V values to be highest for objects with IR excess. This suggest that the material causing the extinction in these sources is nearby, e.g., in the circumstellar disk or in the direct ambient medium from which the disks have been accreting, as otherwise processing of the grain material responsible for the higher R_V should not be expected to be markedly different from that of the other sources. An exception to the trend is B215, which has relatively poorly constrained extinction properties.

4.5.7 Mass-loss rates

Mass-loss sensitive lines available in our optical spectra are Hα, to some extent Hβ, and for O-type stars He II 4686. The determination of the mass-loss rates from Hα and Hβ is hindered by contamination by interstellar and, if present, circumstellar emission. Because of interstellar emission, the line centers, which are most sensitive to mass loss, had to be clipped. An additional complication is potential contamination of the broad wings of the lines due from circumstellar material that has not been clipped. Such broad non-stellar emission could originate from a disk or disk wind. As a result the mass-loss rate will be overestimated because the circumstellar emission will be fitted as if it orignated in the stellar winds. For the hottest and brighter stars ($\log L/L_\odot > 4$) we can place tight constraints on $\dot{M}$. For some of the fainter stars without disk signatures we also constrain mass-loss rates – to the best of our knowledge, for the first time in this part of parameter space – but as the wind signatures

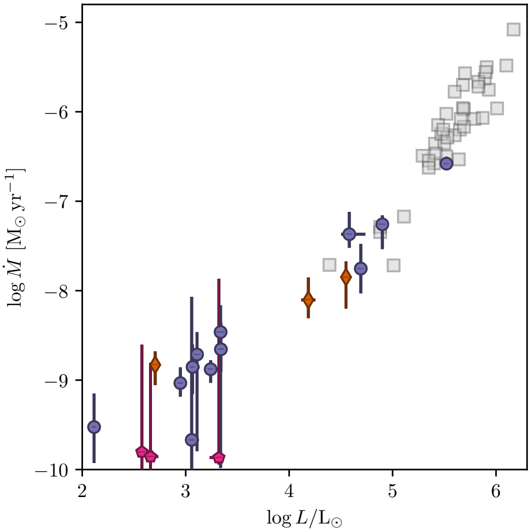

Figure 4.10: Mass-loss rate as function of luminosity for the M17 sample. Markers are identical to Fig. 4.4. Additional sources shown in grey squares are the Galactic OB stars from Repolust et al. (2004), Mokiem et al. (2005), and Crowther et al. (2006).

are extremely weak, we remain cautious with respect to the obtained results. The mass-loss determinations for these $12\,000 - 18\,000$ K and $\sim 10^2 - 2 \times 10^3\, L_\odot$ stars should be treated with care.

Figure 4.10 shows mass-loss rate as function of luminosity along with $\dot{M}$ determined by Repolust et al. (2004), Mokiem et al. (2005), and Crowther et al. (2006) for other Galactic data sets. The values derived by these authors assume smooth winds; we have corrected their rates adopting the same clumping factor ($f_{\rm cl} = 10$) as used in our analysis. We find the mass-loss rates of the brightest stars in our sample to be consistent with these previous studies of Galactic O- and early B-type stars.

For stars without disk signatures that are less bright than $2 \times 10^3\, L_\odot$, we find mass loss rates (in $\mathrm{M}_\odot$ yr^{-1}) up to $\log \dot{M} \sim -8.5$. Although these are extremely low rates, they do show that *the initiation of the stellar outflow happens already during the PMS phase*. Assuming the wind-driving mechanism is radiation pressure on spectra lines, Krtička (2014) predicts mass-loss rates for main-sequence B-type stars in this part of parameters space (their models T14, T16, T18, T20). Typical $\dot{M}$-values are $\sim 10^{-11}\,\mathrm{M}_\odot$ yr^{-1}, i.e., up to about two orders of magnitude less than we find. Taking our results at face value, this either indicates that the theoretical predictions are significantly too low, or, that PMS B-stars suffer from considerably stronger mass loss than main-sequence B-stars in the same part of ($T_{\rm eff}$, L) space. As pointed out above, for the PMS stars with disks we consider the mass-loss rates as tentative upper limits.

4.6 Conclusions

We have analyzed optical spectra of 18 stars in the young star-forming region M17 with spectral types ranging from O4.5 to B9, corresponding to temperatures from 46 000 to 11 000 K, using the stellar atmosphere model Fastwind and fitting algorithm Kiwi-GA. The sources are still (heavily) embedded with visual extinctions between $A_V = 3.6$ and 10.6 mag. Three of the stars show gaseous and dusty circumstellar material, likely to be remnant features of their formation. Three other stars display hot dusty circumstellar material in their SEDs. The sample is unique in that it constitutes a population of massive and intermediate-mass stars close to or on the zero-age main sequence, allowing to study the actual outcome of star formation in this mass range. Our main conclusions are listed below.

- The HRD positions of the six most massive stars ($13 \lesssim M \lesssim 47\,\mathrm{M}_\odot$) are consistent with the theoretical location of the zero-age main sequence as given by the MIST evolutionary tracks; the 12 lower mass stars ($3 \lesssim M \lesssim 7\,M_\odot$) are pre-main-sequence sources. The cluster age is constrained to $0.4^{+0.6}_{-0.2}$ Myr, based on the pre-main-sequence population. We conclude that we have empirically confirmed the predicted ZAMS location in the mass range spanned by the six brightest stars.
- The three sample stars with gaseous disks (B275, B243, B286) are located further from the main sequence than the stars without a disk, which is in line with the hypothesis that these are the least evolved objects in the sample and have not yet lost their accretion disk.
- Within the short time span of the formation process of these stars, we find as strong correlation between age and stellar mass, with lower mass stars being older. This is inconsistent with these stars crossing the birhtline simulaneously during formation.
- We identify a dichotomy between the projected equatorial rotational velocity for stars $M > 13\,M_\odot$, that are O-type stars on the ZAMS, and stars $3 \lesssim M \lesssim 7\,\mathrm{M}_\odot$, that will become B-type stars on the ZAMS. Extrapolating the projected spin velocities to the ZAMS for all stars, the massive ones have $v \sin i \lesssim 0.3\,v_{\mathrm{crit}}$ and the stars of intermediate mass $v \sin i \lesssim 0.6\,v_{\mathrm{crit}}$. This is in line with previous results for well-established main-sequence populations and may suggest different mechanisms for angular momentum accretion between the two groups.
- Surface abundances of C, N, O, and Si are most accurate for the slowly spinning and bright source B311. They match those of the current solar abundances, supporting the young age of M17 and indicating that gas from which the cluster formed has not been significantly chemically enriched relative to the Solar nebula gas.
- No strong spatial pattern of extinction properties can be identified. We do find a correlation between R_V and the presence or absence of circumstellar matter. The stars showing signs of disks have higher R_V values suggesting different size and composition properties of the solid state material in the line of sight.
- For the stars more massive than $10\,M_\odot$ we find mass-loss rates that are in line with observed rates of Galactic main sequence O V-III stars. For the first time, we derive

mass-loss properties for PMS B V-III stars and find rates of up to $10^{-8.5}$ $\mathrm{M_\odot\,yr^{-1}}$. These should be considered as tentative, but at face value establish that stellar winds already initiate in the PMS phase. They are two orders of magnitude higher than predictions for main-sequence B stars by Krtička (2014). If these theoretical rates are correct, possibly PMS-star winds are considerably stronger than MS-star winds.

This unique sample of stars gives insight into the outcome of massive star formation, providing both constraints for star formation theory and initial conditions for stellar evolution. The mass-loss properties of the pre-main-sequence population remain uncertain, but could be improved with more focused studies. More data on the wind diagnostics and the contaminants could benefit such studies. UV detection of the outflows would be very insightful, but extremely difficult to obtain due to strong extinction. Alternatively, JWST observations of the more sensitive Brα might be able to provide better mass-loss estimates (Puls et al. 2008).

Chapter 5

Atmosphere and mass-loss properties of O-type giants in the SMC: Clumped winds at low metallicity

---

F. Backs, S. Brands, A. de Koter, L. Kaper, J. Puls, J. S. Vink, , F. Tramper, H. Sana

Astronomy & Astrophysics, in prep.

Abstract

Context. Mass loss in a stellar wind is an important physical process steering massive star evolution and controlling properties of end-of-life products such as supernova type and compact object mass. To probe its role in massive star evolution over cosmic time, mass loss needs to be studied as function of metallicity. For mass loss to be accurately quantified, the wind structure needs to be established jointly with the characteristics of small-scale inhomogeneities in the outflow, known as 'wind clumping'.

Aims. We aim to improve empirical estimates of mass loss and wind clumping for hot main-sequence massive stars, study the dependence of both properties with metal content and confront our findings to theoretical predictions of mass loss as a function of metallicity.

Methods. Using the model atmosphere code FASTWIND and the genetic algorithm fitting method KIWI-GA, we analyse the optical and ultraviolet spectra of 13 O-type giant to supergiant stars in the Small Magellanic Cloud galaxy, which has a metallicity 1/5th that of the Milky Way. Stellar, global outflow properties, such as mass-loss rate and terminal wind velocity, and wind clumping properties are constrained. To probe the role of metallicity, our findings are compared to studies of Galactic and Large Magellanic cloud samples that are analysed with very comparable prescriptions of wind structure.

Results. We find significant variations in the wind clumping properties of the target stars, with clumping starting at flow velocities $0.01 - 0.23$ of the terminal wind velocity and reaching clumping factors $f_{\rm cl} = 2 - 30$. In the luminosity ($\log L/L_{\odot} = 5.0 - 6.0$) and metallicity ($Z/Z_{\odot} = 0.2 - 1$) range studied, we find that the scaling of mass loss $\dot{M}$ with metallicity Z is *not* invariant for luminosity. Though at $\log L/L_{\odot} = 5.75$ we find $\dot{M} \propto Z^m$ with $m = 1.02 \pm 0.30$, which is within uncertainties in agreement with the pioneering work in the field, we obtain a scaling that is significantly *steeper* at lower metallicities, where $m > 2$. This behaviour is at odds with the recent result of Marcolino et al. (2022), who find a $\dot{M}(Z)$ dependence that is stronger at higher luminosity. We do not find strong indications that wind inhomogeneity properties depend on metallicity.

Conclusions. The monotonically decreasing $m(L)$ behaviour adds a complexity to the functional description of the rate of mass-loss of hot massive stars. Though the trend is present in predictions, it is much weaker than found here. The luminosity range for which m is significantly larger than previously assumed (at $\log L/L_{\odot} \lesssim 5.4$) is however still poorly explored and more studies are needed to thoroughly map the empirical behaviour, particularly so at Galactic metallicity.

5.1 Introduction

Feedback from massive stars plays an important role in the thermal and dynamical evolution of the interstellar medium and halos of galaxies (e.g., Hopkins et al. 2011, 2018; Andersson et al. 2020). It is provided through radiation, powerful stellar outflows and, when ultimately their cores collapse, supernovae (e.g., Dale & Bonnell 2011; Luisi et al. 2016; Geen et al. 2020; Efstathiou 2000; McLeod et al. 2019). The mass and angular momentum lost through their stellar outflows, processes that persist throughout their lives, strongly influence the evolution of massive stars (e.g., Puls et al. 2008; Langer 2012; Renzo et al. 2017; Vink 2022). At Galactic metallicities, e.g., mass loss causes the mass at the end of carbon burning to be 1/2.5 to 1/4 of that of the initial mass for stars that started our their lives with 20 $M_\odot$ or more (Ekström et al. 2012). The cumulative mass loss a massive star experiences throughout evolution is found to be a function of the star's initial metal content (see below): lower metallicity (hot) stars have weaker winds. One consequence of this is that properties of core-collapse supernovae are expected and found to differ for galaxies of low and high metal content. Long-duration gamma-ray-bursts (e.g., Savaglio et al. 2009; Modjaz et al. 2008; Heger et al. 2003) super-luminous supernovae (e.g., Chen et al. 2017), and pair-instability supernovae (e.g., Young et al. 2010) for instance, favor lower metallicity environments. It also implies that the first stars to form in the universe (e.g., Hirano et al. 2015) must have lost relatively little mass (e.g., Kudritzki 2002), with important consequences for their end of life products (e.g., Marigo et al. 2003).

It is therefore of great importance to have an accurate understanding of mass loss from massive stars, including its dependence on metal content. On the theory side, the hot-phase driving mechanism has been identified to be radiation pressure on metal lines of mostly CNO and iron-group elements clustered in the ultraviolet, where the stars emit the bulk of their radiation (e.g., Lucy & Solomon 1970; Castor et al. 1975; Abbott & Lucy 1985; Pauldrach et al. 1986; Puls et al. 1996), and combined stellar atmosphere and hydro-dynamical methods that take into account several 10^5 such lines have been developed to make quantitative predictions (de Koter et al. 1997; Vink et al. 2001; Krtička & Kubát 2018; Björklund et al. 2021). Empirical studies of the mass-loss versus metallicity behaviour probe Galactic, Large Magellanic Cloud (LMC; $Z = 0.5\,Z_\odot$) and Small Magellanic Cloud (SMC; $Z = 0.2\,Z_\odot$) metallicities. When relying on relatively high-luminosity sources ($\log L/L_\odot \gtrsim 5.4$), where wind signatures in Hα and He II 4686 Å are clearly visible, they infer a luminosity independent behaviour $\dot{M} \propto Z^{0.5-0.8}$ (Mokiem et al. 2007; Marcolino et al. 2022). To constrain mass-loss properties for lower luminosity stars, the spectral analysis relies strongly on the ultraviolet spectral range, where UV resonance lines such as C IV 1548,1550 Å provide more sensitive probes of wind strength. Marcolino et al. (2022), using a compilation of UV & optical studies, first addressed this parameter space and tentatively found a weaker or even vanishing dependence on Z: $\dot{M} \propto Z^{0.1}$ at $\log L/L_\odot = 4.5$. They stress that their findings should be tested with larger samples that include more accurate determinations of the terminal velocity of the wind.

Here we undertake such a test, constraining photospheric conditions and a range of wind properties including inhomogeneities in the outflow and terminal velocity. We analyse a sample of O4 to O9.5 giants, bright giants and supergiants in the SMC for which ultraviolet and optical spectra are secured in the context of the *Hubble Space Telescope* ULLYSES (Roman-Duval et al. 2020) and *Very Large Telescope* X-Shooting ULLYSES (Vink et al. 2023) programs. Then, we compare our finding with studies of Galactic (Hawcroft et al. 2021) and LMC stars (Brands et al. in prep.; Hawcroft et al. in prep.) that employ very similar techniques. The ULLYSES and X-shooting ULLYSES programs ultimately aim to provide an empirical library of fully characterized spectral templates for stars at sub-solar metalllicity, among others for use in population synthesis studies.

A major challenge in the empirical determination of mass-loss rates is the presence of inhomogeneity in the wind, also referred to as clumping. These clumps are over-dense regions, contrasted with regions of lower density. Clumps affect the strength of spectral lines both directly and indirectly. Directly in the case of recombination lines, such as Hα and He II 4686 Å, the strength of which depends on the mean of the square of the density of the medium; and indirectly in the case of lines of trace ionic species of which the ionisation balance is shifted significantly due to a changing density. Scattering lines of abundant ionic species, such as C IV 1550 Å, however, may be unaffected by clumping. Because of this difference in behaviour clumping has been suggested and used as solution to differences in inferred mass-loss rate for different diagnostic lines (e.g. Bouret et al. 2003; Fullerton et al. 2006). A so far poorly explored problem is whether wind clumping itself is a function of metallicity and/or luminosity. If so, this may have impact on the derived mass-loss properties and should thus be accounted for in deriving empirical $\dot{M}(Z)$ or $\dot{M}(L, Z)$ relations. This challenging problem too is a goal of this study.

This paper is organised as follows. We describe the data and the sample in Section 5.2 along with the data preparation and normalization process. The model and fitting routine are presented in Section 5.3. Section 5.4 shows and describes the best fit line profiles and the corresponding stellar and wind parameters. In Section 5.5 we briefly discuss the evolutionary stage of the sample stars, present the implications for $\dot{M}(L, Z)$ and list problems and challenges encountered in the analysis. Finally, Section 5.6 lists the main conclusions.

5.2 Data and sample

Our sample consists of 13 SMC O-type giants to supergiants available in ULLYSES DR5 (Roman-Duval et al. 2020) and XShootU eDR1 (Vink et al. 2023; Sana et al. in prep.). The ULLYSES data consists of a mix of FUSE, HST/COS, and HST/STIS spectra, with both archival and new observations. The ULLYSES sample is selected to include presumed-single stars, however, the presence of binaries, also in our sample, cannot be excluded. We use the high level science products as reduced by Roman-Duval et al. (2020). The XShootU data consists of VLT/X-shooter spectra covering the UVB and VIS arms (∼3100–8000 Å). The sample is selected based on data availability in both optical and UV wavelengths, where we required that the UV data covers at least the wavelength range 1150–1700 Å. The sample of stars with their spectral type and available UV observations are listed in Tab. 5.1.

Table 5.1: Sample of SMC O giants, their spectral types, and the UV instruments used.

Target	Spectral type	Ref	UV observations
AV 80	O4-6n(f)p	a	FUSE, G130M, G160M
AV 15	O6.5 II(f)	a	FUSE, E140M
AV 83	O7 Iaf^{+}	a	E140M
AV 95	O7 III((f))	a	FUSE, E140M, E230M
AV 207	O7 III((f))	b	FUSE, G130M, G160M
AV 69	OC7.5 III((f))	a	FUSE, E140M
AV 469	O8.5 II((f))	b	FUSE, E140M
2dFS 163	O8 Ib(f)	c	G130M, G160M
AV 479	O9 Ib	d	FUSE, G130M, G160M
AV 307	O9 III	e	G130M, G160M
AV 70	O9.5 Ibw	f	FUSE, E140M, E230M
AV 372	O9.5 Iabw	f	FUSE, E140M, E230M
AV 327	O9.5 II-Ibw	a	FUSE, E140M

Spectral type reference: a: Walborn et al. (2000), b: Lamb et al. (2016), c: Evans et al. (2004), d: Lennon (1997), e: Garmany et al. (1987), f: Walborn et al. (2002)

All FUSE data is taken with the LWRS aperture, which has a spectral resolution of ∼17,500 and covers 905–1180 Å. AV 307 is the only star for which data is taken with HST/COS using the G130M/1096 grating. This grating covers the wavelength range from 940–1240 Å, and has a resolution of $R \sim 6000$ around $\lambda \sim 1120$ Å. The HST/COS observations using the G130M/1291 and G160M/1611 gratings cover the wavelength range 1141–1783 Å and have a resolution ranging from 11,000 to 19,000. The HST/STIS data that are obtained using the E140M and E230M gratings have a resolution of 45,800 and 30,000, respectively. The E140M grating covers the wavelength range from 1141 to 1708 Å and the E230M grating the wavelengths 1608–2366 Å. If multiple data sets would cover a modelled feature, the used data was chosen based on signal to noise, spectral resolution, and possible systematic effects. The optical data consists of the UVB and VIS arms of VLT/X-shooter. The UVB arm covers 3100–5500 Å and has a resolution of 6700 for the chosen slit width of 0.”8. The VIS arm covers 5500 to 8000 Å with a resolution of 11,400 with the slit width of 0.”7.

The signal-to-noise ratio (SNR) of the data varies depending on the observation and wavelength range. The optical data typically has a high signal-to-noise ratio of >100. The UV data has on average a SNR ∼ 20. In some cases a higher SNR was obtained. The lowest signal-to noise ratio is found in the FUSE data, where it can be only ∼5.

5.2.1 Photometry

Photometric information of the stars is used to determine the line-of-sight extinction. The extinction and the distance are used to determine the absolute K-band magnitude, which is used as luminosity anchor in the analysis. All photometric data is taken from the Bonanos et al. (2010) catalog. The U, B, V, I, J, H, Ks photometric bands were used together with the extinction curves from Fitzpatrick (1999). For the latter, we adopt $R_V = 3.1$ and determine the A_V by fitting the photometry to Castelli-Kurucz model SEDs (Castelli & Kurucz 2004a). For this part of the analysis, the temperature of the model is selected based on the spectral type as listed in Table 5.1 [1].

5.2.2 Data preparation

The spectral fitting relies on normalized line profiles. Therefore, the observed spectra need to be normalized. Incorrectly identifying the continuum affects the strength and shape of spectral lines, so it is of great importance to determine it as accurately as possible. To that end, we attempt to improve on the normalization done by Sana et al. (in prep.) in eDR1 by pursuing the following normalization routine.

We divide the observed spectrum by a normalized CMFGEN model (Hillier & Miller 1998). Ideally, i.e., if the model fits perfectly, this results in a featureless 'pseudo continuum' with noise. This continuum is fitted with a polynomial. The normalized spectrum is then obtained by dividing the observed spectrum by the polynomial. The CMFGEN model parameters are selected from a limited grid of models, in which we use the model that has the lowest χ^2 when comparing the normalized data to the normalized model spectrum. In this process diverging features that are not properly covered in the model, such as wind sensitive lines and interstellar features, are masked, such that they do not affect the polynomial fit or χ^2 determination. The normalization procedure is done locally, i.e., around spectral lines of interest, in the optical, and per grating in the UV spectral range (see below).

By using normalized spectra to fit our models and by using a polynomial to fit the pseudo continuum, we minimize the effect of uncertainties of the extinction might have on the analysis. This is aided by choosing the K-band magnitude as luminosity anchor, as the effect of extinction toward our targets is at most minor at longer wavelengths.

For the UV data the normalization is done simultaneously with the determination of the radial velocity, using the same χ^2 analysis as in the selection of the model. The optical X-shooter data is corrected for its radial velocity using a cross correlation with a selection of hydrogen and helium lines. This should give corrections accurate to $\sim$10 $\mathrm{km\,s^{-1}}$ depending on signal to noise ratio and projected rotational velocities. The UV spectrum of hot stars in the SMC is rich in Fe lines. These lines cover the whole spectral range, making it hard to identify the continuum between the lines. Therefore, the normalization is applied to the full spectrum, for each grating separately.

Differences between the normalization performed in XShootU eDR1 (Sana et al. in prep.) and this work are typically small ($< 1\%$). We ascribe them to some broad local features that have affected the global normalization of Sana et al..

Strong interstellar Lyα absorption is present in all spectra. The wings of this absorption overlaps with the N V λ1240 feature and is often wide enough to affect the C III λ1176 and C IV λ1169 features. Since Lyα is not part of our modelling we correct for it. We fit a Voight-

---

[1] For the spectral type to temperature conversion http://www.isthe.com/chongo/tech/astro/HR-temp-mass-table-byhrclass.html was consulted.

Hjerting function to the affected data (Tepper-García 2006). This results in good fits, which allow us to put the continuum around these features at unity. Features in the spectral regimes of interest that are not modelled, such as missing lines or elements, diffuse interstellar bands, and interstellar absorption lines, are clipped from the observed spectrum. This way they do not affect the fitting efforts.

5.3 Methods

We aim to determine detailed stellar and wind parameters of the sources by calculating model spectra and comparing those to the observations. The model spectra are calculated using the model atmosphere code FASTWIND. One model calculation takes approximately 40 minutes on a single computing core. This allows us to calculate a large number of models in order to fit the data. However, a significant number of models are required to properly explore the high number of free parameters, and their uncertainties, in the large parameter space. Therefore, we use a genetic algorithm to efficiently explore the parameter space and converge to the optimal parameters and their associated uncertainties. Sect. 5.3.1 describes FASTWIND in more detail. The genetic algorithm is covered in Sect. 5.3.2. Finally, in Sect. 5.3.3 we describe the fitting approach and free parameters.

5.3.1 Fastwind

FASTWIND is a stellar atmosphere and radiative transfer code optimized for hot stars and their winds (Santolaya-Rey et al. 1997; Puls et al. 2005; Sundqvist & Puls 2018). The model assumes non-local thermodynamic equilibrium (NLTE) and includes line-blanketing. FASTWIND aims to minimize computational cost. To that end, the elements are split into ‘explicit’ and ‘background’ species. The explicit elements are treated in detail in the co-moving frame, while the background elements are only used to account for line-blocking and line-blanketing. For this reason only explicit elements can be used to produce diagnostic line profiles. FASTWIND uses a pseudo-hydrostatic photosphere that smoothly transitions into a trans-sonic wind. The wind is then described in a parameterized way, with a specified mass-loss rate and a radially increasing smooth-wind β-velocity law asymptotically approaching the terminal velocity v_∞. Additionally, we use the optically-thick clumping prescription as described in Sundqvist & Puls (2018) to account for small-scale inhomogeneities in the outflow. The optically-thick clumped wind is described by a set of six wind structure parameters, $f_{\rm cl}$, $f_{\rm ic}$, $f_{\rm vel}$, $v_{\rm cl,start}$, $v_{\rm cl,max}$ and $v_{\rm windturb}$, which we briefly introduce. For more detailed descriptions, see Sundqvist & Puls (2018); Brands et al. (2022).

The medium is assumed to consist of two components, regions where the density $\rho_{\rm cl}$ is relatively high (’clumps’) and where the density $\rho_{\rm ic}$ is relatively low (’inter-clump medium’). The clumps fill a fraction $f_{\rm vol}$ of the total volume, such that the mean density

$$\langle \rho \rangle = f_{\rm vol}\, \rho_{\rm cl} + (1 - f_{\rm vol})\, \rho_{\rm ic}. \tag{5.1}$$

The density of the rarefied medium in between the clumps is set by the inter-clump density contrast

$$f_{\rm ic} \equiv \frac{\rho_{\rm ic}}{\langle\rho\rangle}. \tag{5.2}$$

The clumping factor $f_{\rm cl}$ relates the mean density to the mean-square density as

$$f_{\rm cl} \equiv \frac{\langle\rho^2\rangle}{\langle\rho\rangle^2} = \frac{f_{\rm vol}\,\rho_{\rm cl}^2 + (1-f_{\rm vol})\,\rho_{\rm ic}^2}{[f_{\rm vol}\,\rho_{\rm cl} + (1-f_{\rm vol})\,\rho_{\rm ic}]^2}, \tag{5.3}$$

such that for a void inter-clump medium ($\rho_{\rm ic} = 0$), $f_{\rm cl} = 1/f_{\rm vol}$ or $f_{\rm vol} = 1/f_{\rm cl}$. For the more general case of a non-void inter-clump medium

$$f_{\rm vol} = \frac{(1-f_{\rm ic})^2}{f_{\rm cl} - 2f_{\rm ic} + f_{\rm ic}^2}. \tag{5.4}$$

All the above parameters are a function of radial distance, which for simplicity of notation is left out. The wind starts to clump at the velocity $v_{\rm cl,start}$ and reaches the maximum value of $f_{\rm cl}$ at $v_{\rm cl,max}$.

Each clump is assumed to have an internal velocity dispersion δv. To put this in perspective, as clumps have a physical size one may relate it to the velocity span of the clumps due to the underlying radially increasing smooth outflow velocity, $\delta v_{\rm sm}$. If the clumps have small internal δv and are located relatively far from one another, the gas in optically thick clumps can only absorb a modest amount of light as Doppler shifts are small and don't spread out line opacity over a wide velocity range. However, if δv is large relative to $\delta v_{\rm sm}$ light will be much more effectively blocked. This effect of porosity in velocity space (termed velocity-porosity or vorocity in Owocki 2008) is quantified using a normalized velocity filling factor $f_{\rm vel}$ that takes values from 0 and 1. Finally, $v_{\rm windturb}$ describes the turbulence in the wind.

The wind structure parameters $f_{\rm ic}, f_{\rm vel}, v_{\rm cl,start}$, and $v_{\rm windturb}$ are defined as function of the clumping factor $f_{\rm cl}$. Therefore, if no inhomogeneities are present in the flow, i.e., the wind is truly smooth, the clumping factor $f_{\rm cl}$ equals unity. In that case, the other wind structure parameters no longer have any effect or meaning. This implies that if the fitting procedure (see below) selects $f_{\rm cl} = 1$ for a model calculation, none of these five detailed structure parameters will impact the line profiles.

5.3.2 Genetic algorithm

Given the large number of parameters is it not feasible to fully explore the parameter space. However, it is essential that all parameters are explored simultaneously, as many parameters are connected and correlated. Determining parameter values sequentially would then likely result in underestimation of uncertainties and possibly a sub-optimal final fit. Therefore, an efficient fitting algorithm is required to fit all parameters simultaneously. A genetic algorithm (GA) was found to be efficient, while remaining robust enough to not get stuck in local minima (e.g Mokiem et al. 2005; Tramper et al. 2014). We use the genetic algorithm Kiwi-GA[1] (Brands et al. 2022) to find the optimal fit parameters, to which we refer for an in-depth discussion

---

[1] https://github.com/sarahbrands/Kiwi-GA

of the method. Kiwi-GA functions both as fitting routine and as FASTWIND wrapper. The algorithm starts out with a set of models of which the parameters result from a random uniform sampling of their reasonable allowed values.

Subsequent 'generations' of models are then generated by combining two models of the 'parent' population. The parameters of those models are mixed, giving the new model the parameter value from either parent. Additionally, the parameters can get a mutation, changing the value. The parent models are selected semi-randomly based on their χ^2 value, with a lower χ^2 giving a higher probability to be selected. The χ^2 value is determined by comparing the normalized model spectra to the observed spectra and its uncertainty. Only a selected set of spectral features is compared (see Section 5.3.3).

Using Kiwi-GA, we are able to fit 15 free parameters and converge to a robust solution in 80 generations. Each generation contains 128 models, resulting in $\sim$10,000 models per target in total. For comparison, this is already less than calculating all parameter value permutations given only two values per parameter ($2^{15} = 32\,768$). A grid consisting of five values per parameter, unrealistically coarse for most parameters, would constitute $\sim 3 \times 10^{10}$ models, and would only be computational-cost effective if more than 3×10^6 stars would be scrutinized to the level pursued here.

5.3.3 Fitting approach

The parameters we aim to constrain are listed in Tab. 5.2. We fitted essential atmosphere parameters such as the effective temperature $T_{\rm eff}$, surface gravity $\log g$, and projected equatorial rotational velocity $v \sin i$, along with the surface abundance of helium, carbon, oxygen, silicon, and if available phosphorus. The wind (structure) parameters we fitted are the mass-loss rate $\dot{M}$, velocity law index β, terminal velocity v_∞, the (maximum) clumping factor $f_{\rm cl}$, the inter-clump density contrast $f_{\rm ic}$, the velocity-porosity $f_{\rm vel}$, the onset velocity of clumping $v_{\rm cl,start}$, and the turbulent wind velocity $v_{\rm windturb}$. We assume the that maximum clumping is reached at $v_{\rm cl,max} = 2 v_{\rm cl,start}$.

The analysis of each star was split into an optical only fit to constrain the projected rotational velocity $v \sin i$ and helium abundance $y_{\rm He}$ of the star. Then, another fit addressing both optical and UV diagnostics was preformed using the $v \sin i$ and $y_{\rm He}$ value from the optical fit. This two step approach was used to ensure the correct value of the rotation was found. From test calculations we found that the $v \sin i$ value was often found to be degenerate with, notably, $v_{\rm windturb}$ in wind lines, allowing slightly better fits in the UV at the cost of worse fits to many optical lines. The helium abundance was fixed in the optical + UV fits as there is little to no sensitivity to this parameter in the UV and would lead to more uncertain and less accurate values. Additionally, the two step approach makes it possible to check for systematic changes or biases caused by including the UV diagnostics.

In the optical-only fits the only free wind parameter is the mass-loss rate. All other wind parameters are fixed to fiducial values of $\beta = 1$, $f_{\rm cl} = 10$, $f_{\rm ic} = 0.1$, $f_{\rm vel} = 0.5$, $v_{\rm cl,start} = 0.05 v_\infty$, $v_{\rm windturb} = 0.1 v_\infty$, and we use the v_∞ from Hawcroft et al. (2023).

Table 5.2: Model parameters fitted in the optical and optical + UV fits.

Run	Free parameters
Optical only	$T_{\rm eff}, g, \dot{M}, v \sin i, y_{\rm He}, \epsilon_{\rm C}, \epsilon_{\rm N}, \epsilon_{\rm O}, \epsilon_{\rm Si}$
Optical + UV	$T_{\rm eff}, g, \epsilon_{\rm C}, \epsilon_{\rm N}, \epsilon_{\rm O}, \epsilon_{\rm Si}, \epsilon_{\rm P}^{\dagger}$ $\dot{M}, \beta, v_\infty, f_{\rm cl}, f_{\rm ic}, f_{\rm vel}, v_{\rm cl,start}, v_{\rm windturb}$

† Only if the P v 1118 and 1128 lines are available.

The spectral features scrutinized in this work are listed in Tab. 5.3. The top and bottom parts of the table list UV and optical diagnostics, respectively. All lines that are part of the same complex were fitted together.

The mix of spectral features of different elements with varying ionization stages allows us to accurately determine the temperature of these stars. The Balmer lines allow for inference of the surface gravity. The large selection of wind sensitive lines, including resonance lines and recombination lines, allows us to constrain the mass loss and terminal velocity, and ideally also wind clumping parameters. We found that the latter does require a relatively strong outflow; see Section 5.4. Additionally, we fitted the CNO-cycle element abundances, and silicon and phosphorus abundances, of which the latter is only fitted in the optical + UV fits. So far, to the best of our knowledge, no studies are available that attempt to fit Si and P surface abundances in O stars in the SMC. However, not many diagnostics are available to study these abundances, with the added complexity that these are also wind sensitive.

The radius of the stars, and therefore luminosity, was determined using the absolute K-band magnitude as an anchor. So, the stellar parameters determine the shape of the SED, which then is scaled with the appropriate radius to match the observed absolute magnitude. The K-band magnitude was chosen as it is widely available and not strongly affected by the interstellar extinction or the thermal radiation of dust. The uncertainty on the absolute magnitude is a result of the uncertainty on the photometry, extinction towards the star, and the distance is taken into account through error propagation. This affects the radius, luminosity, spectroscopic mass, ionizing flux, and mass-loss rate. The latter is affected because we assume $\dot{M}/R_\star^{3/2}$ to be constant (Puls et al. 1996). However, intrinsic uncertainties on the mass-loss rate are typically significantly higher than the uncertainty on the radius. We assume a distance of 62.44 ± 2 kpc to the sources in the SMC (Graczyk et al. 2020; Subramanian & Subramaniam 2009). Here the uncertainty is an estimate of the depth of the SMC, as it is unclear where the source is in the direction of the line-of-sight through the galaxy.

5.3.4 Comparison with evolutionary models

We determined the initial mass, current evolutionary mass, and age using Bonnsai[1] (Schneider et al. 2014). Bonnsai is a Bayesian framework that can compare observed stellar properties with those of evolutionary models to obtain the posterior distribution of additional

---

[1] The BONNSAI web-service is available at www.astro.uni-bonn.de/stars/bonnsai/index.php.

Table 5.3: Diagnostic features used during fitting.

Ion	Wavelength [Å]	Part of complex
Si III	1113.2	Si III 1113
P V	1118.0	P V 1118
P V	1128.0	P V 1128
Si IV	1128.3	P V 1128
C IV	1168.9, 1169.0	C IV 1169†
C III	1174.9, 1175.3, 1175.6, 1175.7, 1176.4, 1177.0	C III 1176†
C III	1247.4	N V 1240
O IV	1338.6, 1343.0, 1343.5	O IV 1340
Si IV	1393.8, 1402.8	Si IV 1400
C IV	1548.2, 1550.8	C IV 1550
He II	1640.4	He II 1640
N III	1747.9, 1751.2, 1751.7	N III 1750
N IV	3478.7, 3483.0, 3485.0	N IV 3480
O III	3961.6	Hϵ
He I	3964.7	Hϵ
H I	3970.1	Hϵ
He II	4025.4	He I 4026
He I	4026.2	He I 4026
C III	4068.9, 4070.3	C III 4070
O II	4069.6, 4069.9, 4072.2 4075.9	C III 4070‡
Si IV	4088.9, 4116.1	Hδ
N III	4097.4, 4103.4	Hδ
He II	4099.9	Hδ
H I	4101.7	Hδ
He I	4143.8	He I 4143
N III	4195.8, 4200.1	He II 4200
He II	4199.6	He II 4200
He II	4338.67	Hγ
H I	4340.5	Hγ
N III	4379.0, 4379.2	He I 4387
He I	4387.9	He I 4387
He I	4471.5	He I 4471
N III	4510.9, 4511.0, 4514.9 4518.1	N III qua
N III	4534.6	He II 4541
He II	4541.4	He II 4541
N III	4634.1, 4640.6, 4641.9	C IIIN III 46
C III	4647.4, 4650.2, 4651.5	C IIIN III 46
He II	4685.6	He II 4686°
He I	4713.1	He I 4713*
N III	4858.7, 4859.0, 4861.3 4867.1, 4867.2, 4873.6	Hβ
He II	4859.1	Hβ
H I	4861.4	Hβ
He I	4921.9	He I 4922
He I	5015.7	He I 5015
He II	5411.3	He II 5411
O III	5592.4	O III 5592
C III	5695.9	C III 5696
C IV	5801.3, 5812.0	C IV 5801
He I	5875.6	He I 5875
He II	6527.1	He II 6527
He II	6559.8	Hα
H I	6562.8	H$\alpha^{\dagger\dagger}$
He I	6678.2	He II 6683
He II	6682.8	He II 6683
He I	7065.2	He I 7065

†) C IV 1169 and C III 1176 can be blended.
‡) O II lines are only included in cooler stars.
○) He II 4685.6 is also included in the C III-N III 4634-4651 complex if the He feature shows strong emission.
*) He I 4713 is merged with He II 4686 if the latter line shows strong emission.
††) H I at 6562.8 is also included in He II 6527.

stellar properties. As input we use the luminosity, temperature, and an upper limit of $v \sin i$ in combination with the SMC evolutionary tracks of (Brott et al. 2011). We use an upper limit for the rotation as we do not include macro turbulence in our modelling (e.g., Simón-Díaz et al. 2017). Therefore, the rotational velocity could be lower than we find. The inferred temperature and luminosity of AV 15, AV 70, and AV 80 are not covered by the SMC model grid of Brott et al. (2011), and we therefore use the LMC grids of Brott et al. (2011) and Köhler et al. (2015) instead. We use the default BONNSAI settings with the exception of the prior for the initial rotation velocity, for which we use the distribution of Ramírez-Agudelo et al. (2013).

5.4 Results

Tables 5.4 and 5.5 show the best fit stellar atmosphere parameters and derived parameters along with their uncertainty. For completeness we include the spectroscopic mass M_{spec}, the number of H I, He I, and He II ionizing photons (Q_0, Q_1, and Q_2, respectively), and the Eddington factor for electron scattering $\Gamma_{\mathrm{Edd,e}}$ in Table 5.5, we do not further discuss these parameters. The helium surface abundance y_{He} and the projected rotational velocity $v \sin i$ are the result of the optical-only fit. All other parameters are from the optical + UV fit. The remainder of the best fit parameters of the optical only fits, which are not the focus of this paper, can be found in Appendix IV.1. Table 5.6 shows the best fit mass-loss and wind structure parameters and their uncertainties. Figs. 5.1 and 5.2 show an overview of the diagnostic lines and line complexes and their fits. More detailed figures of the line profiles and fit results can be found in Appendix IV.4. Below we describe the general fits for the UV and wind lines in Sect. 5.4.1, and optical lines in Sect. 5.4.2. In Sect. 5.4.3 we comment on some poorer fits.

5.4.1 UV and wind lines

Overall the UV lines are well reproduced by the models, with the exception of the phosphorus lines. The optical wind sensitive lines are generally reproduced reasonably well. The fits are described per line group below.

Phosphorus The P V lines at 1118 and 1128 Å are in absorption in all of the sources. The two components of the doublet are very sensitive to the mass-loss properties and temperature of the star. For AV 15, AV 95, AV 207, and AV 307 the best fit line profiles match the observations very well. For the other stars, the best fitting results show a stronger in-filling of the line core or even the start of P-Cygni shapes.

UV Carbon lines The C IV 1550 doublet resonance lines are well reproduced by the models, with clear P-Cygni wind profiles for most stars. The two components of the C IV 1169 and six components of the C III 1176 lines are generally photospheric, with the C IV lines typically being relatively weak. The C III line complex only shows clear wind signatures for AV 83 and AV 372. The photospheric profiles are typically well reproduced, with some exceptions where the model shows some emission from the wind. In those cases, notably AV 479, AV 70, and to a limited extent AV 469, the produced absorption feature is not strong enough.

UV Oxygen lines Only O IV 1340 is modelled in the UV, as in our sample none of the stars show strong or clear O V 1371 lines. The O IV 1340 line, consisting of three transitions, is dominated by the photospheric component for all stars in the sample, with only some blue-shifted absorption for some of the stars. Typically, the lines are well reproduced, however in some cases the best fit model results in a too weak absorption profile, particularly for the blue component.

UV Silicon lines The Si III 1113 line is photospheric for all stars, and in most cases well reproduced by the model. The Si IV 1400 doublets typically show both photospheric and wind features. The line profile resulting from the wind is well reproduced. However, the photospheric component is often underestimated by the model. This could be due to contamination by the superimposed interstellar absorption feature, which is difficult to distinguish from the stellar feature and therefore not clipped from the data.

Helium The He II 1640 line is blended with iron lines on the blue side of the profile, therefore only the red wing can be properly fitted with FASTWIND. Only AV 80 and AV 83 show P-Cygni profiles for this line, which are reasonably well reproduced.

Optical emission lines The main optical wind diagnostics are He II 4686 and Hα. Whereas the main UV wind lines are resonances lines, these are recombination lines. The combination of the two types of lines is essential for constraining the clumping parameters of the wind. The He II 4686 line has proved hard to reproduce in this work. Often the exact strength of the line is not recovered, with a slightly too strong central absorption component. The most extreme case of this is AV 479, where we find a significantly stronger absorption component than is observed. 2dFS 163 shows only a very weak and broad absorption, while the best fit model features a significant emission profile. The Hα lines are typically reproduced quite well within uncertainties. We note that AV 372 and AV 70 show complex line shapes for the hydrogen and helium lines, which are not fully recovered by the model, but the strength of the features are recovered within the uncertainty. The complex of C III and N III lines is well reproduced. These lines are very sensitive to various other stellar parameters, such at temperature and gravity, therefore the uncertainties on the model profiles are substantial, as indicated by the shaded region.

5.4.2 Optical absorption lines

Below is a description of the overall fit of several groups of absorption lines in the optical spectra. Their widths are generally well reproduced, suggesting the $v \sin i$ (combined with macro-turbulence) has been properly determined using the optical only fit.

Hydrogen The hydrogen lines Hβ through Hϵ are recovered nicely with the models, including the wings that are sensitive to the surface gravity of the stars.

Helium The helium lines, good indicators of the accuracy of the temperature determination, fit the observations well, with the exception of 2dFS 163 and AV 327. The observations of both stars show stronger He II lines than the best fit models, suggesting that the temperature is too low. However, the rest of the diagnostics prevent a higher temperature to result in a better overall fit.

Nitrogen, Carbon, Oxygen, Silicon The optical nitrogen and carbon lines are typically well reproduced. The same holds for oxygen, where the O III 5592 line is consistent with the data, and the weak O III and O II lines in blends with other lines are reproduced within the uncertainties. These uncertainties are, however, relatively large, which we tentatively ascribe to the strong temperature sensitivity of these lines. These considerations, combined with the fact that only few lines could be used in the analysis, results in rather large uncertainties on the oxygen abundance.

The silicon lines, located in the wings of Hδ, are reproduced with varying success. The lines are very sensitive to temperature, gravity and mass loss, resulting in both emission and absorption profiles depending on their value. The observed strength of the line therefore varies significantly. This resulted in rather poor fits for AV 83, AV 207, and AV 479.

5.4.3 Anomalous fits

FASTWIND successfully reproduces the observed spectra for most stars, however for a few stars some spectral features could not be fully matched with the model. For three of stars (AV 70, AV 83, and 2dFS 163) the mismatch between model and observation was too significant to consider the inferred stellar parameters to be representative of the source.

2dFS 163 The observed N IV 3480 lines of 2dFS 163 are significantly stronger than those calculated by FASTWIND. Additionally, the strength of He II lines is systematically underpredicted by the model, except for He II 4686. This wind-sensitive line is almost absent in the observed spectrum, but the model predicts a strong emission. The emission is the result of the high clumping factor and mass loss required to reproduce the other wind sensitive lines. This likely also prevented the temperature from increasing further to allow the strength of the He II lines to match the observations, as a higher temperature would result in even stronger emission in He II 4686. Furthermore, the hydrogen and He I lines appear slightly blue shifted, while this does not seem to be the case for the other lines. The He I lines also appear slightly more narrow than the other lines, suggesting a different rotation rate. The Hα line (see Fig. 5.1) is double peaked, as are the Paschen lines, not displayed here. Taken together, we suspect 2dFS 163 to be a composite source. Therefore, this source is left out of further analysis and is marked with a red outline in figures.

AV 83 The spectrum of AV 83 is likely composite. It shows a feature in the red wing of the He II 5411 line that is also visible in the spectrum used by Hillier et al. (2003), but shifted in wavelength resulting in a broad line. The optical He II, C IV, and N IV lines all appear slightly red-shifted compared to the other lines. Some He I lines and the optical Si IV lines show emission that is not reproduced by the model. As a result the best fit parameters of this star are likely not representative of its properties. This source is left out of further analysis and is marked with a red outline in figures.

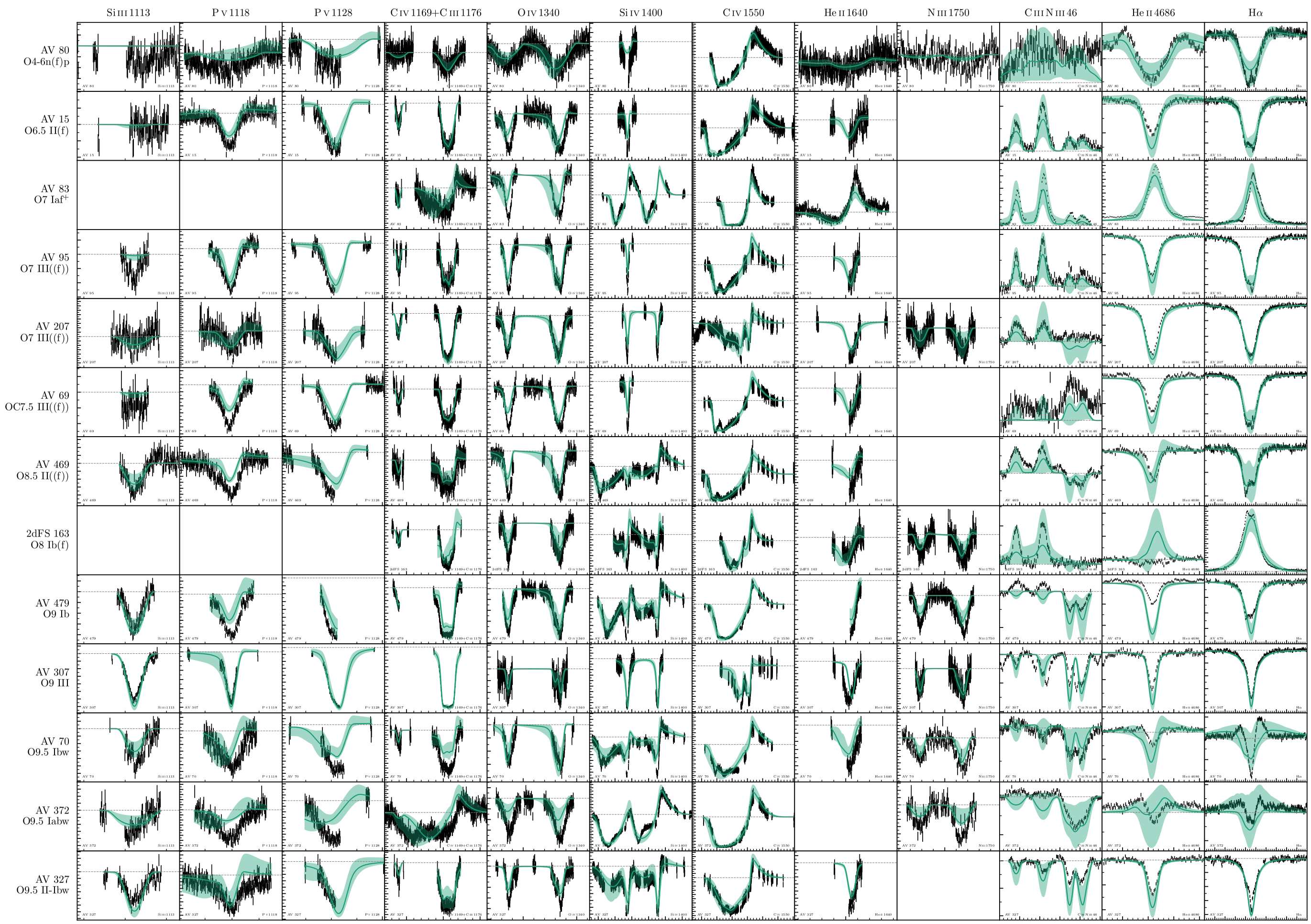

Figure 5.1: Overview of the best fits of the UV and wind sensitive optical lines. The normalized observed data is plotted as black vertical bars with the size of the bar indicating the 1 σ uncertainty on the data. The green line indicates the best fit model and the shaded region is the 1 σ confidence interval of the models. The thin dashed grey lines are at unity. The major ticks on the x-axis indicate steps of 5 Å, and the minor ticks indicate steps of 1 Å. On the y-axis the major ticks indicate steps of 10% of the continuum and the minor ticks indicate 5%. A more detailed figure of the line profiles can be found in Appendix IV.4.

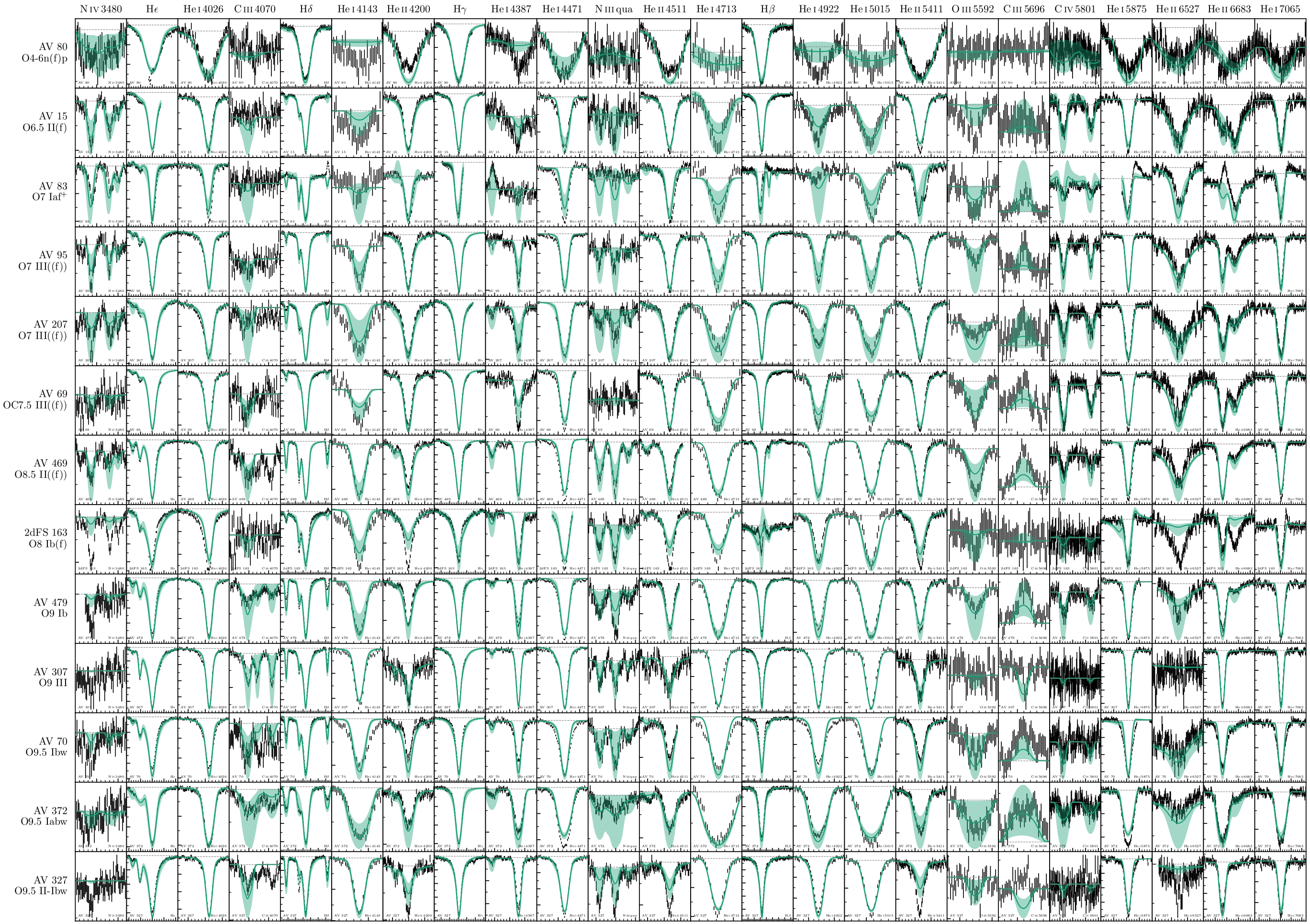

Figure 5.2: As Figure 5.1, but for optical lines of mostly photospheric origin.

AV 70 The He I lines in the spectrum of AV 70 show a broad component, which is not visible in other lines nor is it reproduced by the model. The broad component could suggest the presence of a rapidly rotating cooler companion. This is backed by the apparent flat-bottomed C IV 1550 absorption trough of the P-Cygni profile, for which the flux remains at 30% of the continuum at the bottom. For this reason the star is left out of further analysis and is marked red in figures.

AV 307 Additional absorption lines can be seen in the C III -N III 4630-4655 complex of AV 307. These extra lines coincide with transitions of O II, however, these lines are not observed in any of the other stars in the sample with the exception of AV 327, though in that star the O II lines are considerably weaker. Closer inspection shows the spectrum of AV 307 to be rich in O II lines. AV 307 and AV 327 are the coolest stars in the sample, both with $T_{\rm eff} = 29\,500\,{\rm K}$, and feature the lowest $v \sin i$, with 55 and 80 $\rm km\,s^{-1}$. The abundance of oxygen is found to be higher in AV 327, mainly based on the strength of O IV 1340.

AV 479 The He I and He II lines of AV 479 fit well within the uncertainties, with the exception of He II 4686 for which the best fit model displays a significantly stronger absorption than the observations. The Hα line shows a slightly too strong absorption feature in the model. So, a consistent spectral fit for both the UV and optical wind signatures does not appear feasible: the Si IV 1400 and C IV 1550 lines are fitting well, at the expense of Hα and He II 4686. Therefore, a higher mass loss would be at the expense of the fit quality of the two ultraviolet lines. Similarly, the fit to the optical wind lines could benefit from a higher clumping factor. However, this would affect the ionization structure of Si and C, resulting in a worse fit for the Si IV 1400 and C III 1176 lines. Alternatively, an earlier onset of clumping, i.e., a lower value for $v_{\rm cl,start}$, could also improve the line fits of Hα and He II 4686. Again, this is disfavored for the ultraviolet wind lines.

5.5 Discussion

The main part of this discussion focuses on mass-loss properties of the SMC sample in contrast to comparable samples in the Milky Way and LMC, such as to probe the dependence of mass loss on metallicity. However, we start with a brief discussion of other derived properties such as to better characterize the target stars and their evolutionary state.

5.5.1 Evolutionary state

Figure 5.3 presents our sample of giants, bright giants, and supergiants in the Hertzsprung-Russell Diagram (HRD). The figure shows that though the sample covers a substantial part of the $(T_{\rm eff}, L)$ plane, they all have moved away from the zero-age main sequence, and have ages ranging from approximately 2 to 6 Myr. For three stars (AV 83, 2dFS 163, and AV 70; see also Section 5.4.3) we were not able to determine reliable parameters. While we do present their best fit values, these sources are not considered in the mass-loss rate and clumping analysis that is the topic of the next subsections. In Fig. 5.3, and also in Figs. 5.5 to 5.7 later in this section, these sources are marked with a red border.

Table 5.4: Stellar atmosphere best fit parameters and 1σ uncertainties. Rows with gray text indicate parameter values that are likely not representative of the stellar properties.

Source	$T_{\rm eff}$ [K]	$\log g$	$v \sin i$ [km s^{-1}]	$y_{\rm He}$	$\epsilon_{\rm C}$	$\epsilon_{\rm N}$	$\epsilon_{\rm O}$	$\epsilon_{\rm Si}$	$\epsilon_{\rm P}$
AV 80	41500^{+1250}_{-750}	$3.88^{+0.12}_{-0.10}$	305^{+25}_{-20}	$0.08^{+0.02}_{-0.01}$	$7.7^{+0.1}_{-0.6}$	$7.5^{+0.5}_{-0.2}$	$7.5^{+0.7}_{-0.5}$	$6.7^{+0.5}_{-0.7}$	$3.6^{+0.8}_{-0.2}$
AV 15	39750^{+1250}_{-1500}	$3.70^{+0.10}_{-0.12}$	110^{+10}_{-10}	$0.10^{+0.01}_{-0.01}$	$7.8^{+0.3}_{-0.3}$	$7.8^{+0.4}_{-0.1}$	$7.5^{+0.6}_{-0.6}$	$7.0^{+0.3}_{-0.9}$	$4.3^{+0.2}_{-0.8}$
AV 83	36000^{+1250}_{-1250}	$3.24^{+0.34}_{-0.10}$	80^{+45}_{-20}	$0.18^{+0.06}_{-0.05}$	$7.8^{+0.5}_{-0.7}$	$8.7^{+0.3}_{-0.3}$	$7.8^{+0.3}_{-0.7}$	$8.0^{+0.3}_{-0.5}$	...
AV 95	38250^{+1000}_{-1000}	$3.64^{+0.08}_{-0.12}$	75^{+10}_{-10}	$0.14^{+0.01}_{-0.02}$	$7.5^{+0.3}_{-0.4}$	$7.8^{+0.3}_{-0.4}$	$8.2^{+0.5}_{-0.4}$	$6.6^{+0.6}_{-0.5}$	$4.5^{+0.5}_{-0.6}$
AV 207	38000^{+1250}_{-750}	$3.82^{+0.28}_{-0.12}$	110^{+10}_{-15}	$0.12^{+0.01}_{-0.03}$	$7.7^{+0.4}_{-0.3}$	$7.7^{+0.7}_{-0.6}$	$8.6^{+0.3}_{-0.7}$	$8.1^{+0.4}_{-0.7}$	$5.0^{+1.4}_{-1.9}$
AV 69	36750^{+1000}_{-1250}	$3.50^{+0.16}_{-0.08}$	100^{+10}_{-15}	$0.09^{+0.03}_{-0.01}$	$7.6^{+0.2}_{-0.3}$	$6.4^{+0.8}_{-0.4}$	$8.2^{+0.2}_{-0.5}$	$6.5^{+0.7}_{-0.5}$	$4.1^{+0.3}_{-0.8}$
AV 469	34500^{+1000}_{-1000}	$3.36^{+0.08}_{-0.14}$	85^{+10}_{-10}	$0.20^{+0.03}_{-0.04}$	$7.5^{+0.3}_{-0.2}$	$8.2^{+0.3}_{-0.2}$	$8.1^{+0.8}_{-0.2}$	$7.8^{+0.3}_{-0.2}$	$4.0^{+0.5}_{-0.9}$
2dFS 163	36500^{+250}_{-1250}	$4.14^{+0.02}_{-0.40}$	90^{+35}_{-35}	$0.08^{+0.05}_{-0.01}$	$6.8^{+0.3}_{-0.2}$	$8.0^{+0.3}_{-0.6}$	$7.2^{+0.7}_{-0.6}$	$6.1^{+0.5}_{-0.1}$	...
AV 479	33250^{+1500}_{-1000}	$3.42^{+0.06}_{-0.24}$	90^{+15}_{-5}	$0.13^{+0.04}_{-0.01}$	$7.5^{+0.2}_{-0.2}$	$7.3^{+0.2}_{-0.4}$	$8.2^{+0.4}_{-0.3}$	$7.8^{+0.4}_{-0.1}$	$4.0^{+0.5}_{-0.8}$
AV 307	29500^{+250}_{-250}	$3.46^{+0.16}_{-0.04}$	55^{+15}_{-10}	$0.11^{+0.01}_{-0.03}$	$7.8^{+0.2}_{-0.1}$	$7.7^{+0.3}_{-0.3}$	$7.8^{+0.5}_{-0.1}$	$7.1^{+0.1}_{-0.2}$	$5.5^{+0.8}_{-1.4}$
AV 70	33750^{+500}_{-250}	$3.54^{+0.08}_{-0.06}$	120^{+15}_{-15}	$0.15^{+0.04}_{-0.01}$	$7.2^{+0.1}_{-0.2}$	$7.7^{+0.1}_{-0.8}$	$7.8^{+0.1}_{-0.8}$	$7.3^{+0.4}_{-0.1}$	$3.5^{+1.1}_{-0.5}$
AV 372	30750^{+1500}_{-1250}	$3.10^{+0.16}_{-0.12}$	155^{+15}_{-5}	$0.17^{+0.03}_{-0.03}$	$7.7^{+0.2}_{-0.2}$	$7.7^{+0.8}_{-0.9}$	$8.2^{+0.8}_{-1.2}$	$7.7^{+0.2}_{-0.9}$	$3.2^{+0.9}_{-0.2}$
AV 327	29500^{+250}_{-1000}	$3.28^{+0.18}_{-0.08}$	80^{+10}_{-15}	$0.15^{+0.01}_{-0.04}$	$8.0^{+0.2}_{-0.2}$	$7.7^{+0.7}_{-0.3}$	$8.8^{+0.2}_{-0.6}$	$7.3^{+0.2}_{-0.2}$	$5.0^{+0.8}_{-1.5}$

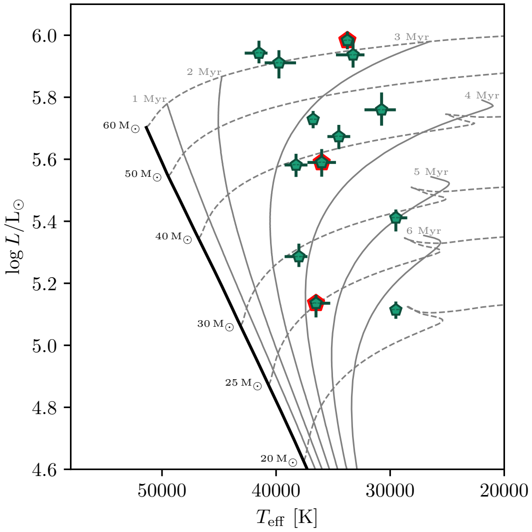

Figure 5.3: Hertzsprung-Russell Diagram of our SMC sample of stars with temperatures and luminosities resulting from fitting. Points with a red border indicate stars with unreliable parameters. Overplotted are the evolutionary tracks (thin solid grey lines) and isochrones (thin dashed grey lines) of Brott et al. (2011). The solid black line indicates the zero age main-sequence. The points are labeled with the name of the object in a small font, visible when zoomed in.

Table 5.5: Derived parameters based on the Fastwind/GA fitting. Rows with gray text indicate parameter values that are likely not representative of the stellar properties.

Source	$\log L/\mathrm{L}_\odot$	$R\,[\mathrm{R}_\odot]$	$M_\mathrm{spec}\,[\mathrm{M}_\odot]$	$\log Q_0$	$\log Q_1$	$\log Q_2$	$\Gamma_\mathrm{Edd,e}$	$M_\mathrm{evo}\,[\mathrm{M}_\odot]$	$M_\mathrm{ini}\,[\mathrm{M}_\odot]$	Age [Myr]
AV 80	$5.94^{+0.04}_{-0.03}$	$18.26^{+0.60}_{-0.63}$	$92.3^{+21.8}_{-16.6}$	$49.66^{+0.06}_{-0.05}$	$48.95^{+0.08}_{-0.05}$	$43.40^{+0.20}_{-1.14}$	$0.25^{+0.05}_{-0.04}$	$62.0^{+4.0}_{-2.8}$	$66.4^{+3.7}_{-3.4}$	$2.0^{+0.1}_{-0.2}$
AV 15	$5.91^{+0.04}_{-0.05}$	$19.20^{+0.70}_{-0.67}$	$67.4^{+12.2}_{-13.5}$	$49.62^{+0.05}_{-0.08}$	$48.83^{+0.07}_{-0.12}$	$42.72^{+0.10}_{-0.91}$	$0.32^{+0.07}_{-0.04}$	$57.8^{+3.3}_{-3.8}$	$61.6^{+3.8}_{-4.1}$	$2.3^{+0.2}_{-0.1}$
AV 83	$5.59^{+0.04}_{-0.05}$	$16.17^{+0.58}_{-0.57}$	$16.6^{+17.8}_{-2.8}$	$49.32^{+0.06}_{-0.10}$	$48.41^{+0.09}_{-0.16}$	$41.55^{+0.16}_{-0.78}$	$0.63^{+0.09}_{-0.32}$	$37.2^{+1.7}_{-2.1}$	$38.0^{+2.1}_{-2.0}$	$3.5^{+0.2}_{-0.2}$
AV 95	$5.58^{+0.04}_{-0.04}$	$14.19^{+0.48}_{-0.48}$	$32.1^{+5.2}_{-6.4}$	$49.24^{+0.06}_{-0.07}$	$48.37^{+0.08}_{-0.11}$	$41.35^{+0.61}_{-0.09}$	$0.32^{+0.05}_{-0.04}$	$38.0^{+1.8}_{-1.6}$	$39.0^{+1.8}_{-1.8}$	$3.2^{+0.2}_{-0.2}$
AV 207	$5.29^{+0.04}_{-0.03}$	$10.23^{+0.34}_{-0.36}$	$25.2^{+19.5}_{-5.4}$	$48.88^{+0.08}_{-0.06}$	$47.98^{+0.13}_{-0.12}$	$42.18^{+0.29}_{-0.46}$	$0.21^{+0.05}_{-0.08}$	$29.2^{+1.2}_{-1.0}$	$29.6^{+1.2}_{-1.0}$	$3.7^{+0.2}_{-0.4}$
AV 69	$5.73^{+0.04}_{-0.05}$	$18.21^{+0.65}_{-0.62}$	$38.3^{+13.6}_{-5.5}$	$49.38^{+0.04}_{-0.07}$	$48.48^{+0.07}_{-0.13}$	$41.53^{+0.65}_{-0.15}$	$0.38^{+0.06}_{-0.08}$	$43.8^{+2.1}_{-1.0}$	$45.8^{+1.7}_{-1.7}$	$3.1^{+0.1}_{-0.1}$
AV 469	$5.67^{+0.04}_{-0.04}$	$19.39^{+0.66}_{-0.66}$	$31.4^{+4.3}_{-7.3}$	$49.23^{+0.05}_{-0.04}$	$48.04^{+0.13}_{-0.08}$	$41.44^{+0.08}_{-0.07}$	$0.40^{+0.08}_{-0.04}$	$39.6^{+2.5}_{-1.4}$	$41.2^{+2.3}_{-1.9}$	$3.5^{+0.1}_{-0.1}$
2dFS 163	$5.14^{+0.03}_{-0.05}$	$9.33^{+0.33}_{-0.30}$	$43.8^{+2.8}_{-25.1}$	$48.59^{+0.06}_{-0.08}$	$47.53^{+0.13}_{-0.16}$	$40.35^{+0.48}_{-0.14}$	$0.08^{+0.10}_{-0.00}$	$24.4^{+0.8}_{-1.0}$	$24.6^{+0.8}_{-1.0}$	$4.4^{+0.4}_{-0.1}$
AV 479	$5.94^{+0.05}_{-0.04}$	$28.27^{+0.97}_{-1.07}$	$76.7^{+6.3}_{-29.7}$	$49.38^{+0.13}_{-0.03}$	$47.92^{+0.42}_{-0.03}$	$41.56^{+0.24}_{-0.03}$	$0.30^{+0.16}_{-0.00}$	$55.6^{+1.2}_{-2.4}$	$58.6^{+1.3}_{-2.6}$	$2.8^{+0.1}_{-0.1}$
AV 307	$5.11^{+0.03}_{-0.03}$	$13.93^{+0.45}_{-0.45}$	$20.4^{+7.9}_{-1.6}$	$47.95^{+0.03}_{-0.12}$	$45.35^{+0.05}_{-0.12}$	$41.63^{+0.06}_{-0.12}$	$0.17^{+0.01}_{-0.05}$	$21.6^{+0.6}_{-0.6}$	$21.8^{+0.6}_{-0.6}$	$6.5^{+0.2}_{-0.2}$
AV 70	$5.98^{+0.03}_{-0.03}$	$28.95^{+0.93}_{-0.93}$	$106.0^{+17.1}_{-11.5}$	$49.43^{+0.04}_{-0.04}$	$48.10^{+0.10}_{-0.12}$	$41.67^{+0.04}_{-0.08}$	$0.24^{+0.02}_{-0.03}$	$60.0^{+2.6}_{-2.5}$	$65.2^{+3.2}_{-2.7}$	$2.5^{+0.1}_{-0.1}$
AV 372	$5.76^{+0.06}_{-0.05}$	$26.95^{+1.00}_{-1.05}$	$33.4^{+10.9}_{-6.7}$	$49.18^{+0.13}_{-0.09}$	$47.36^{+0.57}_{-0.44}$	$41.32^{+0.18}_{-0.22}$	$0.46^{+0.08}_{-0.07}$	$42.6^{+3.6}_{-2.4}$	$44.8^{+3.5}_{-3.0}$	$3.5^{+0.2}_{-0.2}$
AV 327	$5.41^{+0.03}_{-0.04}$	$19.60^{+0.69}_{-0.63}$	$26.7^{+12.0}_{-3.8}$	$48.40^{+0.07}_{-0.27}$	$45.77^{+0.07}_{-0.43}$	$42.08^{+0.03}_{-0.76}$	$0.26^{+0.04}_{-0.08}$	$28.4^{+0.9}_{-1.4}$	$29.0^{+1.0}_{-1.3}$	$5.1^{+0.2}_{-0.2}$

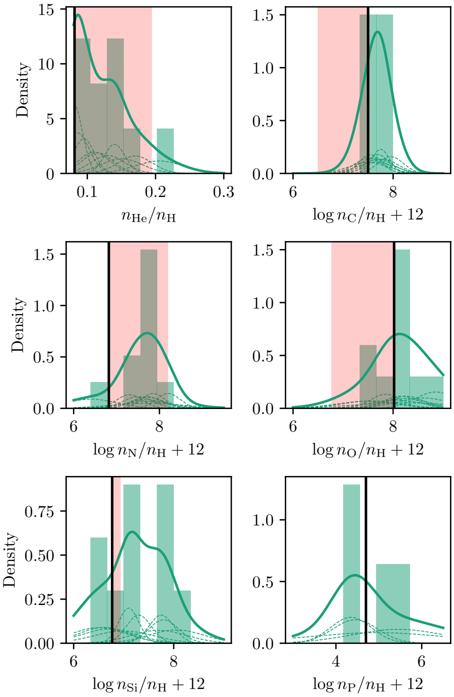

Figure 5.4: Distribution of surface abundances of He, C, N, O, Si, and P from FASTWIND/GA fitting of SMC stars. The green solid line indicates an approximate kernel density estimate of the distribution taking into account the uncertainties on the best fit values. The thin dashed lines show the contribution of the individual sources. The black vertical line shows the baseline abundances from Dopita et al. (2019) for all elements except phosphorus, for which we show the scaled (by 0.2) solar abundance from Asplund et al. (2009). The area marked in red shows the surface depletion or enrichment that can be expected due to mixing based on the evolution of a 40 $\mathrm{M}_{\odot}$ star with an initial rotation of 387 $\mathrm{km\,s^{-1}}$ (Brott et al. 2011). This figure only includes phosphorus abundances when these were constrained. The helium abundances are taken from the optical only fit, all others are from the optical + UV fit.

Table 5.6: Wind structure best fit parameters and 1σ uncertainties. Rows with gray text indicate parameter values that are likely not representative of the wind properties of that star.

Source	$\log \dot{M}$	v_∞ [km s^{-1}]	β	$f_{\rm cl}$	$\log f_{\rm ic}$	$f_{\rm vel}$	$v_{\rm cl,start}/v_\infty$	$v_{\rm windturb}/v_\infty$
AV 80	$-6.24^{+0.05}_{-0.15}$	1775^{+100}_{-50}	$1.35^{+0.60}_{-0.20}$	30^{+17}_{-8}	$-1.6^{+0.3}_{-0.3}$	$0.70^{+0.16}_{-0.16}$	$0.14^{+0.06}_{-0.03}$	$0.01^{+0.07}_{-0.01}$
AV 15	$-6.17^{+0.20}_{-0.23}$	2250^{+125}_{-100}	$1.60^{+0.40}_{-0.35}$	7^{+32}_{-6}	$-2.0^{+0.6}_{-0.1}$	$0.68^{+0.10}_{-0.32}$	$0.16^{+0.10}_{-0.12}$	$0.04^{+0.03}_{-0.05}$
AV 83	$-6.12^{+0.28}_{-0.18}$	1025^{+75}_{-125}	$1.75^{+0.75}_{-0.40}$	8^{+14}_{-5}	$-1.1^{+0.8}_{-0.7}$	$0.82^{+0.14}_{-0.48}$	$0.08^{+0.10}_{-0.02}$	$0.13^{+0.09}_{-0.06}$
AV 95	$-7.12^{+0.20}_{-0.33}$	1850^{+125}_{-75}	$1.50^{+0.70}_{-0.35}$	20^{+29}_{-12}	$-1.4^{+0.7}_{-0.7}$	$0.70^{+0.20}_{-0.26}$	$0.01^{+0.03}_{-0.01}$	$0.03^{+0.07}_{-0.04}$
AV 207	$-7.65^{+0.15}_{-0.55}$	1775^{+275}_{-550}	$1.85^{+0.40}_{-1.10}$	2^{+18}_{-2}	$-1.1^{+0.4}_{-0.9}$	$0.22^{+0.22}_{-0.22}$	$0.01^{+0.23}_{-0.01}$	$0.26^{+0.04}_{-0.18}$
AV 69	$-6.72^{+0.25}_{-0.30}$	1850^{+75}_{-25}	$1.40^{+1.10}_{-0.25}$	12^{+36}_{-3}	$-1.1^{+0.6}_{-0.3}$	$0.46^{+0.24}_{-0.36}$	$0.01^{+0.23}_{-0.01}$	$0.05^{+0.03}_{-0.05}$
AV 469	$-6.27^{+0.25}_{-0.08}$	2025^{+150}_{-50}	$1.10^{+0.10}_{-0.35}$	12^{+19}_{-1}	$-1.4^{+0.3}_{-0.5}$	$0.54^{+0.04}_{-0.32}$	$0.01^{+0.04}_{-0.01}$	$0.08^{+0.07}_{-0.03}$
2dFS 163	$-6.70^{+0.13}_{-0.03}$	1025^{+175}_{-100}	$1.70^{+0.55}_{-0.35}$	50^{+1}_{-13}	$-1.4^{+0.1}_{-0.5}$	$0.24^{+0.14}_{-0.12}$	$0.09^{+0.04}_{-0.03}$	$0.20^{+0.10}_{-0.06}$
AV 479	$-6.27^{+0.25}_{-0.43}$	1650^{+25}_{-175}	$0.90^{+0.05}_{-0.30}$	11^{+20}_{-8}	$-1.3^{+0.4}_{-0.1}$	$0.06^{+0.24}_{-0.06}$	$0.09^{+0.01}_{-0.05}$	$0.15^{+0.09}_{-0.03}$
AV 307	$-8.21^{+0.13}_{-0.25}$	2625^{+100}_{-400}	$0.90^{+0.35}_{-0.25}$	4^{+8}_{-3}	$-1.2^{+0.7}_{-0.5}$	$0.04^{+0.80}_{-0.04}$	$0.12^{+0.04}_{-0.11}$	$0.29^{+0.01}_{-0.19}$
AV 70	$-5.59^{+0.13}_{-0.18}$	1875^{+425}_{-50}	$0.90^{+0.15}_{-0.20}$	14^{+3}_{-9}	$-1.9^{+0.1}_{-0.1}$	$0.02^{+0.22}_{-0.02}$	$0.07^{+0.01}_{-0.03}$	$0.18^{+0.08}_{-0.12}$
AV 372	$-6.02^{+0.30}_{-0.18}$	1650^{+100}_{-100}	$1.80^{+0.50}_{-0.45}$	7^{+21}_{-3}	$-1.1^{+0.4}_{-0.3}$	$0.74^{+0.10}_{-0.48}$	$0.12^{+0.11}_{-0.05}$	$0.24^{+0.06}_{-0.07}$
AV 327	$-7.41^{+0.15}_{-0.38}$	1650^{+300}_{-175}	$0.80^{+0.25}_{-0.25}$	3^{+15}_{-1}	$-1.0^{+0.5}_{-0.6}$	$0.50^{+0.18}_{-0.30}$	$0.23^{+0.07}_{-0.04}$	$0.29^{+0.01}_{-0.05}$

Figure 5.4 shows the derived surface abundances for He, C, N, O, Si, and P. Plotted as well are the SMC baseline abundances following Dopita et al. (2019) for all elements save phosphorous, for which we scaled the Asplund et al. (2009) solar abundances by a factor 1/5. Shown as well are indications of the expected surface abundances, using an initially 40 $M_\odot$ SMC model rotating at the end of formation at 389 km s^{-1} and a typical age of 3 Myr (Brott et al. 2011). For the rotational velocity chosen, the range of helium abundance is well reproduced, though we remark that for lower initial spin rotation-induced mixing is less efficient, hence, $y_{\rm He}$ is only marginally enriched ($y_{\rm He} < 0.1$). The range of nitrogen abundance is well reproduced. C and O abundances are slightly above baseline, albeit with large uncertainties, while depletion is expected. Mixing is not expected to affect silicon and phosphorus. The surface abundances of these elements are poorly constrained; for silicon they are typically above baseline and for phosphorous they cluster around baseline. The latter may be an effect of the sampling. Due to the limited effect of the surface abundance on the strength of the P v doublet the sampling is close to uniform. For example, AV 307 has an excellent fit to the P v lines, but an unconstrained phosphorus abundance due to the dependence on, among other parameters, temperature. Possibly, this correlation is too strong to determine the abundance reliably with only one ionization stage.

We repeat that possibly 2dFS 163, AV 83 and AV 70 are binaries, see Sect. 5.4.3. They are left out of further analysis.

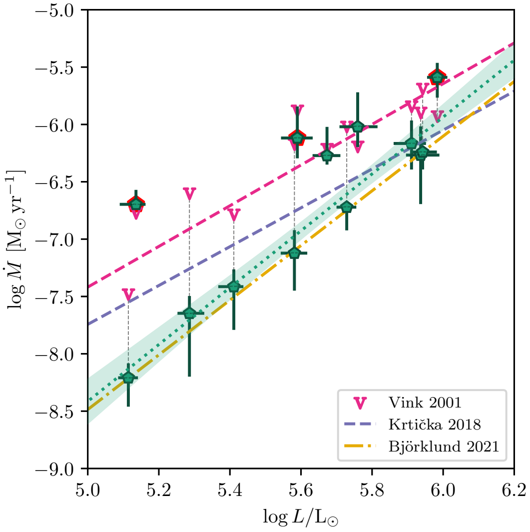

Figure 5.5: Mass-loss rate as function of luminosity. The fit to the empirical mass-loss rates and its uncertainty are indicated with the green dotted line and the shaded region, respectively. The mass-loss rate – luminosity relations of Krtička & Kubát (2018) and Björklund et al. (2021) are shown with the blue and yellow dashed lines, respectively. For the mass loss predictions of Vink et al. (2001), we put the derived parameters into equation (24) of the latter authors to get predicted rates for each star. The magenta ”V” symbols indicate these rates, and the magenta dashed line corresponds to the fit to these points.

5.5.2 Comparison of empirical and predicted mass-loss rates

Following previous works, we will use modified wind momentum as our preferred property in comparing mass-loss characteristics with theory and other empirical samples. This will be the subject of Sect. 5.5.3. Here, however, we first briefly show how the mass-loss rates in our sample compare to predictions for SMC stars.

Figure 5.5 shows the mass-loss rate as function of luminosity, compared to the mass-loss rate predictions of Vink et al. (2001); Krtička & Kubát (2018); Björklund et al. (2021); for the SMC metallicity we assume 20% of solar for all predictions, following Mokiem et al. (2007). The dotted line indicates a linear fit to the empirical mass-loss rates using orthogonal distance regression (ODR, Boggs et al. 1987), given by:

$$\log \dot{M} = (-20.81 \pm 1.48) + (2.48 \pm 0.26) \times \log(L/L_\odot). \tag{5.5}$$

The luminosity dependence that we find is stronger that of the theoretical predictions that are shown in the figure. Overal, the Björklund et al. (2021) mass-loss rate–luminosity relation agrees best with the empirical mass-loss rate from our sample. Vink et al. (2001) and Krtička & Kubát (2018) predict higher mass-loss rates at low luminosity, with the discrepancy decreasing toward higher luminosity. In Section 5.5.3 we investigate the metallicity dependence of the mass-loss rate.

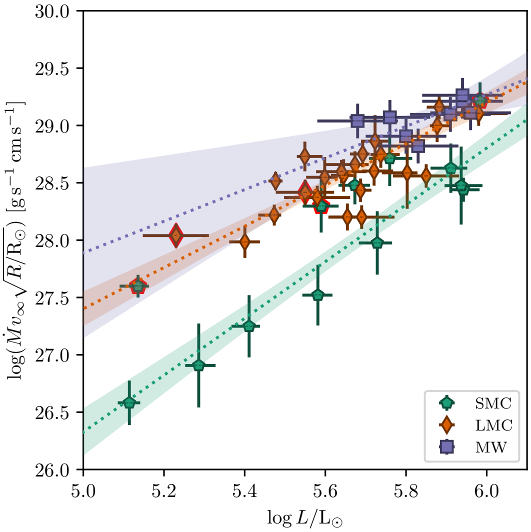

Figure 5.6: Modified wind momentum as function of luminosity for samples of SMC (this work), LMC (Brands et al. in prep.; Hawcroft et al. in prep.) and Galactic stars (Hawcroft et al. 2021). The dotted lines indicate the linear fits to each sub sample.

5.5.3 The dependence of modified wind momentum on luminosity and metallicity

To empirically test the relation between mass loss, luminosity and metallicity, we compare the mass-loss rates of samples of Galactic (Hawcroft et al. 2021), LMC (Brands et al. in prep.; Hawcroft et al. in prep.), and SMC (this work) O III to O I stars. In these studies, the winds have been scrutinized using a FASTWIND GA-analysis of both their optical and UV spectrum in which the inhomogeneous wind structure accounts for optically thick clumping. The homogeneous nature of these analyses – they all apply the same formalism for wind inhomogeneities – allows for the best possible comparison of wind mass loss in different metallicity environments.

To isolate and quantify the impact of metallicity on mass loss from the limited size samples available one resorts to the mechanical momentum of the stellar wind, modified by a term depending on stellar radius. This property, the so-called *modified wind momentum*

$$D = \dot{M} v_\infty \sqrt{\frac{R_\star}{R_\odot}} \;\; [\mathrm{gr\,cm\,s^{-2}}], \tag{5.6}$$

is primarily a function of stellar luminosity and almost independent of stellar mass (Kudritzki et al. 1995; Kudritzki & Puls 2000). Therefore, to compare our sample with other observations and theoretical predictions, we fit the following relation through the observed values

$$\log D = \log D_0 + x \log L/L_\odot. \tag{5.7}$$

Table 5.7: Slopes, x, and offsets, $\log D_0$, of the linear fits to the modified wind momentum (Equation 5.7) of this work, Mokiem et al. (2007), and Marcolino et al. (2022).

Galaxy	x	$\log D_0$
This work		
Milky Way	1.38±0.86	20.99±5.01
LMC	1.87±0.21	18.03±1.19
SMC	2.46±0.26	13.99±1.51
Mokiem (2007)		
Milky Way	1.84±0.17	18.87±0.98
LMC	1.96±0.16	17.88±0.91
SMC	1.84±0.19	18.20±1.09
Marcolino (2022)		
Milky Way	4.16±0.23	5.43±1.28
SMC	3.85±0.29	6.67±1.52

From now on, we will refer to x as the slope, and $\log D_0$ as the offset of the modified wind momentum–luminosity relation. Fig. 5.6 shows the relation for the three samples, using ODR to constrain the fit variables x and $\log D_0$. The empirical relations a differentiated by color: purple for Galactic stars, orange for LMC stars, and green for SMC stars. Though uncertainties for the Galactic sample are sizeable, the overall trend is indeed that the wind momentum increases with metallicity. Furthermore, we find a tentative trend in the slope of the modified wind momentum–luminosity relation, with steeper slopes towards lower metallicities. Our fit values are presented in Table 5.7.

To account for a metallicity dependence of modified wind momentum we fit all three samples simultaneously with the function

$$\log D(L, Z) = \left(a + b \log \frac{Z}{Z_\odot}\right) \log \frac{L}{10^6\, L_\odot} + c \log \frac{Z}{Z_\odot} + d, \tag{5.8}$$

following Krtička & Kubát (2018) and Björklund et al. (2021), where a through d are fitting parameters. We assume $Z_{\rm MW} = {\rm Z}_\odot$, $Z_{\rm LMC} = 0.5\,{\rm Z}_\odot$, and $Z_{\rm SMC} = 0.2\,{\rm Z}_\odot$, consistent with Mokiem et al. (2007), Krtička & Kubát (2018), Björklund et al. (2021), and Marcolino et al. (2022). We take the uncertainty on the metallicity to be $\Delta \log Z/{\rm Z}_\odot = 0.1$, which is conservative considering the typical uncertainties on measured abundances (e.g. Dopita et al. 2019). Figure 5.7 shows the best fit of Equation 5.8 to the data evaluated at $Z = 1, 0.5$ and $0.2\,{\rm Z}_\odot$. The fit shows that over the large range in luminosity probed by the samples, modified wind momentum is not well represented by a luminosity independent power-law dependence on metallicity. For relatively dim stars the metallicity dependence is stronger than for relatively bright stars. Though the fit agrees nicely with the LMC and SMC data points, it slightly overestimates the wind momentum of the MW stars. The parameters a, b, c, d in Eq. (5.8) are strongly correlated, therefore their individual variances are a poor representation of their true uncertainty. The full covariance matrix of the fit can be found in Appendix IV.3.

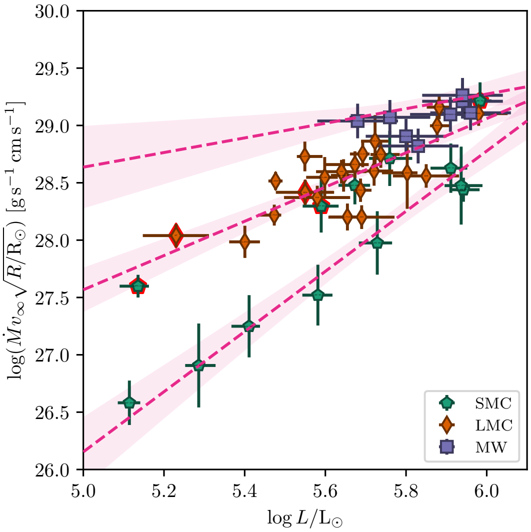

Figure 5.7: Modified wind momentum as function of luminosity and metallicity, as in Figure 5.6, but now with fitted with Equation 5.8 to the to the three samples, instead of separate linear fits for each sample. Magenta dashed lines and pink shaded indicate the best fit and the confidence interval, respectively. Equation 5.8 has been evaluated at $Z = 1.0, 0.5$, and $0.2\ \mathrm{Z}_\odot$.

Comparing the two fitting procedures, we note that the gradient in slope between the direct linear fits to the individual samples is smaller than in the combined fit, as can be seen by comparing Figures 5.6 and 5.7. This is a result of the difference in wind momentum between the Milky Way and the LMC being smaller than the same difference between the LMC and SMC stars, while in both cases the difference in metallicity is similar. As a result the 'metallicity offset' term, c in Equation 5.8, cannot accommodate both differences at once. To mitigate this the 'metallicity slope', b in Equation 5.8, is adjusted. This works because of the lack of relatively low luminosity points in the Milky Way sample. Therefore, caution is advised: our fit result for Equation 5.8 may overestimate the slope in the metallicity dependence. Additional studies of clumped winds of in particular galactic stars with luminosities $\log L/L_\odot \leq 5.6$ are needed to scrutinize this further. Alternatively, the discrepancy between the two fitting results may signal that the parameterization Equation 5.8 is not sufficiently suitable. This could possibly be helped by adding a non-linear (in log-space) metallicity term.

5.5.3.1 Comparison to other empirical studies

Figure 5.8 repeats the fitting results from Fig. 5.6 along with the best values from Mokiem et al. (2007) and Marcolino et al. (2022), who also empirically investigate the metallicity dependence of mass loss. Mokiem et al. (2007) used data from optical studies of Galactic and Magellanic Clouds stars. Mass-loss rates follow from FASTWIND analyses without considering

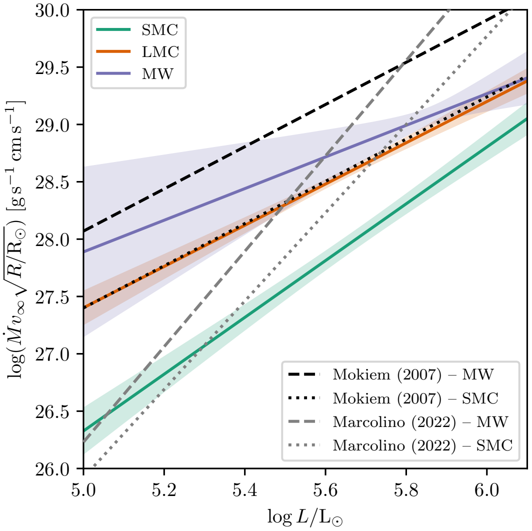

Figure 5.8: Fits to empirically determined modified wind momentum as function of luminosity. The colored solid lines show the fits to the MW, LMC, and SMC samples presented here. The black and grey dashed and dash-dotted lines indicate the modified wind momentum relations from Mokiem et al. (2007) and Marcolino et al. (2022), respectively. The values representing the fits are listed in Table 5.7.

clumping effects. Because ultraviolet diagnostics are not considered, quite a few of their relatively low luminosity sources yield only upper limits for $\dot{M}$. Marcolino et al. (2022) collect results from CMFGEN (Hillier & Miller 1998) studies that rely on both ultraviolet and optical spectra. In these MW and SMC studies an optically thin clumping prescription is used, sometimes yielding only rough estimates of the clumping factor.

Mokiem et al. (2007) estimate the metallicity dependence at only a single luminosity, i.e., $\log L/L_\odot = 5.75$, a typical mean for their sample. Near this luminosity, their slope is not too different from ours. Their wind momentum is however higher than ours, a result of Mokiem et al. not considering clumping. Marcolino et al. (2022) find a significantly steeper slope in the $D(L)$ diagram for both the MW and SMC, with a fairly comparable wind momentum at the luminosity at $\log L/L_\odot$. Interestingly, their MW and SMC curves diverge for higher luminosities while our curves converge.

We quantitatively compare to the pioneering work of Mokiem et al. (2007) by evaluating Equation 5.7 at $\log L/L_\odot = 5.75$ with the SMC, LMC, and MW coefficients as listed in Table 5.7. Under the assumptions that mass loss and terminal velocity scale as

$$\dot{M} \propto Z^m \tag{5.9}$$

and

$$v_\infty \propto Z^n, \tag{5.10}$$

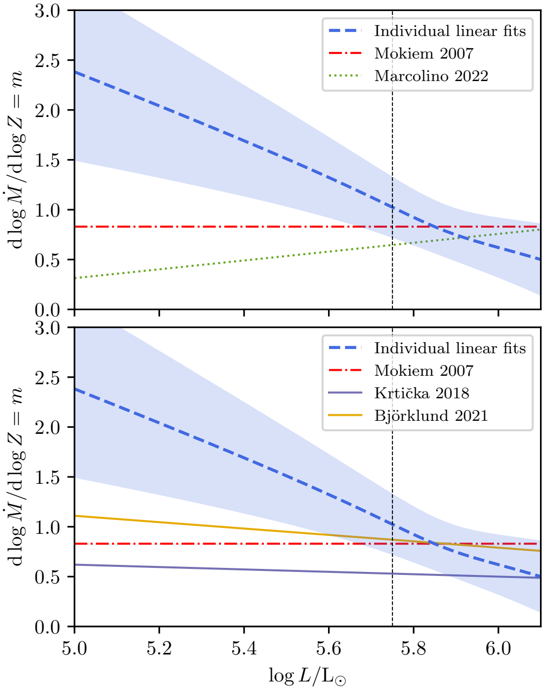

Figure 5.9: Slope of the mass-loss rate as function of metallicity, m, for different values of the luminosity. *Top* panel shows the empirical determinations of Mokiem et al. (2007) and Marcolino et al. (2022) along with our determination based on the linear fits as shown in Fig. 5.6 and Fig. 5.8. *Bottom* panel shows the predicted values of m of Krtička & Kubát (2018) and Björklund et al. (2021), along with our empirical determination. The value of $m = 0.83$ from Mokiem et al. (2007) is also shown for reference. In all cases $\mathrm{d}\log v_\infty/\mathrm{d}\log Z = n = 0.13$ is assumed (Leitherer et al. 1992).

such that

$$m + n = \frac{d\log D_{\mathrm{mom}}}{d\log Z}, \tag{5.11}$$

with $n = 0.13$ (Leitherer et al. 1992), we find from an ODR fitting of the three points

$$m = \frac{d\log \dot{M}}{d\log Z} = 1.02 \pm 0.30. \tag{5.12}$$

This is slightly higher than, but consistent with, the value of Mokiem et al. ($m = 0.83 \pm 0.16$).

In the top panel of Figure 5.9 we repeat this procedure for all luminosities (blue dashed line and light blue uncertainty region). At $\log L/L_\odot = 5.75$, $m = 1.02$ as discussed above. However, we do not find a constant value for m, but higher m for lower luminosities. The luminosity independent result $m = 0.83$ of Mokiem et al. is plotted as a red dot-dashed horizontal line. Plotted with a dotted green line are the results of Marcolino et al. (2022). As their metallicity dependence relies on MW and SMC results only, they do not require a

Table 5.8: Fit parameters of Equation 5.8 to the observed data, compared to Krtička & Kubát (2018) and Björklund et al. (2021).

Parameter	This work	Krtička (2018)	Björklund (2021)
a	0.64	1.64	2.07
b	-2.84	-0.32	-0.73
c	0.71	0.36	0.46
d	29.27	28.88	29.25[†]

[†] An offset of 30.80 is added to match the units of this work.

three-point fitting in order to obtain m. At the reference luminosity $\log L/L_\odot = 5.75$ they find $m \sim 0.6$, lower than Mokiem et al. (2007) and just outside our 1σ confidence interval. They do however find a negative trend of m with luminosity, opposite to our findings and not in line with theoretical predictions and expectations (see below).

5.5.3.2 Comparison to predictions and theoretical considerations

Table 5.8 lists our fit parameters a, b, c, d of Equation 5.8 along with the predicted values from Krtička & Kubát (2018) and Björklund et al. (2021). In order to obtain the values of Krtička & Kubát we calculated the modified wind momentum rates using the values from Tables 1 from both Krtička & Kubát (2017) and Krtička & Kubát (2018) up to 42 500 K. We find a significantly stronger metallicity dependence on the modified wind momentum–luminosity slope (parameter b) than both of the two predictions. Consequently, this implies a stronger metallicity dependence of mass-loss at low luminosity.

The bottom panel of Figure 5.9 again shows our empirical value of m as function of luminosity and $m = 0.83$, but now compared to the two sets of theoretical results. Both predictions show a decreasing trend of m with luminosity as in our empirical findings, albeit much weaker, and opposite to that of the work of Marcolino et al. (2022). Note that especially the Björklund et al. (2021) result is close to the constant m value of Mokiem et al..

In passing, we note that we have done the same analysis for the derived mass-loss rates directly, instead of using modified wind momentum. This can be found in Appendix IV.2. The results from that analysis are consistent with the wind momentum results presented here, suggesting that the value of $\mathrm{d}\log v_\infty / \mathrm{d}\log Z = n = 0.13$ from Leitherer et al. (1992) is reasonable. A very weak dependence of terminal wind speed on metallicity is also reported by Hawcroft et al. (2023).

Can the steeper dependence of mass-loss on metallicity for lower luminosity stars be explained by line-driven wind theory? The original theory by Castor et al. (1975, henceforth CAK), and subsequent CAK-like theories such as Puls et al. (2000); Gayley (1995), and re-formulations of CAK-like theories, such as Lamers & Cassinelli (1999), essentially have a principal scaling

$$\dot{M} \propto \bar{Q}^{(1-\alpha)/\alpha} \cdot L^{1/\alpha} \cdot [M(1-\Gamma)]^{-(1-\alpha)/\alpha}\,, \tag{5.13}$$

where M is the stellar mass, Γ is the Eddington factor for Thomson scattering, $\bar{Q}$ represents the maximum value of the multiplication factor by which the total continuum opacity in the outflow is to be multiplied to also account for line opacities (Gayley 1995), and α may be interpreted as the ratio of line force from optically thick lines to the total force (Puls et al. 2000); hence $0 < \alpha < 1$. For stars not too close to the Eddington limit it thus holds that $\dot{M} \propto L^{1/\alpha}$. Assuming no direct dependence of terminal velocity on luminosity, we arrive at

$$D \propto L^{1/\alpha} = L^{x}, \tag{5.14}$$

where in the last equality we have used Eq. (5.7).

The results in Table 5.7 would thus be matched by a decreasing value of α with metallicity: $\alpha = 0.72, 0.53, 0.41$ for $Z = 1, 0.5, 0.2\ Z_{\odot}$, respectively. Puls et al. (2000) explored the metallicity (and effective temperature and radial depth) dependence of α in OBA-star outflows in the regime $0.1{-}3\ Z_{\odot}$ (their Fig. 27, where $\hat{\alpha} \sim \alpha$). Indeed, CAK-optical depth parameter $t \sim 10^{-5}$ roughly shows a behaviour similar to our findings. However, for higher values of optical depth (i.e., closer to the stellar surface) such a dependence disappears. The overall effect may therefore be modest (such as found by Krtička & Kubát 2018; Björklund et al. 2021), at least in the metallicity regime probed here. Still, further theoretical studies, probing a wider metallicity range, would be extremely helpful in assessing the reasons for the luminosity dependence of the modified wind momentum versus metallicity dependence reporte here and by Marcolino et al. (2022). Such studies may also address the weak empirical dependence of $D(Z)$ at high luminosities found here. This behaviour might possibly indicate that for very strong winds the line force is dominated by optically thick lines, such that a Z-dependence is lost. Alternatively, at high luminosity the Eddington limit may be exceeded already quite deep down in the photosphere, initiating a mass loss that the star is simply not able to cope with, leading to fall-backs and a maximum sustainable mass loss.

In addition to theoretical studies, empirical studies should be pursued to improve coverage of parameter space (especially in the low luminosity regime of galactic stars) and alternatives to the parameterization Eq. (5.8) should be explored.

5.5.4 Wind structure and metallicity

The dependence of mass-loss properties on metallicity as described above is based on analyses that account for the presence of (optically thick and thin) clumps in the outflow as well as associated vorocity. The derived wind structure parameters for our target SMC stars are listed in Table 5.6. They show a wide range of clumping factors $f_{\rm cl}$, from 2-30, and a density of the inter-clump medium that is relatively low, with $f_{\rm ic} \sim 10^{-2} - 10^{-1}$. The velocity-porosity effect, characterised by $f_{\rm vel}$, shows a wide range of value, from 0.04 to 0.74. Clumping consistently starts near the onset of the flow, in the regime $v_{\rm cl,start} \sim 0.01 - 0.23\, v_{\infty}$. For the turbulent velocity our analysis probes the range of values from $0{-}0.3\ v_{\infty}$ only, following earlier empirical results by Groenewegen et al. (1989). We find that results span this full allowed range, with $v_{\rm windturb} \sim 0.01 - 0.29\, v_{\infty}$.

The obtained clumping constraints allows us to probe, for the first time, whether wind-clumping properties themselves are metallicity dependent and thus contribute to the empirical behaviour of $D(L, Z)$. If such a dependency would be strong, an in-depth treatment of clumping would be a prerogative for any empirical study of the dependency of mass loss on metal content. We continue here with caution as these first results should be considered as exploratory only for three important reasons. First, a comparison of clumping properties at different metallicities requires a similar treatment of wind structure to within great detail. For this reason, we opt to only discuss the analyses of the sample of SMC stars described here and of LMC stars described in Brands et al. (in prep.), where very similar methodologies are applied. We thus exclude the study by Hawcroft et al. (2021), who also account for optically thick clumping, but where different assumptions regarding its treatment are adopted. Second, the clumping prescription adopted here still lacks a quantitative comparison to 2D/3D hydro-simulations of radiation-driven outflow, in which wind structure naturally develops (e.g., Sundqvist et al. 2018). Such a comparison would help to assess its appropriateness. Third, the O-star SMC and LMC samples scrutinized here are still relatively small and show some differences in intrinsic properties, with generally hotter and brighter stars in the LMC sample. The latter therefore implies overall somewhat more massive stars, with stronger stellar winds.

Figure 5.10 shows the distribution of the five wind structure parameters ($f_{\rm cl}$, $f_{\rm ic}$, $f_{\rm vel}$, $v_{\rm cl,start}$, $v_{\rm windturb}$) and β, describing the rate of acceleration of the smooth wind flow, at LMC and SMC metallicities. The histograms also show the approximate kernel density estimation (KDE) based on the (often sizable) uncertainty on the parameter values. Note that for the clumping factor the square root of its value is displayed, as for optically thin clumping and a void inter-clump medium the optical wind-diagnostic lines are essentially invariant for the property $\dot{M} \cdot \sqrt{f_{\rm cl}}$. No clear trends with metallicity are seen for $f_{\rm vel}, v_{\rm cl,start}, v_{\rm windturb}$ and β. For both environments very similar regions of parameter space are occupied.

The only hint of a trend of wind inhomogeneity properties with metallicity is for $f_{\rm cl}$ and $f_{\rm ic}$, which appear to show higher values at higher metallicity. At face value this would suggest that the inter-clump medium in the LMC is relatively dense (so, high $f_{\rm ic}$) and that the clumps have high density (so, high $f_{\rm cl}$) but fill only a relatively small fraction of the wind volume. In the wind medium of the SMC stars the inter-clump medium is relatively rarefied, the clumps have modestly high density but fill a relatively large fraction of the wind volume. Whether this indeed implies such differences between the properties of wind structure in the LMC and SMC sample requires additional studies (of larger samples). Possibly, the differences are associated with correlations between clumping properties and other stellar parameters (such as mass loss). However, a search for such dependencies did not yield any convincing correlation. As the clumping properties impact the strength and shape of spectral lines in complex ways, ways that differ from line to line and that vary as a function of stellar properties, we cannot exclude possible degeneracies between parameters in some parts of parameter space. We conclude that the wind properties probed here do not show convincing evidence for a metallicity dependence.

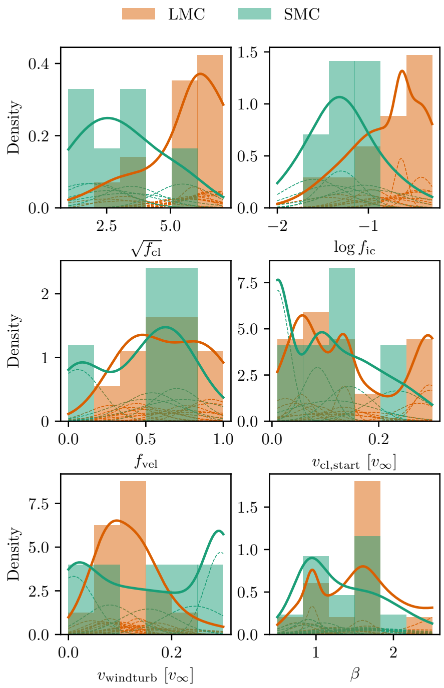

Figure 5.10: Distributions of wind parameters of LMC and SMC XShootU samples (Brands et al. in prep., this work). Solid lines indicate approximate kernel density estimation (KDE) based on uncertainty on the parameter values. The thin dashed lines indicate the contribution of the individual objects to the total KDE. Objects for which the parameters are unconstrained are excluded.

5.5.5 Challenges in the spectral fitting

Our spectral fitting relies on 55 spectral lines and line complexes, an overview of which is given in Table 5.3. To help add to our understanding of quantitative spectroscopy of hot massive stars, we discuss some notable complications.

N v 1240 The N v 1240 wind sensitive line is missing from Table 5.3. This resonance line, located in the wing of the Lyα absorption, is strong and shows a P-Cygni profile. It requires X-ray emission from wind-embedded shocks to have N v abundant enough to reproduce the observed profiles in our sample. X-ray emission is implemented in FASTWIND (Carneiro et al. 2016), however the exact amount of emergent emission as well as the shock temperature remain uncertain (Crowther et al. 2022). As N v is a trace ion (and a resonance line), the line profile is highly sensitive to the X-ray radiation field and, hence, difficult to predict reliably. Test calculations in which we included the line in the analysis resulted in systematically higher nitrogen abundances (for more details see Brands et al. in prep.). We therefore opted to exclude it.

He I singlets In our modelling we consider both singlet and triplet transitions of He I. Najarro et al. (2006) point out the importance of accurately predicting the radiation field near the reasonance transition $1s^2\,{}^1\mathrm{S}{-}2p\,{}^1P^{\circ}$ (at 584 Å) in order to correctly reproduce He I 4387, 4922 and 6678 Å, lines that have $2p\,{}^1P^{\circ}$ as their lower level. In modelling efforts, however, the radiation field near the He I resonance transition may be uncertain due to assumptions on line-blanketing and turbulent velocity. Specifically, the Fe IV ion has two transitions near to 584 Å that may affect the pumping efficiency of the resonance line, hence may impact the diagnostic He I singlet lines. Despite this, we find that in almost all cases the singlet lines are well reproduced. For AV 80 and AV 83 the singlet fits are of relatively poor quality; the triplet lines in these sources fit somewhat better.

The P V problem Fullerton et al. (2006) signal a discrepancy between mass-loss rates determined from the P V 1118,1128 resonance doublet and those determined from Hα, termed the 'P V problem'. The P V doublet would systematically result in lower mass-loss rates. The authors suggest the discrepancy can be solved by introducing clumping in the outflow. Such clumps increase the strength of the Hα recombination line while the P V line is not affected by changes in density directly, though it may be through changes in ionisation as a result of the higher density in the clumps (see Oskinova et al. 2007). Šurlan et al. (2013) successfully reproduce both the P V lines and Hα line with the same mass-loss rate by including micro clumping (analogous to f_{cl}) and macro clumping, the latter being a measure for the porosity of the wind.

Despite our relatively sophisticated and flexible prescription of wind inhomogeneities and leaving the phosphorus abundance a free parameter, we do not get satisfactory fits to the P V lines for part of our sample. This may suggest the applied clumping prescription fails to capture intricacies of wind structure key for the formation of P V or some other cause. Possibly the problem is connected to the poor constraints on the phosphorous abundance.

5.6 Conclusion/Summary

We have analysed ultraviolet ULLYSES and optical X-Shooting ULLYSES spectra of 13 massive O4–O9.5 III-I stars in the SMC using the model atmosphere code FASTWIND and the genetic algorithm fitting approach KIWI-GA. The KIWI-GA approach is the only way in which as much as 15 stellar and wind properties, of which 8 characterise the outflow, may be constrained self-consistently. The study accounts in detail for clumping, porosity, and velocity-porosity properties of the wind, processes that may impact the mass-loss sensitive spectral-line diagnostics.

We find the sample stars originate from $\sim$20–60 $M_{\odot}$ stars. They are somewhat evolved with ages of about 2–7 Myr, but all still to reside on the main sequence. Evidence for their somewhat evolved status, in addition to their temperatures, is an enhanced surface nitrogen abundance. We find indications of a mild surface enrichment of helium. For measured projected rotational velocities $v \sin i$ in the range 55–155 km s^{-1} this is somewhat surprising as single-star evolutionary tracks (by Brott et al. 2011) only predict such enrichment for spin rates of at least 387 km s^{-1}. Though the ULLYSES sample was selected on the basis of an absence of indications of binarity (in existing spectra), we suspect three targets in our sample (2dFS 163, AV 83, AV 70) to have composite spectra. The main focus of the study has been on the stellar wind properties. Excluding the three possible binaries, we find mass-loss rates ranging from $\log \dot{M}\ [M_\odot\ \mathrm{yr}^{-1}] = -7.65$ to -6.02 and terminal velocities of $v_\infty = 1650$ to $2625\ \mathrm{km\,s^{-1}}$. We account for inhomogeneities in the outflows, which we characterise with a medium that partly consists of a spectrum of clumps that may be either optically thick or thin and that may have varying degrees of internal velocity dispersion. Our main findings are:

- The mass-loss rates of our SMC stars compare with predictions of Björklund et al. (2021) to within 0.1−0.2 dex. The theoretical rates of Vink et al. (2001) and Krtička & Kubát (2018) produce a higher mass loss, especially at relatively low luminosity. Care should be taken with this result; Brands et al. (in prep.), using the same modelling approach as ours for a set of LMC stars, find mass-loss rates that lie between the predictions of Vink et al. (2001) and Krtička & Kubát (2018). This shows that a best match in part of parameter space by one set of predictions does not imply the best overall $\dot{M}(L, Z)$ relation.
- Incorporating results from Hawcroft et al. (2021) and Brands et al. (in prep.); Hawcroft et al. (in prep.) for Galactic and LMC stars, we find that in the luminosity interval $\log L/L_\odot = 5.0 - 6.0$ modified wind momentum $D \propto \dot{M} v_\infty R^{1/2}$ is not merely a function of metallicity, but also of luminosity. Relatively low luminosity stars show a stronger dependence on Z than do relatively high luminosity stars. This is at odds with the recent finding of Marcolino et al. (2022), who find an opposite behaviour.
- Eliminating the dependence of terminal velocity on metallicity, we find at a luminosity $\log L/L_\odot = 5.75$ the same $\dot{M} \propto Z^m$ as in the pioneering study by Mokiem et al. (2007): $m = 1.02 \pm 0.30$ in our study versus $m = 0.83 \pm 0.16$ in theirs.
- We use a mathematical formalism to describe $D(L, Z)$ for O-stars in both the Galaxy, LMC and SMC. This recipe does not capture fully the intricate dependencies, and may need revision in the future, but reveals that in particular effort is needed to better populate the sample of low luminosity ($\log L/L_\odot \lesssim 5.6$) Milky Way stars.
- We do not identify trends of wind inhomogeneity properties with metallicity, safe for a tentative finding that the clumping factor f_cl and the contrast between the inter-clump density and the mean density f_ic show higher values with higher metallicity. Though interesting, firm conclusions require larger samples studied in identical ways.

This study is part of the analysis of the ULLYSES and X-Shooting ULLYSES datasets. A full analysis of the ultraviolet and optical spectra of the ~250 targets in this program will greatly further our understanding of the out-flowing atmospheres of massive stars. In parallel to these studies, time-dependent hydro-dynamical simulations that resolve clumping properties are needed to assess whether our analytical prescriptions of wind inhomogeneity properties capture the essential characteristics of wind structure. Such simulations are now becoming available in 2D (Sundqvist et al. 2018) and 3D (Moens et al. 2022).

Chapter

Chapter 2

I.1 Normalized and corrected spectra

The normalized and corrected spectra of B243 and B331 are shown in Fig. I.1. The spectra have only been normalized around the modelled lines. The continuum of B243 at wavelengths longer than 1500 nm deviates due to IR excess from dust emission.

I.2 Model test – HII region

The new hydrogen atom description and extended radiation field were tested by simulating an H II region and comparing the numerically calculated ionization edge with the analytical Strömgren radius. We simulate an O-type star with $T = 38\,000$ K and $L_\star = 1.65 \times 10^5\,\mathrm{L}_\odot$. We surround this star with large gaseous disk with a constant radial density in the mid-plane ($\rho \sim 10^{-20}\,\mathrm{g\,cm^{-3}}$). The disk does not contain dust or poly-cyclic aromatic hydrocarbons (PAHs). The disk material has (proto-)solar abundances. Fig. I.2 shows the ionization fraction in the simulated H II region. A clear ionization edge is visible. The radius at which $n(H) = n(H^+)$

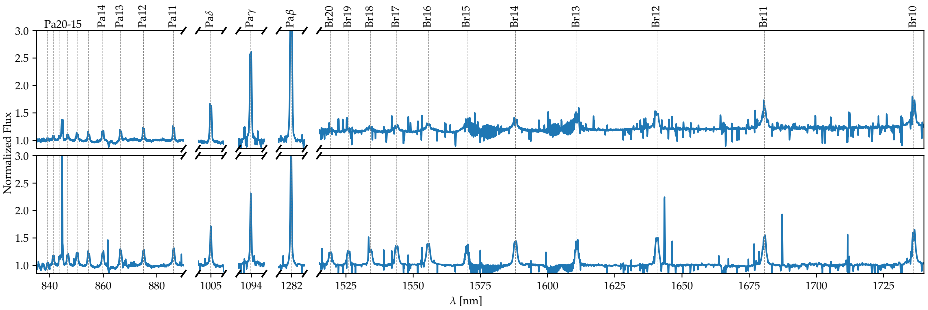

Figure I.1: Normalized and corrected spectra of B243 (top panel) and B331 (bottom panel), focusing on the Paschen and Brackett series. The spectrum of B243 is not normalized at wavelengths longer than 1500 nm due to the normalization method's incompatibility with the IR excess.

matches the analytically calculated Strömgren radius, which is indicated by the dashed white line. The surface layer of the disk has a lower density, which moves the ionization edge to a larger distance from the star. The theoretical prediction of the Strömgren radius is based on the number of ionizing photons emitted and the recombination rate of electrons and protons which depends on the temperature and density of the circumstellar medium. We only consider case B recombination with the coefficient

$$\alpha_{\mathrm{B}}(T) = 2.54 \times 10^{-13} T_4^{-0.8163-0.0208 \ln T_4} \quad [\mathrm{cm^3\,s^{-1}}] \tag{I.1}$$

by Draine (2011), with $T_4 = \frac{T}{10^4}$. The radius at which the medium becomes neutral, the Strömgren radius, can then be described as

$$R_{\mathrm{S}} = \left(\frac{3}{4\pi}\right)^{1/3} \left(\frac{Q_{\mathrm{ion}}}{\alpha_{\mathrm{B}}}\right)^{1/3} n_H^{-2/3} \tag{I.2}$$

with n_H the hydrogen particle density and Q_{ion} the rate at which hydrogen ionizing photons are produced. In this system $Q_{\mathrm{ion}} \sim 5 \times 10^{48}\,\mathrm{s^{-1}}$.

As the ionization edge of the model and the Strömgren theory agree, we conclude that the hydrogen photo-ionization and recombination balance is calculated correctly in the model.

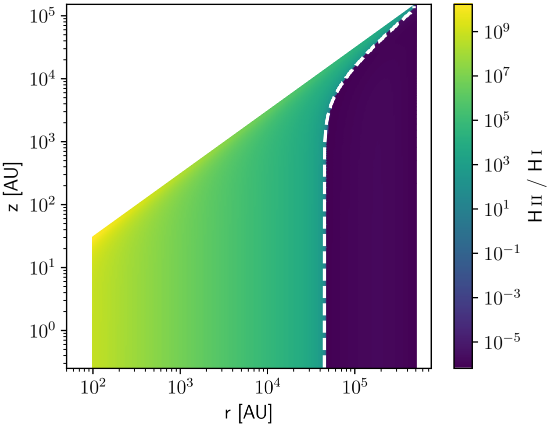

Figure I.2: H II region simulated with ProDiMo. The colour indicates the ratio between neutral and ionized hydrogen. The white dashed line indicates the analytically calculated Strömgren radius based on the radiation field, temperature and density of the medium.

I.3 Correlations and grid behaviour

The parameters chosen to be varied have some degeneracy, which can result in large uncertainties in their best fit value. Additionally, the coarseness of the grid can result in what we will refer to as a 'noisy' χ^2 statistic. This noise is the result of the correlation between parameters and misalignment in the step size of the grid and correlation strength. This can be seen

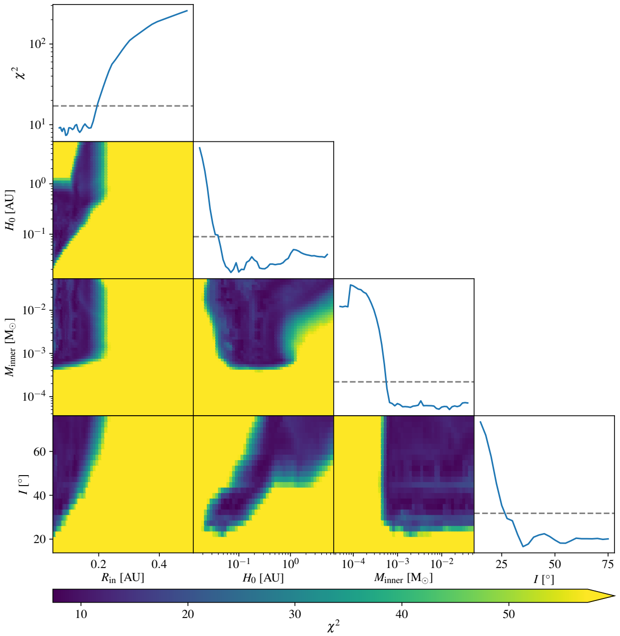

Figure I.3: Corner plot indicating the χ^2 value for the model fit to the Pa-12 emission line of B243 as function of each of the parameters and each parameter combination. The dashed line in each top panel indicates the 1σ threshold.

in the top panels of each column of Fig. I.3 and Fig. I.4. When exploring a parameter, the optimal values of the remaining parameters can only be approximated to a limited degree. The optimal value is likely to lie between grid points. The size of this deviation varies for each point and results in a varying accuracy to which the minimum χ^2 can be determined. This affects the accuracy of the optimal fit values and their uncertainties. In order to minimize this effect the coarse model grid is interpolated.

I.3.1 Correlations

We find correlations between the mass and scale height, inclination and scale height, and the inclination and mass as indicated in Fig. I.3 and Fig. I.4. An increase in mass can result in a similar line profile by increasing the scale height and inclination of the disk. This results in degeneracy allowing a relatively large range of parameter values to fit to the data. This degeneracy combined with the coarseness of the grid results in noisy χ^2 values as function of a given parameter. When the parameter value moves to a different grid point, the optimal value of another parameter might lie between two grid points and will be missed. This results in a higher χ^2 value. Therefore, the accuracy of the minimum χ^2 for a given parameter is limited.

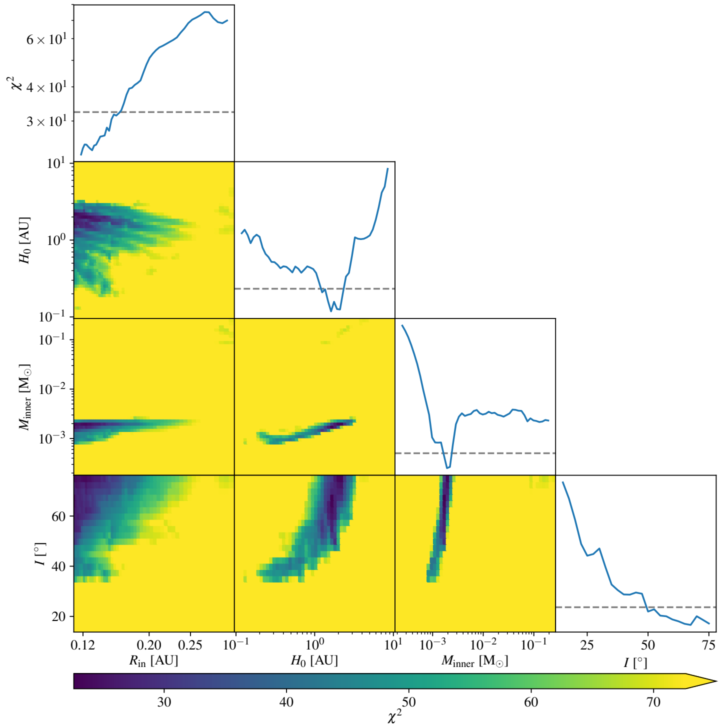

Figure I.4: Corner plot indicating the χ^2 value for the model fit to the Pa-12 emission line of B331 as function of each of the parameters and each parameter combination. The dashed line in each top panel indicates the 1σ threshold.

Chapter II

Chapter 3

II.1 Accuracy of the age determination

The effective temperature and bolometric correction of the luminosity class V stars are taken from Pecaut & Mamajek (2013); for the luminosity class III stars, we used the calibrations from Alonso et al. (1999) for spectral types F0-F9, and for G4-M5 stars we used the calibration of Cox (2000). In order to calculate the luminosity of the observed targets, we used the absolute K-band magnitude assuming the Indebetouw et al. (2005) extinction law to derive the K-band extinction A_K. We then obtained the absolute magnitudes by scaling the apparent magnitudes to the distance of the clusters (1336^{+68}_{-76} pc for M8 and 1770^{+140}_{-120} pc for NGC 6357; Kuhn et al. 2019). The luminosities were obtained by using the bolometric correction and the absolute magnitudes. Finally, we determined the age of the regions by comparing the position of the observed stars to MESA isochrones obtained from the MIST project (Paxton et al. 2011, 2013, 2015; Dotter 2016; Choi et al. 2016). The isochrones and tracks used have a solar metallicity and an initial rotational velocity of $v_{\rm ini} = 0.4\,v_{\rm crit}$, the age obtained using tracks with $v_{\rm ini} = 0$ are within the reported error bars.

Here we discuss some of the issues that might affect the age determination and compare our age estimates with those published in the literature. *i)* Binarity could affect the luminosity determination by making stars look brighter than they actually are. Given the spacing of the isochrones at the young age of M8 and NGC 6357, this does not have a significant effect on our age determination. *ii)* The use of different evolutionary tracks could lead to different age estimates; for example, Martins & Palacios (2013) show that the main-sequence age for different models could vary by $\sim$ 0.7 Myr for a 20 $M_\odot$ isochrone. In our case, this uncertainty is likely smaller than that caused by the uncertainty on the spectral type. *iii)* The age determination may depend on the adopted extinction law. By using the Nishiyama et al. (2009) extinction law, we obtain lower A_K values and, therefore, slightly fainter objects. Nevertheless, given that the extinction in these three regions is relatively modest ($A_{K,\rm max} \sim 2.5$), the difference in luminosity produced by the various extinction laws does not significantly affect the age determination. *iv)* The classification of the earliest spectral type (O3) is normally degenerate (see e.g., Wu et al. 2014, 2016). In the case of NGC 6357, the most massive star is of spectral type O3.5. The fact that its spectral type is uncertain could affect the lower age limit. To avoid this, we determined the age based on the whole population, including the low-mass PMS stars, instead of focusing only on the massive stars.

Arias et al. (2007) estimated the age of M8 to be < 3 Myr based on the low-to-intermediate mass PMS population and Feigelson et al. (2013) estimated the age of the pre-main sequence stars in M8 between $\sim 0.8-2.5$ Myr, which is in agreement with our estimate – including the massive stars – of $1-3$ Myr. Massi et al. (2015) determined the age of NGC 6357 at $1-3$ Myr based on the visual and NIR color-magnitude and color-color diagrams. By comparing the whole population of stars with MIST isochrones, we estimate an age of 0.5 to 3 Myr for this cluster.

We find that the age obtained for the studied regions by looking only at the massive stars is consistent with the age obtained only from the low-mass PMS stars. If the late-K and M-type stars near the Hayashi track were cluster members, we would obtain a younger age ($\sim 0.1-1$ Myr younger) for the PMS stars compared to that of the massive stars only.

II.2 Lines used to measure the radial velocity

Table II.1: Radial velocities and lines used to measure the radial velocity for each star in M8.

Name	RV (km s^{-1})	Br-12	Br-11	HeI	Br-10	HeI	Brγ
14	-14.1 ± 7.5	x	x	x	x	x	x
16	-17.4 ± 8.1	x	x		x		x
24	-57.1 ± 7.4		x	x	x	x	x
33	1.3 ± 16.0	x	x		x		x
36	-5.1 ± 7.6			x	x	x	x
51	-10.2 ± 9.0	x	x	x	x	x	x
60	78.4 ± 12.4	x	x	x		x	x
73	56.6 ± 12.4	x	x				x
79	-38.1 ± 10.0	x	x	x		x	
F44	28.5 ± 7.2			x		x	x
O10	11.6 ± 13.0	x	x	x	x	x	x
O11	-52.9 ± 35.5		x				x
O5	-2.9 ± 9.0			x	x	x	x
O6	29.9 ± 15.4	x	x		x		x
O7	-24.5 ± 13.1	x	x	x	x	x	x
O8	17.1 ± 16.6	x	x	x		x	

II.3 Distribution of radial velocities of the OB stars in M8 and NGC 6357

II.4 Comparison to previous work

We compare the σ_{RV} distribution obtained with the distribution presented in Sana et al. (2017). Therefore, we sampled clusters of 12 stars with $P_{\mathrm{cutoff}}= 1.4$ days and $f_{\mathrm{bin}}= 0.7$ and

Table II.2: Radial velocities and lines used to measure the radial velocity for each star in NGC6357.

Name	RV ($\mathrm{km\,s^{-1}}$)	Br-12	Br-11	HeI	Br-10	HeI	Brγ
107	9.5±14.7		x		x		
112	74.8±9.0		x	x	x	x	x
118	16.5±13.1		x	x		x	x
16	9.8±8.1		x	x	x	x	x
22	62.1±16.2	x	x	x	x	x	x
73	40.4±11.5			x	x	x	x
88	−70.1±12.4		x	x	x	x	x
B0	10.7±8.3		x	x	x	x	x
B10	32.8±2.9			x	x	x	x
B11	53.9±7.1		x	x		x	x
B13	76.1±14.4		x	x		x	x
B15	38.1±4.4			x		x	x
B1	−73.6±12.1		x	x	x	x	x
B2	−7.0±4.0			x		x	x
B4	−7.1±13.2		x	x		x	x
B6	43.3±13.3	x	x		x		x
B7	12.7±4.1			x		x	x
B8	−41.3±10.8		x	x	x	x	x
B9	0.5±2.4			x		x	
O0	4.0±11.0			x		x	x
O1	36.7±5.3			x		x	x
O2	35.6±10.1	x		x	x	x	x

the radial velocity measurement errors of M17. This results in a $\sigma_{\mathrm{RV}}= 40.9^{+18.9}_{-16.1}$ $\mathrm{km\,s^{-1}}$ for the method described above. Sana et al. (2017) found a lower value of $\sigma_{\mathrm{RV}}= 35.0^{+21.9}_{-14.9}$ $\mathrm{km\,s^{-1}}$. The confidence intervals of the two values overlap due to the width of the distribution.

We assessed the correctness of our method by generating a parent population using numerically calculated two body orbits. The binary star systems were generated in a similar way as described above. Each system is described by a primary mass, mass ratio, period, and eccentricity using identical distributions as before. The orbits of the binaries were simulated in a two dimensional plane. Only a single orbit starting at periastron was simulated numerically using a fourth order Runge-Kutta method (Dormand & Prince 1980). The systems were tested on their stability by integrating for a large number of orbits. The velocity was obtained by selecting a random time step from the orbit. The two dimensional x and y velocities were converted to a radial velocity using a randomly generated inclination and longitude of periastron. Finally, the effect of cluster dynamics was added to the radial velocity.

The radial velocities calculated from the numerical two body orbits were combined with the radial velocities of single stars to generate a new parent population of 10^5 stars. This parent population can be sampled as described above to generate a σ_{RV} distribution. Using the same cluster properties, we produced a σ_{RV} distribution for M17 with $f_{\mathrm{bin}}= 0.7$ and $P_{\mathrm{cutoff}}= 1.4$ days. This resulted in $\sigma_{\mathrm{RV}}= 40.5^{+18.6}_{-16.0}$ $\mathrm{km\,s^{-1}}$, which agrees closely with this

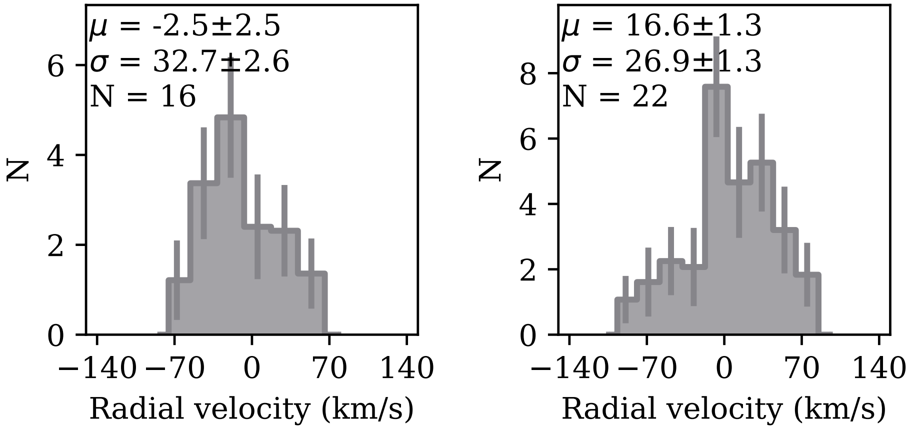

Figure II.1: Distribution of radial velocities for the massive stars in M8 and NGC 6357.

work. No significant difference with this work was found for any binary fraction or cutoff period.

Chapter III

Chapter 4

III.1 Extinction fits

The extinction towards each of the stars varies strongly. Figure III.1 shows an overview of the reddened and dereddened SEDs of the stars. The corresponding A_V and R_V values are also indicated. Figure III.2 shows the correlation between A_V and R_V for each star. Some stars show strong correlations, this can be due to a small number of photometric data points being available for the fit. B215 only has four data points available for the fit, as the longer wavelength data shows strong IR excess emission. As a result the three free parameters of the fit become quite degenerate and we find a strong correlation. However, the resulting uncertainty on A_V and R_V, and the absolute magnitude remains limited, see Table 4.3. The best fit value might be unreliable and subject to significant change if more photometric data are added.

III.2 Mass discrepancy

Herrero et al. (1992) first note the difference between spectroscopic surface gravity of stars and their inferred evolutionary model surface gravity. Since then improved models have decreased the gap, particularly above $15\,\mathrm{M}_\odot$ (e.g Herrero et al. 2002). However, Repolust et al. (2004) find a systematic offset for stars above $15\,\mathrm{M}_\odot$. Figure III.3 shows the evolutionary mass at the ZAMS as function of the spectroscopic mass. No clear trend or offset is visible at the low mass end. At higher masses there appears to be a slight trend in which higher evolutionary masses are found. One outlier stands out, which is B272 showing a significantly higher spectroscopic mass than evolutionary mass. This is due to the high surface gravity found. A possible cause of the high value of $\log g$ could be the low signal-to-noise ratio and contamination in the spectrum, resulting in a strange temperature and gravity combination as best fit.

III.3 Fit summaries

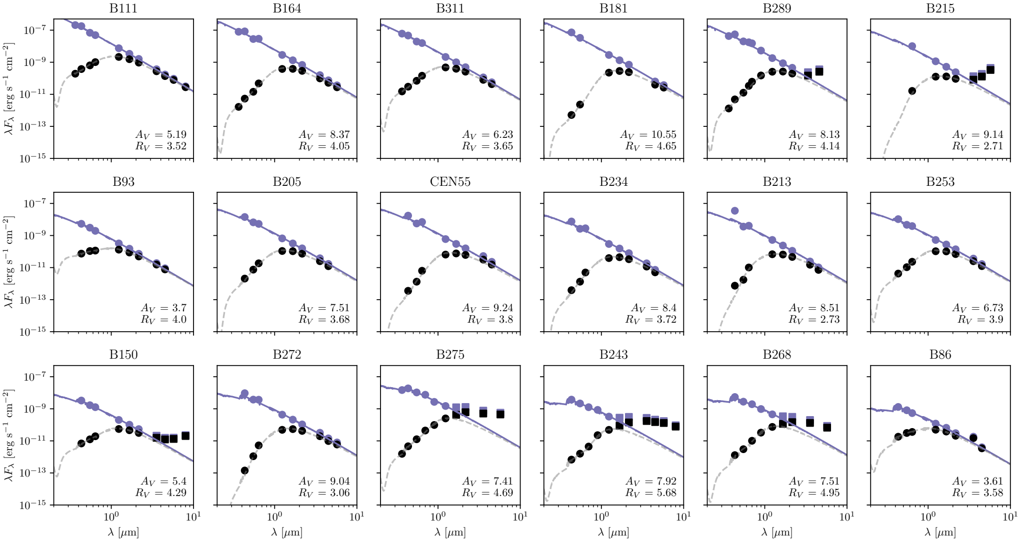

Figure III.1: Observed and dereddened SED of each star. Black squares and dots indicate observed photometric data, purple markers indicate dereddened data. The squares indicate data with IR excess emission, these are not used for the determination of the extinction. The dashed grey line shows the reddened stellar model and the purple solid line is the original stellar model.

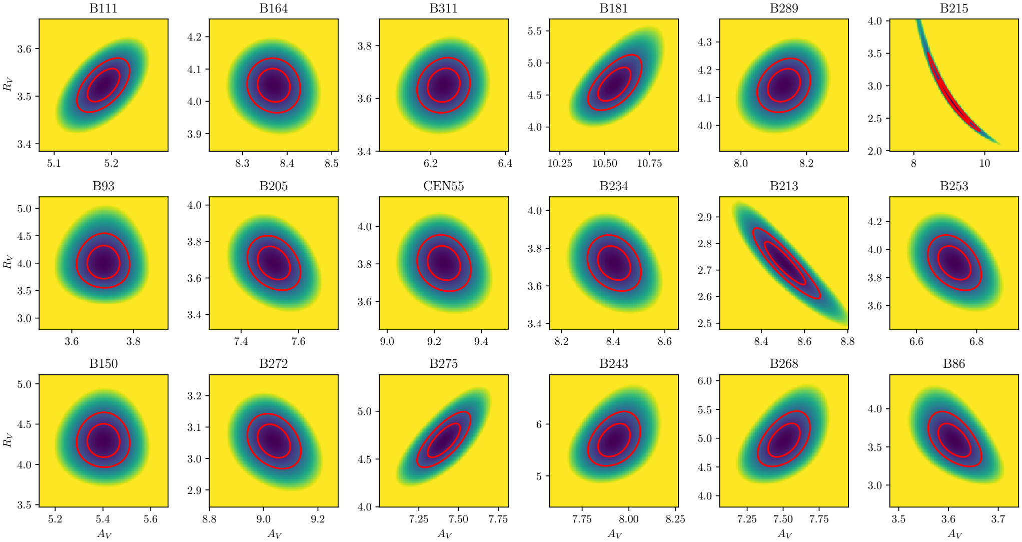

Figure III.2: A_V and R_V correlations found in the fitting process. The color indicates the χ^2 value of the combination of A_V and R_V and the red lines indicate the 1 and 2 σ confidence contours.

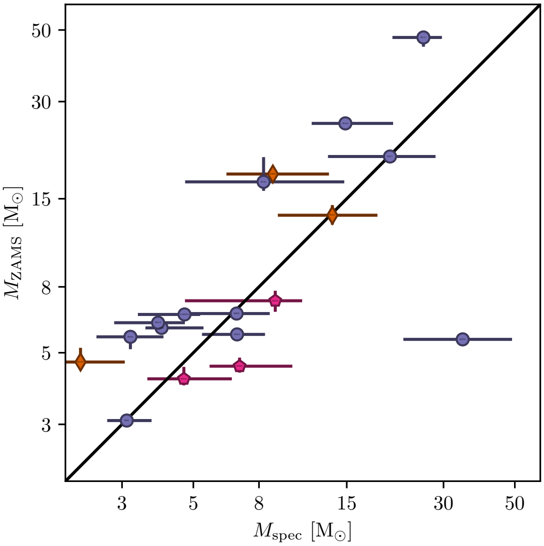

Figure III.3: Mass based on evolutionary tracks plotted against mass based on spectroscopy. Markers are identical to Figure 4.4.

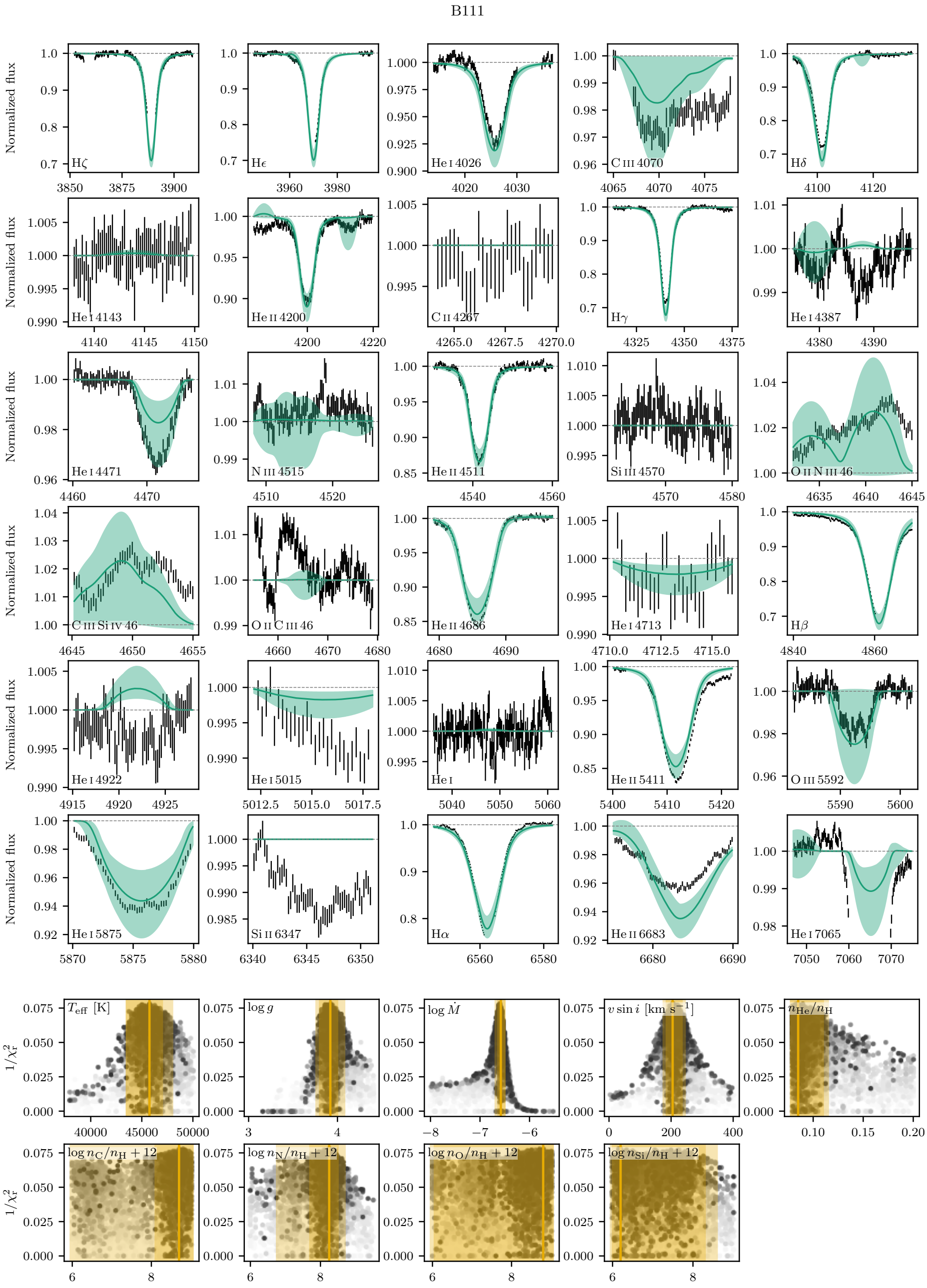

Figure III.4: Same as Figure 4.3, but for B111.

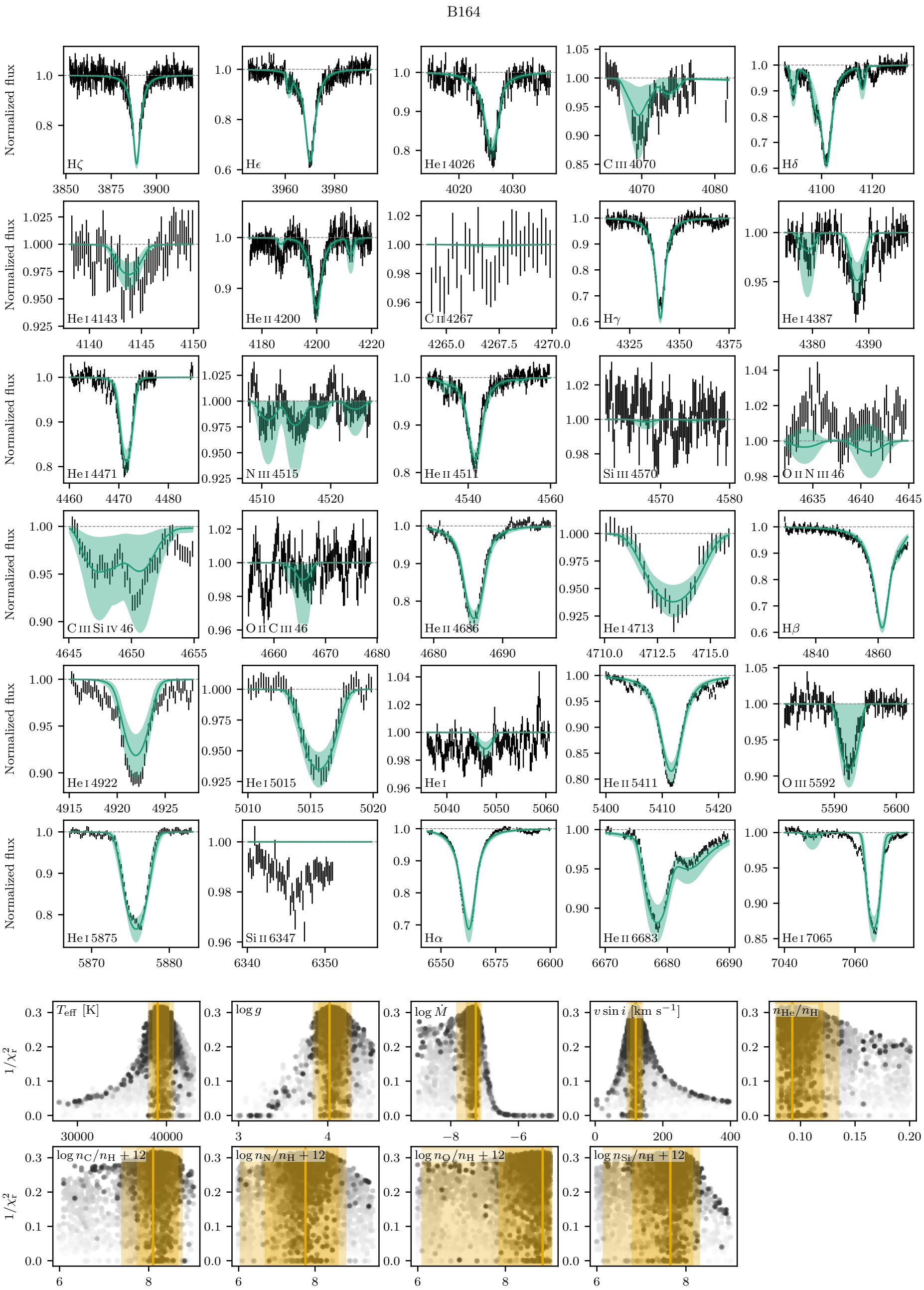

Figure III.5: Same as Figure 4.3, but for B164.

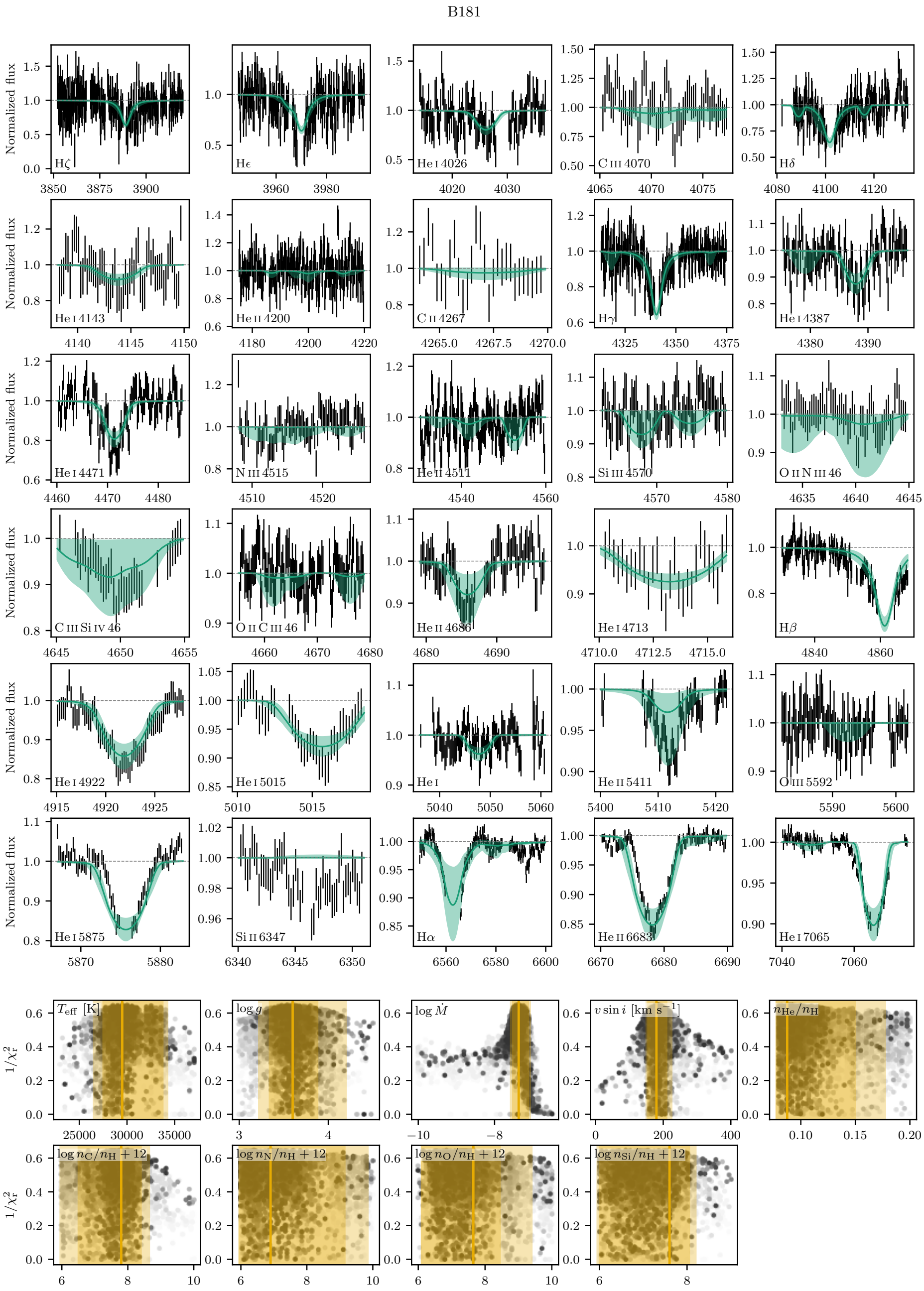

Figure III.6: Same as Figure 4.3, but for B181.

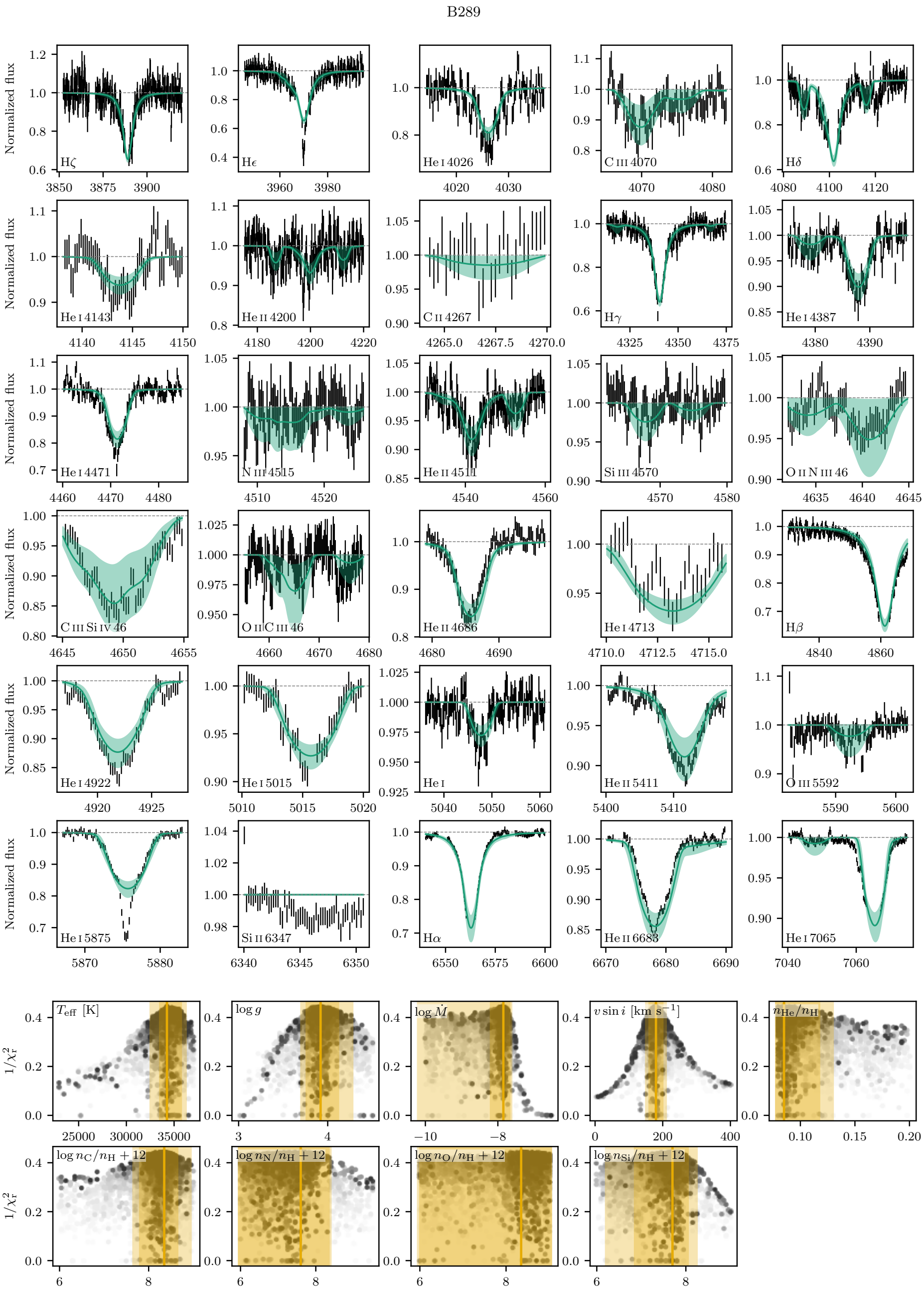

Figure III.7: Same as Figure 4.3, but for B289.

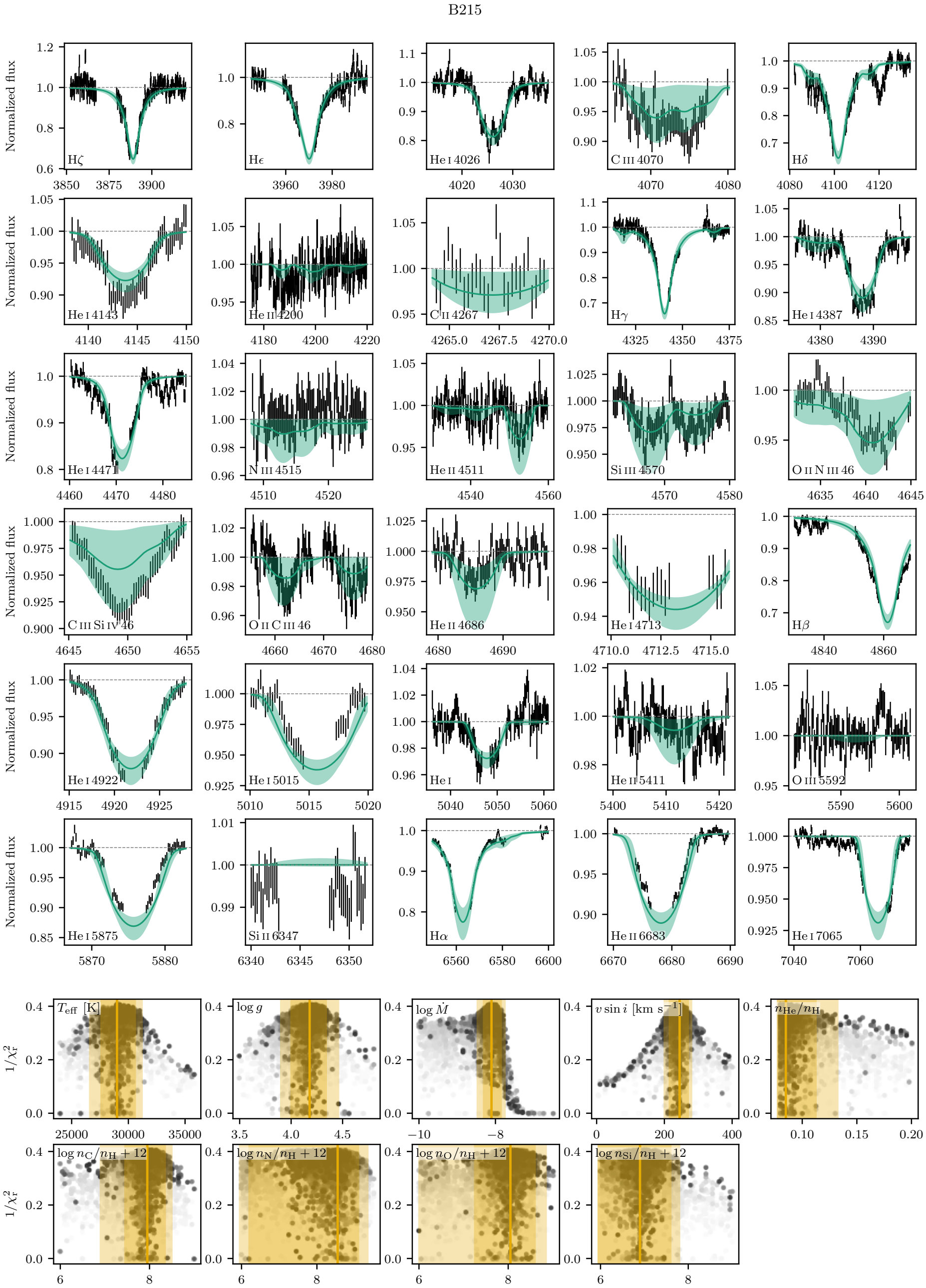

Figure III.8: Same as Figure 4.3, but for B215.

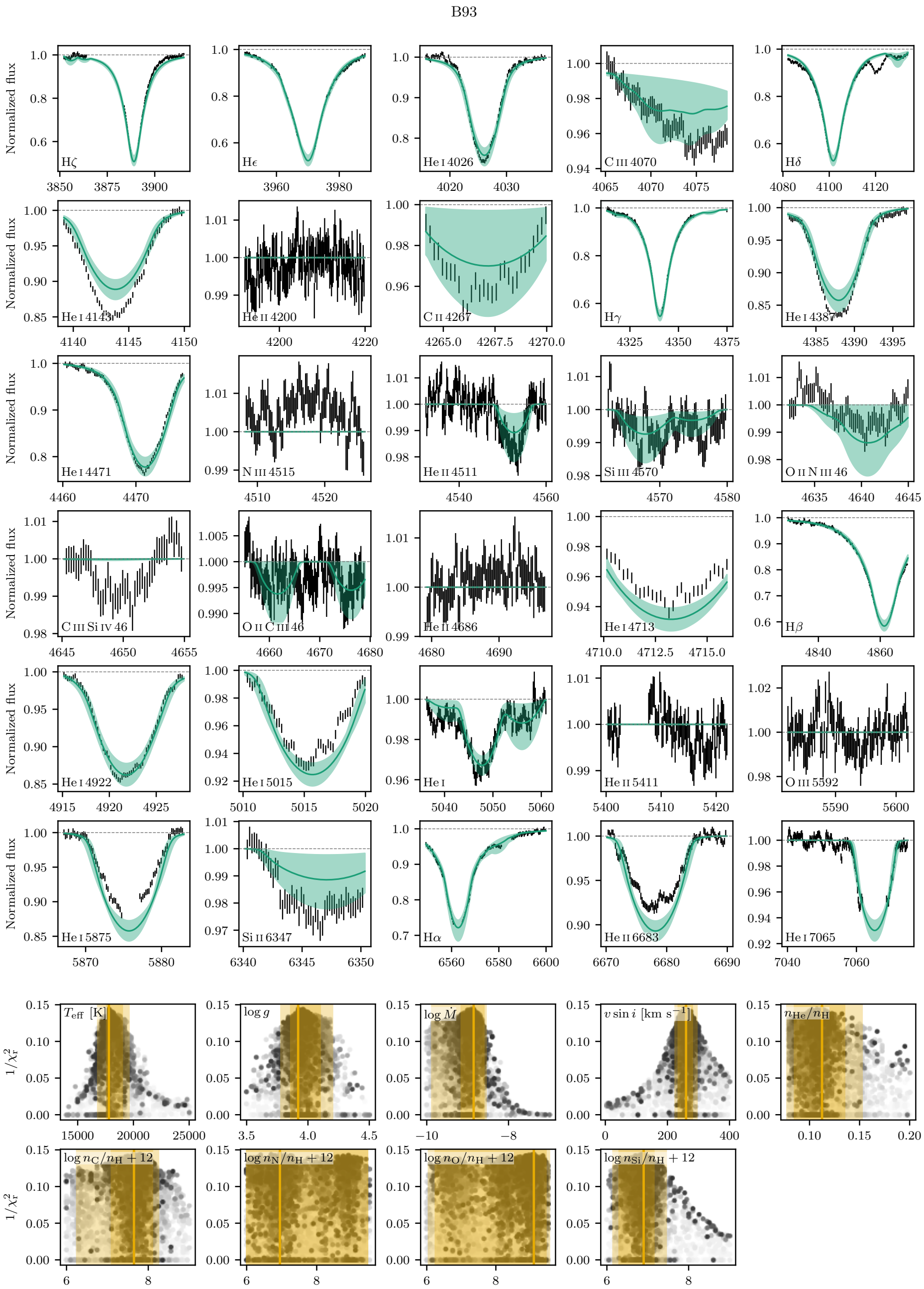

Figure III.9: Same as Figure 4.3, but for B93.

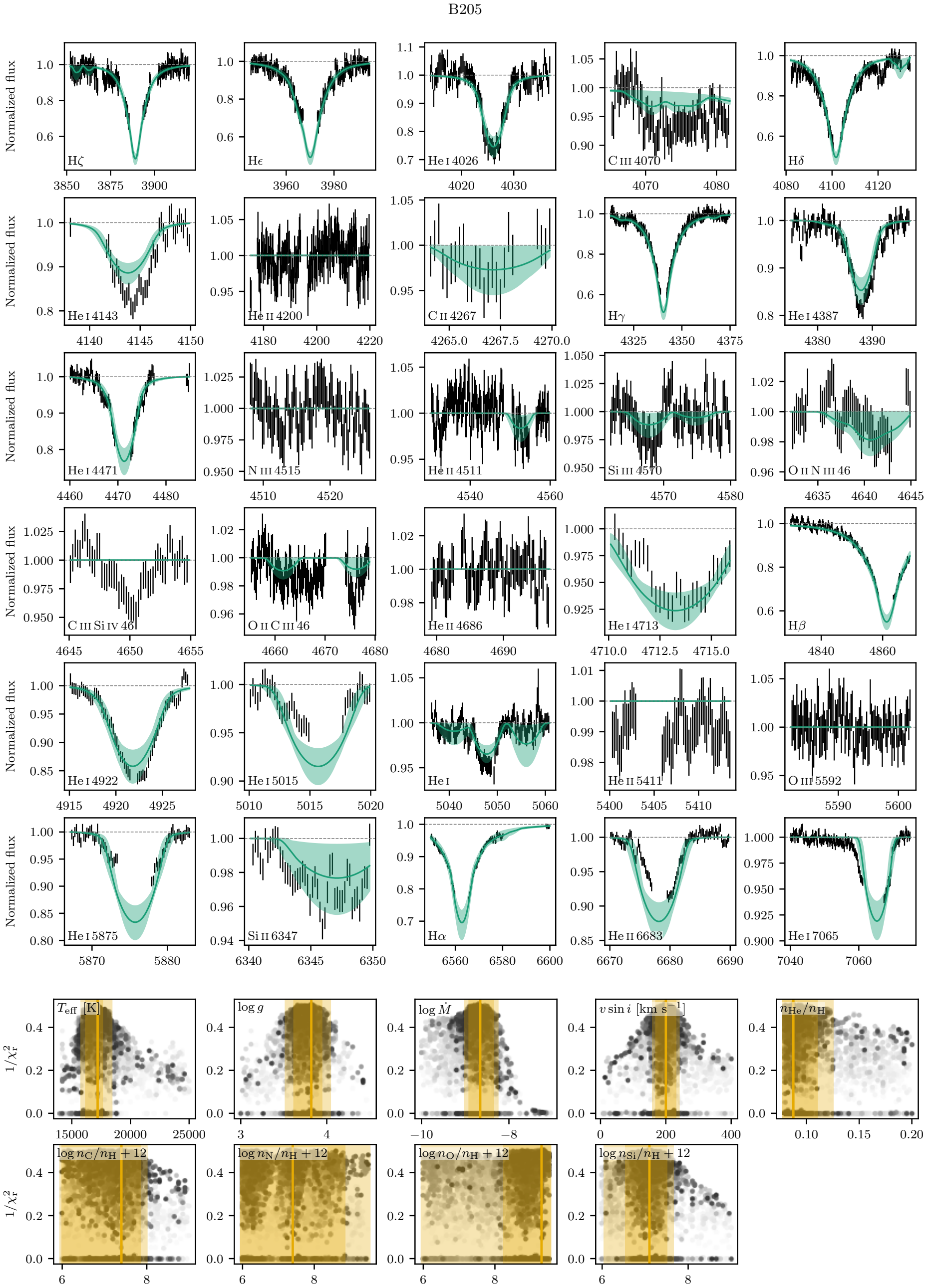

Figure III.10: Same as Figure 4.3, but for B205.

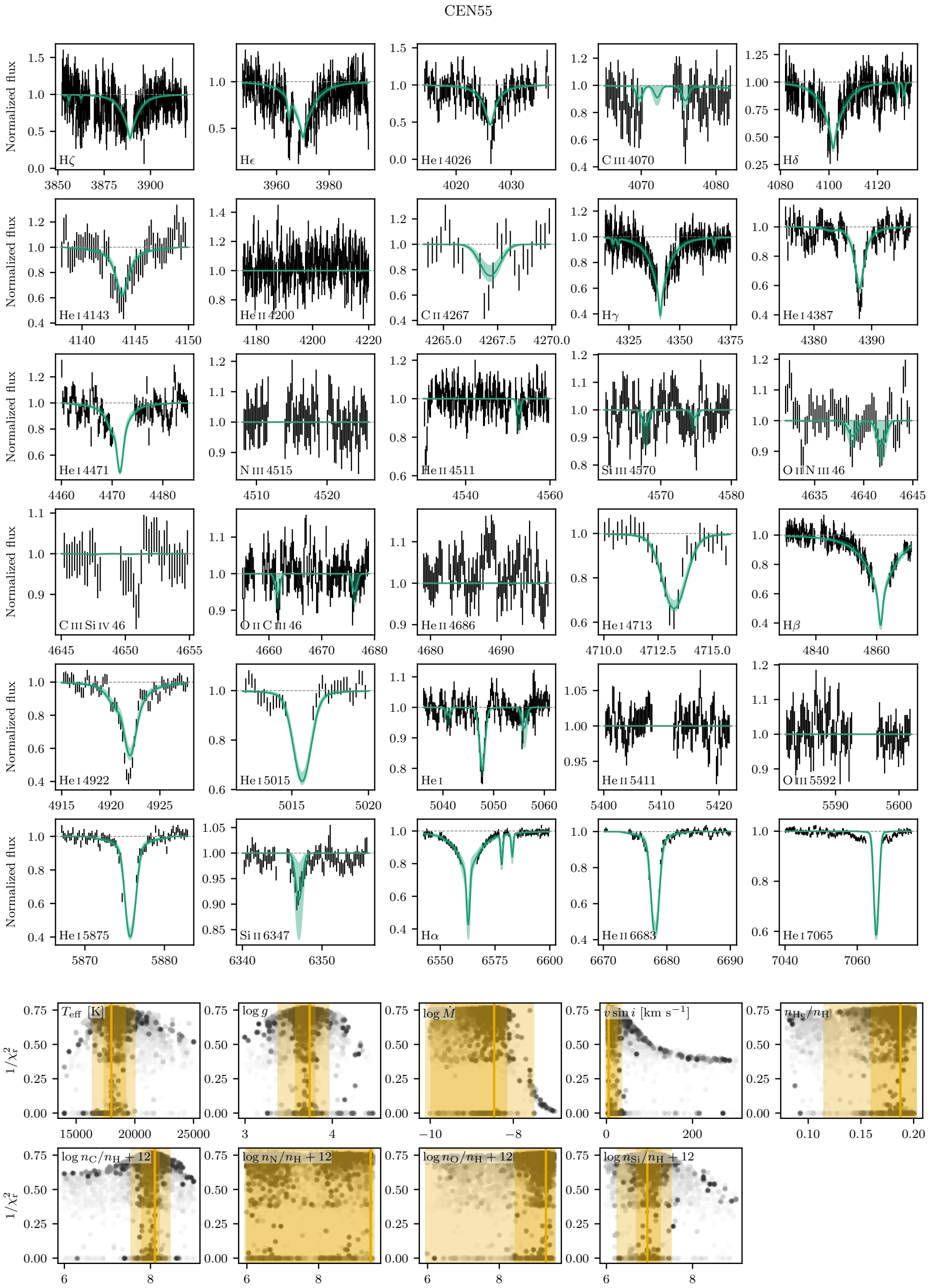

Figure III.11: Same as Figure 4.3, but for CEN55.

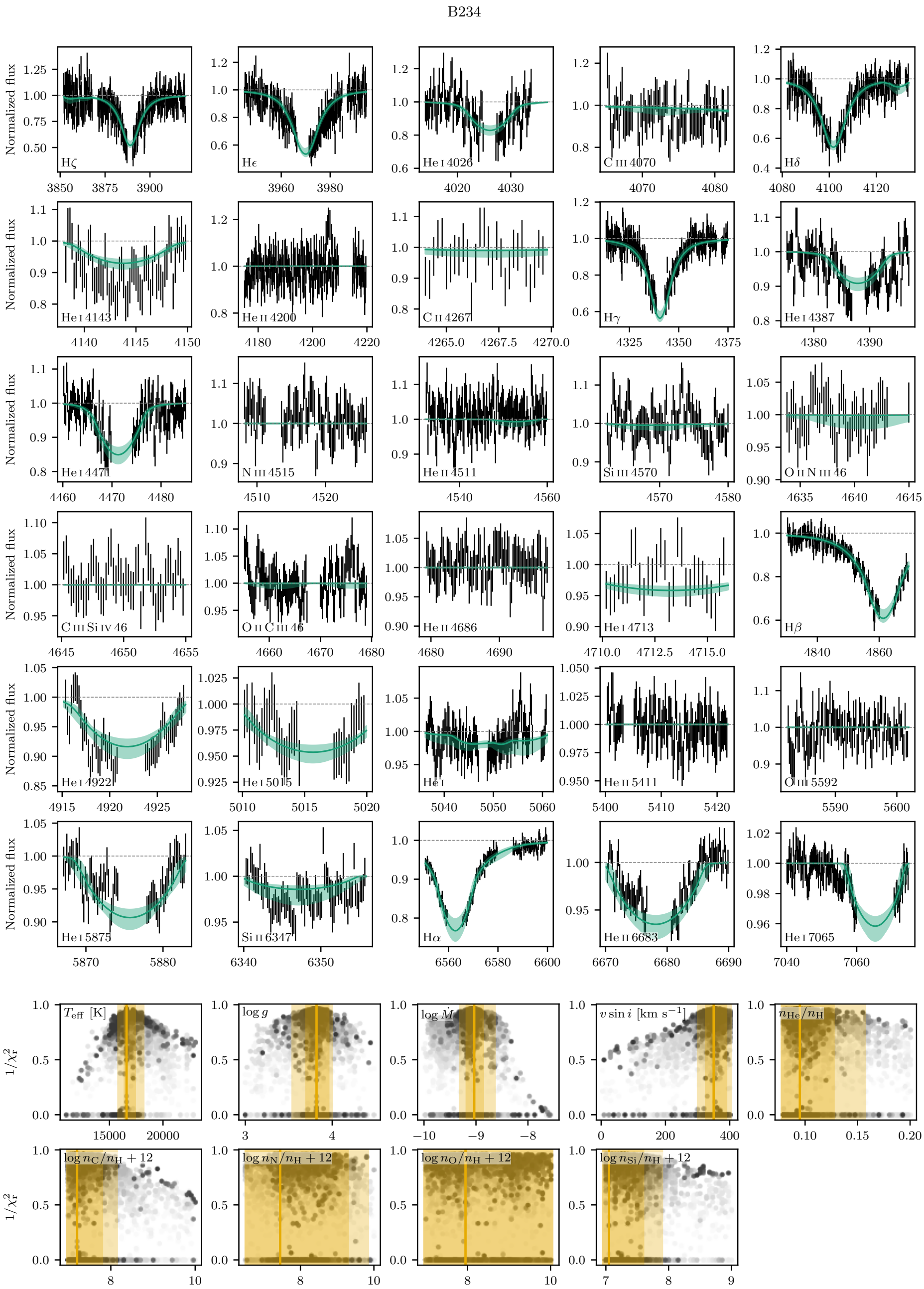

Figure III.12: Same as Figure 4.3, but for B234.

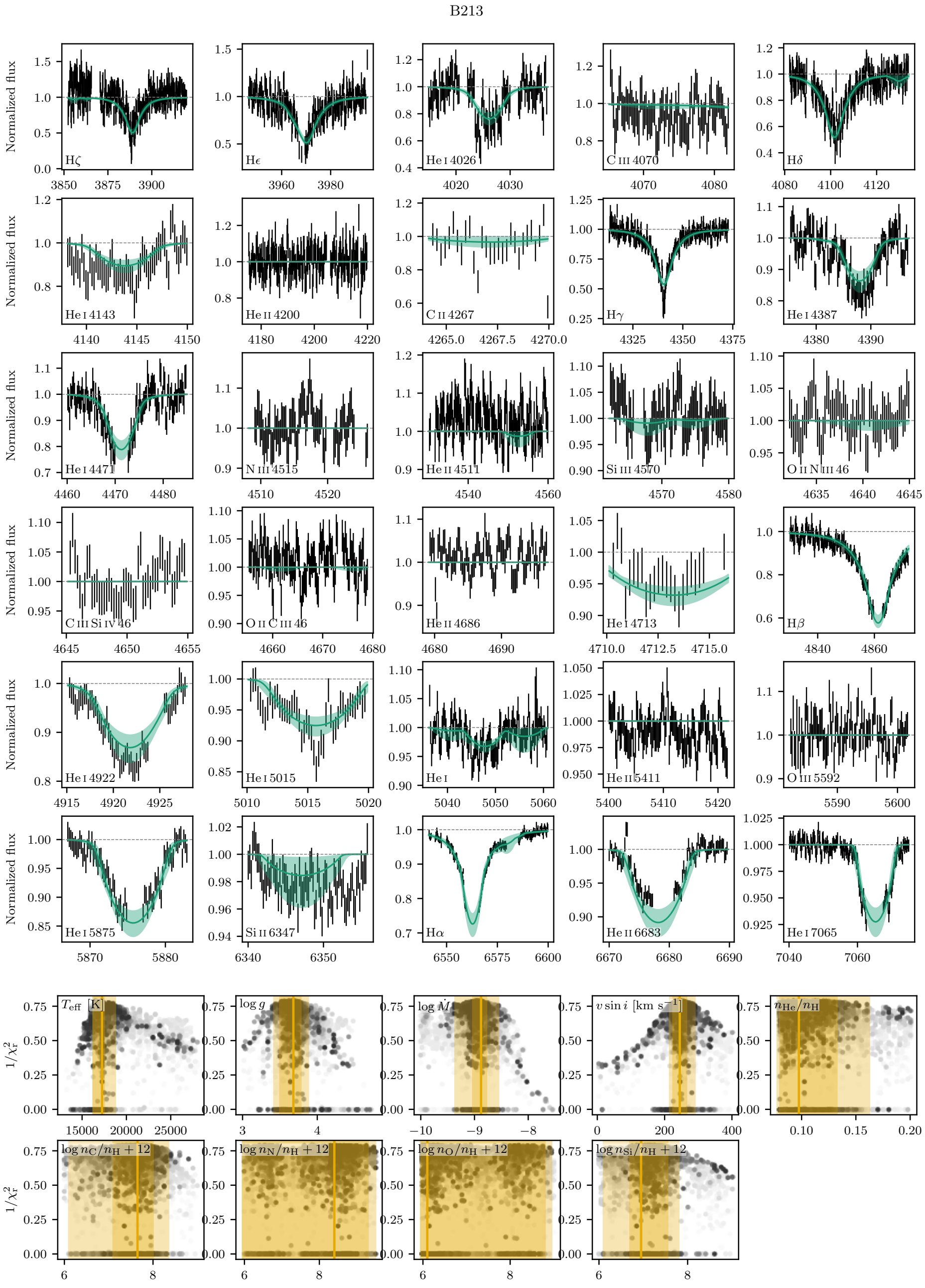

Figure III.13: Same as Figure 4.3, but for B213.

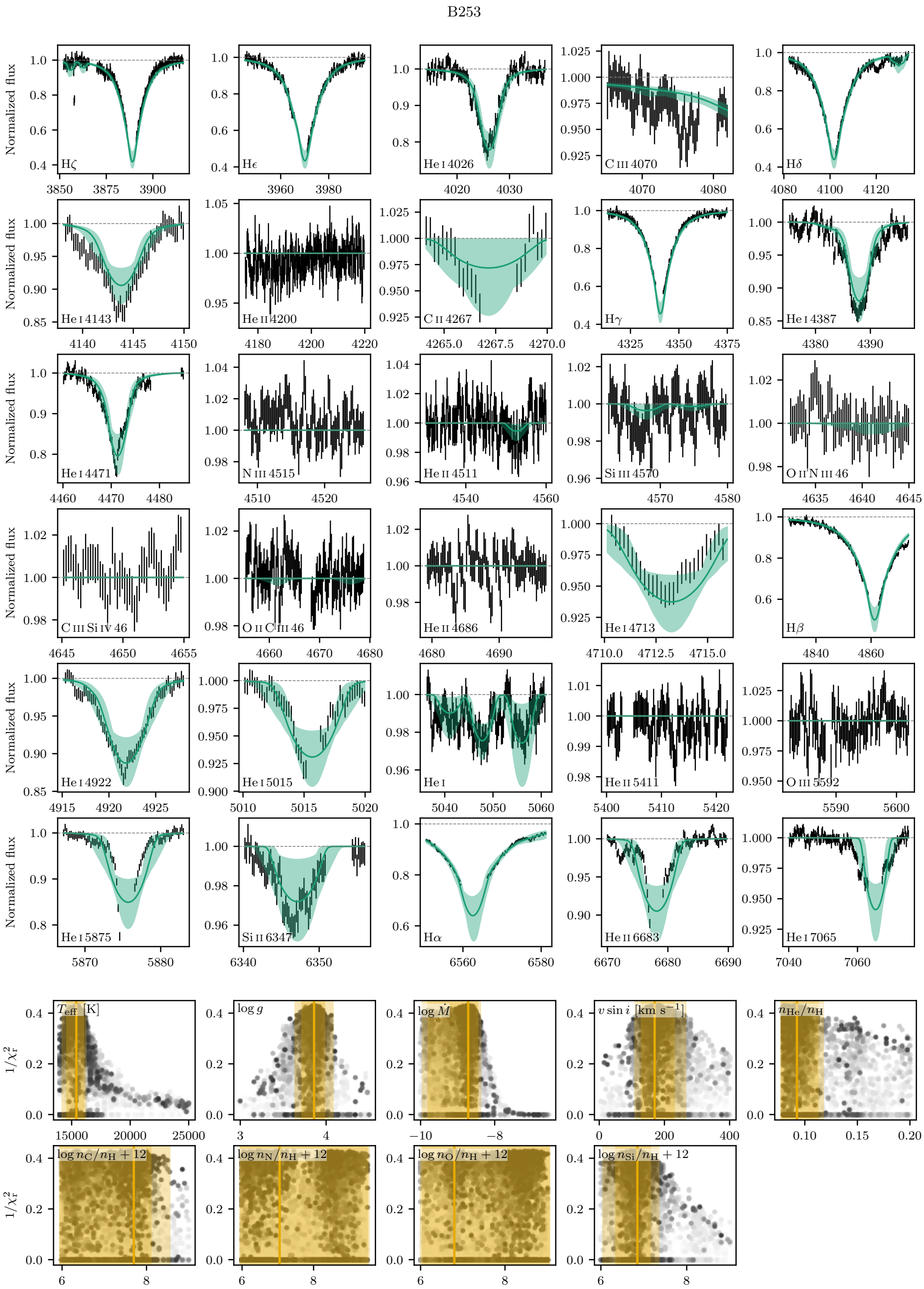

Figure III.14: Same as Figure 4.3, but for B253.

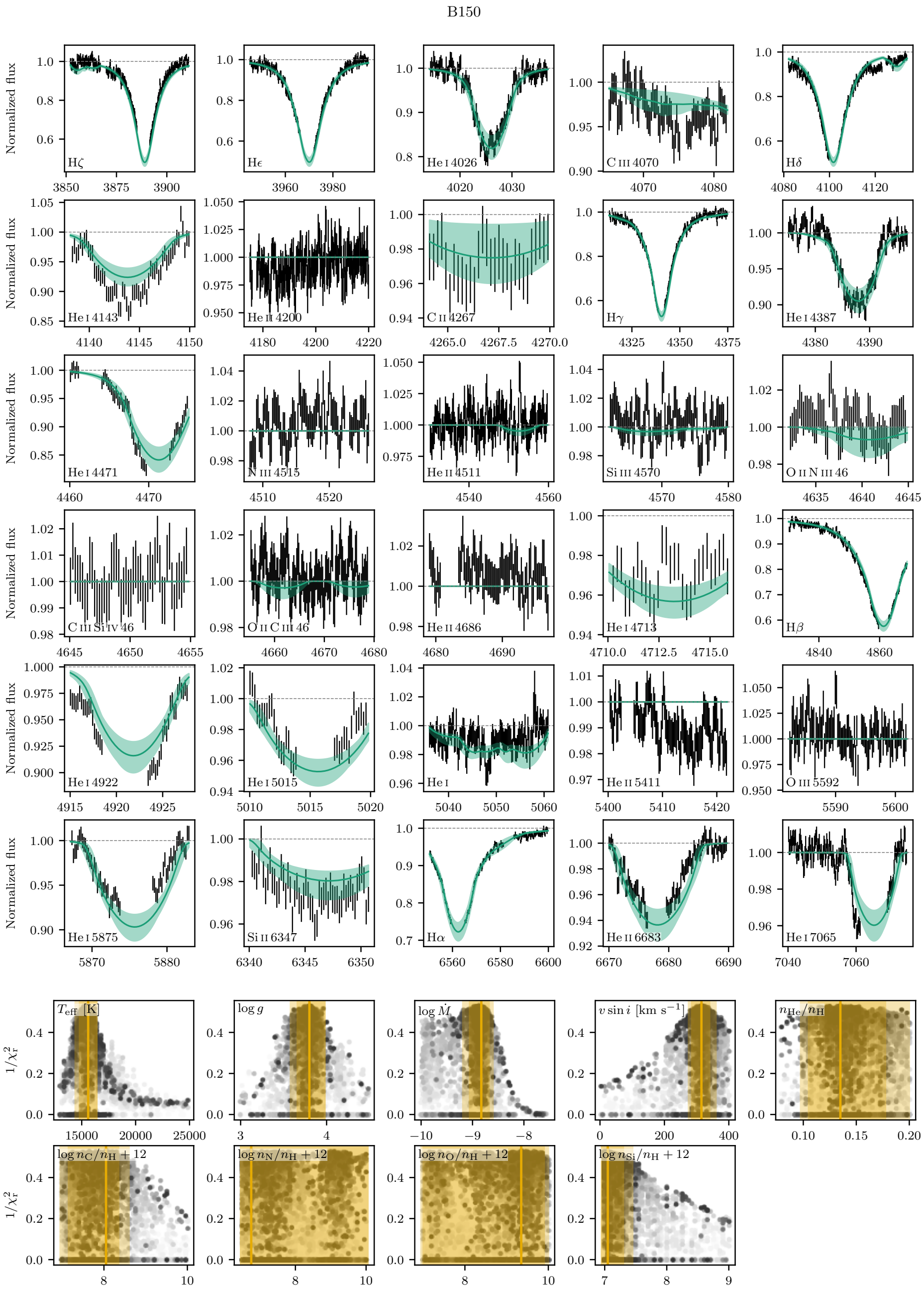

Figure III.15: Same as Figure 4.3, but for B150.

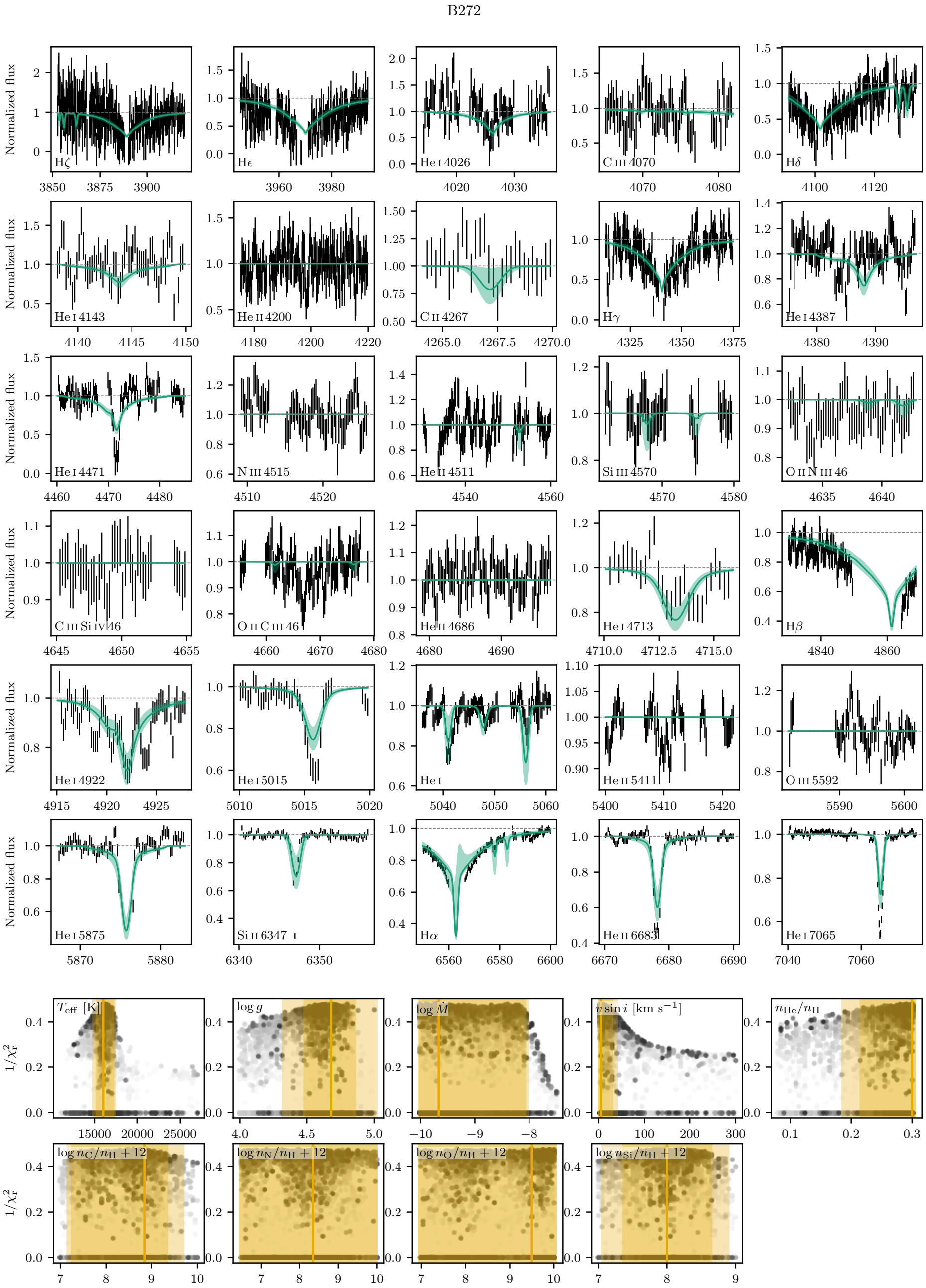

Figure III.16: Same as Figure 4.3, but for B272.

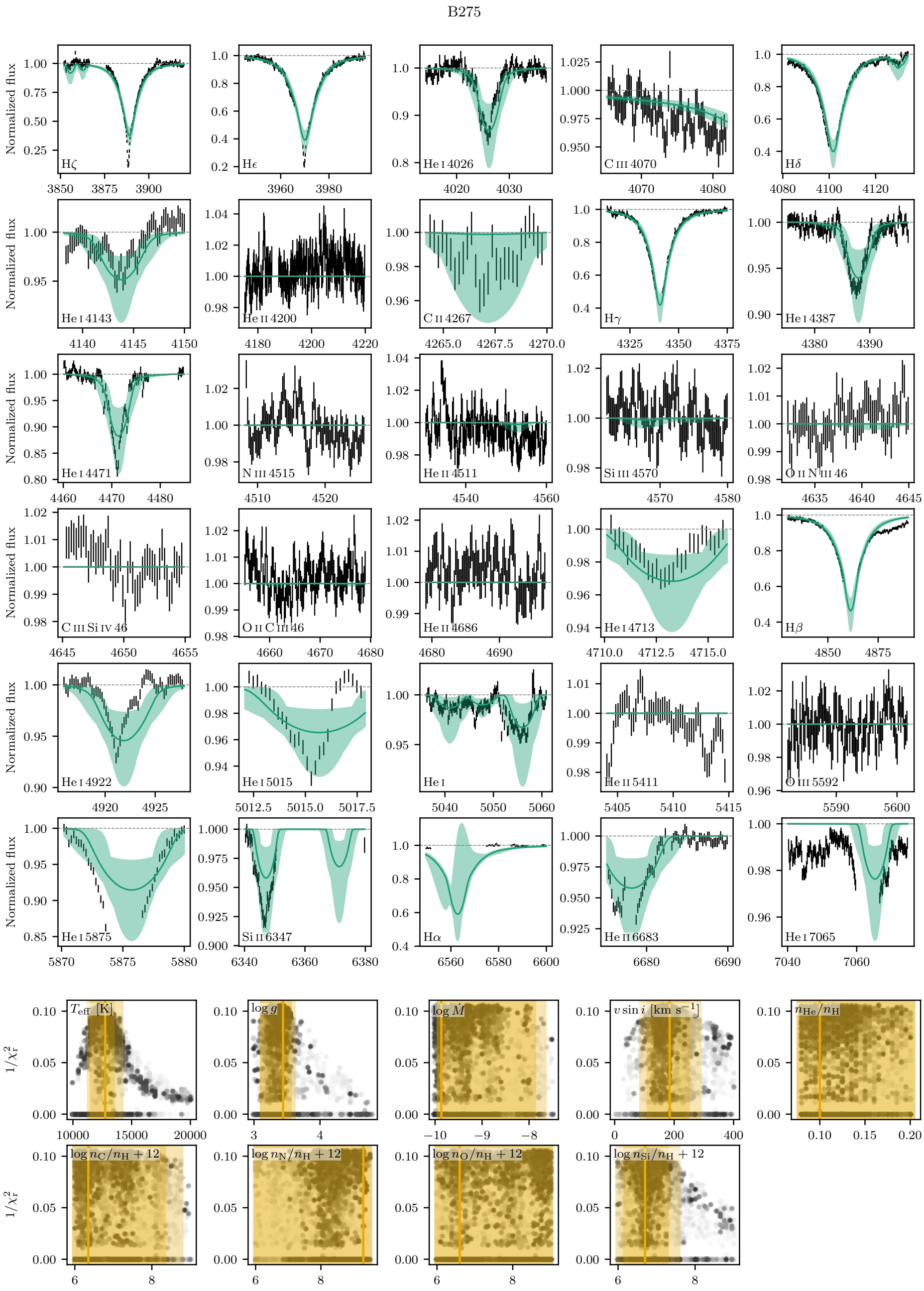

Figure III.17: Same as Figure 4.3, but for B275.

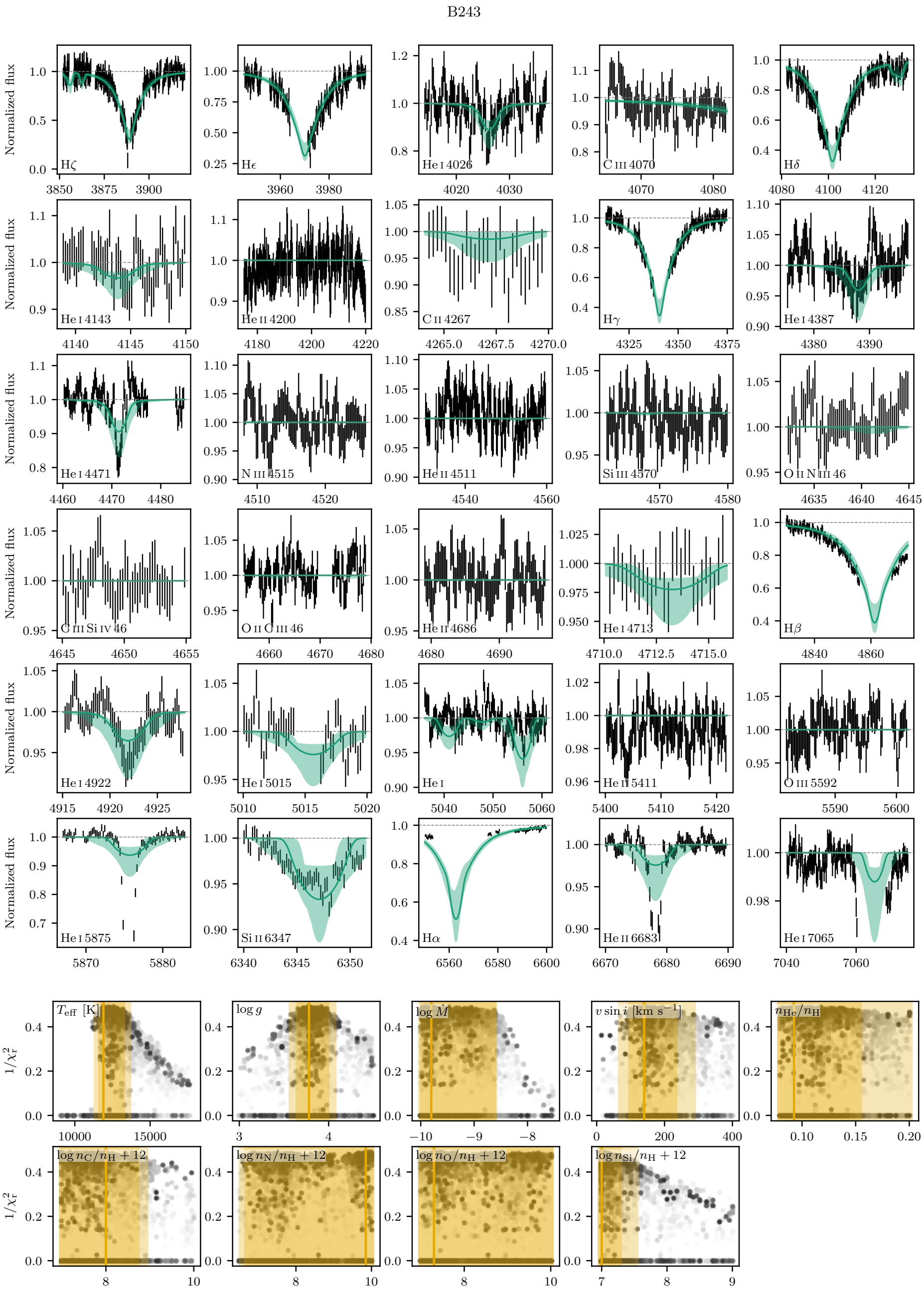

Figure III.18: Same as Figure 4.3, but for B243.

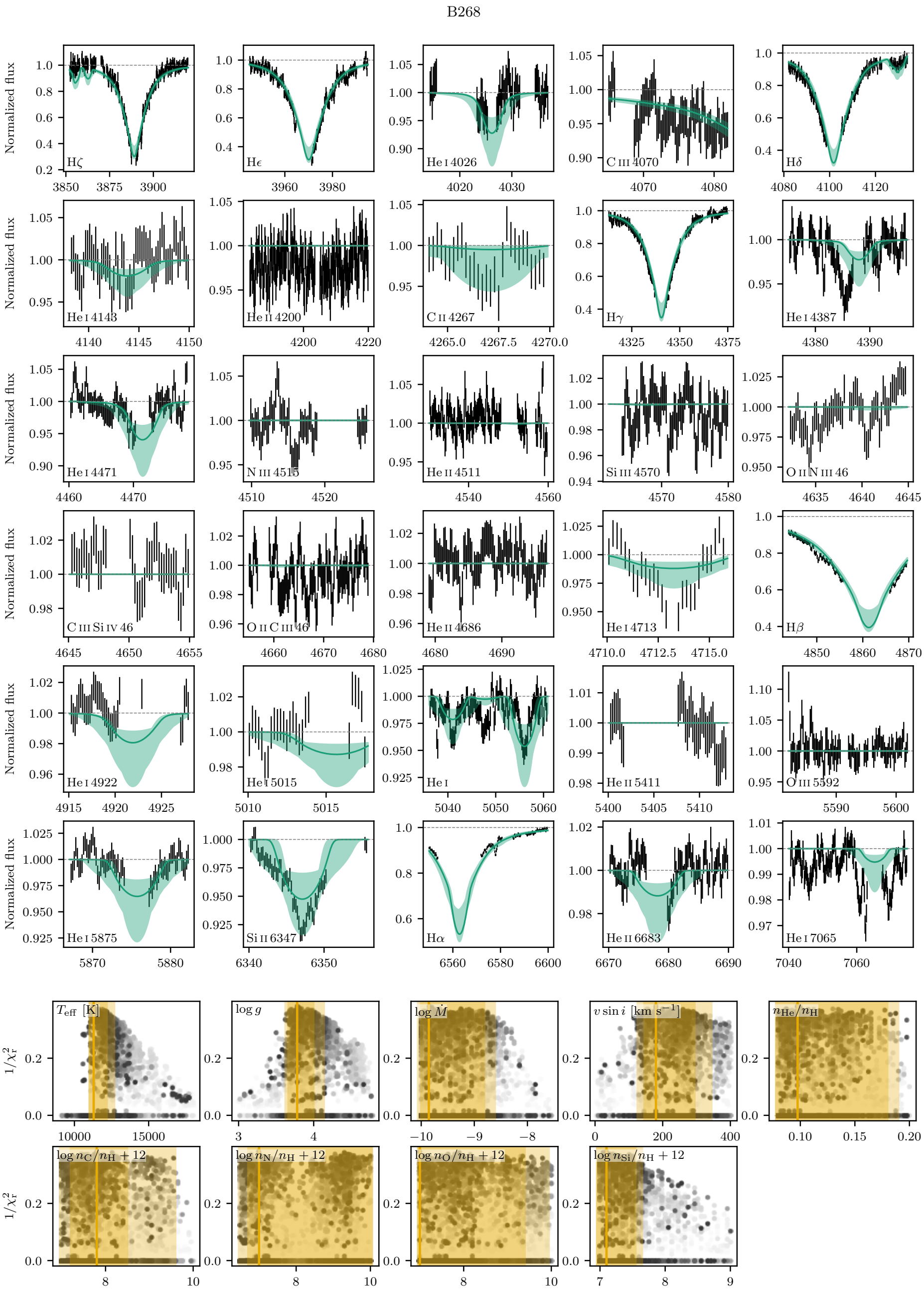

Figure III.19: Same as Figure 4.3, but for B268.

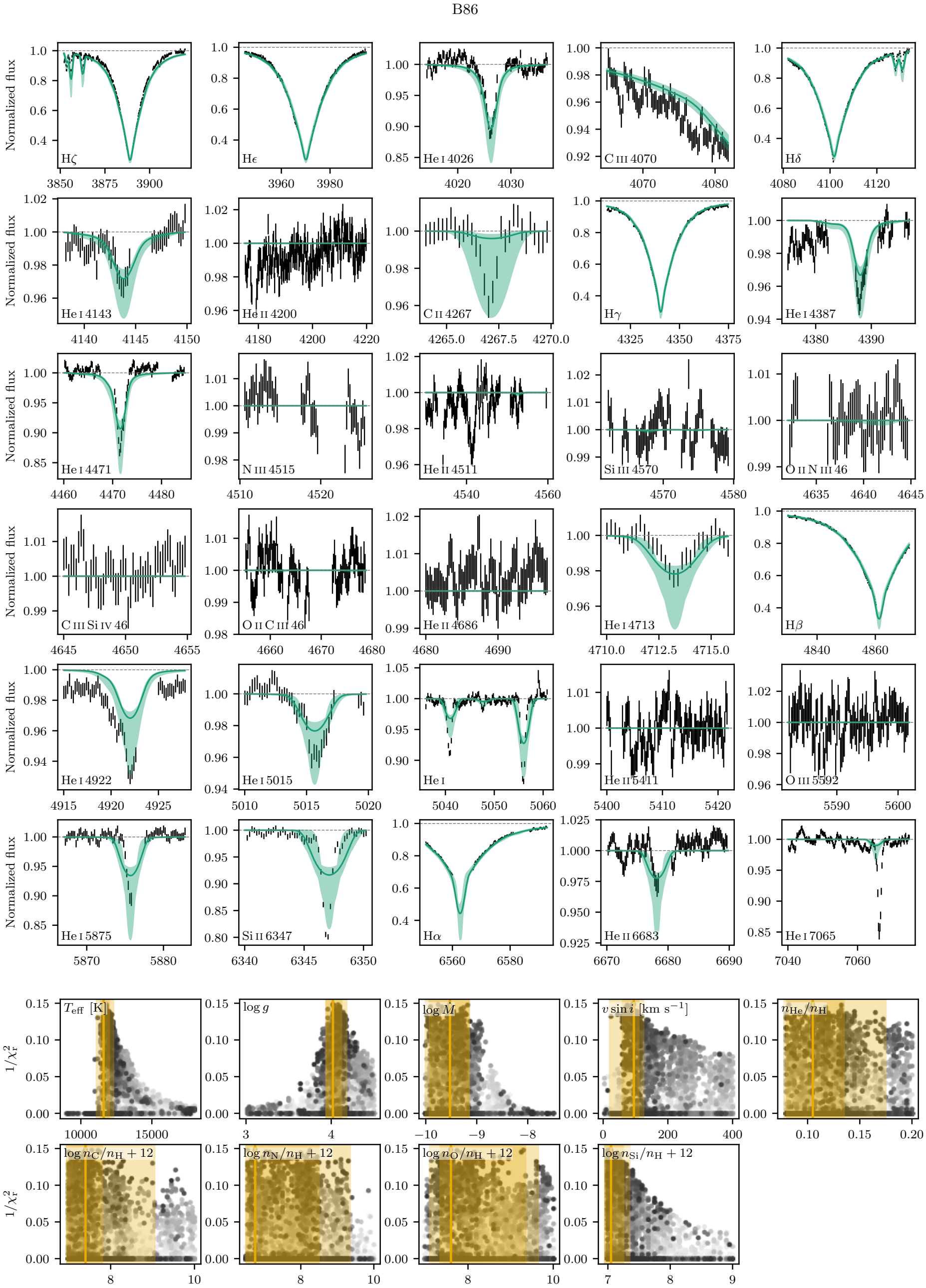

Figure III.20: Same as Figure 4.3, but for B86.

Chapter IV

Chapter 5

IV.1 Optical results

Here we briefly discuss the optical only fits and how they compare to the optical + UV fits. Table IV.1 lists the best fit values of the free parameters used in the optical only fits. Here we fixed $\beta = 1$, $f_{\rm cl} = 10$, $f_{\rm ic} = 0.1$, $f_{\rm vel} = 0.5$, $v_{\rm cl,start} = 0.05$, $v_{\rm windturb} = 0.1$, and we use the v_∞ from Hawcroft et al. (2023). Generally the optical only fits agree well with the fits using the full set of diagnostics. The most significant deviations are found in the lower mass-loss rates, with the optical-only fits resulting in significantly higher values at the low mass loss end. The available diagnostics in the optical are not well suited for constraining low rates, as the sensitivity of the line profiles to the mass-loss rate drops significantly. The wind diagnostics in the UV remains sensitive to lower values of the mass-loss rate. This indicates the importance of the UV diagnostic features in constraining low mass-loss rates.

IV.2 Mass loss relations

Here we show the same analysis as Section 5.5.3, but now fitting directly the mass-loss rates, rather than the modified wind momentum.

Figure IV.1 shows the mass-loss rate as function of the luminosity for each of the samples. The dotted lines indicate linear fits to the individual samples. The slope and offsets of these fits are listed in Table IV.2. A general trend of increased mass-loss rate for increased metallicity is visible. We fitted the linear fits at $\log L/{\rm L}_\odot = 5.75$ to determine the mass loss metallicity relation, and find $d\log\dot{M}/d\log Z = m = 1.01 \pm 0.26$, consistent with the wind momentum results.

Table IV.1: Best fit parameters and uncertainties of optical only fits. Rows with gray text indicate parameter values that are likely not representative of the stellar properties.

Source	$T_{\rm eff}$ [K]	$\log g$	$v \sin i$ [km s^{-1}]	$\log \dot{M}$	$y_{\rm He}$	$\epsilon_{\rm C}$	$\epsilon_{\rm N}$	$\epsilon_{\rm O}$	$\epsilon_{\rm Si}$
AV 80	43250^{+500}_{-250}	$3.84^{+0.12}_{-0.06}$	305^{+25}_{-20}	$-6.14^{+0.08}_{-0.05}$	$0.08^{+0.02}_{-0.01}$	$8.2^{+0.1}_{-0.8}$	$7.5^{+0.4}_{-0.4}$	$7.0^{+0.7}_{-0.8}$	$6.4^{+0.7}_{-0.4}$
AV 15	40500^{+750}_{-750}	$3.64^{+0.08}_{-0.06}$	110^{+10}_{-10}	$-6.07^{+0.08}_{-0.05}$	$0.10^{+0.01}_{-0.01}$	$7.5^{+0.3}_{-0.6}$	$7.8^{+0.2}_{-0.2}$	$6.1^{+1.1}_{-0.1}$	$6.3^{+0.5}_{-0.3}$
AV 83	37000^{+1750}_{-1750}	$3.24^{+0.24}_{-0.12}$	80^{+45}_{-20}	$-5.87^{+0.05}_{-0.05}$	$0.18^{+0.06}_{-0.05}$	$7.4^{+0.3}_{-1.4}$	$8.6^{+0.4}_{-0.3}$	$7.0^{+1.8}_{-1.1}$	$6.5^{+1.4}_{-0.6}$
AV 95	37750^{+1000}_{-250}	$3.60^{+0.08}_{-0.04}$	75^{+10}_{-10}	$-6.50^{+0.03}_{-0.08}$	$0.14^{+0.01}_{-0.02}$	$7.4^{+0.1}_{-0.5}$	$7.8^{+0.1}_{-0.1}$	$8.2^{+0.2}_{-0.8}$	$6.7^{+0.2}_{-0.7}$
AV 207	38250^{+750}_{-750}	$3.86^{+0.06}_{-0.06}$	110^{+10}_{-15}	$-7.02^{+0.13}_{-0.10}$	$0.12^{+0.01}_{-0.03}$	$7.5^{+0.2}_{-0.8}$	$7.9^{+0.1}_{-0.3}$	$8.4^{+0.4}_{-0.6}$	$6.5^{+0.4}_{-0.5}$
AV 69	36750^{+1500}_{-250}	$3.48^{+0.12}_{-0.06}$	100^{+10}_{-15}	$-6.47^{+0.08}_{-0.05}$	$0.09^{+0.03}_{-0.01}$	$7.5^{+0.4}_{-0.5}$	$6.7^{+0.2}_{-0.7}$	$6.2^{+1.1}_{-0.3}$	$6.8^{+0.3}_{-0.8}$
AV 469	33750^{+1000}_{-1000}	$3.24^{+0.12}_{-0.08}$	85^{+10}_{-10}	$-6.00^{+0.05}_{-0.08}$	$0.20^{+0.03}_{-0.04}$	$7.3^{+0.4}_{-0.4}$	$8.3^{+0.1}_{-0.3}$	$8.0^{+0.7}_{-0.2}$	$7.2^{+0.4}_{-0.3}$
2dFS 163	33500^{+750}_{-750}	$3.54^{+0.24}_{-0.18}$	90^{+35}_{-35}	$-6.20^{+0.08}_{-0.05}$	$0.08^{+0.05}_{-0.01}$	$7.2^{+0.5}_{-1.2}$	$7.8^{+0.6}_{-1.3}$	$6.2^{+2.0}_{-0.3}$	$6.2^{+0.7}_{-0.2}$
AV 479	33750^{+250}_{-750}	$3.34^{+0.04}_{-0.10}$	90^{+15}_{-5}	$-6.04^{+0.05}_{-0.08}$	$0.13^{+0.04}_{-0.01}$	$7.5^{+0.2}_{-0.2}$	$7.5^{+0.4}_{-0.2}$	$7.8^{+0.5}_{-1.0}$	$6.9^{+0.4}_{-0.2}$
AV 307	29250^{+250}_{-1750}	$3.42^{+0.06}_{-0.18}$	55^{+15}_{-10}	$-6.88^{+0.08}_{-0.28}$	$0.11^{+0.01}_{-0.03}$	$7.5^{+0.4}_{-0.3}$	$7.8^{+0.5}_{-0.3}$	$8.0^{+0.2}_{-0.5}$	$6.7^{+0.5}_{-0.3}$
AV 70	30750^{+750}_{-1000}	$3.02^{+0.06}_{-0.08}$	120^{+15}_{-15}	$-5.75^{+0.08}_{-0.05}$	$0.15^{+0.04}_{-0.01}$	$7.3^{+0.3}_{-0.2}$	$7.7^{+0.2}_{-0.2}$	$7.0^{+1.6}_{-1.0}$	$6.6^{+0.4}_{-0.2}$
AV 372	29750^{+1250}_{-500}	$2.88^{+0.14}_{-0.06}$	155^{+15}_{-5}	$-5.91^{+0.05}_{-0.05}$	$0.17^{+0.03}_{-0.03}$	$7.7^{+0.3}_{-0.3}$	$7.6^{+0.3}_{-0.2}$	$8.3^{+0.7}_{-2.2}$	$7.3^{+0.2}_{-0.5}$
AV 327	31750^{+750}_{-1000}	$3.26^{+0.10}_{-0.08}$	80^{+10}_{-15}	$-6.47^{+0.10}_{-0.18}$	$0.15^{+0.01}_{-0.04}$	$7.2^{+0.2}_{-0.3}$	$7.8^{+0.2}_{-0.4}$	$7.8^{+0.5}_{-1.7}$	$6.8^{+0.3}_{-0.2}$

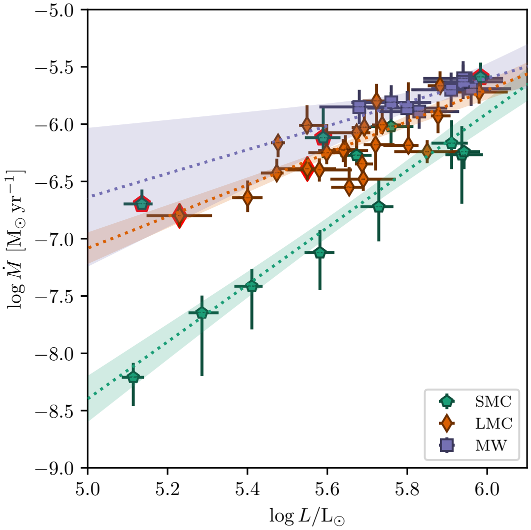

Figure IV.1: Mass-loss rates as function of luminosity for samples of SMC (this work), LMC (Brands et al. in prep.; Hawcroft et al. in prep.), and MW stars (Hawcroft et al. 2021). The dotted lines indicate the linear fits to the data for each of the metallicities, with the shaded region the 1σ confidence interval on the fit. The parameters of the fit are listed in Table IV.2.

Table IV.2: Slopes and offsets of the linear fits to the mass-loss rate as function of luminosity.

Galaxy	Slope	Offset
Milky Way	1.04±0.70	-11.82±4.07
LMC	1.49±0.19	-14.60±1.05
SMC	2.48±0.26	-20.81±1.48

IV.3 Fit covariance

The covariance matrix of the fit of Equation 5.8 to the empirically determined modified wind momentum rates is

$$Cov(a,b,c,d) = \begin{bmatrix} 0.18 & 0.34 & 0.06 & 0.03 \\ 0.34 & 0.90 & 0.17 & 0.06 \\ 0.06 & 0.17 & 0.06 & 0.02 \\ 0.03 & 0.06 & 0.02 & 0.01 \end{bmatrix}. \tag{IV.1}$$

IV.4 Fit summaries

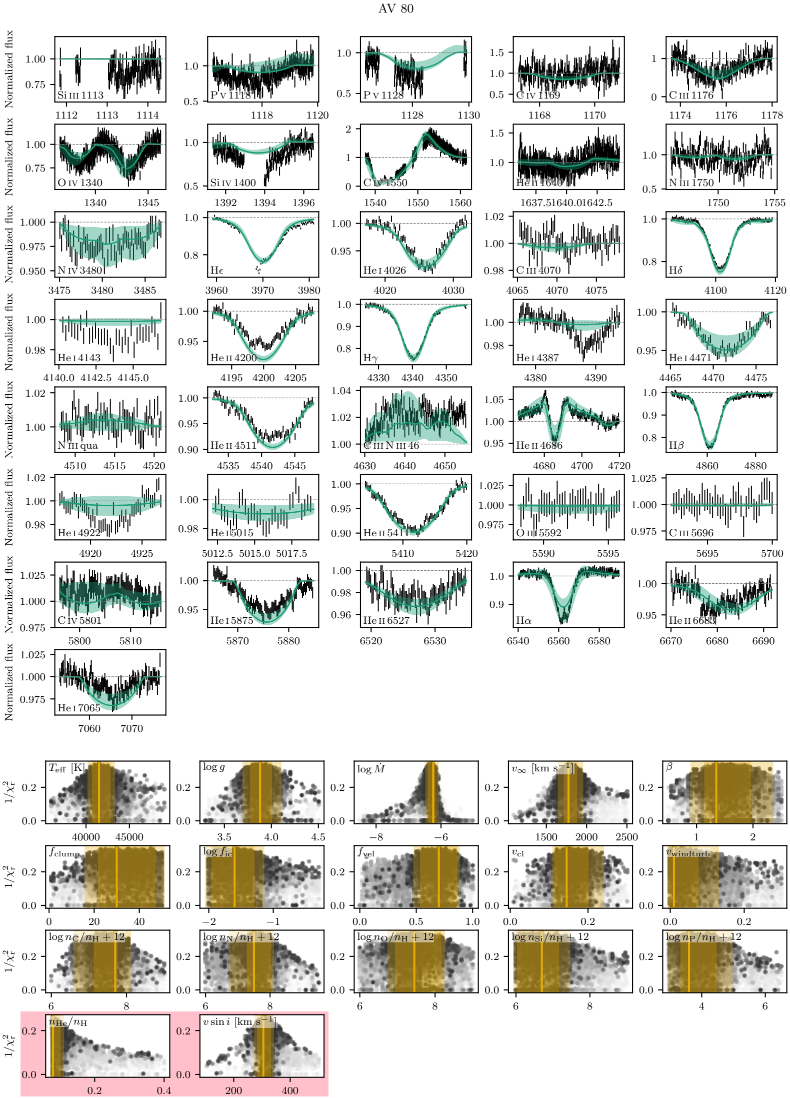

Figure IV.2: Overview of the fitting results of AV 80. The *top* part shows the line profiles included in the fitting process, with the name of each feature indicated in the bottom left. The green line shows the best fit, with the shaded region showing the 1σ uncertainty on the model fit. The black vertical bars indicate the observed flux, with the length indicating the uncertainty. The horizontal axis shows the wavelength in Å. The *bottom* part shows the distribution of $1/\chi^2_\mathrm{r}$ for each parameter (indicated on the top left), with χ^2_r the reduced χ^2 value. Each scatter point indicates one FASTWIND model calculated by Kiwi-GA. The color indicates the generation in which the model was computed, with light gray the first generation and black the last. The horizontal yellow line indicates the best fit value for each parameter, and the shaded regions are the 1 and 2 σ confidence intervals. The distributions in the red shaded area are from the optical only GA fit.

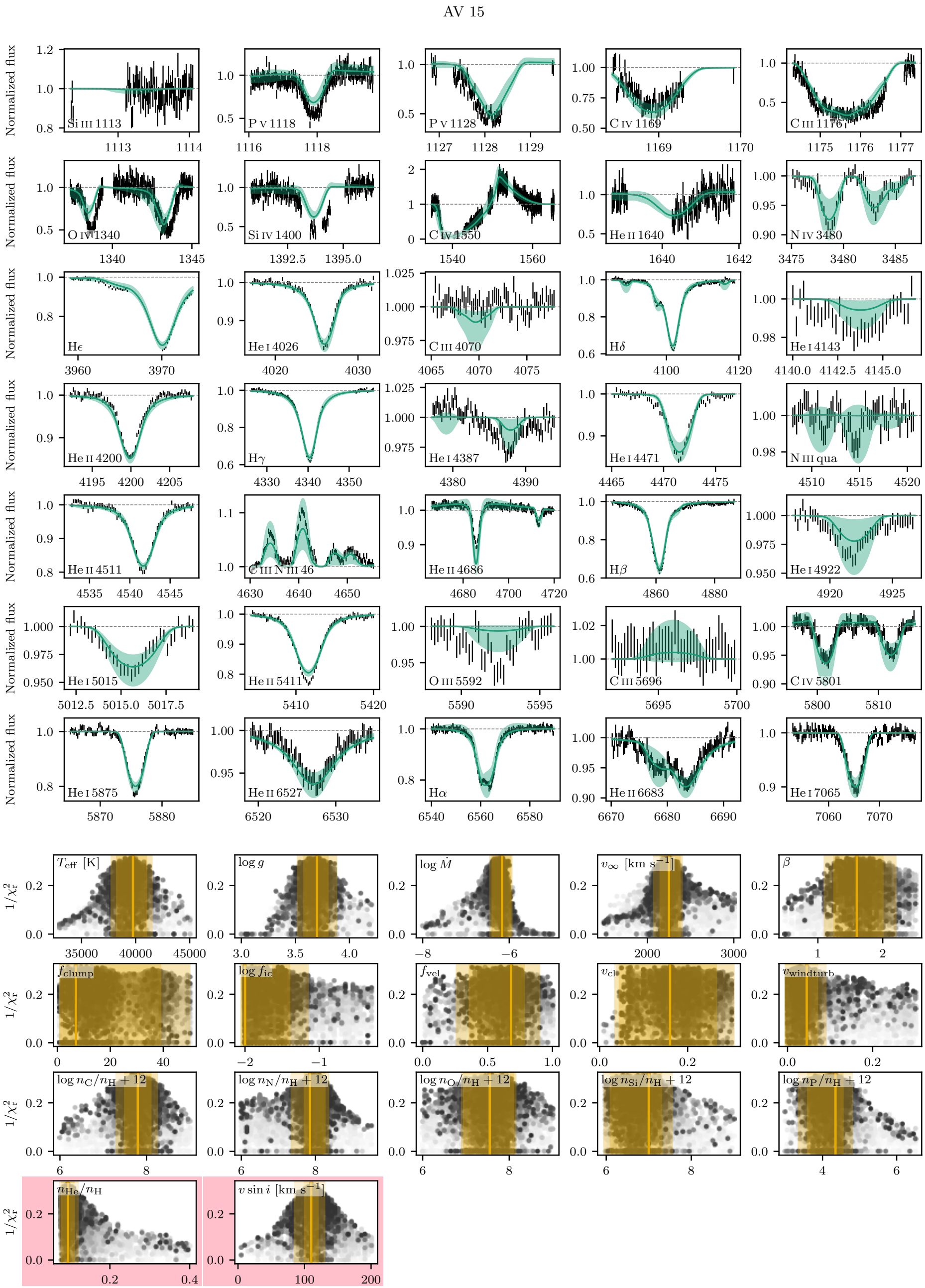

Figure IV.3: Same as Figure IV.2, but for AV 15.

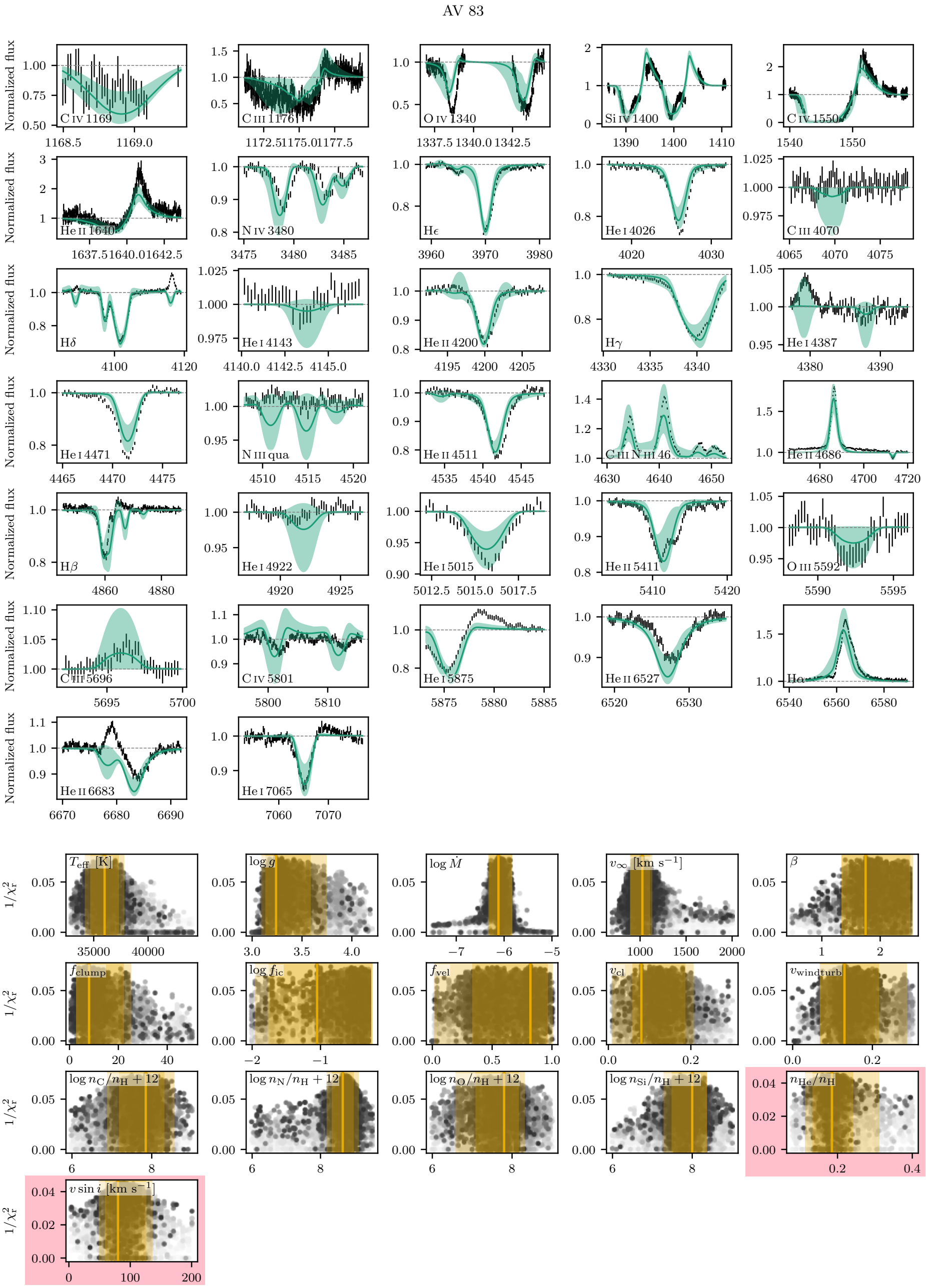

Figure IV.4: Same as Figure IV.2, but for AV 83.

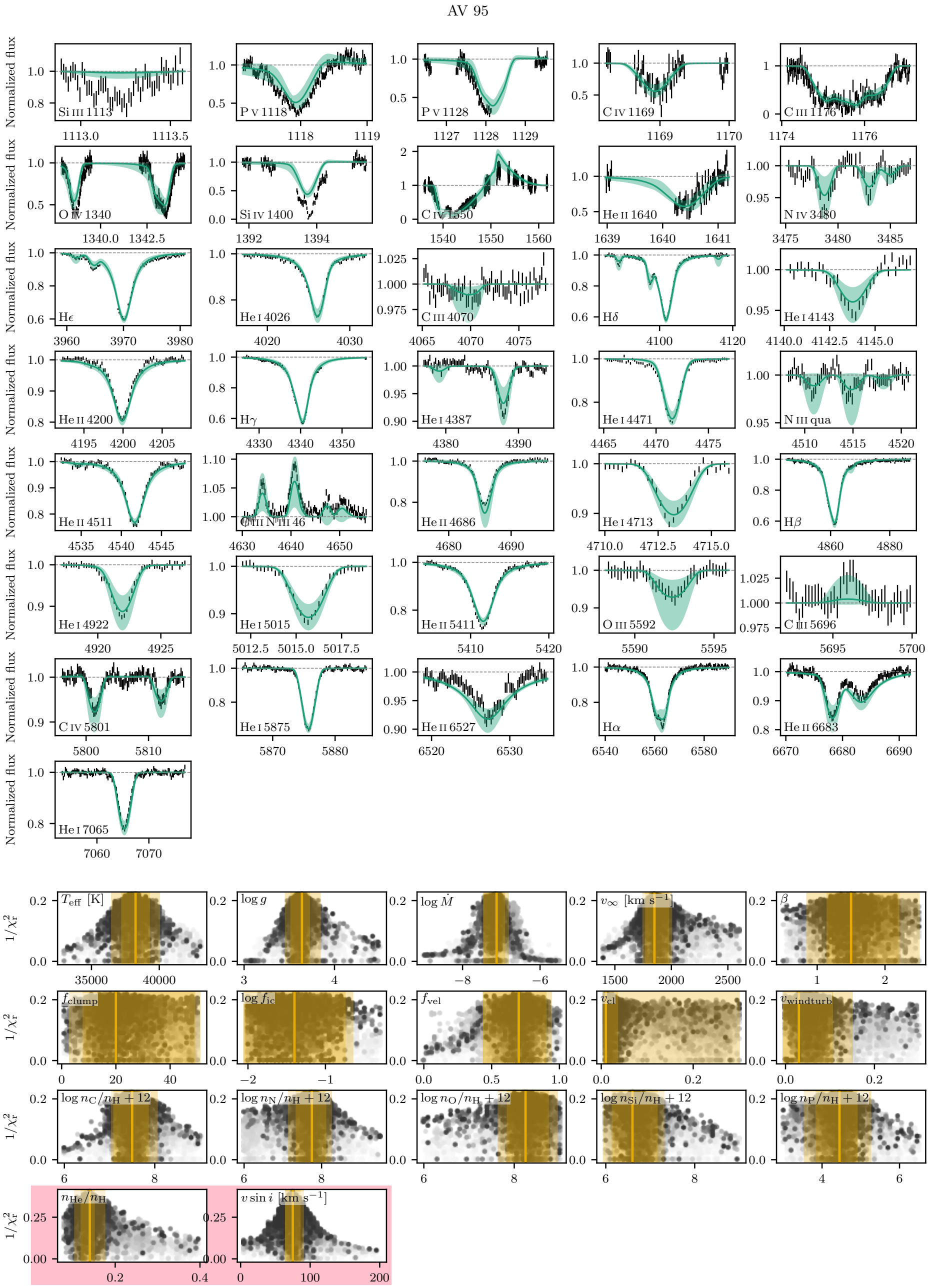

Figure IV.5: Same as Figure IV.2, but for AV 95.

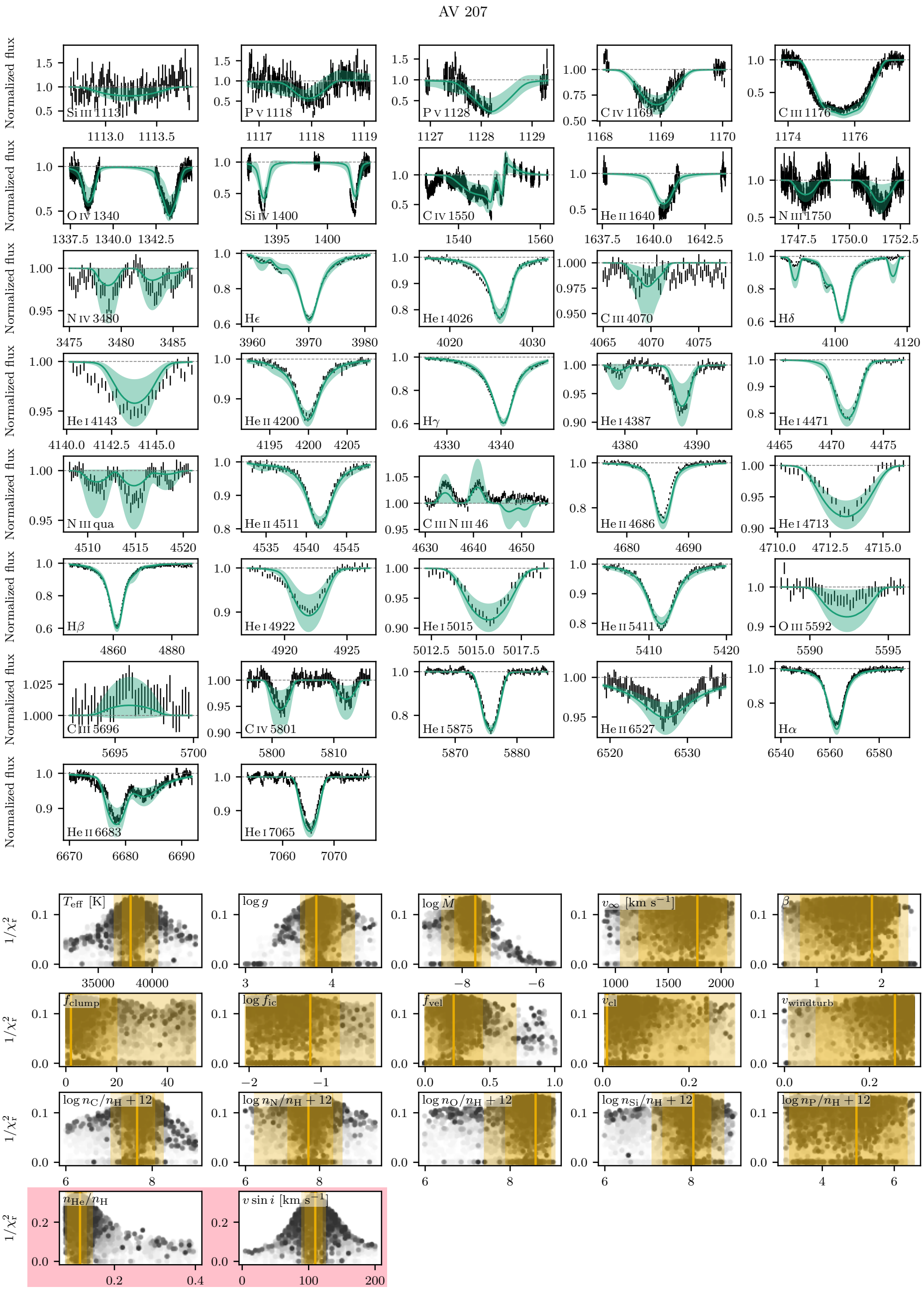

Figure IV.6: Same as Figure IV.2, but for AV 207.

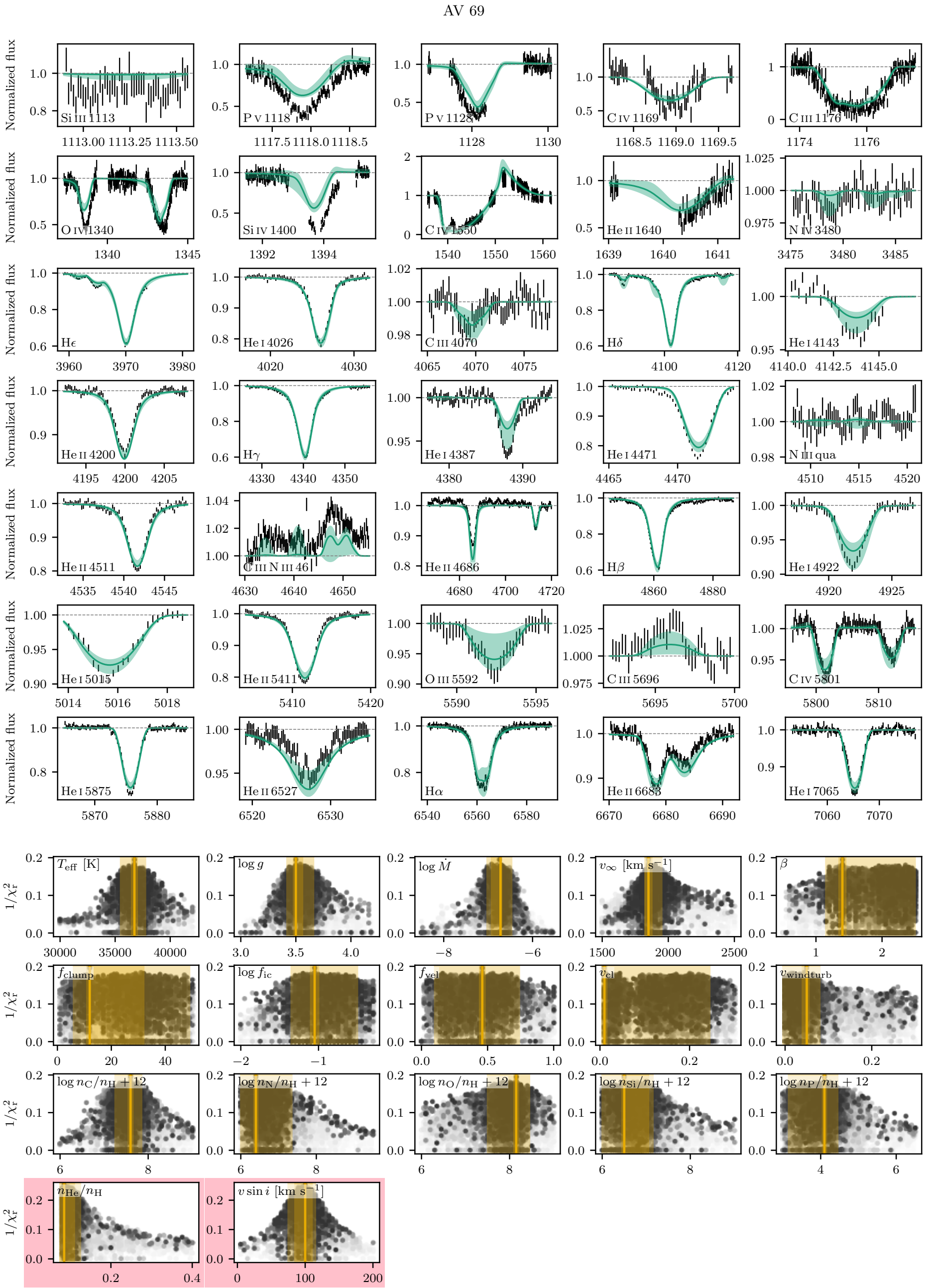

Figure IV.7: Same as Figure IV.2, but for AV 69.

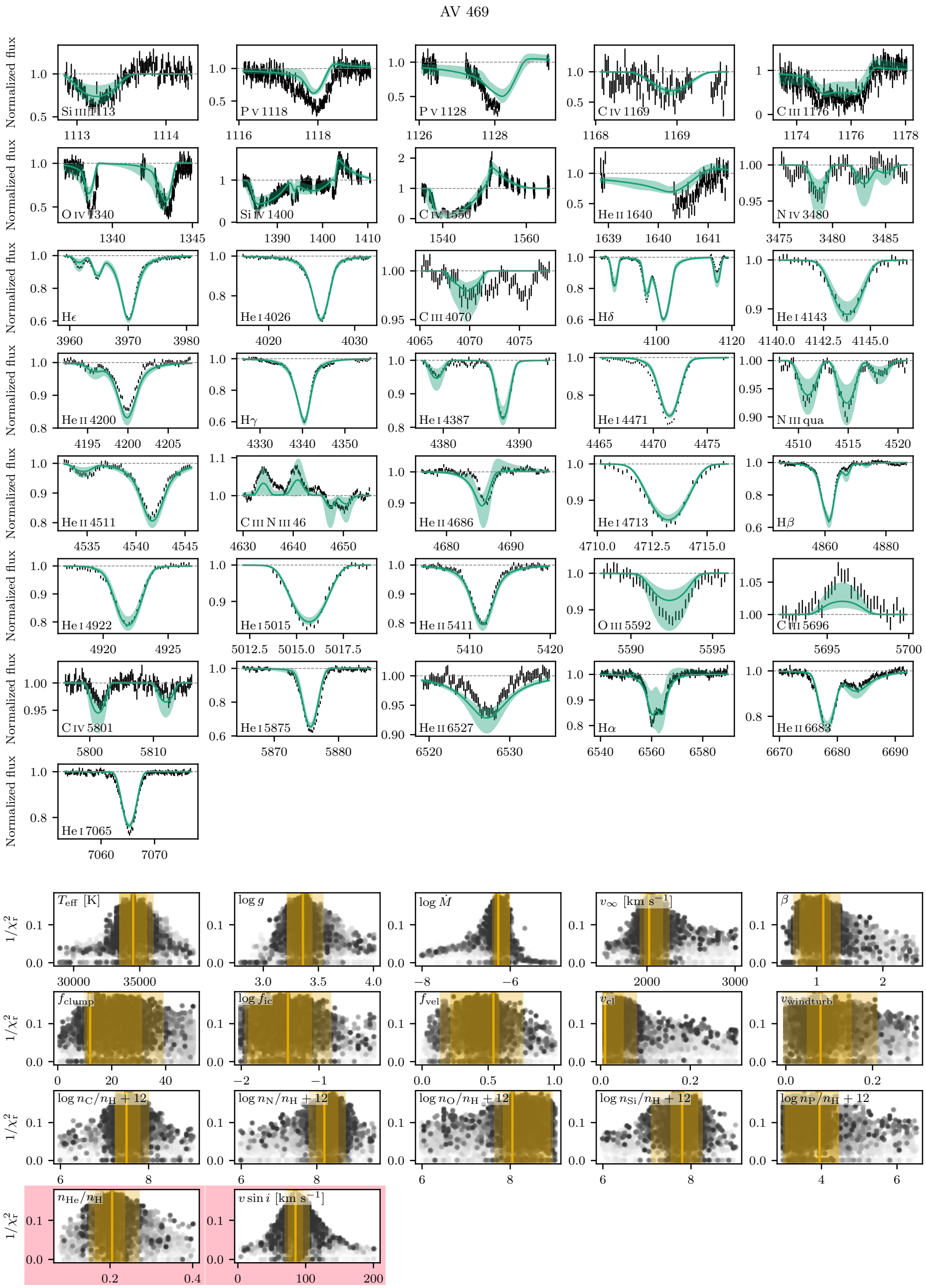

Figure IV.8: Same as Figure IV.2, but for AV 469.

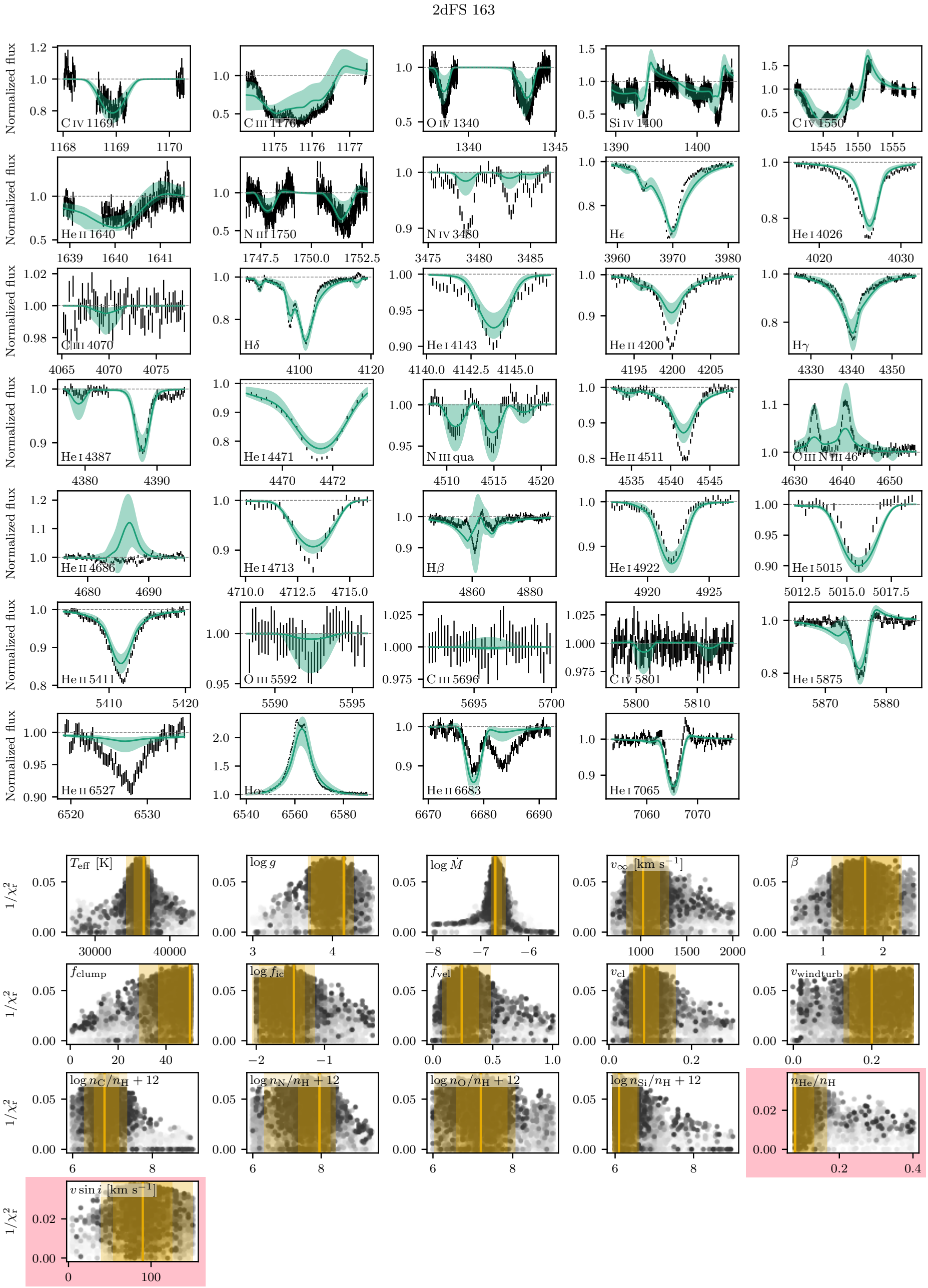

Figure IV.9: Same as Figure IV.2, but for 2dFS 163.

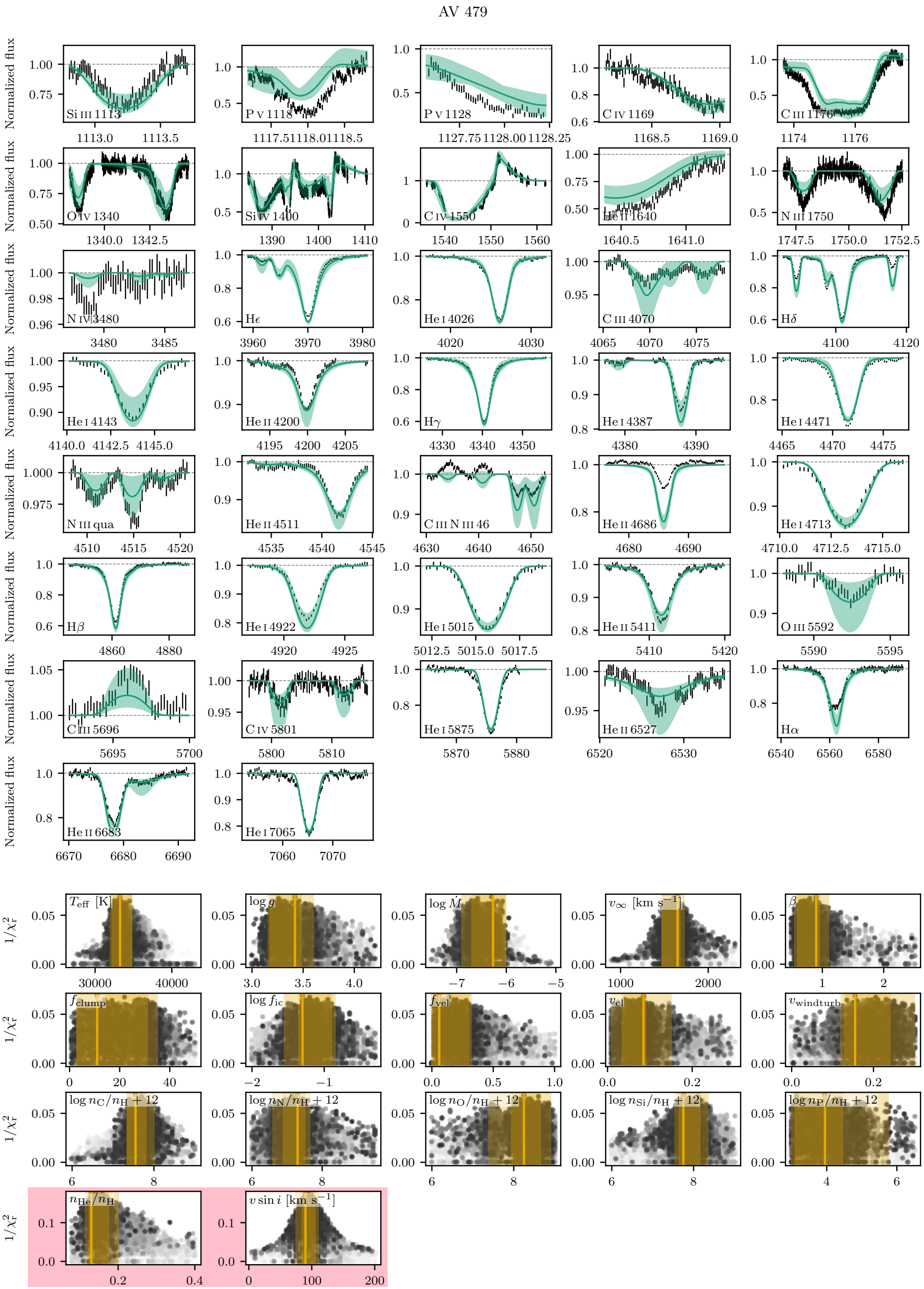

Figure IV.10: Same as Figure IV.2, but for AV 479.

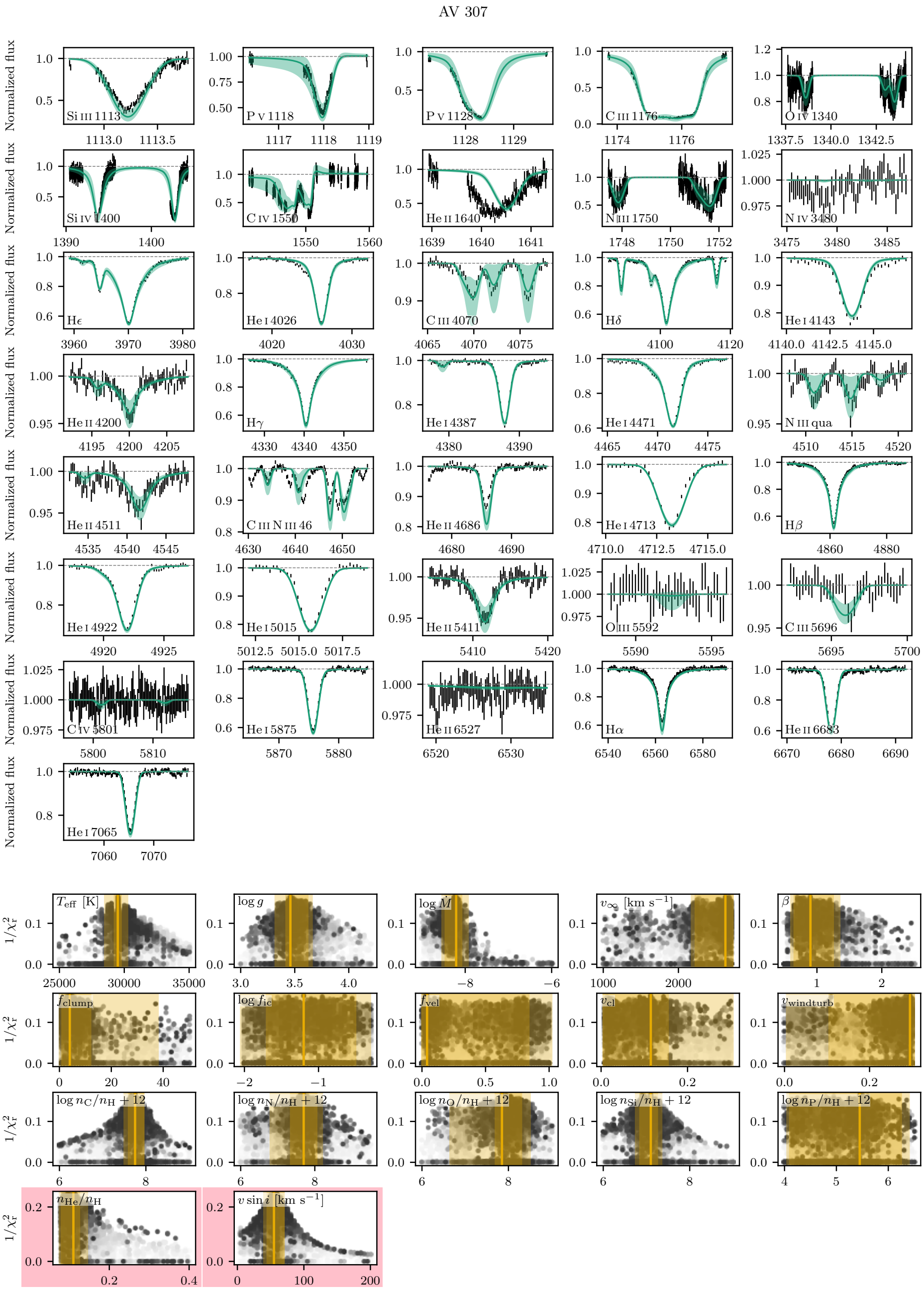

Figure IV.11: Same as Figure IV.2, but for AV 307.

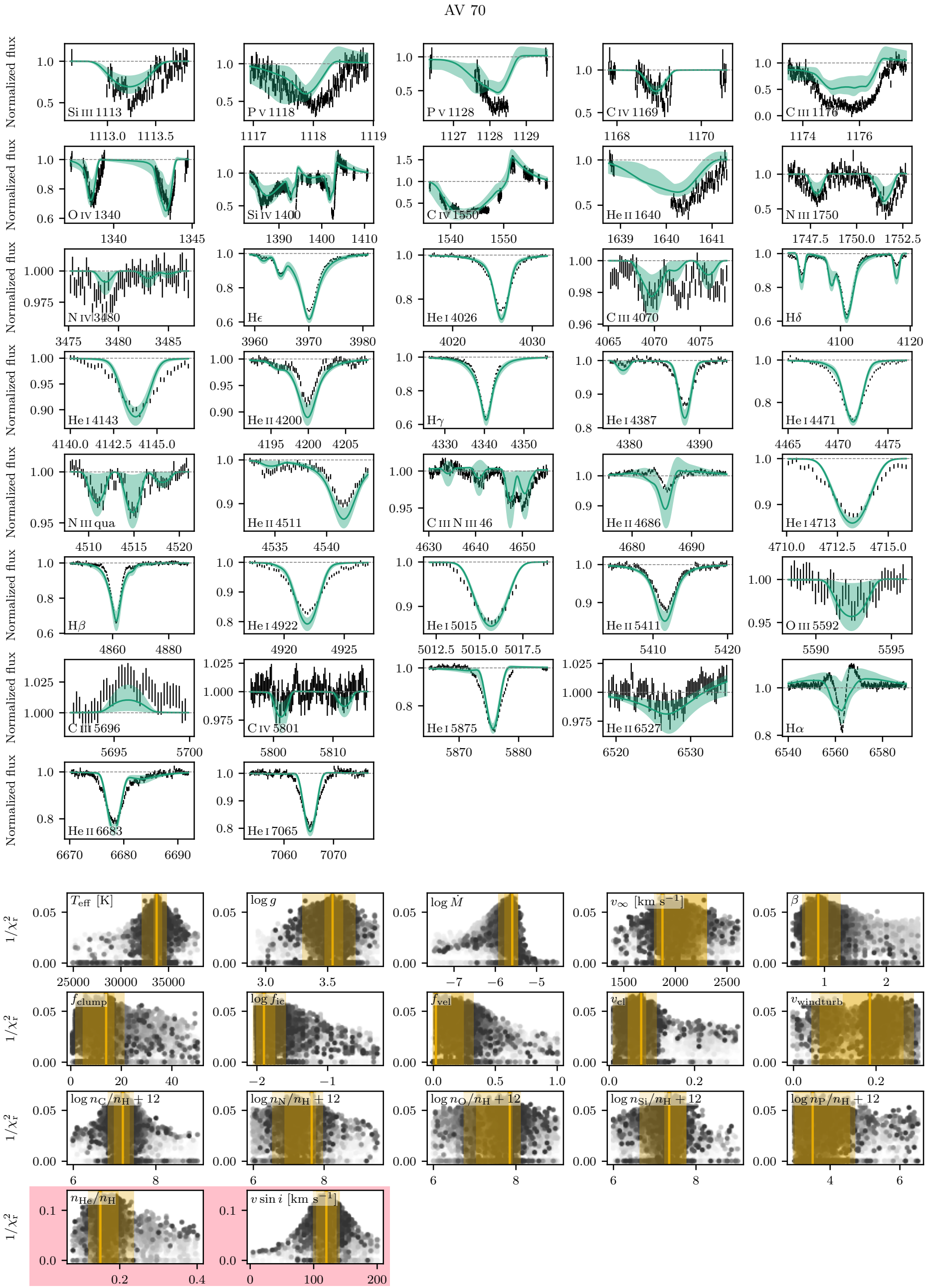

Figure IV.12: Same as Figure IV.2, but for AV 70.

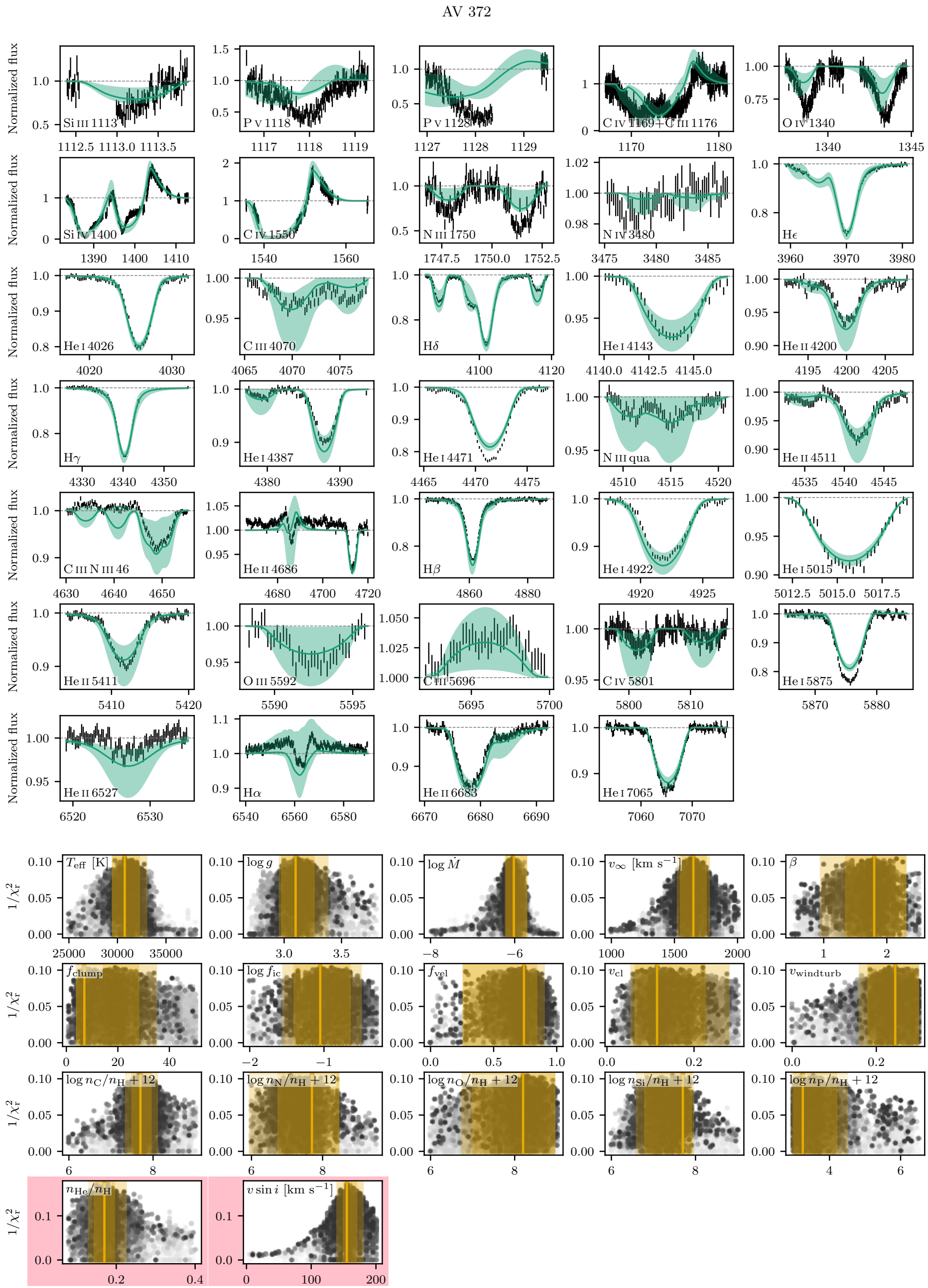

Figure IV.13: Same as Figure IV.2, but for AV 372.

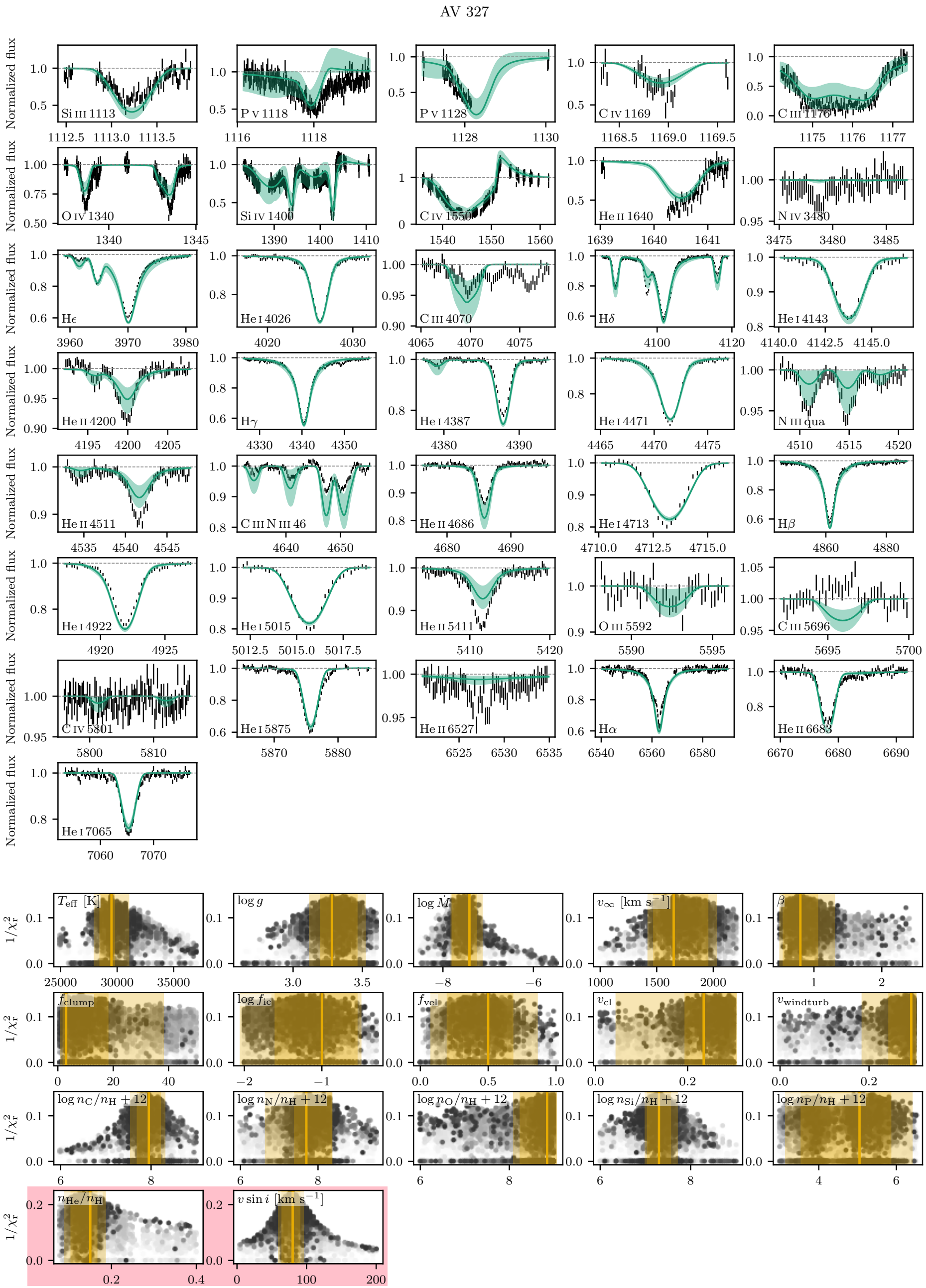

Figure IV.14: Same as Figure IV.2, but for AV 327.

Bibliography

2023, Astronomical Society of the Pacific Conference Series, Vol. 534, Protostars and Planets VII, *Protostars and Planets VII*

Abbott, B. P., Abbott, R., Abbott, T. D., et al. 2016, *Observation of Gravitational Waves from a Binary Black Hole Merger*, Phys. Rev. Lett., 116, 061102

Abbott, B. P., Abbott, R., Abbott, T. D., et al. 2017, *Multi-messenger Observations of a Binary Neutron Star Merger*, ApJ, 848, L12

Abbott, D. C., Bieging, J. H., Churchwell, E., & Cassinelli, J. P. 1980, *VLA radio continuum measurements of mass loss from early-type stars.*, ApJ, 238, 196

Abbott, D. C. & Lucy, L. B. 1985, *Multiline transfer and the dynamics of stellar winds.*, ApJ, 288, 679

Alecian, E., Wade, G. A., Catala, C., et al. 2013, *A high-resolution spectropolarimetric survey of Herbig Ae/Be stars - I. Observations and measurements*, MNRAS, 429, 1001

Alexander, R. D., Clarke, C. J., & Pringle, J. E. 2006, *Photoevaporation of protoplanetary discs - II. Evolutionary models and observable properties*, MNRAS, 369, 229

Allard, F., Homeier, D., & Freytag, B. 2012, *Models of very-low-mass stars, brown dwarfs and exoplanets*, Philosophical Transactions of the Royal Society of London Series A, 370, 2765

Almeida, L. A., Sana, H., Taylor, W., et al. 2017, *The Tarantula Massive Binary Monitoring. I. Observational campaign and OB-type spectroscopic binaries*, A&A, 598, A84

Alonso, A., Arribas, S., & Martínez-Roger, C. 1999, *The effective temperature scale of giant stars (F0-K5). II. Empirical calibration of* T_{eff} *versus colours and [Fe/H]*, A&AS, 140, 261

Andersson, E. P., Agertz, O., & Renaud, F. 2020, *How runaway stars boost galactic outflows*, MNRAS, 494, 3328

Apai, D., Bik, A., Kaper, L., Henning, T., & Zinnecker, H. 2007, *Massive Binaries in High-Mass Star-forming Regions: A Multiepoch Radial Velocity Survey of Embedded O Stars*, ApJ, 655, 484

Araya, E., Hofner, P., Kurtz, S., Olmi, L., & Linz, H. 2008, *Thermal Methanol Observations of the Outflow from the G31.41+0.31 Hot Molecular Core*, ApJ, 675, 420

Aresu, G., Kamp, I., Meijerink, R., et al. 2011, *X-ray impact on the protoplanetary disks around T Tauri stars*, A&A, 526, A163

Arias, J. I., Barbá, R. H., & Morrell, N. I. 2007, *Pre-main-sequence stars in the Lagoon Nebula (M8)*, MNRAS, 374, 1253

Asplund, M., Grevesse, N., Sauval, A. J., & Scott, P. 2009, *The Chemical Composition of the Sun*, ARA&A, 47, 481

Backs, F., Poorta, J., Rab, C., et al. 2023, *Massive pre-main-sequence stars in M17. Modelling hydrogen and dust in MYSO disks*, A&A, 671, A13

Bagnulo, S., Landstreet, J. D., Fossati, L., & Kochukhov, O. 2012, *Magnetic field measurements and their uncertainties: the FORS1 legacy*, A&A, 538, A129

Balbus, S. A. & Hawley, J. F. 1998, *Instability, turbulence, and enhanced transport in accretion disks*, Reviews of Modern Physics, 70, 1

Barbá, R. H., Gamen, R., Arias, J. I., & Morrell, N. I. 2017, *OWN Survey: a spectroscopic monitoring of Southern Galactic O and WN-type stars*, Proceedings of the International Astronomical Union, 12, 89

Bate, M. R. 2009, *Stellar, brown dwarf and multiple star properties from hydrodynamical simulations of star cluster formation*, MNRAS, 392, 590

Bate, M. R. 2018, *On the diversity and statistical properties of protostellar discs*, MNRAS, 475, 5618

Bate, M. R., Bonnell, I. A., & Bromm, V. 2002, *The formation of close binary systems by dynamical interactions and orbital decay*, MNRAS, 336, 705

Baume, G., Rodríguez, M. J., Corti, M. A., Carraro, G., & Panei, J. A. 2014, *A deep and wide-field view at the IC 2944/2948 complex in Centaurus**, MNRAS, 443, 411

Beltrán, M. T. & de Wit, W. J. 2016, *Accretion disks in luminous young stellar objects*, A&A Rev., 24, 6

Benjamin, R. A., Churchwell, E., Babler, B. L., et al. 2003, *GLIMPSE. I. An SIRTF Legacy Project to Map the Inner Galaxy*, PASP, 115, 953

Bik, A., Henning, T., Stolte, A., et al. 2012, *Age Spread in W3 Main: Large Binocular Telescope/LUCI Near-infrared Spectroscopy of the Massive Stellar Content*, ApJ, 744, 87

Bik, A., Kaper, L., & Waters, L. B. F. M. 2006, *VLT K-band spectroscopy of massive young stellar objects in (ultra-)compact HII regions*, A&A, 455, 561

Björklund, R., Sundqvist, J. O., Puls, J., & Najarro, F. 2021, *New predictions for radiation-driven, steady-state mass-loss and wind-momentum from hot, massive stars. II. A grid of O-type stars in the Galaxy and the Magellanic Clouds*, A&A, 648, A36

Blondel, P. F. C. & Djie, H. R. E. T. A. 2006, *Modeling of PMS Ae/Fe stars using UV spectra*, A&A, 456, 1045

Boggs, P. T., Byrd, R. H., Donaldson, J. R., & Schnabel, R. B. 1987, *ODRPACK Software for Weighted Orthogonal Distance Regression.*, Tech. rep., COLORADO UNIV AT BOULDER DEPT OF COMPUTER SCIENCE

Bonanos, A. Z., Lennon, D. J., Köhlinger, F., et al. 2010, *Spitzer SAGE-SMC Infrared Photometry of Massive Stars in the Small Magellanic Cloud*, AJ, 140, 416

Bonnell, I. A. & Bate, M. R. 2005, *Binary systems and stellar mergers in massive star formation*, MNRAS, 362, 915

Bonnell, I. A. & Bate, M. R. 2006, *Star formation through gravitational collapse and competitive accretion*, MNRAS, 370, 488

Bonnell, I. A., Bate, M. R., Clarke, C. J., & Pringle, J. E. 2001, *Competitive accretion in embedded stellar clusters*, MNRAS, 323, 785

Bordier, E., Frost, A. J., Sana, H., et al. 2022, *The origin of close massive binaries in the M17 star-forming region*, A&A, 663, A26

Bouret, J. C., Lanz, T., Hillier, D. J., et al. 2003, *Quantitative Spectroscopy of O Stars at Low Metallicity: O Dwarfs in NGC 346*, ApJ, 595, 1182

Brands, S. A., Backs, F., & de Koter, A. in prep., *X-Shooting ULLYSES: massive stars at low metallicity – The clumped winds of O-type (super)giants in the Large Magellanic Cloud*, A&A

Brands, S. A., de Koter, A., Bestenlehner, J. M., et al. 2022, *The R136 star cluster dissected with Hubble Space Telescope/STIS. III. The most massive stars and their clumped winds*, A&A, 663, A36

Brent, R. P. 1973, *Some Efficient Algorithms for Solving Systems of Nonlinear Equations*, SIAM Journal on Numerical Analysis, 10, 327

Bressan, A., Marigo, P., Girardi, L., et al. 2012, *PARSEC: stellar tracks and isochrones with the PAdova and TRieste Stellar Evolution Code*, MNRAS, 427, 127

Bromm, V., Yoshida, N., Hernquist, L., & McKee, C. F. 2009, *The formation of the first stars and galaxies*, Nature, 459, 49

Broos, P. S., Feigelson, E. D., Townsley, L. K., et al. 2007, *The Young Stellar Population in M17 Revealed by Chandra*, ApJS, 169, 353

Broos, P. S., Getman, K. V., Povich, M. S., et al. 2013, *Identifying Young Stars in Massive Star-forming Regions for the MYStIX Project*, ApJS, 209, 32

Brott, I., de Mink, S. E., Cantiello, M., et al. 2011, *Rotating massive main-sequence stars. I. Grids of evolutionary models and isochrones*, A&A, 530, A115

Butler, S. E. & Dalgarno, A. 1980, *Charge transfer of C/+/ and S/+/ in diffuse nebulae*, A&A, 85, 144

Calvet, N. & Gullbring, E. 1998, *The Structure and Emission of the Accretion Shock in T Tauri Stars*, ApJ, 509, 802

Campbell, E. K., Holz, M., Gerlich, D., & Maier, J. P. 2015, *Laboratory confirmation of* ${C_{60}}^{+}$ *as the carrier of two diffuse interstellar bands*, Nature, 523, 322

Cantiello, M., Yoon, S. C., Langer, N., & Livio, M. 2007, *Binary star progenitors of long gamma-ray bursts*, A&A, 465, L29

Caratti o Garatti, A., Stecklum, B., Weigelt, G., et al. 2016, *Tracing jet emission at the base of a high-mass YSO. First AMBER/VLTI observations of the Br*γ *emission in IRAS 13481-6124*, A&A, 589, L4

Carneiro, L. P., Puls, J., Sundqvist, J. O., & Hoffmann, T. L. 2016, *Atmospheric NLTE models for the spectroscopic analysis of blue stars with winds. III. X-ray emission from wind-embedded shocks*, A&A, 590, A88

Castelli, F. & Kurucz, R. L. 2004a, *Is missing Fe I opacity in stellar atmospheres a significant problem?*, A&A, 419, 725

Castelli, F. & Kurucz, R. L. 2004b, *New Grids of ATLAS9 Model Atmospheres*, ArXiv Astrophysics e-prints

Castor, J. I., Abbott, D. C., & Klein, R. I. 1975, *Radiation-driven winds in Of stars.*, ApJ, 195, 157

Castor, J. I. & Lamers, H. J. G. L. M. 1979, *An atlas of theoretical P Cygni profiles.*, ApJS, 39, 481

Cesaroni, R., Beltrán, M. T., Zhang, Q., Beuther, H., & Fallscheer, C. 2011, *Dissecting a hot molecular core: the case of G31.41+0.31*, A&A, 533, A73

Cesaroni, R., Galli, D., Lodato, G., Walmsley, M., & Zhang, Q. 2006, *The critical role of disks in the formation of high-mass stars*, Nature, 444, 703

Cesaroni, R., Galli, D., Neri, R., & Walmsley, C. M. 2014, *Imaging the disk around IRAS 20126+4104 at subarcsecond resolution*, A&A, 566, A73

Charbonneau, P. 1995, *Genetic Algorithms in Astronomy and Astrophysics*, ApJS, 101, 309

Chen, T.-W., Smartt, S. J., Yates, R. M., et al. 2017, *Superluminous supernova progenitors have a half-solar metallicity threshold*, MNRAS, 470, 3566

Chini, R., Elsaesser, H., & Neckel, T. 1980, *Multicolour UBVRI photometry of stars in M 17*, A&A, 91, 186

Chini, R., Hoffmeister, V. H., Nasseri, A., Stahl, O., & Zinnecker, H. 2012, *A spectroscopic survey on the multiplicity of high-mass stars*, MNRAS, 424, 1925

Choi, J., Dotter, A., Conroy, C., et al. 2016, *Mesa Isochrones and Stellar Tracks (MIST). I. Solar-scaled Models*, ApJ, 823, 102

Churchwell, E. 1990, *Statistical analysis of measurement error models and applications*, in Contemporary mathematics (American Mathematical Society), Vol. 112, Hot Star Workshop III: The Earliest Phases of Massive Star Birth, ed. P. Brown & W. Fuller, 186

Cox, A. N. 2000, Allen's astrophysical quantities

Cox, N. L. J., Cami, J., Farhang, A., et al. 2017, *The ESO Diffuse Interstellar Bands Large Exploration Survey (EDIBLES) . I. Project description, survey sample, and quality assessment*, A&A, 606, A76

Crowther, P. A., Broos, P. S., Townsley, L. K., et al. 2022, *X-ray properties of early-type stars in the Tarantula Nebula from T-ReX*, MNRAS, 515, 4130

Crowther, P. A., Hillier, D. J., Evans, C. J., et al. 2002, *Revised Stellar Temperatures for Magellanic Cloud O Supergiants from Far Ultraviolet Spectroscopic Explorer and Very Large Telescope UV-Visual Echelle Spectrograph Spectroscopy*, ApJ, 579, 774

Crowther, P. A., Lennon, D. J., & Walborn, N. R. 2006, *Physical parameters and wind properties of galactic early B supergiants*, A&A, 446, 279

Dale, J. E. & Bonnell, I. 2011, *Ionizing feedback from massive stars in massive clusters: fake bubbles and untriggered star formation*, MNRAS, 414, 321

De Becker, M., Rauw, G., Manfroid, J., & Eenens, P. 2006, *Early-type stars in the young open cluster IC 1805. II. The probably single stars HD15570 and HD15629, and the massive binary/triple system HD15558*, A&A, 456, 1121

de Koter, A., Heap, S. R., & Hubeny, I. 1997, *On the Evolutionary Phase and Mass Loss of the Wolf-Rayet–like Stars in R136a*, ApJ, 477, 792

de Mink, S. E., Langer, N., Izzard, R. G., Sana, H., & de Koter, A. 2013, *The Rotation Rates of Massive Stars: The Role of Binary Interaction through Tides, Mass Transfer, and Mergers*, ApJ, 764, 166

de Mink, S. E. & Mandel, I. 2016, *The chemically homogeneous evolutionary channel for binary black hole mergers: rates and properties of gravitational-wave events detectable by advanced LIGO*, MNRAS, 460, 3545 de Mink, S. E., Pols, O. R., & Hilditch, R. W. 2007, *Efficiency of mass transfer in massive close binaries. Tests from double-lined eclipsing binaries in the SMC*, A&A, 467, 1181

de Wit, W. J., Hoare, M. G., Oudmaijer, R. D., et al. 2011, *Mid-infrared interferometry towards the massive young stellar object CRL 2136: inside the dust rim*, A&A, 526, L5

de Wit, W. J., Testi, L., Palla, F., & Zinnecker, H. 2005, *The origin of massive O-type field stars: II. Field O stars as runaways*, A&A, 437, 247

Derkink, A. R., Ramírez-Tannus, M., & Kaper, L. 2023, subm., *Pre-main-sequence stars in M17 – Spectroscopic variability*, A&A

Dopita, M. A., Seitenzahl, I. R., Sutherland, R. S., et al. 2019, *Calibrating Interstellar Abundances Using Supernova Remnant Radiative Shocks*, AJ, 157, 50

Dormand, J. R. & Prince, P. J. 1980, *A family of embedded Runge-Kutta formulae*, Journal of computational and applied mathematics, 6, 19

Dotter, A. 2016, *MESA Isochrones and Stellar Tracks (MIST) 0: Methods for the Construction of Stellar Isochrones*, ApJS, 222, 8

Draine, B. T. 2003, *Interstellar Dust Grains*, ARA&A, 41, 241

Draine, B. T. 2011, Physics of the Interstellar and Intergalactic Medium

Dubrulle, B., Morfill, G., & Sterzik, M. 1995, *The dust subdisk in the protoplanetary nebula.*, Icarus, 114, 237

Duez, V. & Mathis, S. 2010, *Relaxed equilibrium configurations to model fossil fields . I. A first family*, A&A, 517, A58

Dufton, P. L., Langer, N., Dunstall, P. R., et al. 2013, *The VLT-FLAMES Tarantula Survey. X. Evidence for a bimodal distribution of rotational velocities for the single early B-type stars*, A&A, 550, A109

Dullemond, C. P. & Dominik, C. 2004, *Flaring vs. self-shadowed disks: The SEDs of Herbig Ae/Be stars*, A&A, 417, 159

Dullemond, C. P., Dominik, C., & Natta, A. 2001, *Passive Irradiated Circumstellar Disks with an Inner Hole*, ApJ, 560, 957

Dunstall, P. R., Dufton, P. L., Sana, H., et al. 2015, *The VLT-FLAMES Tarantula Survey. XXII. Multiplicity properties of the B-type stars*, A&A, 580, A93

Efstathiou, G. 2000, *A model of supernova feedback in galaxy formation*, MNRAS, 317, 697

Ekström, S., Georgy, C., Eggenberger, P., et al. 2012, *Grids of stellar models with rotation. I. Models from 0.8 to 120 M at solar metallicity (Z = 0.014)*, A&A, 537, A146

Eldridge, J. J. & Stanway, E. R. 2016, *BPASS predictions for binary black hole mergers*, MNRAS, 462, 3302

Ellerbroek, L. E., Bik, A., Kaper, L., et al. 2013, *<ASTROBJ>RCW36</ASTROBJ>: characterizing the outcome of massive star formation*, A&A, 558, A102

Evans, C. J., Howarth, I. D., Irwin, M. J., Burnley, A. W., & Harries, T. J. 2004, *A 2dF survey of the Small Magellanic Cloud*, MNRAS, 353, 601

Eversberg, T., Lépine, S., & Moffat, A. F. J. 1998, *Outmoving Clumps in the Wind of the Hot O Supergiant ζ Puppis*, ApJ, 494, 799

Fairlamb, J. R., Oudmaijer, R. D., Mendigutía, I., Ilee, J. D., & van den Ancker, M. E. 2015, *A spectroscopic survey of Herbig Ae/Be stars with X-shooter - I. Stellar parameters and accretion rates*, MNRAS, 453, 976

Fairlamb, J. R., Oudmaijer, R. D., Mendigutia, I., Ilee, J. D., & van den Ancker, M. E. 2017, *A spectroscopic survey of Herbig Ae/Be stars with X-Shooter - II. Accretion diagnostic lines*, MNRAS, 464, 4721

Feigelson, E. D., Townsley, L. K., Broos, P. S., et al. 2013, *Overview of the Massive Young Star-Forming Complex Study in Infrared and X-Ray (MYStIX) Project*, ApJS, 209, 26

Feldmeier, A., Puls, J., & Pauldrach, A. W. A. 1997, *A possible origin for X-rays from O stars.*, A&A, 322, 878

Fitzpatrick, E. L. 1999, *Correcting for the Effects of Interstellar Extinction*, PASP, 111, 63

Fossati, L., Castro, N., Schöller, M., et al. 2015, *B fields in OB stars (BOB): Low-resolution FORS2 spectropolarimetry of the first sample of 50 massive stars*, A&A, 582, A45

Fouqué, P., Chevallier, L., Cohen, M., et al. 2000, *An absolute calibration of DENIS (deep near infrared southern sky survey)*, A&AS, 141, 313

Fregeau, J. M., Cheung, P., Portegies Zwart, S. F., & Rasio, F. A. 2004, *Stellar collisions during binary-binary and binary-single star interactions*, MNRAS, 352, 1

Frost, A. J., Oudmaijer, R. D., de Wit, W. J., & Lumsden, S. L. 2021, *Unveiling the traits of massive young stellar objects through a multi-scale survey*, A&A, 648, A62

Fujii, M. S. & Portegies Zwart, S. 2011, *The Origin of OB Runaway Stars*, Science, 334, 1380

Fullerton, A. W., Massa, D. L., & Prinja, R. K. 2006, *The Discordance of Mass-Loss Estimates for Galactic O-Type Stars*, ApJ, 637, 1025

Furlan, E., Luhman, K. L., Espaillat, C., et al. 2011, *The Spitzer Infrared Spectrograph Survey of T Tauri Stars in Taurus*, ApJS, 195, 3

Gangi, M., Nisini, B., Antoniucci, S., et al. 2020, *GIARPS High-resolution Observations of T Tauri stars (GHOsT). II. Connecting atomic and molecular winds in protoplanetary disks*, A&A, 643, A32

Garmany, C. D., Conti, P. S., & Massey, P. 1987, *Studies of Massive Stars in the Magellanic Clouds. II. New Spectral Classifications of OB Stars in the SMC*, AJ, 93, 1070

Garufi, A., Meeus, G., Benisty, M., et al. 2017, *Evolution of protoplanetary disks from their taxonomy in scattered light: Group I vs. Group II*, A&A, 603, A21

Gayley, K. G. 1995, *An Improved Line-Strength Parameterization in Hot-Star Winds*, ApJ, 454, 410

Geen, S., Bieri, R., Rosdahl, J., & de Koter, A. 2021, *The geometry and dynamical role of stellar wind bubbles in photoionized H II regions*, MNRAS, 501, 1352

Geen, S. & de Koter, A. 2022, *Bottling the champagne: dynamics and radiation trapping of wind-driven bubbles around massive stars*, MNRAS, 509, 4498

Geen, S., Hennebelle, P., Tremblin, P., & Rosdahl, J. 2015, *Photoionization feedback in a self-gravitating, magnetized, turbulent cloud*, MNRAS, 454, 4484

Geen, S., Hennebelle, P., Tremblin, P., & Rosdahl, J. 2016, *Feedback in Clouds II: UV photoionization and the first supernova in a massive cloud*, MNRAS, 463, 3129

Geen, S., Pellegrini, E., Bieri, R., & Klessen, R. 2020, *When H II regions are complicated: considering perturbations from winds, radiation pressure, and other effects*, MNRAS, 492, 915

Glassgold, A. E., Najita, J., & Igea, J. 1997, *X-Ray Ionization of Protoplanetary Disks*, ApJ, 480, 344

Gorti, U. & Hollenbach, D. 2009, *Photoevaporation of Circumstellar Disks By Far-Ultraviolet, Extreme-Ultraviolet and X-Ray Radiation from the Central Star*, ApJ, 690, 1539

Graczyk, D., Pietrzyński, G., Thompson, I. B., et al. 2020, *A Distance Determination to the Small Magellanic Cloud with an Accuracy of Better than Two Percent Based on Late-type Eclipsing Binary Stars*, ApJ, 904, 13

Grant, S. L., Espaillat, C. C., Brittain, S., Scott-Joseph, C., & Calvet, N. 2022, *Tracing Accretion onto Herbig Ae/Be Stars Using the Brγ Line*, ApJ, 926, 229

Gravity Collaboration, Caratti o Garatti, A., Fedriani, R., et al. 2020, *The GRAVITY young stellar object survey. II. First spatially resolved observations of the CO bandhead emission in a high-mass YSO*, A&A, 635, L12

GRAVITY Collaboration, Karl, M., Pfuhl, O., et al. 2018, *Multiple star systems in the Orion nebula*, A&A, 620, A116

Groenewegen, M. A. T., Lamers, H. J. G. L. M., & Pauldrach, A. W. A. 1989, *The winds of O-stars. II. The terminal velocities of stellar winds ofO-type stars.*, A&A, 221, 78

Gvaramadze, V. V. & Bomans, D. J. 2008, *Search for OB stars running away from young star clusters. I. NGC 6611*, A&A, 490, 1071

Hanson, M. M., Howarth, I. D., & Conti, P. S. 1997, *The Young Massive Stellar Objects of M17*, ApJ, 489, 698

Hartmann, L., Hewett, R., & Calvet, N. 1994, *Magnetospheric accretion models for T Tauri stars. 1: Balmer line profiles without rotation*, ApJ, 426, 669

Hauschildt, P. H., Allard, F., & Baron, E. 1999, *The NextGen Model Atmosphere Grid for* $3000<=T_{eff}<=10{,}000$ *K*, ApJ, 512, 377

Hawcroft, C., Mahy, L., & Sana, H. in prep., *Empirical mass-loss rates and clumping properties of O-type stars in the LMC*, A&A

Hawcroft, C., Sana, H., Mahy, L., et al. 2021, *Empirical mass-loss rates and clumping properties of Galactic early-type O supergiants*, A&A, 655, A67

Hawcroft, C., Sana, H., Mahy, L., et al. 2023, *X-Shooting ULLYSES: Massive stars at low metallicity. III. Terminal wind speeds of ULLYSES massive stars*, arXiv e-prints, arXiv:2303.12165

Heger, A., Fryer, C. L., Woosley, S. E., Langer, N., & Hartmann, D. H. 2003, *How Massive Single Stars End Their Life*, ApJ, 591, 288

Hénault-Brunet, V., Evans, C. J., Sana, H., et al. 2012, *The VLT-FLAMES Tarantula Survey. VII. A low velocity dispersion for the young massive cluster R136*, A&A, 546, A73

Henrichs, H. F., Hammerschlag-Hensberge, G., Howarth, I. D., & Barr, P. 1983, *Episodic mass loss and narrow lines in Gamma Cassiopeiae and in otherearly-type stars.*, ApJ, 268, 807

Henrichs, H. F., Kaper, L., & Nichols, J. S. 1994, *The extent of variability in the stellar wind of the O7.5 giant* ξ *Persei*, A&A, 285, 565

Herrero, A., Kudritzki, R. P., Vilchez, J. M., et al. 1992, *Intrinsic parameters of galactic luminous OB stars.*, A&A, 261, 209

Herrero, A., Puls, J., & Najarro, F. 2002, *Fundamental parameters of Galactic luminous OB stars VI. Temperatures, masses and WLR of Cyg OB2 supergiants*, A&A, 396, 949

Hillier, D. J. 2008, *On the influence of clumping on O and Wolf-Rayet spectra*, in Clumping in Hot-Star Winds, ed. W.-R. Hamann, A. Feldmeier, & L. M. Oskinova, 93

Hillier, D. J., Lanz, T., Heap, S. R., et al. 2003, *A Tale of Two Stars: The Extreme O7 Iaf+ Supergiant AV 83 and the OC7.5 III((f)) star AV 69*, ApJ, 588, 1039

Hillier, D. J. & Miller, D. L. 1998, *The Treatment of Non-LTE Line Blanketing in Spherically Expanding Outflows*, ApJ, 496, 407

Hirano, S., Hosokawa, T., Yoshida, N., Omukai, K., & Yorke, H. W. 2015, *Primordial star formation under the influence of far ultraviolet radiation: 1540 cosmological haloes and the stellar mass distribution*, MNRAS, 448, 568

Hirashita, H. & Voshchinnikov, N. V. 2014, *Effects of grain growth mechanisms on the extinction curve and the metal depletion in the interstellar medium*, MNRAS, 437, 1636

Hobbs, L. M., York, D. G., Thorburn, J. A., et al. 2009, *Studies of the Diffuse Interstellar Bands. III. HD 183143*, ApJ, 705, 32

Hoffmeister, V. H., Chini, R., Scheyda, C. M., et al. 2008, *The Stellar Population of M17*, ApJ, 686, 310

Hopkins, P. F., Quataert, E., & Murray, N. 2011, *Self-regulated star formation in galaxies via momentum input from massive stars*, MNRAS, 417, 950

Hopkins, P. F., Wetzel, A., Kereš, D., et al. 2018, *How to model supernovae in simulations of star and galaxy formation*, MNRAS, 477, 1578

Hosokawa, T., Offner, S. S. R., & Krumholz, M. R. 2011, *On the Reliability of Stellar Ages and Age Spreads Inferred from Pre-main-sequence Evolutionary Models*, ApJ, 738, 140

Hosokawa, T. & Omukai, K. 2009, *Evolution of Massive Protostars with High Accretion Rates*, ApJ, 691, 823

Hosokawa, T., Yorke, H. W., & Omukai, K. 2010, *Evolution of Massive Protostars Via Disk Accretion*, ApJ, 721, 478

Huang, W., Gies, D. R., & McSwain, M. V. 2010, *A Stellar Rotation Census of B Stars: From ZAMS to TAMS*, ApJ, 722, 605

Ilee, J. D., Fairlamb, J., Oudmaijer, R. D., et al. 2014, *Investigating the inner discs of Herbig Ae/Be stars with CO bandhead and Brγ emission*, MNRAS, 445, 3723

Indebetouw, R., Mathis, J. S., Babler, B. L., et al. 2005, *The Wavelength Dependence of Interstellar Extinction from 1.25 to 8.0 μm Using GLIMPSE Data*, ApJ, 619, 931

Ingleby, L., Calvet, N., Herczeg, G., et al. 2013, *Accretion Rates for T Tauri Stars Using Nearly Simultaneous Ultraviolet and Optical Spectra*, ApJ, 767, 112

Ivanova, N., Justham, S., Chen, X., et al. 2013, *Common envelope evolution: where we stand and how we can move forward*, A&A Rev., 21, 59

Jefferies, J. T. 1968, Spectral line formation

Kamp, I., Thi, W.-F., Woitke, P., et al. 2017, *Consistent dust and gas models for protoplanetary disks. II. Chemical networks and rates*, A&A, 607, A41

Kamp, I., Tilling, I., Woitke, P., Thi, W. F., & Hogerheijde, M. 2010, *Radiation thermo-chemical models of protoplanetary disks. II. Line diagnostics*, A&A, 510, A18

Kassis, M., Deutsch, L. K., Campbell, M. F., et al. 2002, *Mid-Infrared Observations of M17*, AJ, 124, 1636

Kausch, W., Noll, S., Smette, A., et al. 2015, *Molecfit: A general tool for telluric absorption correction. II. Quantitative evaluation on ESO-VLT/X-Shooterspectra*, A&A, 576, A78

Kee, N. D. & Kuiper, R. 2019, *Line-driven ablation of circumstellar discs: IV. The role of disc ablation in massive star formation and its contribution to the stellar upper mass limit*, MNRAS, 483, 4893

Keszthelyi, Z., Meynet, G., Martins, F., de Koter, A., & David-Uraz, A. 2021, *The effects of surface fossil magnetic fields on massive star evolution - III. The case of τ Sco*, MNRAS, 504, 2474

Kim, K. H., Watson, D. M., Manoj, P., et al. 2013, *Transitional Disks and Their Origins: An Infrared Spectroscopic Survey of Orion A*, ApJ, 769, 149

Kiminki, D. C. & Kobulnicky, H. A. 2012, *An Updated Look at Binary Characteristics of Massive Stars in the Cygnus OB2 Association*, ApJ, 751, 4

Kobayashi, C., Karakas, A. I., & Lugaro, M. 2020, *The Origin of Elements from Carbon to Uranium*, ApJ, 900, 179

Kobulnicky, H. A., Kiminki, D. C., Lundquist, M. J., et al. 2014, *Toward Complete Statistics of Massive Binary Stars: Penultimate Results from the Cygnus OB2 Radial Velocity Survey*, ApJS, 213, 34

Köhler, K., Langer, N., de Koter, A., et al. 2015, *The evolution of rotating very massive stars with LMC composition*, A&A, 573, A71

Koumpia, E., de Wit, W. J., Oudmaijer, R. D., et al. 2021, *The first interferometric survey of massive YSOs in the K-band. Hot dust, ionised gas, and binarity at au scales*, A&A, 654, A109

Kouwenhoven, M. B. N., Brown, A. G. A., Portegies Zwart, S. F., & Kaper, L. 2007a, *The primordial binary population. II.. Recovering the binary population for intermediate mass stars in Scorpius OB2*, A&A, 474, 77

Kouwenhoven, M. B. N., Brown, A. G. A., Portegies Zwart, S. F., & Kaper, L. 2007b, *The primordial binary population. II.. Recovering the binary population for intermediate mass stars in Scorpius OB2*, A&A, 474, 77

Kramida, A. 2019, *NIST's atomic databases for applied and fundamental science*, in APS Meeting Abstracts, Vol. 2019, APS Division of Atomic, Molecular and Optical Physics Meeting Abstracts, N09.004

Kratter, K. M., Matzner, C. D., Krumholz, M. R., & Klein, R. I. 2010, *On the Role of Disks in the Formation of Stellar Systems: A Numerical Parameter Study of Rapid Accretion*, ApJ, 708, 1585

Kraus, S., Hofmann, K.-H., Menten, K. M., et al. 2010, *A hot compact dust disk around a massive young stellar object*, Nature, 466, 339

Kraus, S., Monnier, J. D., Che, X., et al. 2012, *Gas Distribution, Kinematics, and Excitation Structure in the Disks around the Classical Be Stars β Canis Minoris and ζ Tauri*, ApJ, 744, 19

Kroupa, P. 2001, *On the variation of the initial mass function*, MNRAS, 322, 231

Krtička, J. 2014, *Mass loss in main-sequence B stars*, A&A, 564, A70

Krtička, J. & Kubát, J. 2017, *Comoving frame models of hot star winds. II. Reduction of O star wind mass-loss rates in global models*, A&A, 606, A31

Krtička, J. & Kubát, J. 2018, *Global hot-star wind models for stars from Magellanic Clouds*, A&A, 612, A20

Krumholz, M. R., Klein, R. I., McKee, C. F., Offner, S. S. R., & Cunningham, A. J. 2009, *The Formation of Massive Star Systems by Accretion*, Science, 323, 754

Kudritzki, R. P. 2002, *Line-driven Winds, Ionizing Fluxes, and Ultraviolet Spectra of Hot Stars at Extremely Low Metallicity. I. Very Massive O Stars*, ApJ, 577, 389

Kudritzki, R. P., Lennon, D. J., & Puls, J. 1995, *Quantitative Spectroscopy of Luminous Blue Stars in Distant Galaxies*, in Science with the VLT, ed. J. R. Walsh & I. J. Danziger, 246

Kudritzki, R.-P. & Puls, J. 2000, *Winds from Hot Stars*, ARA&A, 38, 613

Kuhn, M. A., Hillenbrand, L. A., Sills, A., Feigelson, E. D., & Getman, K. V. 2019, *Kinematics in Young Star Clusters and Associations with Gaia DR2*, ApJ, 870, 32

Kuiper, R., Klahr, H., Beuther, H., & Henning, T. 2010, *Circumventing the Radiation Pressure Barrier in the Formation of Massive Stars via Disk Accretion*, ApJ, 722, 1556

Kunitomo, M., Guillot, T., Takeuchi, T., & Ida, S. 2017, *Revisiting the pre-main-sequence evolution of stars. I. Importance of accretion efficiency and deuterium abundance*, A&A, 599, A49

Lada, C. J. & Lada, E. A. 2003, *Embedded Clusters in Molecular Clouds*, ARA&A, 41, 57

Lamb, J. B., Oey, M. S., Segura-Cox, D. M., et al. 2016, *The Runaways and Isolated O-Type Star Spectroscopic Survey of the SMC (RIOTS4)*, ApJ, 817, 113

Lamers, H. J. G. L. M. & Cassinelli, J. P. 1999, Introduction to Stellar Winds

Lancaster, L., Ostriker, E. C., Kim, J.-G., & Kim, C.-G. 2021, *Star Formation Regulation and Self-pollution by Stellar Wind Feedback*, ApJ, 922, L3

Langer, N. 2012, *Presupernova Evolution of Massive Single and Binary Stars*, ARA&A, 50, 107

Lau, R. M., Hankins, M. J., Han, Y., et al. 2022, *Nested dust shells around the Wolf-Rayet binary WR 140 observed with JWST*, Nature Astronomy, 6, 1308

Leitherer, C., Robert, C., & Drissen, L. 1992, *Deposition of Mass, Momentum, and Energy by Massive Stars into the Interstellar Medium*, ApJ, 401, 596

Lennon, D. J. 1997, *Revised spectral types for 64 B-supergiants in the Small Magellanic Cloud: metallicity effects.*, A&A, 317, 871

Lim, B., Sung, H., Kim, J. S., Bessell, M. S., & Karimov, R. 2014, *Sejong Open Cluster Survey (SOS) - II. IC 1848 cluster in the H II region W5 West*, MNRAS, 438, 1451

Lim, W., De Buizer, J. M., & Radomski, J. T. 2020, *Surveying the Giant H II Regions of the Milky Way with SOFIA. II. M17*, ApJ, 888, 98

Lin, D. N. C. & Papaloizou, J. 1986, *On the Tidal Interaction between Protoplanets and the Protoplanetary Disk. III. Orbital Migration of Protoplanets*, ApJ, 309, 846

Lin, M.-K., Krumholz, M. R., & Kratter, K. M. 2011, *Spin-down of protostars through gravitational torques*, MNRAS, 416, 580

Lodders, K. 2003, *Solar System Abundances and Condensation Temperatures of the Elements*, ApJ, 591, 1220

Lubow, S. H. & D'Angelo, G. 2006, *Gas Flow across Gaps in Protoplanetary Disks*, ApJ, 641, 526

Lucy, L. B. & Solomon, P. M. 1970, *Mass Loss by Hot Stars*, ApJ, 159, 879

Lucy, L. B. & White, R. L. 1980, *X-ray emission from the winds of hot stars.*, ApJ, 241, 300

Luisi, M., Anderson, L. D., Balser, D. S., Bania, T. M., & Wenger, T. V. 2016, *H II Region Ionization of the Interstellar Medium: A Case Study of NGC 7538*, ApJ, 824, 125

Lynden-Bell, D. & Pringle, J. E. 1974, *The evolution of viscous discs and the origin of the nebular variables.*, MNRAS, 168, 603

Mandel, I. & de Mink, S. E. 2016, *Merging binary black holes formed through chemically homogeneous evolution in short-period stellar binaries*, MNRAS, 458, 2634

Marcolino, W. L. F., Bouret, J. C., Rocha-Pinto, H. J., Bernini-Peron, M., & Vink, J. S. 2022, *Wind properties of Milky Way and SMC massive stars: empirical Z dependence from CMFGEN models*, MNRAS, 511, 5104

Marigo, P., Chiosi, C., & Kudritzki, R. P. 2003, *Zero-metallicity stars. II. Evolution of very massive objects with mass loss*, A&A, 399, 617

Martins, F. & Palacios, A. 2013, *A comparison of evolutionary tracks for single Galactic massive stars*, A&A, 560, A16

Mason, B. D., Hartkopf, W. I., Gies, D. R., Henry, T. J., & Helsel, J. W. 2009, *The High Angular Resolution Multiplicity of Massive Stars*, AJ, 137, 3358

Massi, F., Giannetti, A., Di Carlo, E., et al. 2015, *Young open clusters in the Galactic star forming region NGC 6357*, A&A, 573, A95

McKee, C. F. & Tan, J. C. 2003, *The Formation of Massive Stars from Turbulent Cores*, ApJ, 585, 850

McLeod, A. F., Dale, J. E., Evans, C. J., et al. 2019, *Feedback from massive stars at low metallicities: MUSE observations of N44 and N180 in the Large Magellanic Cloud*, MNRAS, 486, 5263

Mendigutía, I. 2020, *On the Mass Accretion Rates of Herbig Ae/Be Stars. Magnetospheric Accretion or Boundary Layer?*, Galaxies, 8, 39

Mendigutía, I., Calvet, N., Montesinos, B., et al. 2011, *Accretion rates and accretion tracers of Herbig Ae/Be stars*, A&A, 535, A99

Mihalas, D. 1978, Stellar atmospheres

Modigliani, A., Goldoni, P., Royer, F., et al. 2010, *The X-shooter pipeline*, in Proc. SPIE, Vol. 7737, Observatory Operations: Strategies, Processes, and Systems III, 773728

Modjaz, M., Kewley, L., Kirshner, R. P., et al. 2008, *Measured Metallicities at the Sites of Nearby Broad-Lined Type Ic Supernovae and Implications for the Supernovae Gamma-Ray Burst Connection*, AJ, 135, 1136

Moe, M. & Di Stefano, R. 2017, *Mind Your Ps and Qs: The Interrelation between Period (P) and Mass-ratio (Q) Distributions of Binary Stars*, ApJS, 230, 15

Moe, M. & Kratter, K. M. 2018, *Dynamical Formation of Close Binaries during the Pre-main-sequence Phase*, ApJ, 854, 44

Moens, N., Poniatowski, L. G., Hennicker, L., et al. 2022, *First 3D radiation-hydrodynamic simulations of Wolf-Rayet winds*, A&A, 665, A42

Mokiem, M. R., de Koter, A., Puls, J., et al. 2005, *Spectral analysis of early-type stars using a genetic algorithm based fitting method*, A&A, 441, 711

Mokiem, M. R., de Koter, A., Vink, J. S., et al. 2007, *The empirical metallicity dependence of the mass-loss rate of O- and early B-type stars*, A&A, 473, 603

Mottram, J. C., Vink, J. S., Oudmaijer, R. D., & Patel, M. 2007, *On the difference between Herbig Ae and Herbig Be stars*, MNRAS, 377, 1363

Moura, T., Alencar, S. H. P., Sousa, A. P., Alecian, E., & Lebreton, Y. 2020, *Spectroscopic analysis of accretion/ejection signatures in the Herbig Ae/Be stars HD 261941 and V590 Mon*, MNRAS, 494, 3512

Muñoz, D. J., Miranda, R., & Lai, D. 2019, *Hydrodynamics of Circumbinary Accretion: Angular Momentum Transfer and Binary Orbital Evolution*, ApJ, 871, 84

Müller, T. W. A. & Kley, W. 2013, *Modelling accretion in transitional disks*, A&A, 560, A40

Najarro, F., Hillier, D. J., Puls, J., Lanz, T., & Martins, F. 2006, *On the sensitivity of He I singlet lines to the Fe IV model atom in O stars*, A&A, 456, 659

Nguyen-Luong, Q., Nakamura, F., Sugitani, K., et al. 2020, *Large-scale Molecular Gas Distribution in the M17 Cloud Complex: Dense Gas Conditions of Massive Star Formation?*, ApJ, 891, 66

Nishiyama, S., Tamura, M., Hatano, H., et al. 2009, *Interstellar Extinction Law Toward the Galactic Center III: J, H, K_S Bands in the 2MASS and the MKO Systems, and 3.6, 4.5, 5.8, 8.0 μm in the Spitzer/IRAC System*, ApJ, 696, 1407

Ochsendorf, B. B., Ellerbroek, L. E., Chini, R., et al. 2011, *First firm spectral classification of an early-B pre-main-sequence star: B275 in <ASTROBJ>M 17</ASTROBJ>*, A&A, 536, L1

Oh, S. & Kroupa, P. 2016, *Dynamical ejections of massive stars from young star clusters under diverse initial conditions*, A&A, 590, A107

Oliva, A. & Kuiper, R. 2023, *Modeling disks and magnetic outflows around a forming massive star. I. Investigating the two-layer structure of the accretion disk*, A&A, 669, A80

Oliva, G. A. & Kuiper, R. 2020, *Modeling disk fragmentation and multiplicity in massive star formation*, A&A, 644, A41

Oskinova, L. M., Hamann, W. R., & Feldmeier, A. 2007, *Neglecting the porosity of hot-star winds can lead to underestimating mass-loss rates*, A&A, 476, 1331

Oudmaijer, R. D., Ababakr, K. M., & Fairlamb, J. R. 2017, *The formation and evolution of Herbig Ae/Be stars .*, Mem. Soc. Astron. Italiana, 88, 605

Owen, J. E., Ercolano, B., Clarke, C. J., & Alexand er, R. D. 2010, *Radiation-hydrodynamic models of X-ray and EUV photoevaporating protoplanetary discs*, MNRAS, 401, 1415

Owocki, S. 2004, *Stellar wind mechanisms and instabilities*, in EAS Publications Series, Vol. 13, EAS Publications Series, ed. M. Heydari-Malayeri, P. Stee, & J. P. Zahn, 163–250

Owocki, S. P. 2008, *Dynamical simulation of the "velocity-porosity" reduction in observed strength of stellar wind lines*, in Clumping in Hot-Star Winds, ed. W.-R. Hamann, A. Feldmeier, & L. M. Oskinova, 121

Palla, F. & Stahler, S. W. 1990, *The birthline for intermediate-mass stars*, ApJ, 360, L47

Palla, F. & Stahler, S. W. 1993, *The Pre-Main-Sequence Evolution of Intermediate-Mass Stars*, ApJ, 418, 414

Parker, E. N. 1955, *Hydromagnetic Dynamo Models.*, ApJ, 122, 293

Pauldrach, A., Puls, J., & Kudritzki, R. P. 1986, *Radiation-driven winds of hot luminous stars. Improvements of the theory and first results.*, A&A, 164, 86

Paxton, B., Bildsten, L., Dotter, A., et al. 2011, *Modules for Experiments in Stellar Astrophysics (MESA)*, ApJS, 192, 3

Paxton, B., Cantiello, M., Arras, P., et al. 2013, *Modules for Experiments in Stellar Astrophysics (MESA): Planets, Oscillations, Rotation, and Massive Stars*, ApJS, 208, 4

Paxton, B., Marchant, P., Schwab, J., et al. 2015, *Modules for Experiments in Stellar Astrophysics (MESA): Binaries, Pulsations, and Explosions*, ApJS, 220, 15

Pecaut, M. J. & Mamajek, E. E. 2013, *Intrinsic Colors, Temperatures, and Bolometric Corrections of Pre-main-sequence Stars*, ApJS, 208, 9

Peter, D., Feldt, M., Henning, T., & Hormuth, F. 2012, *Massive binaries in the Cepheus OB2/3 region. Constraining the formation mechanism of massive stars*, A&A, 538, A74

Peters, T., Klessen, R. S., Mac Low, M.-M., & Banerjee, R. 2010, *Limiting Accretion onto Massive Stars by Fragmentation-induced Starvation*, ApJ, 725, 134

Poelarends, A. J. T., Herwig, F., Langer, N., & Heger, A. 2008, *The Supernova Channel of Super-AGB Stars*, ApJ, 675, 614

Poorta, J., Ramírez-Tannus, M. C., de Koter, A., et al. 2023, *Massive pre-main-sequence stars in M17: 1^{st} and 2^{nd} overtone CO bandhead emission and the thermal infrared*, arXiv e-prints, arXiv:2305.01436

Povich, M. S., Churchwell, E., Bieging, J. H., et al. 2009, *The Extended Environment of M17: A Star Formation History*, ApJ, 696, 1278

Povich, M. S., Stone, J. M., Churchwell, E., et al. 2007, *A Multiwavelength Study of M17: The Spectral Energy Distribution and PAH Emission Morphology of a Massive Star Formation Region*, ApJ, 660, 346

Puls, J., Kudritzki, R. P., Herrero, A., et al. 1996, *O-star mass-loss and wind momentum rates in the Galaxy and the Magellanic Clouds Observations and theoretical predictions.*, A&A, 305, 171

Puls, J., Springmann, U., & Lennon, M. 2000, *Radiation driven winds of hot luminous stars. XIV. Line statistics and radiative driving*, A&AS, 141, 23

Puls, J., Urbaneja, M. A., Venero, R., et al. 2005, *Atmospheric NLTE-models for the spectroscopic analysis of blue stars with winds. II. Line-blanketed models*, A&A, 435, 669

Puls, J., Vink, J. S., & Najarro, F. 2008, *Mass loss from hot massive stars*, A&A Rev., 16, 209

Rab, C., Güdel, M., Woitke, P., et al. 2018, *X-ray radiative transfer in protoplanetary disks. The role of dust and X-ray background fields*, A&A, 609, A91

Ramírez-Agudelo, O. H., Sana, H., de Mink, S. E., et al. 2015, *The VLT-FLAMES Tarantula Survey. XXI. Stellar spin rates of O-type spectroscopic binaries*, A&A, 580, A92

Ramírez-Agudelo, O. H., Simón-Díaz, S., Sana, H., et al. 2013, *The VLT-FLAMES Tarantula Survey. XII. Rotational velocities of the single O-type stars*, A&A, 560, A29

Ramírez-Tannus, M., Derkink, A. R., & Kaper, L. in prep., *Pre-main-sequence stars in M17 – Binarity*, A&A

Ramírez-Tannus, M. C., Backs, F., de Koter, A., et al. 2021, *A relation between the radial velocity dispersion of young clusters and their age. Evidence for hardening as the formation scenario of massive close binaries*, A&A, 645, L10

Ramírez-Tannus, M. C., Kaper, L., de Koter, A., et al. 2017, *Massive pre-main-sequence stars in M17*, A&A, 604, A78

Ramírez-Tannus, M. C., Poorta, J., Bik, A., et al. 2020, *The young stellar content of the giant H II regions M 8, G333.6-0.2, and NGC 6357 with VLT/KMOS*, A&A, 633, A155

Reach, W. T., Megeath, S. T., Cohen, M., et al. 2005, *Absolute Calibration of the Infrared Array Camera on the Spitzer Space Telescope*, PASP, 117, 978

Reed, B. C. 2003, *Catalog of Galactic OB Stars*, AJ, 125, 2531

Renzo, M., Ott, C. D., Shore, S. N., & de Mink, S. E. 2017, *Systematic survey of the effects of wind mass loss algorithms on the evolution of single massive stars*, A&A, 603, A118

Repolust, T., Puls, J., & Herrero, A. 2004, *Stellar and wind parameters of Galactic O-stars. The influence of line-blocking/blanketing*, A&A, 415, 349

Rice, W. K. M., Armitage, P. J., Bonnell, I. A., et al. 2003, *Substellar companions and isolated planetary-mass objects from protostellar disc fragmentation*, MNRAS, 346, L36

Riello, M., De Angeli, F., Evans, D. W., et al. 2021, *Gaia Early Data Release 3. Photometric content and validation*, A&A, 649, A3

Rivero González, J. G., Puls, J., Najarro, F., & Brott, I. 2012, *Nitrogen line spectroscopy of O-stars. II. Surface nitrogen abundances for O-stars in the Large Magellanic Cloud*, A&A, 537, A79

Roman-Duval, J., Proffitt, C. R., Taylor, J. M., et al. 2020, *Ultraviolet Legacy Library of Young Stars as Essential Standards (ULLYSES): Data Release I*, Research Notes of the American Astronomical Society, 4, 205

Rose, S. C., Naoz, S., & Geller, A. M. 2019, *Companion-driven evolution of massive stellar binaries*, MNRAS, 488, 2480

Rosen, A. L. 2022, *A Massive Star Is Born: How Feedback from Stellar Winds, Radiation Pressure, and Collimated Outflows Limits Accretion onto Massive Stars*, ApJ, 941, 202

Rygl, K. L. J., Wyrowski, F., Schuller, F., & Menten, K. M. 2010, *Initial phases of massive star formation in high infrared extinction clouds *. I. Physical parameters*, A&A, 515, A42

Salpeter, E. E. 1955, *The Luminosity Function and Stellar Evolution.*, ApJ, 121, 161

Sana, H., de Koter, A., de Mink, S. E., et al. 2013, *The VLT-FLAMES Tarantula Survey. VIII. Multiplicity properties of the O-type star population*, A&A, 550, A107

Sana, H., de Mink, S. E., de Koter, A., et al. 2012, *Binary Interaction Dominates the Evolution of Massive Stars*, Science, 337, 444

Sana, H. & Evans, C. J. 2011, *The multiplicity of massive stars*, in IAU Symposium, Vol. 272, Active OB Stars: Structure, Evolution, Mass Loss, and Critical Limits, ed. C. Neiner, G. Wade, G. Meynet, & G. Peters, 474–485

Sana, H., Gosset, E., Nazé, Y., Rauw, G., & Linder, N. 2008, *The massive star binary fraction in young open clusters - I. NGC 6231 revisited*, MNRAS, 386, 447

Sana, H., Le Bouquin, J. B., Lacour, S., et al. 2014, *Southern Massive Stars at High Angular Resolution: Observational Campaign and Companion Detection*, ApJS, 215, 15

Sana, H., Ramírez-Tannus, M. C., de Koter, A., et al. 2017, *A dearth of short-period massive binaries in the young massive star forming region M 17. Evidence for a large orbital separation at birth?*, A&A, 599, L9

Sana, H., Tramper, F., & Abdul-Masih, M. in prep., *X-Shooting ULLYSES: Massive Stars at low metallicity II. DR1: Advanced optical data products for the Magellanic Clouds.*, A&A

Sanna, A., Kölligan, A., Moscadelli, L., et al. 2019, *Discovery of a sub-Keplerian disk with jet around a 20 $M_\odot$ young star. ALMA observations of G023.01-00.41*, A&A, 623, A77

Santolaya-Rey, A. E., Puls, J., & Herrero, A. 1997, *Atmospheric NLTE-models for the spectroscopic analysis of luminous blue stars with winds.*, A&A, 323, 488

Sarre, P. J. 2006, *The diffuse interstellar bands: A major problem in astronomical spectroscopy*, Journal of Molecular Spectroscopy, 238, 1

Savaglio, S., Glazebrook, K., & Le Borgne, D. 2009, *The Galaxy Population Hosting Gamma-Ray Bursts*, ApJ, 691, 182

Schneider, F. R. N., Izzard, R. G., Langer, N., & de Mink, S. E. 2015, *Evolution of Mass Functions of Coeval Stars through Wind Mass Loss and Binary Interactions*, ApJ, 805, 20

Schneider, F. R. N., Langer, N., de Koter, A., et al. 2014, *Bonnsai: a Bayesian tool for comparing stars with stellar evolution models*, A&A, 570, A66

Schneider, F. R. N., Podsiadlowski, P., Langer, N., Castro, N., & Fossati, L. 2016, *Rejuvenation of stellar mergers and the origin of magnetic fields in massive stars*, MNRAS, 457, 2355

Schultz, G. V. & Wiemer, W. 1975, *Interstellar reddening and IR-excesses of O and B stars.*, A&A, 43, 133

Sharples, R., Bender, R., Agudo Berbel, A., et al. 2013, *First Light for the KMOS Multi-Object Integral-Field Spectrometer*, The Messenger, 151, 21

Shu, F. H., Adams, F. C., & Lizano, S. 1987, *Star formation in molecular clouds - Observation and theory*, ARA&A, 25, 23

Simón-Díaz, S. 2020, in Reviews in Frontiers of Modern Astrophysics; From Space Debris to Cosmology, 155–187

Simón-Díaz, S., Godart, M., Castro, N., et al. 2017, *The IACOB project . III. New observational clues to understand macroturbulent broadening in massive O- and B-type stars*, A&A, 597, A22

Skrutskie, M. F., Cutri, R. M., Stiening, R., et al. 2006, *The Two Micron All Sky Survey (2MASS)*, AJ, 131, 1163

Sota, A., Maíz Apellániz, J., Morrell, N. I., et al. 2014, *The Galactic O-Star Spectroscopic Survey (GOSSS). II. Bright Southern Stars*, ApJS, 211, 10

Spitzer, L. 1978, Physical processes in the interstellar medium

Steiger, J. H. 1998, *A note on multiple sample extensions of the RMSEA fit index*, Structural Equation Modeling: A Multidisciplinary Journal, 5, 411

Stoop, M., Derkink, A. R., & Kaper, L. 2023, submitted, *The early evolution of young massive clusters. The kinematic history of NGC 6618/M17*, A&A

Stoop, M., Kaper, L., de Koter, A., et al. 2023, *The early evolution of young massive clusters. The kinematic history of NGC 6611/M16*, A&A, 670, A108

Strom, K. M., Strom, S. E., Edwards, S., Cabrit, S., & Skrutskie, M. F. 1989, *Circumstellar Material Associated with Solar-Type Pre-Main-Sequence Stars: A Possible Constraint on the Timescale for Planet Building*, AJ, 97, 1451

Subramanian, S. & Subramaniam, A. 2009, *Depth estimation of the Large and Small Magellanic Clouds*, A&A, 496, 399

Sundqvist, J. O., Owocki, S. P., & Puls, J. 2018, *2D wind clumping in hot, massive stars from hydrodynamical line-driven instability simulations using a pseudo-planar approach*, A&A, 611, A17

Sundqvist, J. O. & Puls, J. 2018, *Atmospheric NLTE models for the spectroscopic analysis of blue stars with winds. IV. Porosity in physical and velocity space*, A&A, 619, A59

Sundqvist, J. O., Puls, J., & Feldmeier, A. 2010, *Mass loss from inhomogeneous hot star winds. I. Resonance line formation in 2D models*, A&A, 510, A11

Sundqvist, J. O., Puls, J., Feldmeier, A., & Owocki, S. P. 2011, *Mass loss from inhomogeneous hot star winds. II. Constraints from a combined optical/UV study*, A&A, 528, A64

Sundqvist, J. O., Puls, J., & Owocki, S. P. 2014, *Mass loss from inhomogeneous hot star winds. III. An effective-opacity formalism for line radiative transfer in accelerating, clumped two-component media, and first results on theory and diagnostics*, A&A, 568, A59

Sung, H., Bessell, M. S., Chun, M.-Y., et al. 2017, *An Optical and Infrared Photometric Study of the Young Open Cluster IC 1805 in the Giant H II Region W4* , ApJS, 230, 3

Tan, J. C., Beltrán, M. T., Caselli, P., et al. 2014, *Massive Star Formation*, in Protostars and Planets VI, ed. H. Beuther, R. S. Klessen, C. P. Dullemond, & T. Henning, 149

Tepper-García, T. 2006, *Voigt profile fitting to quasar absorption lines: an analytic approximation to the Voigt-Hjerting function*, MNRAS, 369, 2025

Thi, W. F., Woitke, P., & Kamp, I. 2011, *Radiation thermo-chemical models of protoplanetary discs - III. Impact of inner rims on spectral energy distributions*, MNRAS, 412, 711

Tramper, F., Sana, H., de Koter, A., Kaper, L., & Ramírez-Agudelo, O. H. 2014, *The properties of ten O-type stars in the low-metallicity galaxies IC 1613, WLM, and NGC 3109*, A&A, 572, A36

van der Meij, V., Guo, D., Kaper, L., & Renzo, M. 2021, *Confirming NGC 6231 as the parent cluster of the runaway high-mass X-ray binary HD 153919/4U 1700-37 with Gaia DR2*, A&A, 655, A31

van Gelder, M. L., Kaper, L., Japelj, J., et al. 2020, *VLT/X-shooter spectroscopy of massive young stellar objects in the 30 Doradus region of the Large Magellanic Cloud*, A&A, 636, A54

Vernet, J., Dekker, H., D'Odorico, S., et al. 2011, *X-shooter, the new wide band intermediate resolution spectrograph at the ESO Very Large Telescope*, A&A, 536, A105

Vink, J. S. 2022, *Theory and Diagnostics of Hot Star Mass Loss*, ARA&A, 60, 203

Vink, J. S., de Koter, A., & Lamers, H. J. G. L. M. 2001, *Mass-loss predictions for O and B stars as a function of metallicity*, A&A, 369, 574

Vink, J. S., Mehner, A., Crowther, P. A., et al. 2023, *X-Shooting ULLYSES: Massive stars at low metallicity. I. Project description*, A&A, 675, A154

Virtanen, P., Gommers, R., Oliphant, T. E., et al. 2020, *SciPy 1.0: Fundamental Algorithms for Scientific Computing in Python*, Nature Methods, 17, 261

Vogelsberger, M., Genel, S., Sijacki, D., et al. 2013, *A model for cosmological simulations of galaxy formation physics*, MNRAS, 436, 3031

Šurlan, B., Hamann, W. R., Aret, A., et al. 2013, *Macroclumping as solution of the discrepancy between Hα and P v mass loss diagnostics for O-type stars*, A&A, 559, A130

Šurlan, B., Hamann, W. R., Kubát, J., Oskinova, L. M., & Feldmeier, A. 2012, *Three-dimensional radiative transfer in clumped hot star winds. I. Influence of clumping on the resonance line formation*, A&A, 541, A37

Wade, G. A., Bagnulo, S., Drouin, D., Landstreet, J. D., & Monin, D. 2007, *A search for strong, ordered magnetic fields in Herbig Ae/Be stars*, MNRAS, 376, 1145

Wade, G. A., Neiner, C., Alecian, E., et al. 2016, *The MiMeS survey of magnetism in massive stars: introduction and overview*, MNRAS, 456, 2

Walborn, N. R., Fullerton, A. W., Crowther, P. A., et al. 2002, *Far Ultraviolet Spectroscopic Explorer Atlas of OB Stars in the Magellanic Clouds*, ApJS, 141, 443

Walborn, N. R., Lennon, D. J., Heap, S. R., et al. 2000, *The Ultraviolet and Optical Spectra of Metal-deficient O Stars in the Small Magellanic Cloud*, PASP, 112, 1243

Wang, C., Langer, N., Schootemeijer, A., et al. 2022, *Stellar mergers as the origin of the blue main-sequence band in young star clusters*, Nature Astronomy, 6, 480

Wellstein, S. & Langer, N. 1999, *Implications of massive close binaries for black hole formation and supernovae*, A&A, 350, 148

Whelan, J. & Iben, Icko, J. 1973, *Binaries and Supernovae of Type I*, ApJ, 186, 1007

Wichittanakom, C., Oudmaijer, R. D., Fairlamb, J. R., et al. 2020, *The accretion rates and mechanisms of Herbig Ae/Be stars*, MNRAS, 493, 234

Woitke, P., Kamp, I., & Thi, W.-F. 2009, *Radiation thermo-chemical models of protoplanetary disks. I. Hydrostatic disk structure and inner rim*, A&A, 501, 383

Woitke, P., Min, M., Pinte, C., et al. 2016, *Consistent dust and gas models for protoplanetary disks. I. Disk shape, dust settling, opacities, and PAHs*, A&A, 586, A103

Woodall, J., Agúndez, M., Markwick-Kemper, A. J., & Millar, T. J. 2007, *The UMIST database for astrochemistry 2006*, A&A, 466, 1197

Woosley, S. E., Langer, N., & Weaver, T. A. 1993, *The Evolution of Massive Stars Including Mass Loss: Presupernova Models and Explosion*, ApJ, 411, 823

Wright, A. E. & Barlow, M. J. 1975, *The radio and infrared spectrum of early type stars undergoing mass loss.*, MNRAS, 170, 41

Wright, E. L., Eisenhardt, P. R. M., Mainzer, A. K., et al. 2010, *The Wide-field Infrared Survey Explorer (WISE): Mission Description and Initial On-orbit Performance*, AJ, 140, 1868

Wu, S.-W., Bik, A., Bestenlehner, J. M., et al. 2016, *The massive stellar population of W49: A spectroscopic survey*, A&A, 589, A16

Wu, S.-W., Bik, A., Henning, T., et al. 2014, *The discovery of a very massive star in W49*, A&A, 568, L13

Xiang, F. Y., Li, A., & Zhong, J. X. 2017, *Diffuse Interstellar Bands and the Ultraviolet Extinction Curves: The Missing Link Revisited*, ApJ, 835, 107

Xu, Y., Moscadelli, L., Reid, M. J., et al. 2011, *Trigonometric Parallaxes of Massive Star-forming Regions. VIII. G12.89+0.49, G15.03-0.68 (M17), and G27.36-0.16*, ApJ, 733, 25

Yoon, S. C., Woosley, S. E., & Langer, N. 2010, *Type Ib/c Supernovae in Binary Systems. I. Evolution and Properties of the Progenitor Stars*, ApJ, 725, 940

Young, D. R., Smartt, S. J., Valenti, S., et al. 2010, *Two type Ic supernovae in low-metallicity, dwarf galaxies: diversity of explosions*, A&A, 512, A70

Zapata, L. A., Ho, P. T. P., Schilke, P., et al. 2009, *A Ring/Disk/Outflow System Associated with W51 North: A Very Massive Star in the Making*, ApJ, 698, 1422

Zapata, L. A., Palau, A., Ho, P. T. P., et al. 2008, *Forming an early O-type star through gas accretion?*, A&A, 479, L25

Zeidler, P., Sabbi, E., Nota, A., et al. 2018, *The Young Massive Star Cluster Westerlund 2 Observed with MUSE. I. First Results on the Cluster Internal Motion from Stellar Radial Velocities*, AJ, 156, 211

Zinnecker, H. & Yorke, H. W. 2007, *Toward Understanding Massive Star Formation*, ARA&A, 45, 481

Contributions from co-authors

Here we list bibliographic information of the papers included in this thesis. The relative contribution of every coauthor is represented by their place in the author list (all chapters of this thesis were written under the supervision of profs. Alex de Koter and Lex Kaper).

Chapter 2: Massive pre-main-sequence stars in M17: Modelling hydrogen and dust in MYSO disks
F. Backs, J. Poorta, Ch. Rab, A. R. Derkink, A. de Koter, L. Kaper, M. C. Ramírez-Tannus, I. Kamp
Astronomy & Astrophysics, 2023, 671, A13

Chapter 3: A relation between the radial velocity dispersion of young clusters and their age: Evidence for hardening as the formation scenario of massive close binaries
M.C. Ramírez-Tannus, **F. Backs**, A. de Koter, H. Sana, H. Beuther, A. Bik, W. Brandner, L. Kaper, H. Linz, Th. Henning, J. Poorta,
Astronomy & Astrophysics, 2021, 645, L10

- MCRT did the radial velocity determination. FB did the Monte Carlo simulations. The paper was written by MCRT and FB.

Chapter 4: Stellar properties of the young cluster M17
F. Backs, S. Brands, A.R. Derkink, M. C. Ramírez-Tannus, A. de Koter, L. Kaper, J. Puls
Astronomy & Astrophysics, in prep.

Chapter 5: Atmosphere and mass-loss properties of O-type giants in the SMC: Clumped winds at low metallicity
F. Backs, S. Brands, A. de Koter, L. Kaper, J. Puls, J. S. Vink, , F. Tramper, H. Sana
Astronomy & Astrophysics, in prep.

English summary

The official start of a star's life is when thermonuclear reactions begin in the center that convert hydrogen to helium. The star is said to have arrived on the zero-age main sequence (ZAMS). Its subsequent life is predestined by several of its ZAMS properties of which total stellar mass and angular momentum, chemical composition, magnetic field strength, and the possible presence of one or more nearby companions are the most important ones. Especially initial mass is a critical parameter. Stars that have an initial mass that is at least eight times the mass of the Sun are considered massive. Unlike lower mass stars, they do not develop a degenerate core in their post-main sequence life and end as core-collapse supernovae.

During the core hydrogen burning or main-sequence phase massive stars are hot and luminous. Their surfaces can have temperatures up to $\sim$50 000 K, compared to 5 700 K for the Sun. Their luminosities may exceed a million times that of the Sun, essentially because a higher core pressure – needed to resist the gravity of more mass – causes a higher energy production rate per unit stellar mass. Massive stars hence burn through their nuclear fuel faster than lower mass stars, and consequently live shorter lives. Massive stars reach ages of at most 50 Myr, whereas the Sun is expected to exist for 12 Gyr. Their short lifetimes imply that massive stars are typically found in star-forming regions. The lifetime difference may be so extreme that the most massive stars may already have ended their lives while low-mass stars in the same star-forming event have not yet reached the ZAMS.

The combination of high surface temperature and luminosity creates a strong flux of energetic photons passing through the atmosphere of the star. This typically ultraviolet and optical light is absorbed and re-emitted in spectral lines of mostly metal species, such as iron, and transfers net outward momentum from the radiation field to the gas in the surface layers. This initiates a trans-sonic radial outflow or stellar wind that can become so strong that over the lifetime of the star more than half of the initial mass is lost to the interstellar medium.

Because of their intense radiation fields, powerful stellar winds, and energetic final explosions, massive stars strongly impact the evolution of the cosmos. They clear out the gas in their ambient media by creating hot, ionized bubbles, possibly halting local star formation. Their stellar winds and life-ending supernovae inject copious amounts of gas, momentum, and energy in the interstellar medium, possibly initiating star formation elsewhere. The concerted actions of many massive stars even produce galactic outflows. Over cosmic time, these strong feedback processes have played an important role in the formation and evolution of galaxies and the universe itself and constitute a critical step in our cosmic origin. Radiation from the first generations of massive stars ever to have formed, for instance, likely is a strong contributor to the re-ionization of the intergalactic medium at redshifts of about 30 to 11. Part of the material ejected by massive stars is in the form of newly processed elements, thereby supplying their host galaxies with the building blocks of terrestrial planets and life.

For all these reasons it is of great importance to understand the birth, life, and death of massive stars.

1 The birth of massive stars

To properly understand the life of a massive star we need to know the origin and initial conditions of the star. The bright H II region M17 is our test bed for the outcome of massive star formation. This bubble of hot ionized gas contains a young cluster in which the stars have started forming less than a million years ago. Fig. A shows images of this stellar nursery from the Two Micron All Sky Survey (2MASS) and the VLT Survey Telescope (VST). Both images are displaying the same part of the sky. The top image is at longer wavelengths and where light suffers less absorption and scattering by dust particles interspersed in the nebular gas. The bright region shows the core of the cluster. It is surrounded by cool dust and gas visible as dark bands, with some of the red light from the stars behind shining through. Light absorbing dusty clouds are visible in front of the cluster in the bottom image as dark filamentary structures.

1.1 Circumstellar disks

Massive stars likely form, similar to their lower mass counterparts, through disk accretion. In this formation process a large gas cloud collapses into a disk through which the material can flow onto the central star. The material, as it gets closer to the central star, heats up and emits several unique diagnostic features. Among these features are double-peaked emission lines of various atoms and molecules such as hydrogen and carbon monoxide, and continuum emission from hot dust. The shape and strength of these spectral features give insight into the properties of the circumstellar material.

Chapter 2 focuses on two stars in M17, B243 and B331. These two stars are exceptional as Very Large Telescope (VLT) X-Shooter spectra reveal both their stellar atmosphere and circumstellar disk features. Additionally, photometric data shows that these stars also have hot circumstellar dust around them. These things combined indicate that they are in the final stages of their formation. We performed a detailed analysis of the double-peaked hydrogen emission lines and dust emission using *Pro*toplanetary *Di*sk *Mo*del PRODIMO. This model self-consistently calculates the heating and cooling of the disk material as well as the chemical processes that happen within the disk. The model then calculates the strength of the emitted lines and continuum, which allows us to determine the properties of the disk. This analysis showed that both disks reach close to, or even touch, the central stars. The lack of gap a between the disk and star suggests that the material can directly flow from the disk to the star, and is not transported along magnetic field lines. Additionally, we find that the mass of

Figure A: Giant H II region M17 in the Sagittarius-Carina arm of the Milky Way. The images have the same field of view ($\sim$18'). *Top panel*: Composite image based on the *Two Micron All Sky Survey* (2MASS) data with the J band represented in blue, H in green, and K in red. *Bottom panel*: Composite image from *VLT Survey Telescope* (VST) OmegaCAM with the G band represented in blue, R in green, and I in red. Credit: ESO/INAF-VST/OmegaCAM.

the disks are very low, limiting the effect the disks can still have on the central stars at their current evolutionary stage. Furthermore, the disks of both stars show signs or perturbation. The best fit model for B243 shows a disk with a radial extent of only a few AU, suggesting it has been truncated. The disk of B331 shows a large dust free inner cavity, indicating a dust clearing process. These findings shed some light onto the processes taking place during the final phase of the assembly of massive stars.

1.2 Binary star formation

An additional complication in the formation of massive stars is their multiplicity. The majority of massive stars are found in close binary systems. Stars in close orbits are likely to affect each others' evolution in significant ways, such as transferring mass and angular momentum or even merging. Orbital periods of massive stars can be constrained from radial velocity shifts due to their orbital motion and are on the order of a few days to months. However, a study of the radial velocities of the stars in M17 reveals little to no variation in their velocities. This suggests that either the stars in M17 are divergent in the sense that they are not actually in binary systems, or that the stars are in binary systems, but have large orbital periods. The latter causes small orbital velocities due to the slower motion of the stars, making it hard to identify them as binery systems. Chapter 3 studies a collection of young clusters and finds a trend in the typical orbital period of binary systems with age of the cluster. This means that stars start their lives in wide orbits with their companion, and grow closer over time. Fig. B sketches two possible scenarios to explain this hardening process. The first shows interactions between the circumstellar disks of young stars. Through such interactions, energy and angular momentum can be removed from the stars in their orbit allowing the components to grow close. Alternatively, the second scenario shows a process in which a third star is involved. The third star perturbs the inner two changing their orbit, making them slowly grow closer together. The wide orbital separation at birth affects theories that describe the formation of massive stars.

1.3 Young populations

The end result of the formation process remains elusive for the more massive stars. The moment that marks the end of star formation is essential, as it is the starting point of many stellar evolution models, and an important anchor point in the life of a star. The end of formation is typically defined as the moment at which the energy production in a star is dominated by hydrogen fusion. This is referred to as the ZAMS. The main sequence is the part of the stellar life in which it burns hydrogen. In Chapter 4 we determine the properties of a diverse population of stars in M17 through quantitative spectroscopy. We use VLT/X-Shooter observations and FASTWIND stellar atmosphere models to determine wind and atmosphere properties of the stars. We find stars with masses below 10 solar masses to be in the pre-main-sequence phase, so hydrogen fusion has not started yet for those stars. The more massive stars (masses above 10 solar masses), have reached the main-sequence but are still close to the ZAMS. Stars are rarely observed in this early evolutionary phase. Our

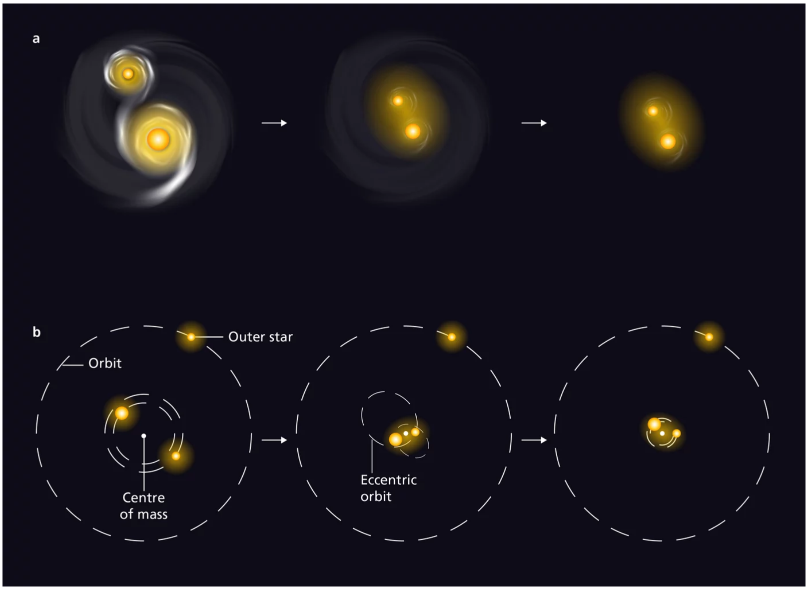

Figure B: Two scenarios for the hardening of binaries. The top panel shows the hardening as a result of circumstellar disk interactions. The two disks create a drag that allow the stars to grow closer together. In the bottom panel the scenario involved a third star. This star perturbs the binary resulting in an altered orbit. When the orbit settles again it is smaller than before.

observed sample of stars ($M > 10\,\mathrm{M}_\odot$) matches the theoretical predictions of the luminosity and temperature of stars on the ZAMS. This confirms theoretical predictions in a mass range for which the ZAMS location is very hard to empirically identify. For the lower mass stars that are still on the pre-main-sequence we do not fully understand the ages we find. There is a strong trend with the mass and the age of the stars that suggests that the more massive stars are the last to have started forming. The physics of the earliest phases of the formation for these 3 to 7 solar mass stars remain relatively poorly understood and the time scales involved are uncertain. At this phase of the evolution (younger than a million years old) stars of this mass range may not be the ideal to precisely determine the age of a cluster. Nonetheless, our age estimate of the cluster is consistent with other findings.

2 The winds of massive stars

In Chapter 5 we perform a similar study as in Chapter 4, but here focus on the winds of the hot giants and supergiants in the Small Magellanic Cloud (SMC). In addition to optical data from VLT we also use UV data from the Hubble Space Telescope. The SMC is a dwarf galaxy near the Milky Way. The metallicity, which is the mass fraction of elements heavier than helium, of the SMC is roughly five times lower than that of the Sun. The amount of heavy elements in the universe is ever increasing as they are formed through nuclear reactions in stars. Therefore, the stars in the SMC are representatives of stars that formed in an earlier universe, a more metal poor universe.

The metal content of stars is relevant to their lives as it impacts the amount of mass they lose over time. The strong radiation field of massive stars is absorbed (and re-emitted) in the spectral lines of mostly metal species in the outer most layers of the stars causing pressure pushing the material out. This interaction is stronger if heavier elements are more abundant, therefore stars with more metals drive stronger outflows of material.

These winds are likely not completely smooth, but instead have irregularities in their density, referred to as clumps. The 'clumpiness' of the wind affects the appearance of the diagnostic features used to measure the rate at which gas is transported out in the outflow, or mass-loss rate. For a given mass-loss rate some spectroscopic lines such as the hydrogen line Hα, can become significantly more pronounced if the wind is clumped. However, other lines, for example the nitrogen line N v 1240, can become significantly weaker if the wind is clumped. It is therefore of great importance to understand the clumping properties of a stellar wind when determining the mass-loss rate.

Chapter 5 analyses the stellar atmosphere as well as the wind structure of a population of SMC stars. The atmosphere properties are essential to getting accurate wind properties. We compare the wind properties found in this study of the SMC to comparable studies of the Large Magellanic Cloud (LMC) and the Milky Way (MW). Of these three samples the MW is most metal rich followed by the LMC. The SMC is the most metal poor. We find the SMC to have the weakest winds and the MW to have the strongest winds as expected. However, we also find that the difference in wind strength differs more between the samples at lower luminosity. For the fainter stars, the metal content plays a bigger role in the mass-loss rate than for the brightest stars.

We also compare the clumpiness of the wind between the SMC and LMC samples. We find a tentative trend that the outflow is more clumped for the more metal rich sample. However, this does still require more robust and thorough testing.

Nederlandse samenvatting

Het officiële begin van het leven van een ster is wanneer in het centrum thermonucleaire reacties beginnen waarbij waterstof wordt omgezet in helium. Op dat moment bereikt de ster het begin van de hoofdreeks (ZAMS, uit Engels zero-age main sequence). Zijn verdere leven wordt bepaald door verschillende ZAMS-eigenschappen, waarvan de totale stellaire massa en het impulsmoment, de chemische samenstelling, de magnetische veldsterkte en de mogelijke aanwezigheid van een of meer metgezellen in de buurt de belangrijkste zijn. Vooral de beginmassa is een kritieke parameter. Sterren met een beginmassa die minstens acht keer zo groot is als de massa van de zon worden als zwaar beschouwd. In tegenstelling tot sterren met een lagere massa ontwikkelen ze geen gedegenereerde kern in hun leven na de hoofdreeks en eindigen ze hun leven in een supernova.

Tijdens de waterstofverbranding in de kern, de hoofdreeksfase, zijn zware- sterren heet en fel. Hun oppervlakken kunnen temperaturen tot 50 000 K hebben, vergeleken met 5 700 K voor de zon. Hun lichtkracht kan meer dan een miljoen keer zo groot zijn als die van de zon, voornamelijk omdat de hogere druk in de kern - veroorzaakt door de grotere drukkende massa - zorgt voor een hogere energieproductie per stellaire massa-eenheid. Zware sterren verbruiken hun kernbrandstof dus sneller dan sterren met een lagere massa en leven daardoor korter. Zware sterren bereiken leeftijden van hooguit 50 miljoen jaar, terwijl de zon naar verwachting 12 miljoen jaar zal bestaan. Door hun korte levensduur worden zware sterren meestal gevonden in stervormingsgebieden. Het verschil in levensduur kan zo extreem zijn dat de meest zware sterren hun leven al hebben beëindigd, terwijl lichte sterren in dezelfde stervormingsfase de ZAMS nog niet hebben bereikt.

De combinatie van hoge oppervlaktetemperatuur en helderheid creëert een sterke flux van energetische fotonen die door de atmosfeer van de ster gaan. Dit typisch ultraviolette en optische licht wordt geabsorbeerd en opnieuw uitgezonden in spectraallijnen van voornamelijk metaalsoorten, zoals ijzer, en brengt netto momentum van het stralingsveld over naar het gas in de oppervlaktelagen. Dit zet een transsonische radiale uitstroom of stellaire wind in gang die zo sterk kan worden dat tijdens de levensduur van de ster meer dan de helft van de oorspronkelijke massa verloren gaat aan het interstellaire medium.

Door hun intense stralingsvelden, krachtige stellaire winden en energieke uiteindelijke explosies zijn zware sterren echte kosmische influencers. Ze ruimen het gas in hun omringende gebieden op door hete, geïoniseerde bellen te creëren, waardoor lokale stervorming mogelijk wordt stopgezet. Hun stellaire winden en supernovae die hun leven beëindigen, injecteren grote hoeveelheden gas, momentum en energie in het interstellaire medium, waardoor elders stervorming op gang kan komen. De gezamenlijke acties van veel zware sterren veroorzaken zelfs galactische winden. In de loop van de kosmische tijd hebben deze sterke terugkoppelingsprocessen een belangrijke rol gespeeld in de vorming en evolutie van sterrenstelsels en het heelal zelf. Straling van de eerste generaties zware sterren die ooit zijn gevormd, heeft bijvoorbeeld waarschijnlijk sterk bijgedragen aan de re-ionisatie van het intergalactische medium bij roodverschuivingen van ongeveer 30 tot 11. Een deel van het materiaal dat door zware sterren wordt uitgestoten, is in de vorm van nieuw verwerkte elementen, waardoor hun gaststelsels worden voorzien van de bouwstenen van planeten en leven.

Om al deze redenen is het van groot belang om de geboorte, het leven en de dood van zware sterren te begrijpen.

1 De geboorte van zware sterren

Om het leven van een zware ster goed te kunnen begrijpen, moeten we de oorsprong en de beginomstandigheden van de ster kennen. Het heldere H II gebied M17 is ons testgebied voor het ontstaan van zware sterren. Deze bubbel van heet geïoniseerd gas bevat een jonge sterrenhoop waarin de vorming van sterren minder dan een miljoen jaar geleden is begonnen. Figuur A toont beelden van deze sterrenkwekerij van de Two Micron All Sky Survey (2MASS) en de VLT Survey Telescope (VST). Beide afbeeldingen tonen hetzelfde deel van de hemel. De bovenste afbeelding heeft een langere golflengte en kan daarom beter door de stofabsorptie heen kijken. Het heldere gebied toont de kern van de sterrenhoop. Deze is omgeven door koel stof en gas, zichtbaar als donkere banden, waar wat rood licht van de achterliggende sterren doorheen schijnt. Stofwolken zijn zichtbaar aan de voorkant van de sterrenhoop in de onderste afbeelding als donkere filamenteuze structuren.

Zware sterren worden waarschijnlijk op dezelfde manier gevormd als hun tegenhangers met een lagere massa, door middel van schijfaccretie. In dit vormingsproces stort een grote gaswolk ineen tot een schijf waar in het materiaal naar de centrale ster kan stromen. Naarmate het materiaal dichter bij de ster komt, warmt het op en zendt het verschillende unieke diagnostische kenmerken uit. Deze kenmerken zijn onder andere (dubbel-gepiekte) emissielijnen van verschillende atomen en moleculen zoals waterstof en koolmonoxide-emissie, en continuümemissie van heet stof. De vorm en sterkte van deze kenmerken geven inzicht in de eigenschappen van het circumstellaire materiaal.

1.1 Circumstellaire schijven

Hoofdstuk 2 richt zich op twee sterren in M17, B243 en B331. Deze twee sterren zijn uitzonderlijk omdat VLT (Very Large Telescope) X-Shooter spectra zowel de ster atmosfeer als de kenmerken van de circumstellaire schijf laten zien. Daarnaast laten fotometrische gegevens zien dat deze sterren ook hete stofschijven om zich heen hebben. Dit alles wijst erop dat deze sterren zich in de laatste fase van hun vorming bevinden. We hebben een gedetailleerde analyse uitgevoerd van de dubbele-gepiekte waterstofemissielijnen en stofemissies met behulp

Figuur A: Het grote H II gebied M17 in de Sagittarius-Carina arm van de Melkweg. De afbeeldingen hebben hetzelfde beeldveld van ongeveer 18 boogminuten. De bovenste afbeelding bestaat uit fotos van de *Two Micron All Sky Survey* (2MASS), waarbij de data van de J band blauw is gekleurd, de H band is groen, en de K band rood. De onderste afbeelding gemaakt met de *VLT Survey Telescope* (VST) OmegaCAM door de G band in het blauw, R band in het groen, en I band in het rood te combineren. Credit: ESO/INAF-VST/OmegaCAM.

van *Pro*toplanetary *Di*sk *Mo*del PRODIMO. Dit model berekent zelfconsistent de opwarming en afkoeling van het schijfmateriaal en de chemische processen die in de schijf plaatsvinden. Het model berekent vervolgens de sterkte van de uitgezonden lijnen en het continuüm. Door de radiale en verticale structuur van de schijf te variëren, bepalen we de eigenschappen van de schijf. Uit deze analyse bleek dat de schijf de centrale ster dicht nadert of zelfs raakt. Het ontbreken van een kloof tussen de schijf en de ster suggereert dat het materiaal direct van de schijf naar de ster kan stromen, en dat geaccretteerd materiaal geen magnetische veldlijnen van de ster volgt. Bovendien vinden we dat de massa van de schijf erg laag is, waardoor het effect van de schijf op de ster in het huidige evolutiestadium beperkt is. Bovendien vertonen de schijven van beide sterren tekenen van verstoring. Het best passende model voor B243 laat een schijf zien met een radiale omvang van slechts enkele astronomische eenheden[1], wat suggereert dat de schijf is afgeknot. De schijf van B331 vertoont een grote stofvrije binnenholte, wat duidt op een stofverwijderingsproces. Deze vondsten werpen licht op de processen die plaatsvinden tijdens de assemblage van zware sterren.

1.2 Dubbelster stervorming

Een extra complicatie bij de vorming van zware sterren is dat de meeste zware sterren worden aangetroffen in nauwe dubbelster systemen. Sterren in nauwe banen beïnvloeden elkaars evolutie waarschijnlijk op belangrijke manieren, zoals het uitwisselen van massa of zelfs samensmelten. Typische omlooptijden van zware sterren zijn in de orde van enkele dagen tot maanden. Dit is gebaseerd op radiale snelheidsverschuivingen als gevolg van de omloopbewegingen van de sterren. Een studie van de radiale snelheden van de sterren in M17 laat echter weinig tot geen variatie in hun snelheden zien. Dit suggereert dat de sterren in M17 ofwel divergent zijn en geen dubbelster systemen vormen, of dat de sterren wel een dubbelster systeem vormen, maar grote omlooptijden hebben. Dit laatste veroorzaakt kleine omloopsnelheden door de langzamere beweging van de sterren, waardoor ze op een enkele ster lijken. Hoofdstuk 3 bestudeert een verzameling jonge clusters en vindt een trend in de typische omlooptijd van dubbelster systemen met de leeftijd van de cluster. Dit betekent dat sterren hun leven beginnen in wijde banen met hun wederhelft en na verloop van tijd dichter naar elkaar toe groeien. Figuur B schetst twee mogelijke scenario's om dit "verhardingsproces"te verklaren. Het eerste scenario laat interacties zien tussen de circumstellaire schijven van jonge sterren. Door de interactie kunnen energie en impulsmoment worden ontnomen worden van de sterren, waardoor ze naar elkaar toe groeien. Het tweede voorbeeld laat een proces zien waarbij een derde ster betrokken is. De derde ster verstoort de binnenste twee, waardoor hun baan verandert en ze langzaam naar elkaar toe groeien. Dit heeft invloed op de bestaande theoriën over sterformatie.

1.3 Jonge ster populaties

Het eindresultaat van het vormingsproces blijft moeilijk te achterhalen voor de zwaardere sterren. Het moment dat het einde van stervorming markeert is essentieel, omdat het het

---

[1] Een astronomische eenheid is de afstand tussen de zon en de aarde.

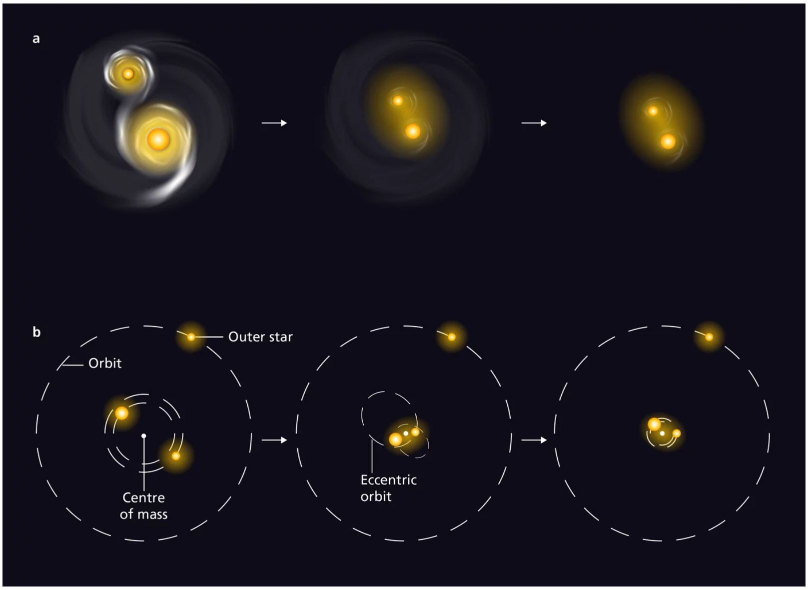

Figuur B: Twee scenario's voor het dichter naar erlkaar brengen van dubbelster systemen. Het bovenste scenario laat een situatie zien waarin het circumstellaire materiaal van twee sterren een wisselwerking met de sterren en elkaar hebben. In dit process kan impulsmoment en energie het systeem onstappen via de schijven. Het onderste scenario schetst een drie-ster systeem waarin de buitenste ster de binnenste twee verstoort in hun baan. Dit zorgt voor een elliptische baan, die over tijd weer circelvormig wordt, waarbij de sterren dichter naar elkaar bewegen.

startpunt is van veel sterevolutiemodellen en een belangrijk ankerpunt in het leven van een ster. Het einde wordt meestal gedefinieerd als het moment waarop de energieproductie in een ster wordt gedomineerd door waterstoffusie. Dit wordt het begin van de hoofdreeks (ZAMS[1]) genoemd. De hoofdreeks is het deel van het leven van een ster waarin waterstof wordt verbrand. In Hoofdstuk 4 bepalen we de eigenschappen van een diverse populatie sterren in M17 door middel van kwantitatieve spectroscopie. We gebruiken VLT/X-Shooter observaties en modellen van de steratmosfeer om de wind- en atmosferische eigenschappen van de sterren te bepalen. De sterren met een massa van minder dan 10 zonsmassa's bevinden zich nog voor de hoofdreeks, dus bij deze sterren is de waterstoffusie nog niet begonnen. De zwaardere sterren (met een massa van meer dan 10 keer die van de zon) hebben de hoofdreeks bereikt en staan heel dicht bij de ZAMS. Sterren worden zelden waargenomen in deze evolutionaire fase, waardoor er onzekerheid is over de eigenschappen van zulke sterren.

Onze collectie waargenomen sterren komt echter overeen met de theoretische voorspellingen van de helderheid en temperatuur van sterren op de ZAMS. Dit geeft aan dat we de belangrijkste eigenschappen van nieuw gevormde sterren theoretisch goed begrijpen. We begrijpen de leeftijden van sterren voor de hoofdreeks nog echter niet volledig. We vinden

---

[1] van zero age main sequence

een sterke trend tussen de massa en de leeftijd van de sterren die suggereert dat de zwaardere sterren als laatste zijn begonnen met vormen. De fysica van de vroegste vormingsfasen van deze sterren met een massa van 3 tot 7 zonsmassa's wordt nog steeds relatief slecht begrepen en de betrokken tijdschalen zijn onzeker. In deze fase van de evolutie (jonger dan een miljoen jaar) zijn sterren van dit massabereik misschien niet ideaal om de leeftijd van een cluster nauwkeurig te bepalen. Desalniettemin komt onze leeftijdsschatting van de sterrenhoop overeen met eerdere bevindingen.

2 De winden van zware sterren

In Hoofdstuk 5 voeren we een soortgelijke studie uit als in Hoofdstuk 4, maar hier richten we ons op de winden van de hete reuzen en superreuzen in de Kleine Magelhaense Wolk (KMW) en gebruiken we naast optische data van de VLT ook ultra violet data van de Hubble Space Telescope. De KMW is een dwergstelsel in de buurt van de Melkweg. De metalliciteit, een maat voor de hoeveelheid zware elementen ten opzichte van waterstof, van de KMW is ruwweg vijf keer zo laag als die van de zon. De hoeveelheid zware elementen in het heelal neemt steeds verder toe naarmate ze in sterren worden gevormd. De eerste sterren hadden geen zware elementen en na verloop van tijd worden sterren steeds metaalrijker. Daarom zijn de sterren in de KMW vertegenwoordigers van sterren die gevormd zijn in een vroeger heelal, een heelal dat armer was aan metalen.

Het metaalgehalte van sterren is relevant voor hun leven, omdat het van invloed is op de hoeveelheid massa die ze in de loop van de tijd verliezen. Het sterke stralingsveld van zware sterren heeft een wisselwerking met het gas in de buitenste lagen van de sterren, waardoor het materiaal onder druk komt te staan. Deze wisselwerking is sterker voor zwaardere elementen, waardoor sterren met meer metalen een sterkere uitstroom van materiaal, of sterwind, veroorzaken.

Deze winden zijn waarschijnlijk niet helemaal glad, maar hebben in plaats daarvan onregelmatigheden in hun dichtheid, of klonten. De ”klonterigheid”van de wind beïnvloedt het uiterlijk van de diagnostische kenmerken die worden gebruikt om de hoeveelheid materiaal in de uitstroom, oftewel het massaverlies, te meten. Voor een gegeven massaverliessnelheid kunnen bijvoorbeeld sommige spectroscopische lijnen, zoals de waterstoflijn H$alpha$, aanzienlijk geprononceerder worden als de wind samengeklonterd is. Andere lijnen, bijvoorbeeld de sterk geïoniseerde stikstoflijn N v,1240, kunnen echter aanzienlijk zwakker worden als de wind samengeklonterd is. Het is daarom van groot belang om het samenklonteren van een stellaire wind te begrijpen bij het bepalen van het massaverlies.

Hoofdstuk 5 analyseert zowel de steratmosfeer als de windstructuur van een populatie KMW-sterren. De eigenschappen van de atmosfeer zijn essentieel om nauwkeurige eigenschappen van de wind te krijgen. We vergelijken de windeigenschappen die gevonden zijn in deze studie van de KMW met vergelijkbare studies van de Grote Magelhaense Wolk (GMW) en de Melkweg (MW). Van deze drie stelsels is de MW het meest metaalrijk, gevolgd door de GMW. De KMW is het meest metaalarm. Zoals verwacht heeft de KMW de zwakste winden en de MW de sterkste. We zien echter ook dat het verschil in windsterkte tussen de sterren groter is bij lagere helderheid. Voor de minder heldere sterren speelt het metaalgehalte een grotere rol in de massaverliessnelheid dan voor de helderste sterren.

We vergelijken ook de klonterigheid van de wind tussen de GMW- en KMW-monsters. We vinden een voorzichtige trend dat de uitstroom meer klonterig is voor het meer metaalrijke monster. Dit moet echter nog robuuster en grondiger worden getest.

Acknowledgements

It has only been 10 years, but here it is. The end of my thesis. When I first stepped into the halls of Science Park I did not expect to be roaming these corridors for this long. Yet here we are. It has been a journey and it has been fun. Thanks all!

> *How lucky I am to have something that makes saying goodbye so hard.*
> – Winnie the Pooh

Oke, maybe there is more to say and just that. All these years have been full of fantastic experiences, adventures, and struggles; from trips to exciting places to being locked up at home due to a global pandemic[1]. I have been enriched as a person by all the amazing people around me. The API is a wonderful and special place to do research, full of caring, fun, and interesting people. The people make the API, but the API also makes the people. There are many people to thank for this. I will not be able to do my gratitude justice by what I will write below, because words are hard.

First I want to thank my supervisors Alex and Lex. You have guided me through my projects for the last $\sim$6 years with much vigor. You care deeply about producing good science, but also about the well being of all group members. Alex, your eternal didactic questions have made think a lot, but also learn a lot, thank you for that. I still regularly go back to your lecture notes to check things I definitely did not forget after learning them in SART. Meetings with you are a joy as there is a relaxed atmosphere, maybe because you first ramble about golf or football for a while before getting to business. Lex, your unbridled enthusiasm will never cease to amaze me. One lost scatter point on a plot I never intended to show anyone can get you all riled up with ideas and suggestions. You are full of scientific energy and desire to explore every question that is raised. This enthusiasm is infectious and has made me wish that there are more hours in the day and days in the week to give me time to investigate.

Then to my paranymphs, Annelotte and Caspar. You are some of the most different people in the institute, but probably more similar than you think. Annelotte you are a wildy energetic person who cannot sit still. It is spectacular to see you function. You are always happy and upbeat and helped me keep my sanity in these last stretches of my PhD. You are always ready to discuss the events of the outside world. I'll miss that, so keep me posted if anything interesting happens. But next to that we have had many interesting and insightful scientific discussions in our corner of the office. Even if sometimes it was just to use the other as a rubber ducky, it has been of great help. Caspar, your calm and collected vibes are a relaxing experience. Our friendship started late in my adventure, but has grown fast, but not as fast as Frodo. I have greatly appreciated you hospitality and amazing food in these last bits of my stay here at science park. We have explored infinite oceans and small backyards and I hope many more adventures are to come. I have thrown the most random and diverse questions at you and you have always delivered with great and genuine answers, which means a lot to me.

The massive stars group has of course also been essential to the completion of this thesis. Hanneke, thank you for your critical and sharp view, I am glad you are not in my committee. Handing you a paper draft means needing to rethink half of the content, but also elevating it to a higher level. Sarah, you have taught me a lot, from the intricate details of fitting atmosphere models to ”Do not mess with R_V”. Working with you is energizing, fun, and a little intimidating. Mitchel, please stop moving our stars around, they were perfectly fine where they were. Huib, Henny, I greatly appreciate all the insights you have shared in the group meetings. Silvia, Floris, Caspar, and now Adam as well, thank you for making life

---

[1] Which still lingers as I have been stricken by covid at the time of writing these acknowledgements...

complicated by asking about triples. Sam, Zsolt, Ylva, Manos, Mathieu, Jan, Rob, Jure, thank you all for all the knowledge you have spread to me and others.

Macla, thank you for putting down the basis of most of my thesis. Most of the Chapters concern M17, this is not a coincidence. Your work has been essential and the starting point of many of my projects. It is a great joy to work with you and Chapter 3 very much helped me survive the pandemic. Thank you, and Annelotte, for collecting and reducing the data that I was free to throw some models at. Jorick, Hughues, Frank, Jo, you have been essential to this thesis as well. The chapters are build on and inspired by your work and could not have happened without your direct or indirect contributions. This is from theories to build on to acquiring and reducing data, and writing codes. You have supplied essential ingredients of this thesis. Thank you, Inga and Christian, for guiding me in the usage of ProDiMo and assisting me in the world of circumstellar disk fitting. Thank you Carsten for welcoming me into your group meeting to learn about the intricacies of circumstellar disks.

On to the beginning of the PhD. Saying yes to the question ”Are you in?” on the first day of my PhD was one of the best choices I could have made. It was the creation of the Cairo Crew. Before I knew it everything was sorted and were were going to Egypt to see all of it, in just a few days time. Ben, Kenzie, thank you for this amazing start and the adventures that followed. Ben, at the time of writing we share 28 WhatsApp groups. I am not sure what that means, but I guess we have been up to stuff. I am fairly sure at least half of those are cycle trips to national parks and other exotic Dutch destinations. I have seen more of the Netherlands than I ever expected due to your eternal desire to explore. Yet... what could have happened at Twello? Kenzie, I am still regularly entertained by memory of the rescue mission to get you out of your own house (thanks Gregor). It is a good thing we went to Svalbard, it was the trip that broke the curse. I finally did not get ill on a trip with you. I am ready for the next one. You are a great friend and a joy to be around.

David, thank you for bringing such deep quotes to our lives. This profound wisdom that lives inside of your brain is just unimaginable, unreachable, and yet we saw it. You are always energetic and enthusiastic and pushing to do fun things, it’s amazing. Thank you for all the most weird chats one could possibly have and putting up with the most random questions without context. I will forever be amazed that you are all knowing when it comes to mozzarella. Thank you David, for dragging me to three different countries just so that you can get married and for providing Vlad and me with such a romantic getaway. Vlad, it would have never worked out between us. The romance just wasn’t there, but we will always have Orvieto. Thanks Vlad, for always wanting better for everyone. You are one of the most kind and caring people I know, keep it up. You have been a major force in the social life at API, which still has lasting effects, thank you for that.

Vatsal, there is never a dull moment with you around. You are eternally entertaining. I will forever picture you eating a cookie with a giant fireball behind you. Deniz, thank you for all your hot takes and wild theories. You have the ability to shake things up by throwing in a wild ”what if” or ”but.” Your curiousity is unparalleled. Alex, thanks for the great evenings with a beers and laughs in the Oerknal and your passionate discussions about sports and F1. Inés, no party is complete without you, thank you for being the life of every party. You bring

great joy and energy everywhere you go. Eleanor, it is impressive how much you do and still function. You are an amazing and kind person. Eva, thank you for being such an inspiration. You are the biggest go-getter I know and I feel nothing can stop you. Arkadip, thanks for all the random little conversations about nothing, but also for the incredible photos and videos you make. They are pretty insane. Dimitris, you are the teddy bear of API and everyone should experience a hug from you. Claire, thank you for giving me an opportunity to call an ambulance for the first time in my life and for sharing one of the most miserable moments of my life in the same agony. Lets never do either of those things again. Oli, I don't think I know anyone who is as much into every sport as you are, it is impressive. Niloo and Patrick, thank you for the fun Mario Kart sessions.

Stefanie, thank you for being a carrier of the API spirit. You are one of the kindest and most compassionate people I know. You wish the best for everyone and try your best to enforce it. It is truly admirable. Mitchel, thank you for showing me your true self in that cave, hmhc. Keep up the shenanigans. Mark, Omar, thank you for sharing your skills of recognizing the random spot on earth we are at based on a piece of tape on a car. I would not know what to do without this knowledge. Also, Mark, thanks for sharing footage of me that I considered lost. Evert, don't bully Martin too much, he already does that enough himself. Martin, thanks for all the coffee breaks, card games, and late night 'wisdom' in the Oerknal[1]. Thank you for being part of the furniture in API. A lot of the continuity within API comes from you and your stubborn dedication to maintaining some traditions. It is admirable, but don't be too hard on the new kids.

Mara, Mai, Milena, Kim, and your predecessors, Esther, Susan, and Renee, thank you for keeping the API running. We would all be lost without you. Milena, you bring infinite energy to the office, along with chaos and fun. I will miss the T-day rituals. Mia, you are a ray of sunshine strolling through the corridors of the institute. You are always happy and make sure that everyone feels welcome and comfortable. Your desire to help everyone is endless and incredible. Truly spectacular. Thanks for the many walks, May. Mara, you are a much needed and greatly appreciated voice of reason and stability in the secretariat. I appreciate that you put up with the little forced chats when I come to steal some fruit and question where the bananas went. Kim, I am pretty sure the institute crumbles without you. Thanks for keeping this ship afloat. Susan, I wonder if you should be co-promotor on some theses. Thanks for being there for the APIs.

Pragya, thanks for enduring my random monologues about nothing when I enter or leave the office. Luckily, you have Adam in these last few weeks to take over this burden, thanks Adam. I'll never forget the pretty disappointing rave we attended under a bridge near Amstelpark. Eleonora, thank you for not being too creeped out by the random selfies appearing on your phone and for always being kind and helpful. Dante, thank you for bringing the banger that is Kaptein to my life, it would not have been complete without it. Tomer, thank you for the many interesting scientific discussions.

---

[1] Yes, we know, your bike is there.

Nathalie, thank you for looking after API, you care deeply about the people and actually show that. Jason, thank you for being Jason. Thanks Ralph, for the many anecdotes and funny stories at the coffee table. Thanks for all amicable threats and comments, Rudy, they make me feel at home. Carsten, thank you for being the captain of this ship, we would sink without you. Thanks Phil, for your fairly entertaining rants. Jacco, your interesting and odd facts are appreciated.

Floris, Kate, Subhrat, (Mitchel), thank you for continuing the most important committee in API history, the committee with the most meetings and most events. I am of course talking about the Borrel Committee. API would no longer be complete without it. Lieke, thank you for pushing for the creation of this essential committee.

Niek, thank your for informing us of your concerts, it is a great joy to attend them. Bas, we have the strangest, most random, conversations. I think we never had a normal chat. Not that I mind though. I appreciate them. Iris, your real and healthy lunches inspire me to do the same. Though, I do tend to fail most of the time.

Thanks you, Arend, Micheal, and Ciarán, for being my minions. It has been fun and educational to tell you what to do.

Devarshi, thank you for inheriting my position, and thank you, +47...080, for inheriting it from him. It may not always be glamorous but it is important. Dion, thank you for bringing plants to the public spaces of the API, and keeping (most of) them alive.

Thanks, Vlad, David, Alex, el Greco, for the API sports. I was glad to show off my amazing football skills. Ruggero, maybe you get to admire them again one day. Tom, Evert, Jan, Tuomo, el Greco, Tomer, thanks for pizza. Thanks Esther for making the outreach easy and accessible.

Macla, Alice, thank you for introducing me to the office hour bouldering sessions. It has rekindled my passion for bouldering and raises the question if that Fontainebleau trip will still happen. Though I must admit, I now mostly boulder outside of office hours. Thanks David, Alex, +47...080, Vatsal, Alicia, Elspeth, Johan, Calum, Eleanor, Claire, Sam, Ben, for joining the bouldering sessions. But also a big thank you to all the named and unnamed bouldering buddies at USC: Christoff, Millon, Dillon, Malka, Maurice, Terrance, Mediocre Boys, Alex, James, David, Penny, Greek Buzzcut Guy, and the many other people who's names I have forgotten or have never known.

Eleonora and Adam, thanks in advance for taking good care of James and his friends. Hinna, thank you for being my new neighbor and putting up with me. Please, supervise Eleonora and Adam with their new duties.

I would also like to thank many of the APIs that went before me, Macla, Alice, Alicia, Kaustubh, Kamen, Samayra, Jakob, Matteo (but you're back anyways), Smriti, Ylva, Mathieu, Gullo, Nina, Georgi, Amruta, Tom, and more.., for making the API what it is and showing me the way.

Vriendjes en vriendinnetjes, ik wil jullie natuurlijk ook graag bedanken. Jullie zijn van groot belang geweest in veel van mijn vormende jaren. Van Mario Karten in tussenuren tot derde kerstdagborrels tot diep in de nacht, de blije middelbare school jaren hebben mij de nerd gemaakt die ik nu nog altijd ben. Dank voor alle goede tijden en gezellige avonden. We zijn nu allemaal wat verspreid, maar mogen er nog vele volgen.

Gekke boisss! Bedankt bij het helpen doorstaan van de bachelor jaren. We studeerden zo hard dat camera crews ons volgden (oke alleen die ene keer dan, ik nog steeds geen idee waar die fotos heen zijn). Daarna op met drie man op Joeps fiets naar de stad en met de eerste trein weer naar huis. Ik voel me een beetje een oude man nu... Bedankt voor deze mooie jaren.

ICDEF! pH, Bram! Thanks voor de vele rondjes tafelvoetbal en LOTR Risk. Ik heb geen idee hoe we iets gedaan kregen met zo veel pauzes en zo veel halfbakken chocomel uit de automaten. Tito! Bedankt voor de goede master jaren. Ons geweldige La Palma project inspireert nog altijd nieuwe generaties studenten hetzelfde te doen. Onze treinreis bracht me klaar om te beginnen naar de eerste dagen van mijn PhD.

En dan de rest. P, Heleen, bedankt voor alle steun door alle jaren heen. Jullie hebben mij de vrijheid gegeven om te doen wat ik maar wil. Ik heb mij altijd gesterkt gevoeld in mijn keuzes door het vertrouwen dat jullie in mij hebben. Zelfs zonder enige vervolg plannen of ideeën lieten jullie mij op pad gaan. Ik heb geen idee wat jullie goed of juist fout hebben gedaan om het zo ver te laten komen, maar dit is het resultaat. Een boek dat je niet voor je plezier leest. Verder wil ik graag iedereen van de ontbijtgang bedanken. De gezellige, maar ook zeer chaotische, ontbijtjes en ander activiteiten brengen de nodige afleiding en perspectief in het leven. Dit is essentieel geweest. Bedankt voor alles.

Love you all,

Frank

The real stars are the friends we made along the way.
– Benjamin Sutlieff